Inaugural dissertation
for
obtaining the doctoral degree
of the
Combined Faculty of Mathematics, Engineering and Natural Sciences
of the
Ruprecht - Karls - University
Heidelberg

Presented by

M.Sc. Yu-Le Wu
born in: Taipei
Oral examination: June 24th, 2022

Maximum-likelihood model fitting for quantitative analysis of SMLM data

Referees: Prof. Dr. Michael Knop
Dr. Anna Kreshuk

„You cannot connect dots looking forward, but you can connect dots looking backwards.“

Steve Jobs

Published and released works I contributed to that are not described in this thesis:

Li, Y., **Wu, Y.-L.**, Hoess, P., Mund, M., Ries, J. 2019. Depth-dependent PSF calibration and aberration correction for 3D single-molecule localization. *Biomedical Optics Express*, **10**(6), 2708–2718.

Thevathasan, J. V.*, Kahnwald, M.*, Cieśliński, K., Hoess, P., Peneti, S. K., Reitberger, M., Heid, D., Kasuba, K. C., Hoerner, S. J., Li, Y., **Wu, Y.-L.**, Mund, M., Matti, U., Pereira, P. M., Henriques, R., Nijmeijer, B., Kueblbeck, M., Sabinina, V. J., Ellenberg, J., Ries, J. 2019. Nuclear pores as versatile reference standards for quantitative superresolution microscopy. *Nature Methods*, **16**(10), 1045–1053.

Cieslinski, K., **Wu, Y.-L.**, Nechyporenko, L., Hörner, S. J., Conti, D., Ries, J. 2021. Nanoscale structural organization and stoichiometry of the budding yeast kinetochore. *bioRxiv*.

Parts of the work described in this thesis have been published or released:

Wu, Y.-L.*, Tschanz, A.*, Krupnik, L.*, Ries, J. 2020. Quantitative Data Analysis in Single-Molecule Localization Microscopy. *Trends in Cell Biology* **30**: 837–851.

Wu, Y.-L., Hoess, P., Tschanz, A., Matti, U., Mund, M., Ries, J. 2021. Maximum-likelihood model fitting for quantitative analysis of SMLM data. *bioRxiv*.

Mund, M., Tschanz, A., **Wu, Y.-L.**, Frey, F., Mehl, J. L., Kaksonen, M., Avinoam, O., Schwarz, U. S., Ries, J. 2022. Superresolution microscopy reveals partial preassembly and subsequent bending of the clathrin coat during endocytosis. *bioRxiv*.

This work was carried out at the European Molecular Biology Laboratory in Heidelberg from October 2017 to March 2022 under the supervision of Dr. Jonas Ries.

Abstract

Super-resolution techniques have enabled fluorescence microscopy to surpass the diffraction limit of light and resolve nanoscale biological structures with molecular specificity. As with other microscopy data, quantitative analyses of super-resolution images have enabled great insight into the underlying architecture of many macromolecular structures. However, this is still a challenging process, especially in the field of single-molecule localization microscopy (SMLM). Unlike pixelated images yielded by most microscopy techniques, SMLM data is composed of a list of fluorophore coordinates and their specific positional uncertainties. Therefore, applying pixel-based approaches to SMLM data requires image rendering, which can cause loss of information and can complicate the analysis. These drawbacks can be mitigated by using coordinate-based approaches.

However, currently available coordinate-based approaches in SMLM are typically only applicable to simple geometries or require identical structures. These approaches do not support a basic task in structural analysis: postulating a model with a suitable underlying geometry to probe key parameters in a biological structure.

Here, I present LocMoFit (Localization Model Fit), a new framework for fitting a parameterized geometric model to SMLM data at the level of localizations. Based on maximum likelihood estimation, LocMoFit extracts meaningful parameters from individual structures and can select the most suitable model.

Using the nuclear pore complex, microtubules, and clathrin-mediated endocytosis (CME) as examples, I demonstrate the application of LocMoFit in *in situ* structural biology for extracting descriptive parameters of complex, heterogeneous and even dynamic structures. Beyond that, I further showcase applications including assembling multi-protein distribution maps of six nuclear pore components, calculating single-particle averages without any structural prior, and reconstructing the progression of endocytosis - a highly dynamic process - from static snapshots.

On the one hand, the quantitative analysis allowed to address a long-standing controversy of how the clathrin coat is rearranged during CME in mammalian cells. On the other hand, the dynamic reconstruction of representative endocytic proteins over the endocytic progression shows the potential of revealing previously unknown nanoscale features that may be associated with force generation during CME in yeast.

To ensure all these functionalities are accessible, I implemented LocMoFit as open-source and provided instructions and model templates. A simulation engine and visualization routines are also supplied for users to examine the plausibility of their

own analysis, which is also what I used to validate the robustness of the framework in this work. With these, I believe LocMoFit will enable any user to extend the information that can be faithfully extracted from SMLM data.

Zusammenfassung

Superauflösende Techniken haben es der Fluoreszenzmikroskopie ermöglicht, die Beugungsgrenze des Lichts zu überwinden und biologische Strukturen im Nanobereich mit molekularer Spezifität aufzulösen. Wie auch bei anderen Mikroskopiedaten hat die quantitative Analyse von superaufgelösten Aufnahmen neue biologische Erkenntnisse ermöglicht. Allerdings stellen solche Untersuchungen noch immer eine Herausforderung dar, insbesondere in der Einzelmolekül-Lokalisationsmikroskopie (engl. *single-molecule localization microscopy*, SMLM). Im Gegensatz zu den pixelbasierten Bildern der meisten Mikroskopietechniken bestehen SMLM-Daten aus einer Liste von Fluorophor-Koordinaten und den Unsicherheiten, mit denen sie bestimmt wurden. Daher erfordert die Anwendung von pixelbasierten Ansätzen auf SMLM-Daten die Rekonstruktion eines Bildes, was zum Verlust von Informationen führt und die Analyse erschweren kann. Diese Nachteile können durch die Verwendung koordinatenbasierter Verfahren verringert werden.

Derzeit verfügbare koordinatenbasierte Verfahren sind jedoch in der Regel nur auf einfache Geometrien anwendbar oder erfordern identische Strukturen. Damit unterstützen sie eine grundlegende Aufgabe der Strukturanalyse nicht: die Erstellung eines geometrischen Modells, um wichtige Parameter einer biologischen Struktur zu untersuchen.

Hier stelle ich LocMoFit (engl. *Localization Model Fit*) vor, ein neues Verfahren welches das Fitten eines parametrisierten geometrischen Modells an SMLM-Daten ermöglicht, und direkt auf der Ebene der Fluorophor-Koordinaten angewendet wird. Auf der Grundlage der Maximum-Likelihood-Methode extrahiert LocMoFit aussagekräftige Parameter aus einzelnen Strukturen und kann das am besten geeignete Modell auswählen.

Am Beispiel von Kernporenkomplexen, Mikrotubuli und Clathrin-vermittelter Endozytose (engl. *clathrin-mediated endocytosis*, CME) demonstriere ich die Anwendung von LocMoFit in der *in situ* Strukturbiologie zur Extraktion von Parametern komplexer, heterogener und sogar dynamischer Strukturen. Darüber hinaus stelle ich weitere Anwendungen vor, darunter die Bestimmung der räumlichen Verteilung von sechs Kernporenkomponenten, die Berechnung einer Durchschnittsstruktur aus einzelnen Partikeln ohne strukturelles Vorwissen und die dynamische Rekonstruktion des Verlaufs der Endozytose – eines hochdynamischen Prozesses – aus statischen Einzelaufnahmen.

Einerseits ermöglichte die quantitative Analyse der CME in Säugetierzellen die Aufklärung einer langjährigen Kontroverse darüber, wie die Clathrin-Hülle während des Prozesses umgeordnet wird. Andererseits zeigt die dynamische Rekonstruktion

vier verschiedener Proteine – die als Beispiel für verschiedene endozytotische Module dienen – während der Endozytose in Hefe das Potenzial von LocMoFit, bisher unbekannte Merkmale im Nanobereich aufzudecken, die mit der Krafterzeugung während der CME im Zusammenhang stehen könnten.

Um all diese Funktionalitäten leicht zugänglich zu machen, habe ich LocMoFit als Open-Source-Programm implementiert und Anleitungen und Modellvorlagen bereitgestellt. Funktionen zur Simulation und Visualisierung sind ebenfalls enthalten, damit die Nutzer die Plausibilität ihrer eigenen Analysen überprüfen können. Ich glaube, dass LocMoFit es jedem Nutzer ermöglicht, mehr Informationen aus SMLM-Daten zu extrahieren.

Acknowledgments

I am grateful to people who have taken part in my PhD work and life in the last 4.5 years.

First of all, I would like to thank you Jonas for having me in your wonderful group so that I can work with amazing people on exciting projects. I benefited from your supervision style a lot. You allowed me to explore my own ways and gave me key instructions and advice at the same time. You always take your time, try your best and are always patient whenever I need your guidance and support. You keep up a great group atmosphere, spirit, and traditions. All these are amazing. Thank you!

I would also like to say thank you to my TAC members Dr. Anna Kreshuk, Prof. Michael Knop, and Dr. Martin Beck for your discussion and advice. Thank you to Anna and Michael Knop for reviewing this thesis. I also want to thank you Prof. Ulrich Schwarz for your participation in my thesis defense committee.

Thank you to EMBLers for making EMBL a great place for doing research. Thank you to the people I have met in Heidelberg and life in Germany.

Thank you to all present and past members of the Ries group. Thank you Jonas, Ulf, Markus, Joran, Kostek, Li-Ling, Yiming, Jervis, Philipp, Aline, Robin, Angie, Takahiro, Sheng, Michal, Soheil, Sarah, Daniel, Julia, Sudheer, Alex, Maurice, Anindita, Lucas, Eric, Cheng-Yu, Amir, Andreas, Leo, Tomas, Lisa, Vincent, Marija, Jan, Veronika, Jonas, Lisa, Eva, and Saeed. We together make the group so diverse and multicultural, as part of the group culture. It is fantastic not only to work with you guys, but also to enjoy lunches, parties, retreats, and more activities together. Yes, we have done many things together. I miss the time when some of us went running as a group and when we played GeoGuessr together. I am honored to be responsible for the game start countdown, even though I am not good at the game. Even our time during train rides to conferences was also enjoyable because we always chatted and shared a lot. In the beginning, getting things around Germany was not that easy for me. Thanks for the help and hints from many of you.

I am thankful for the help from Philipp, Ulf, Robin, and Markus in translating documents and phone calls. Many thanks to Li-Ling for inviting me to dinners on Taiwanese traditional holidays, to Yiming for introducing me to the Chinese community at EMBL, to Joran for bringing a lot of laughter to the lab, to Jervis and Kostek for your trust to let me contribute to your projects, to Maurice, Anindita, and Lucas for being like permanent lab members, to Aline and Leo for contributing to our review paper, to Tomas for memes and bad jokes, to Sheng for feeding us on the train, to Angie for your creativity (especially during the cultural Karaoke), and to Aline and Takahiro for our language/culture exchange. Thank you Lisa for contributing to the kinetochore project on data analysis and illustrating the pretty model schematic. Thank you Vincent for letting me contribute a bit to your VR project. Thanks all users (Philipp, Aline, Maria, Ivana, Markus, and Tomas) of LocMoFit for your feedback. There are too many good people and good things that we have done together in these years. Please forgive me that there is not enough space to mention them all.

I would like to especially thank some labmates. Thank you to Philipp and Aline for your valuable input to my thesis, for hunting typos, and for backing me up till the last minute. Thank you Philipp for letting me take part in your project and helping me get the hang of experiment-related things when I started my PhD. The project was the root of the work described in this thesis. I have learned (a bit) from how you organize things in a very systematic way. Thank you for the good places you recommended when I traveled around Germany. I also liked our cultural exchanges a lot.

Thank you Aline for being the first routine user of LocMoFit and for the bugs you actively reported, which really helped improve the software. Thank you for writing the review paper with me. Coordination between three main contributors is not easy and it was my first time writing a review paper. But we made it! Thank you for always thinking of your labmates, bringing us cakes from your grandma, and Swiss cheese.

Thank you Markus for genuinely sharing your knowledge, thoughts, and many constructive suggestions and help. Thank you for always taking your time and effort when I turned to you. You always hyped your labmates up when we overlooked our contributions. That means a lot to me.

Thank you Ulf for your support in all aspects. You helped me to get things around not only in the lab but also in life. Thanks for showing how beautiful Heidelberg is from your boat. You really know so many things and, most importantly, always be willing to help others. Huge respect!

Thanks the other predocs in the batch of 2017. It was really nice to take the predoc course, organize events, and enjoy parties with you guys. Especially to Huiting, Jane, Vaishali, Daja, Stefano, Stephanie, Danila, and Liang, for all the food outings, hot pots, potluck, and birthday parties. Thanks Stefano for the ride to Strasbourg and the time we spent together there. Thanks Mathias for the dinners at your place, language exchange, our time at cafes, and for helping me move.

By the way, in this chapter, instead of blaming, I can only say 'thank you' to Covid-19 for letting me know how precious normal life used to be.

Thank you Shan for your company, endless support, and your care and love. 很多時刻，總是會第一時間的想到妳。很開心能有個人一起分享生活中的一切，不論大小或好壞。很高興妳來到德國，讓我們能每週見面，能一起完成很多事。妳也是個完美旅伴。沒有妳的旅行漸漸變得索然無味。謝謝妳在方方面面的支持與幫助。特

別感妳在過去幾個月的體諒，很多想一起做的事都被迫延後，行程要遷就於我。還有太多文字無法乘載的，希望妳感受得到。

Finally, I would also like to thank my friends and family in Taiwan. 感謝我的爸爸吳映請、媽媽李映嫺、弟弟吳昱妥。謝謝你們對我的全力支持，讓我可以沒有後顧之憂的完成學業。謝謝你們每個週末的等候，等著我們定期的視訊，讓我感受到你們的陪伴。也謝謝朋友們的支持。雖然因為距離的限制，沒能常聯絡，也錯過了許多你們的重要時刻。但回台灣時，你們總會願意出來敘敘舊，用行動維繫我們的友誼。謝謝你們。

Table of Contents

List of Figures

List of Tables

List of Algorithms

List of Abbreviations

4Pi-SMS	4Pi-Single-Molecule Switching
AF647	Alexa Fluor 647
$\mathbf{AIC_C}$	Corrected version of the Akaike information criterion
ASAP	Automated Structures Analysis Program
BFP	Back focal plane
CALM	Clathrin assembly lymphoid myeloid leukaemia protein
CBM	Clathrin-binding motif
CH	Calponin homology
CLR	Calponin-like repeat
CME	Clathrin-mediated endocytosis
CP	Capping protein
CR	Cytoplasmic ring
DBSCAN	Density-Based Spatial Clustering of Applications with Noise
DMEM	Dulbecco's modified Eagle's medium
DMEM/F12	Dulbecco's modified Eagle's medium combined with Nutrient Mixture F-12
dSALM	Direct Supercritical-Angle Localization Microscopy
dSTORM	Direct STochastic Optical Reconstruction Microscopy
EH	Eps15-homology
EMU	Easier Micro-Manager User interface
ExM	Expansion Microscopy
F-actin	Actin filament
FBS	Fetal bovine serum
FoV	Field of view
fPALM	Fluorescence PhotoActivated Localization Microscopy
G-actin	Globular actin
GFP	Green fluorescent protein
iPALM	Interferometric PhotoActivated Localization Microscopy
JF	Janelia Fluor
LocMoFit	Localization Model Fit
M1	Microscope 1
M2	Microscope 2
MINFLUX	MINimal emission FLUXes

ML	Machine learning
MLE	Maximum likelihood estimation
NA	Numerical aperture
NL-SIM	Non-Linear Structured Illumination Microscopy
NPC	Nuclear pore complex
NPF	Nucleation promoting factor
NR	Nucleoplasmic ring
Nup	Nucleoporin
PAINT	Point Accumulation for Imaging in Nanoscale Topography
PALM	PhotoActivated Localization Microscopy
pan-ExM	Pan-Expansion microscopy
PDF	Probability density function
PERPL	Pattern Extraction from Relative Positions of Localizations
PR	Proline-rich
PSF	Point spread function
RESOLFT	REversible Saturable OpticaL Fluorescence Transitions
ROI	Region of interest
RPD	Relative position distribution
SAF	Supercritical angle fluorescence
SH3	SRC homology 3
SIM	Structured Illumination Microscopy
SMLM	Single-Molecule Localization Microscopy
STED	STimulated Emission Depletion
STORM	STochastic Optical Reconstruction Microscopy
TH	Tail homology
TIRF	Total Internal Reflection Fluorescence
ToMATo	Topological Mode Analysis Tool
UAA	Unnatural amino acids
UAF	Undercritical angle fluorescence
UIM	Ubiquitin-interacting motif
WH1	WASP homology 1
WH2	WASP homology 2

1 Introduction

Seeing is believing. Granted by microscopy, the ability to visualize things smaller than naked eyes can see has revolutionized biological research. This change can be dated to 1665 when Robert Hooke discovered 'cells' using a microscope (Hooke, 1667). Later in 1677, Antonie van Leeuwenhoek observed 'small animals' in rainwater, again bringing microscopy to the attention of the public (van Leewenhoeck, 1677). Centuries later, fluorescence microscopy, invented in 1911 (Heimstädt, 1911), has become a common tool and fostered the development of many fields including cell biology. Progress in labeling strategies such as fluorescently labeled antibodies (Coons *et al.*, 1942) and fluorescent proteins (Chalfie *et al.*, 1994; Prasher *et al.*, 1992) has illuminated the targets of interest and allowed the observation of biological processes that had been previously invisible.

The application range of fluorescence microscopy has been expanded also by technical advances such as the Total Internal Reflection Fluorescence (TIRF) microscope and confocal microscope (Thorn, 2016). However, the diffraction of light causes the pattern of a point light source imaged by an optical microscope to be no longer a point but a blurred disc. In conventional microscopy, the blurring causes the emitters that are less than a few hundreds of nanometers apart to overlap so that they cannot be resolved (Abbe, 1873). This limit had remained a challenge until the invention of super-resolution microscopy techniques.

1.1 Super-resolution microscopy

When two point sources of light are closer than a minimal distance, they become indistinguishable under a microscope. The minimal distance d, according to the criteria derived by Rayleigh (Rayleigh, 1903), is given as follows:

$$d = \frac{0.61\lambda}{n\sin\theta} = \frac{0.61\lambda}{\mathrm{NA}} \tag{1.1}$$

Here, λ is the wavelength of the observed light, n is the refractive index of the imaging medium, and θ is the half opening angle of the objective lens. $n\sin\theta$ can be also represented as the numerical aperture (NA), which defines the resolving power of a microscope objective.

In the following sections, I will discuss the new techniques that have been invented in the past decades to break the diffraction limit in fluorescence microscopy (Figure 1.1).

1.1.1 Structured illumination microscopy (SIM)

Because of the diffraction limit, fine details, or high-frequency structures of the imaged target, cannot be acquired with a conventional microscope. By transferring high-frequency structures in the specimen to the low-frequency space that is observable by a microscope, SIM (Gustafsson, 2000) improves the resolution by a factor of up to 2 based on a structured pattern of illumination (Figure 1.1a). This improvement relies on Moiré fringes, which are the lower-frequency interference pattern of two superimposed non-identical fine patterns. In SIM, these two patterns are the imaged target and a known pattern of structured illumination, where periodic parallel sinusoidal stripes are the most common pattern. For the same imaged target, shifting and rotating the illumination pattern yields different sets of Moiré fringes that contain different parts of the high-frequency structure. Therefore, by combining these sets of fringes, more complete high-frequency information can be reconstructed. This reconstruction requires computational analyses that are usually performed in the Fourier space. Furthermore, by creating the same pattern along the axial direction, SIM can be extended to the third spatial dimension (Gustafsson *et al.*, 2008).

In principle, SIM does not require specialized fluorophores, although bright and photostable fluorophores are preferred. This preference is to fulfill the premise that the imaged structure remains identical across all images acquired subsequently. Benefiting from its relatively low illumination power requirement and widefield mode, SIM has lower phototoxicity and higher imaging rate compared to most other super-resolution techniques, making SIM suitable for live-cell imaging. Further advances of SIM, such as non-linear SIM (NL-SIM) (Gustafsson, 2005; Rego *et al.*, 2012) and light-sheet SIM (Breuninger *et al.*, 2007; Keller *et al.*, 2010), have opened up the application range of SIM with improved resolution and reduced phototoxicity. However, we have to keep in mind that the imperative data processing of SIM can potentially cause artifacts (Schaefer *et al.*, 2004) that have to be evaluated and avoided (Ball *et al.*, 2015; Förster *et al.*, 2016).

SIM has been used to visualize single nuclear pore complexes (NPCs) in 3D in fixed cells (Schermelleh *et al.*, 2008), and the dynamics of clathrin-mediated endocytosis together with the cortical actin cytoskeleton in live cells (Li *et al.*, 2015).

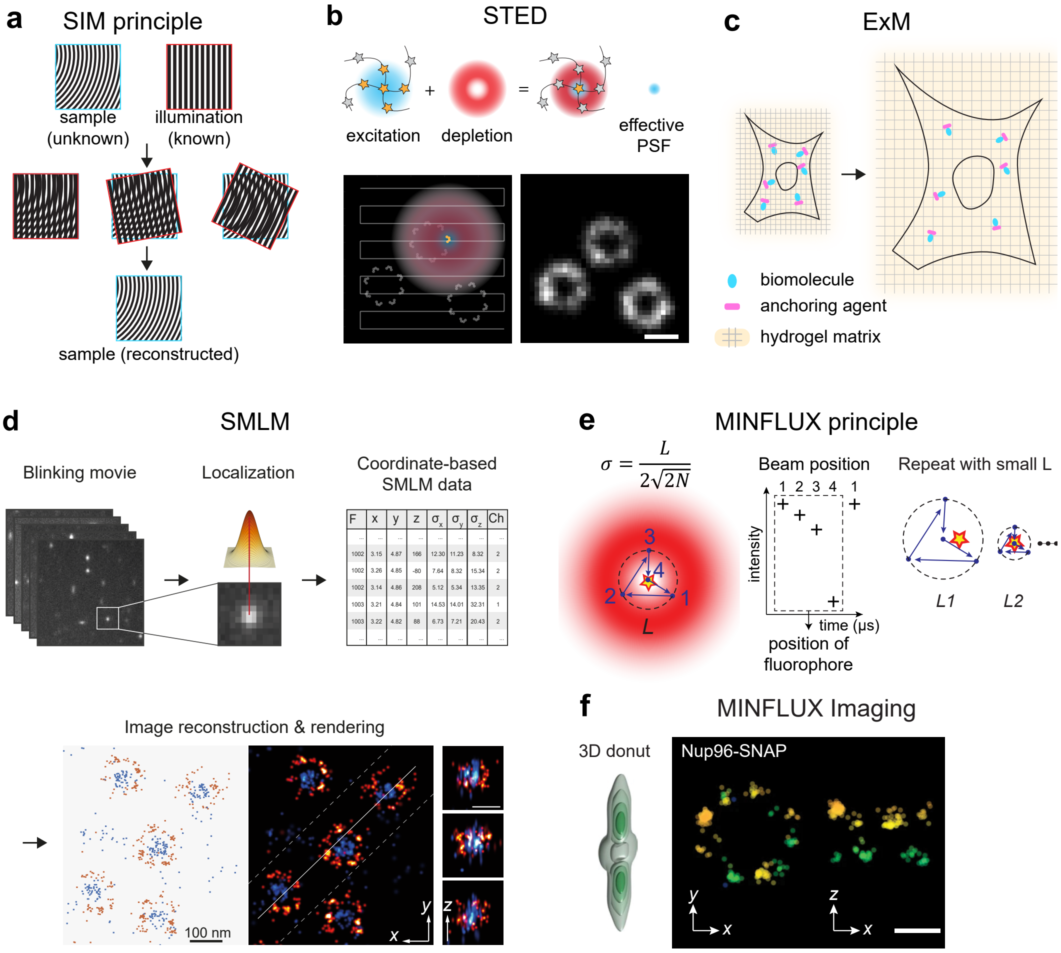

Figure 1.1 | Overview of super-resolution microscopy techniques. (**a**) Structured illumination microscopy (SIM). By superpositioning the unknown high-frequency sub-diffraction pattern in the sample with a structured sinusoidal illumination, Moiré fringes can be generated, which carry the partial information of the unknown pattern as an observable lower-frequency pattern. By integrating Moiré fringes created with different orientations of the illumination pattern, the unknown pattern can be reconstructed, with the resolution improved twofold. (**b**) Stimulated emission depletion (STED). The donut-shaped depletion beam superpositioned with the excitation beam suppresses the fluorescence emission in the periphery, thereby reducing the size of the effective point spread function (PSF). The superpositioned beams raster scan across the field of view (FoV), yielding a super-resolution image. (**c**) Expansion microscopy (ExM). By embedding and covalently linking biomolecules to a hydrogel which gets swelled subsequently, structures within the biological specimen get expanded and therefore enlarged. The enlargement allows resolving of diffraction-limited structures by conventional microscopes. (**d**) Single-molecule localization microscopy (SMLM). Single emitters of photoactivatable fluorophores labeling specific biomolecules are acquired in the frames of a blinking movie. Positions of these non-overlapping emitters can be obtained by fitting a PSF. A super-resolution image can then be reconstructed and rendered based on the list containing the fitted positions or localizations, and their uncertainties. (**e-f**) Minimal emission fluxes (MINFLUX). A donut-shaped excitation beam is used to probe a single emitter with a specific scanning pattern. Here, a typically used triangular pattern is illustrated. The fluorophore's position is estimated geometrically based on the photons detected from the positions. This approach leads to the dependence of localization precision σ on the scanning pattern size L and photon count N. Iteratively scanning with decreasing size L and updating the center position achieves better localization precision. The use of a 3D donut can extend MINFLUX to 3D imaging. *Subpanels b, c, e, f have been adapted from Liu* et al., *2022 with permission. Subpanel d has been adapted from Wu* et al., *2020, on which I am the co-first author, with permission.*

1.1.2 Stimulated emission depletion (STED)

STED is a scanning imaging technique that yields higher resolution than SIM. STED achieves super-resolution by reducing the effective size of the PSF to the sub-diffraction range (Figure 1.1b). In practice, this is implemented by positioning a donut-shaped depletion illumination on top of the focus of the excitation laser beam to confine the fluorescence to the center of the donut (Hell and Wichmann, 1994). Scanning through the sample with such a sub-diffraction PSF produces a super-resolution image without the need for data processing after image acquisition. The depletion illumination is red-shifted (so-called *STED beam*) compared to the excitation and emission maxima. The STED beam induces the stimulated emission of an excited fluorophore: instead of returning back to the original ground state and releasing the emission spontaneously, the fluorophore returns back to a ground vibrational state with higher energy and releases red-shifted photons that have the same wavelength as the STED beam. 3D STED can be achieved by incorporating another incoherent STED beam producing a bottle-shaped focus to confine the fluorescence axially.

In principle, a higher power of the STED beam reduces the size of the central zero intensity more and yields better resolution. However, the higher power increases photobleaching and phototoxicity, so a reasonable power has to be adapted for sample compatibility. Therefore, the typical resolution achieved by STED is between 30 to 80 nm (Sydor *et al.*, 2015).

The generalized STED concept is adapted to RESOLFT (REversible Saturable OpticaL Fluorescence Transitions), which requires a fluorophore that has two reversibly switchable distinct states that can be optically converted (Hofmann *et al.*, 2005). In RESOLFT, usually a donut-shaped illumination that can switch the fluorophore to an invisible off state is used to replace the STED beam. The off-switching illumination usually requires much less intensity compared to the STED beam and hence drastically reduces the phototoxicity caused by imaging.

Optimized STED and RESOLFT can be used for performing live imaging, including the study of dendritic spines in mouse brain (Berning *et al.*, 2012; Steffens *et al.*, 2021) and dynamics of sub-organelle structures (Stephan *et al.*, 2019; Damenti *et al.*, 2021).

1.1.3 Expansion microscopy (ExM)

Instead of pushing the limit of optical resolution, sub-diffraction resolution has been also achieved by tweaking the sample preparation such as physically expanding the sample in ExM (Figure 1.1c; Chen *et al.*, 2015). In the post-expansion sample, the space between molecules in a sub-diffraction region is physically expanded by a factor of 4 to 10 and the molecules become resolvable by diffraction-limited microscopes such as a standard confocal microscope (Wassie *et al.*, 2019).

Practically, the fixed sample is embedded in a dense network of a swellable hydrogel based on acrylamide. The hydrogel is then swelled by water, so as the embedded sample therein. Prior to the expansion, the biomolecules of interest (DNA/RNA/protein, etc.) or labels have to be anchored to the hydrogel network to retain their relative positions. Afterwards, to retain the structural integrity of the post-expansion sample, protease digestion or protein denaturation before expansion is necessary. Based on different protocols, the fluorescence labeling can be done pre- or post-expansion. The latter option has the advantage of having the fluorophore not rendered non-fluorescent by covalent modifications during the polymerization reaction of the hydrogel. Because the expansion of the spacing between the label and target is avoided, the linkage error can be reduced proportionally to the expansion factor (Zwettler *et al.*, 2020).

The modified sample preparation protocol is independent of the optical setup and therefore can be combined with other super-resolution techniques such as single-molecule localization microscopy (see the next section 1.1.4; the combined technique is termed ExSMLM; Zwettler *et al.*, 2020) to further improve the resolution. However, ExM is not live cell compatible, regardless of the protocol being used. In addition, non-isotropic expansion can distort the embedded biological structure (Thevathasan *et al.*, 2019). Iterative ExM with unspecific labeling of the whole proteome (pan-ExM) has achieved EM-like ultrastructural context of cells (M'Saad and Bewersdorf, 2020).

1.1.4 Single-molecule localization microscopy (SMLM)

1.1.4.1 The working principle of SMLM

SMLM is again a widefield imaging method. In conventional microscopy, all fluorophores are excited at the same time, resulting in the fluorophores distributed in a sub-diffraction region indistinguishable because of overlapping emitters. SMLM takes advantage of some fluorophores that can be turned on and off (so-called blinking) to separate the emitters of fluorophores in subsequent time points or camera frames (Figure 1.1d). In each frame, the density of the emitters is low enough so they do not overlap with each other. Therefore, the centroids of emitters can be faithfully determined as the molecular positions (usually called localizations) of the fluorophores. This procedure is repeated until the majority of the fluorophores are bleached, resulting in a table of localization coordinates and their respective uncertainties. A super-resolved image can then be reconstructed based on this table.

SMLM is a term that encompasses several techniques including PhotoActivated Localization Microscopy (PALM), STochastic Optical Reconstruction Microscopy (STORM), and Point Accumulation for Imaging in Nanoscale Topography (PAINT). They share the same principle as described above but achieve blinking differently. Albeit not defined strictly, conventionally, PALM refers to SMLM that use a photoswitchable fluorescence protein, whereas a synthetic dye is used in STORM. In

PAINT, blinking is achieved by binding and unbinding of fluorogenic molecules that become fluorescent upon binding. In the PAINT extension DNA-PAINT, instead of a fluorogenic molecule, the binding and unbinding are realized by a fluorescent dye-conjugated DNA strand that binds to its complementary DNA strand labeling the structure of interest (Jungmann *et al.*, 2010).

1.1.4.2 Resolution in SMLM

The resolution of SMLM is determined by two factors: the localization precision and the sampling rate. Localization precision determines how precise an emitter can be localized. In the ideal case, i.e., without any background and with small pixel size, the localization precision can be determined as:

$$\sigma_{x,y} \geq \frac{\sigma_{\mathrm{PSF}}}{\sqrt{N}}. \tag{1.2}$$

Here σ_{PSF} is the size of the PSF, and N is the photon count (Thompson *et al.*, 2002). The localization precision represents the spread (standard deviation) of a Gaussian describing the localization distribution as if it results from repeated measurements of the same fluorophore. Therefore, a worse localization precision corresponds to a higher uncertainty of localizing the fluorophore. Accordingly, this equation implies that a brighter and more in-focus emitter yields a more precise localization.

The sampling rate of the structure is the second factor. Now, imagine a continuous structure such as a line decorated by localizations continuously. If the labeling density is too low, the underlying structure will not be represented (e.g., the line appears as short segments or random clusters), hence we still get a rather low resolution despite good localization precision. This is in line with the theorem widely used in signal processing, stating that sampling twice than the desired frequency is required (Nyquist, 1928).

In SMLM, the following equation describes the relation between sampling rate and resolution (Shroff *et al.*, 2008):

$$R_{\mathrm{Nyquist}} = \frac{2}{\sqrt[d]{\rho}}. \tag{1.3}$$

Here $d = 1, 2, 3$ is the spatial dimensionality of the data, and ρ is the labeling density. This equation is sufficient to describe resolution if $R_{\mathrm{Nyquist}} \gg \sigma_{x,y}$. Otherwise, the resolution has been revised to be

$$R_{\mathrm{overall}} = \sqrt{\sigma_{x,y}^2 + R_{\mathrm{Nyquist}}^2} \tag{1.4}$$

to incorporate the effect of $\sigma_{x,y}$ (Legant *et al.*, 2016). These equations are based on the Nyquist–Shannon sampling theorem, which assumes that each sampling happens with an equal spacing. In SMLM, the stochastic nature of localizations does not fulfill such an assumption. A higher localization density is thus required to achieve the desired resolution (Legant *et al.*, 2016).

These theorems were derived based on continuous structures. However, for a discrete structure such as the nuclear pore complex (NPC; described in Section 1.3), increasing density of localization does not necessarily provide more information about the scturcture. Labeling efficiency, the fraction of target proteins that are detected by imaging, is instead a more relevant factor.

1.1.4.3 3D SMLM

One way to extend SMLM to 3D is by encoding the third dimension in the PSF. The key concept is to make the PSF shape depth-dependent, from which we can extract the axial positions of emitters. A conventional but yet powerful way is to introduce astigmatism to the light path, which elongates the PSF differently at distinct axial positions. With the astigmatic PSF, an imaging depth of 1 µm can be achieved. To expand the axial range, different PSF engineering methods have been proposed, which differ in the shape of the PSF. For example, a double-helix PSF enables an axial range of 2 µm and a tetrapod PSF 20 µm. The axial information can also be acquired via different microscope configurations. For example, by simultaneously imaging in multiple focal planes acquired by splitting the emitted fluorescence in different optical paths (Juette *et al.*, 2008; Hajj *et al.*, 2014). This has achieved an imaging depth of 4 µm (Hajj *et al.*, 2014). Another method is interferometric PhotoActivated Localization Microscopy (iPALM) or 4Pi-Single-Molecule Switching (4Pi-SMS). In 4Pi-SMS, emission from the same fluorophore is collected by two objectives (one above and one below the imaging plane) and directed into two different light paths. The different length of the paths creates a phase shift between the two emission beams, which are then brought to interference and generate four different interference patterns encoding axial information (Hell and Stelzer, 1992). The interference patterns are extremely sensitive in the axial direction, thereby enabling an isotropic resolution (Jia *et al.*, 2014).

With supercritical angle fluorescence (SAF), 3D information can be acquired independently of the PSF shape. SAF is the portion of fluorescence that is above the critical angle after being directed into the material with higher refractive index, e.g., from the imaging medium to the coverslip, when the source fluorophore is very close to the interface (Hellen and Axelrod, 1987; Novotny, 1997). The major portion of the fluorescence through the interface are under the critical angle, hence the name undercritical angle fluorescence (UAF). SAF intensity has an almost exponential decay in response to the increasing axial position of a fluorophore, thus providing precise axial resolution. However, it only works within a few hundreds nm of the coverslip because the intensity is undetectable for deeper fluorophores (Deschamps *et al.*, 2014; Bourg *et al.*, 2015). SAF intensity also depends on the brightness of the emitter and thus requires a normalization by UAF. dSALM (direct Supercritical-Angle Localization Microscopy), the most recent implementation of SAF-based 3D SMLM, achieves an axial localization precision of 4 nm by efficiently measuring SAF and UAF (Dasgupta *et al.*, 2021).

Despite the development of new techniques, the simplicity of astigmatic PSF still makes it the most common implementation of routine 3D SMLM.

1.1.4.4 Fluorophores in localization microscopy

Fluorescent proteins The earliest implementations of SMLM were based on fluorescent proteins that can be "turned on" from an undetectable state to a detectable state . This transition can be achieved by photoactivation, as used in fluorescence PhotoActivation Localization Microscopy (fPALM) (Hess *et al.*, 2006), or photoconversion, as used in PALM (Betzig *et al.*, 2006). Photoactivatable proteins, such as the photoactivatable version of GFP (green fluorescent protein; Patterson and Lippincott-Schwartz, 2002), involve the activation of the fluorophore from a non-fluorescent dark state to a fluorescent bright state (Figure 1.2a). Photoconvertible proteins, such as EosFP (Nienhaus *et al.*, 2005) and the more photostable mMaple (McEvoy *et al.*, 2012), involve the conversion of the fluorophores' spectra from one range to another that can be selectively detected by the camera (Figure 1.2b). These transitions are based on either chemical modification, backbone cleavage, or cis-trans isomerizations (Lukyanov *et al.*, 2005). When its transition is reversible, the fluorescent protein is referred to as photoswitchable, such as Dronpa (Ando *et al.*, 2004). Photoswitch allows the fluorescent protein to go through multiple activation cycles, leading to more detectable localizations and thus higher sampling (Durisic *et al.*, 2012).

Fluorescent proteins can be genetically fused to the target protein, when which is labeled endogenously at each locus, every protein copy is labeled in principle, thus having the highest labeling efficiency. However, in practice, labeling efficiencies typically do not exceed 70 % (Thevathasan *et al.*, 2019) because of undetectable labels due to factors including incorrect folding and incomplete chromophore maturation of the fluorophore, incompatible local pH, and photobleaching.

A downside is that the weaker fluorescence emitted by fluorescent proteins compared to synthetic dyes commonly used in SMLM, leading to worse localization precision. Furthermore, most fluorescent proteins tend to form oligomers, which could cause mislocalization or aggregation of the labeled target protein (Landgraf *et al.*, 2012; Wang *et al.*, 2014). This issue can be mitigated by engineering the fluorescence protein to be more monomeric, such as mMaple3 in comparison to mMaple (Wang *et al.*, 2014).

Organic dyes To have the advantage of higher photon counts, it is desirable to use organic dyes for SMLM. However, the dyes used in conventional microscopy

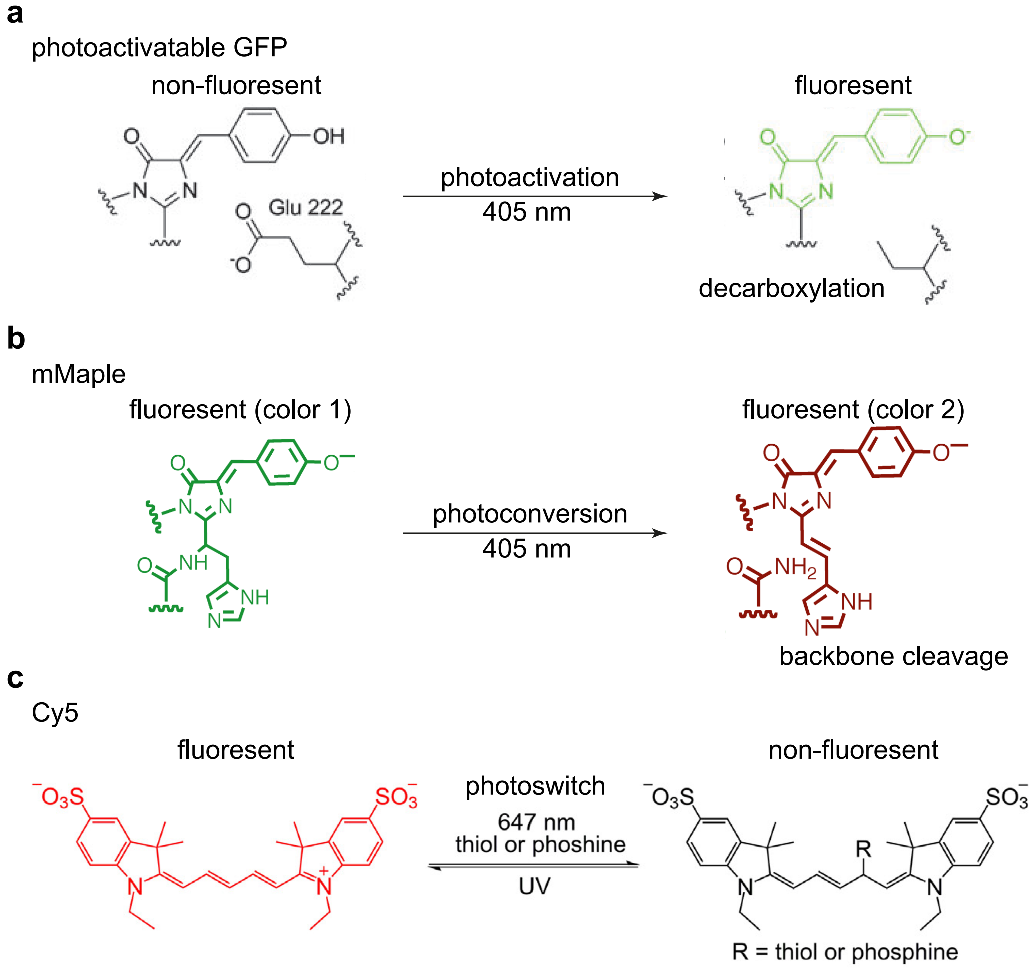

Figure 1.2 | Photoinduction mechanisms of fluorophores. Fluorophores can undergo photoinduction through photoactivation (fluorophore changes from a non-fluorescent to a fluorescent state; **a**) and photoconversion (fluorescence shifts from one wavelength to another; **b**). The reversible photoinduction is often specifically termed photoswitching (**c**). *Subpanels a & c have been adapted from Sample* et al.*, 2009; Chozinski* et al.*, 2014 with permission. Subpanel b has been adapted from McEvoy* et al.*, 2012, distributed under CC0 1.0 Universal (CC0 1.0) Public Domain Dedication.*

typically cannot be photoswitched. Therefore, to use existing dyes for SMLM, either specific imaging buffers or modifications to the dyes are required. Apart from being bright, an ideal photoswitchable dye for SMLM has to be photostable, with a low on-off duty cycle and with high switching cycles. The duty cycle, the ratio of time that a fluorescent dye is in a detectable state, determines the maximum density of emitting fluorophores in each image frame (Dempsey *et al.*, 2011). Therefore, a higher duty cycle corresponds to a fast imaging speed.

These criteria make dyes from the xanthene and cyanine groups popular in SMLM. Actually, the first implementation of STORM is based on cyanine dyes Cy3 and Cy5, which are used in a pair as the activator and the reporter, respectively (Rust *et al.*, 2006). Prior to activation, Cy5 excited by red laser light (633 nm) is turned into its dark state by thiols provided in the buffer to form a thiol-cyanine adduct (Figure 1.2c). Adjacent Cy3 then absorbs green light (532 nm), transferring energy to the Cy5 molecule and activating it. This cycle can be iterated for several times until the dye is photobleached. In direct STORM (dSTORM), the activator has been shown as unnecessary, as it can be replaced by UV light, achieving direct photoswitch (without an activator dye; Dempsey *et al.*, 2009). The same mechanism has been applied to Alexa Fluor 647 (AF647), a Cy5 derivative that is brighter and thus used in many studies.

Another group of commonly used dyes is photoactivatable xanthene dyes. In this group, silicon rhodamines are favored because of their red-shifted emission and cell-permeability (Koide *et al.*, 2011). These dyes have an equilibrium between a fluorescent zwitterion and a non-fluorescent lactone. To facilitate their use in SMLM, usually a caging group is attached to the dyes to "lock" them in their non-fluorescent form (Lukinavičius *et al.*, 2013; Grimm *et al.*, 2017). Upon illumination of UV light, the caging group can be released and the dye molecule is turned to its fluorescent form (Grimm *et al.*, 2013; Lukinavičius *et al.*, 2013). This photoactivation is irreversible and requires only UV illumination, therefore specific imaging buffers are not needed. Commonly used dyes also include rhodamine derived Janelia Fluor (JF) dyes, which provide options across various spectra (Grimm *et al.*, 2017).

1.1.4.5 Labeling strategies

Apart from the fluorophore, the labeling strategy has a direct impact on the image quality in many aspects including linkage error, labeling efficiency, and specificity. Linkage error arises from the displacement between the fluorophore and the target molecule. Depending on the labeling strategies, the displacement ranges from a few to ~25 nm, which is often detectable with the resolution of SMLM, complicating the inference of the true location of the target molecule. Another factor, labeling efficiency, reflects the fraction of target molecules that carries an effective label, determining the sampling rate of the labeled structure. Low labeling specificity, on the other hand, can result in unspecific staining, causing unwanted background localizations and/or artifacts.

Covalent labeling Fluorescent labels can be directly linked to the target molecule through covalent bonds. One common and straightforward way is to fuse a gene encoding the target protein genetically with a fluorescent protein. With this live-cell compatible labeling, every target protein carries one label, resulting in high labeling specificity and labeling efficiency, and in theory zero background. Note that the labeling efficiency still cannot reach 100 %, as discussed in Section 1.1.4.4. The linkage error induced by this approach is mild, roughly the size (2 to 5 nm) of the fluorescent protein (Rodriguez *et al.*, 2017).

To benefit from the high brightness of synthetic dyes, a covalent label can be realized using self-labeling enzymes. Unlike the previous strategy, here the fluorescent proteins are substituted with engineered enzymes. Although these enzymes themselves are not fluorescent, they can be covalently linked to their fluorescent dye-conjugated ligands through their enzyme function. For example, SNAP-tag is a mutated version of the human DNA repair enzyme O^6-alkylguanine-DNA-alkyltransferase. SNAP-tag specifically reacts with its bio-orthogonal substrate benzylguanine that is conjugated with dyes (e.g, AF647) in a irreversible manner (Keppler *et al.*, 2003). Other common options are CLIP-tag, which is a modified version of SNAP-tag that reacts with O^2-benzylcytosine (Gautier *et al.*, 2008), and Halo-tag, which is a bacterial haloalkane dehalogenase that reacts with primary chloroalkane (Los *et al.*, 2008). These membrane-permeable substrates render self-labeling enzymes suitable for live cell imaging. However, this characteristic is often compromised when an impermeable conjugated dye, e.g., AF647, is used.

The aforementioned labeling strategies usually incorporate the tags to N- and C-termini of the target proteins to not disturb the protein functions. In contrast, site-specific labeling is enabled by using unnatural amino acids (UAAs), where a non-proteinogenic amino acid with a functional group is incorporated into the sequence of the target protein (Horisawa, 2014). Dyes can be covalently linked to the functional group via 'click chemistry', resulting in the smallest linkage error of all labeling approaches. However, this technique is complicated because it requires the co-expression of a tRNA, its respective tRNA synthetase, and a mutated version of the protein of interest (Wang *et al.*, 2001). This system also can suffer from the low expression level of the mutated protein. The mutated protein's truncated version that does not incorporate the UAA can also be expressed, leading to low labeling efficiency and protein malfunction (Elia, 2021). In addition, UAAs that are free or incorporated into non-target proteins can cause unspecific background.

Affinity-based probes The previously mentioned approaches involve cell or protein engineering, which requires additional effort and time. On the other hand, antibodies have been widely used for labeling target proteins in cell biology, thus can be a readily option, especially when they are commercially available. The labeling can be performed with a fluorophore-conjugated primary antibody that specifically binds to the target, or with a fluorophore-conjugated secondary antibody in addition to an unconjugated primary antibody it binds to. The major shortcoming of using antibodies is the large linkage error (~10 nm to 25 nm) resulting from their large molecular size (~150 kDa). Nanobodies, an antibody fragment containing a single monomeric variable antibody domain, can be used similarly to antibodies but reduce linkage error significantly due to the much smaller size (~13 kDa) (Pleiner *et al.*, 2015). Nanobodies can be obtained commercially or be produced with screening techniques including phage display (Holliger and Hudson, 2005). Other alternatives are small binding molecules that can be selected to have affinity to specific target proteins. Such molecules that have been applied in SMLM include affimers (Carrington *et al.*, 2019), which are single-stranded oligonucleotides, and aptamers (Strauss *et al.*, 2018), which are small polypeptides.

1.1.4.6 Multi-color SMLM

To study the spatial relations between different proteins, imaging different targets in the same field of view is required. In SMLM, this can be achieved by simultaneous labeling of different targets with spectrally well-separated fluorophores, which are then imaged simultaneously on separate camera channels or sequentially on a single detector (Dempsey *et al.*, 2011). However, finding imaging buffers and acquisition parameters that suit all used fluorophores can be challenging because they usually favor different imaging conditions, as discussed in 1.1.4.4. Other limitations include registration errors introduced by field-dependent and chromatic aberrations.

Ratiometric SMLM is another approach to achieve multi-color SMLM. It uses spectrally overlapping fluorophores that can be excited by the same wavelength and produce highly overlapping emission spectra. During image acquisition, the emissions are split into two spectral channels, and the intensity ratio of the emitters between the two channels identifies specific fluorophores (Schönle and Hell, 2007; Zhang *et al.*, 2020). This approach avoids the registration error because position information can be acquired based on only one channel.

Using the same fluorophore to detect different targets through the same channel is another option. In this approach, termed multiplexing, the blinking kinetics is the same when imaging individual targets because they are labeled by the same fluorophore. Only one channel is used so spectral cross-talk and chromatic aberrations can be avoided. One implementation of this approach is to combine different activators with the same reporter (see *Organic dyes* in Section 1.1.4.4), so that targets labeled with distinct activators can be activated by different wavelengths but still yield the same emission spectrum (Bates *et al.*, 2007). Another implementation of multiplexing is to use different probes to label distinct targets and detect them sequentially with the same fluorophore, with washing steps between different detections. This can be achieved in STORM by using different primary antibodies and respective secondary antibodies conjugated with the same dye (Klevanski *et al.*, 2020), or in DNA-PAINT by labeling different targets with their own specific docking stands, followed by iterating cycles of adding, imaging, and removing the respective complementary imager strands conjugated with the same fluorophore (Schueder *et al.*, 2017). A limitation of sequential multiplexing is that each target is imaged in an independent round, lacking a common structure that can be used as the reference for alignment and drift correction. Therefore, the addition of fiducial markers to the sample is commonly used to provide such a reference (Jungmann *et al.*, 2014).

1.1.4.7 High-throughput SMLM

The long acquisition time of SMLM is a major technical challenge, hampering the throughput required for statistical significance in, e.g., structural quantification and particle averaging. Through years of development, approaches to increasing throughput have been established. One of these approaches is automated SMLM imaging (Holden *et al.*, 2014; Beghin *et al.*, 2017; Mund *et al.*, 2018), which enables unsupervised data acquisition over hours or days by reducing user intervention. Throughput can also be increased by expanding the information that can be acquired in the same amount of time. One example is to increase the field of view by incorporating new homogeneous illumination schemes (Deschamps *et al.*, 2016; Douglass *et al.*, 2016; Stehr *et al.*, 2019). Another example is to increase the imaging speed, either by switching the fluorophores faster using a stronger activation laser (Lin *et al.*, 2015; Thompson *et al.*, 2002) or by increasing the density of emitters per frame. A drawback of the faster switching is that the image quality is compromised by photobleaching induced by the high excitation laser power, suffering from loss of fluorophores and reduced photon counts. (Diekmann *et al.*, 2020). High-density imaging, on the other hand, results in overlapping emitters and thus requires multi-emitter fitting algorithms (Zhu *et al.*, 2012; Huang *et al.*, 2016; Babcock and Zhuang, 2017; Barentine *et al.*, 2019; Nehme *et al.*, 2020), deep learning–based high-density fitters (Speiser *et al.*, 2021), or optimization of PSF engineering (Nehme *et al.*, 2020).

1.1.4.8 Minimal emission fluxes (MINFLUX)

MINFLUX is a recent advance in super-resolution microscopy (Figure 1.1e,f). This technique produces the same type of data (i.e., localization coordinates and their uncertainties) as other SMLM techniques but based on a different working principle. This scanning-based approach probes an activated photoactivatable fluorophore with a donut-shaped beam, same as the pattern used in STED for depletion but here for excitation (Balzarotti *et al.*, 2017; Eilers *et al.*, 2018; Gwosch *et al.*, 2020).

Instead of the fitted position of an emitter in a camera frame, the precisely controlled position of the beam is used as the position readout. Theoretically, when the central minimum of the illumination pattern is located at the position of the molecule, no fluorescence can be generated. A position slightly off-center can generate fluorescence with intensity determined by the illumination pattern. By scanning positions around the fluorophore based on the predefined scanning pattern, the emitter's position can be geometrically solved based on the number of detected photons (Gwosch *et al.*, 2020; Schmidt *et al.*, 2021). Combining iteratively scanning with shrinking the radius of the scanning pattern simultaneously further improves the precision.

MINFLUX has been shown to resolve the NPC structure based on the nucleoporin Nup96 tagged with the photoconvertible fluorescent protein mMaple with high precision (2 nm) and low photon budget in a living cell. Although this is a milestone, the imaging speed, e.g., ~2 min for acquiring one NPC (Gwosch *et al.*, 2020), is too slow for most dynamic processes in living cells. Moreover, imaging the whole structure of interest at different time points requires to revisit the same fluorophores iteratively. This requirement cannot be fulfilled yet because no photoactivatable fluorophore can undergo sufficient switching cycles in a live-cell compatible manner.

1.2 Quantitative data analysis in SMLM

Now with SMLM, we can visualize much more structural details which was not possible with conventional microscopy. Quantitative analysis of these structural features is necessary to link them to biological functions. However, extraction of quantitative measures is commonly done by applying pixel-based analysis to rendered super-resolution images. This adds another layer of complexity to the analyses and makes exploiting the full information in the SMLM coordinates difficult because of the obscuring effects caused by rendering (Baddeley *et al.*, 2010). To avoid such an issue, I suggest to analyze the SMLM coordinates directly with coordinate-based algorithms. This would allow us to interpret the the underlying biology more reliably and quantitatively (Nicovich *et al.*, 2017). In the following, I will discuss the state-of-the-art of coordinate-based approaches (Figure 1.3).

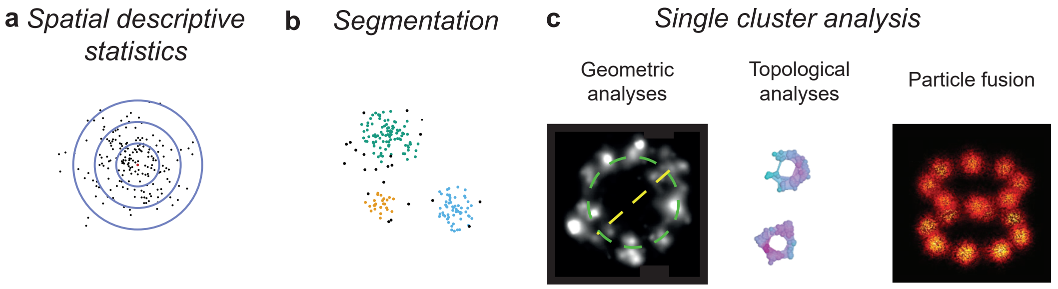

Figure 1.3 | Overview of data analysis in SMLM. Data analysis approaches that are applied to coordinate-based SMLM data directly, avoiding the requirement for prior image reconstruction. The analysis methods can be classified as spatial descriptive statistics (**a**), segmentation of single clusters (**b**), and analysis of single clusters (**c**). *Adapted from Wu* et al., *2020, on which I am the co-first author, with permission. Individual components in* **c** *are adapted from Shi* et al., *2017; Pike* et al., *2018; Heydarian* et al., *2021 with permisison.*

1.2.1 Spatial descriptive statistics

The first class of the approaches is spatial descriptive statistics (Figure 1.4a). It can be used to study overall spatial distribution patterns (random, clustered, or dispersed) across the entire region of interest. The term 'clusters' refers to the regions where the density of molecules is higher than that of the surroundings when the distribution is non-uniform. We are interested in the distributions of molecules because they are usually linked to biological functions. For example, the oligomerization state of a receptor is related to its signaling activity (Pageon *et al.*, 2016). Spatial descriptive statistics covers different algorithms such as the pair correlation function $g(r)$ (Sengupta *et al.*, 2011) and the Ripley's K function $K(r)$ (Owen *et al.*, 2010) that allow extracting features including the average size and density of all clusters. Both these algorithms profile the localization density as a function of the length scale but calculate the density differently. $g(r)$ draws concentric rings with increasing radii around each localization and calculates the average localization density for rings with the same size (ii,iii in Figure 1.4a). Fitting $g(r)$ with a Gaussian or exponential function has been used to quantify the cluster size (iv,v in Figure 1.4a; Sengupta *et al.*, 2011; Shivanandan *et al.*, 2016). Terms for fluorophore reactivation have been proposed to be incorporated to reduce false clustering (Sengupta *et al.*, 2011). In the Ripley's K function $K(r)$, however, concentric disks are used instead of rings. $L(r) - r$, a $K(r)$ derivative where $L(r) = \sqrt{K(r)/\pi}$, is more commonly used than $K(r)$ itself. This is because $L(r) - r$ is more intuitive as it outputs zero for a random distribution, a positive value for a clustered, and a negative value for a dispersed. The use of concentric rings and disks makes $K(r)$ a cumulative distribution function and $g(r)$ a probability density function, respectively. The difference makes the pair correlation function less robust to noise (e.g., nonspecific labeling) but accumulate less errors like fluorophore reactivation induced overcounting (Deschout *et al.*, 2014). Both functions have been applied to characterize the connections between density of clusters and cellular/functional states (Owen *et al.*, 2010; Sengupta *et al.*, 2011). Recently, PERPL (Pattern Extraction from Relative Positions of Localizations; Curd *et al.*, 2021), derived from the pair correlation function, was developed to extract the structural features that are repetitively present in the data, e.g., the radius and symmetry of the NPC (vi-viii in Figure 1.4a).

However, spatial descriptive statistics are limited by their high sensitivity to repeatedly localized fluorophores and large-scale heterogeneity. The "average" nature of these approaches also convolutes the interpretation of the results.

1.2.2 Segmentation of single clusters

To avoid the limitation of spatial descriptive statistics, individual clusters can be identified and analyzed separately. The process of identifying clusters and their localizations is called segmentation (Figure 1.4b). Having single clusters identified,

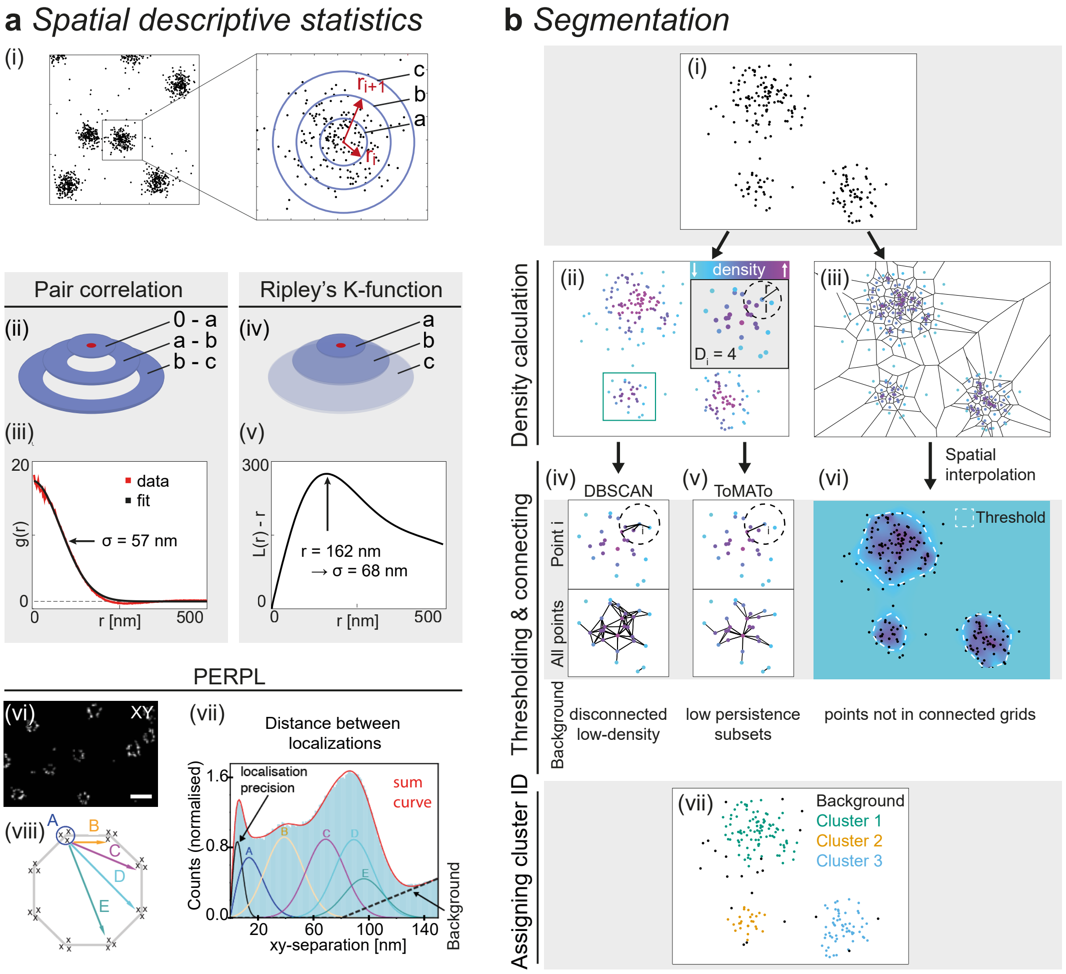

Figure 1.4 | Clustering analyses in SMLM. (**a**) Spatial descriptive statistics. Simulated Gaussian clusters (i) are used as the example data. In pair correlation analysis, concentric rings (ii) with increasing radii (a, b, and c) are placed around each localization. The resulting profile (iii) across length scales (each corresponding to a ring) is calculated based on the density per ring, followed by averaging over all localizations. The cluster size can be estimated by performing a Gaussian fit to the pair correlation function. Ripley's K-function is similar to the pair correlation function, except that the concentric rings are replaced by disks (iv). The peak in Ripley's $L(r) - r$ function (v), a derivative of the K-function, represents the full width at half maximum of the Gaussian clusters. PERPL (Pattern Extraction from Relative Positions of Localizations) is an analysis based on the relative position distribution (RPD), closely related to the above-mentioned functions. It can be applied to extract parameters of repetitive structures. For example, Nup107 in the nuclear pore complex (vi) is converted to its RPD (vii), which is fitted with a model curve (red) derived from a potential model (viii). In vii, the colors of the component distributions of the sum curve indicate their origin in the model (viii). (**b**) Examples of segmentation approaches. In density-based approaches, the density (ii) of neighbors within a user-specified spacing r for each localization is first calculated. In DBSCAN (Density-Based Spatial Clustering of Applications with Noise), all neighbors are connected, compared to the connection of a point to its highest-density neighbor in ToMATo (Topological Mode Analysis Tool). A cluster ID is then assigned to localizations in the same "tree". Density can be defined differently, e.g., by the inverse area of Voronoi polygons (iii). Afterwards, a density map (vi) can be calculated, where clusters can be determined by thresholding. *Adapted from Wu* et al.*, 2020, on which I am the co-first author, with permission. The PERPL-related components are taken from Curd* et al.*, 2020 which is distributed under Creative Commons Attribution License (CC BY-NC-ND 4.0.)*

basic parameters including the size and density of each cluster can be easily quantified. The major steps in segmentation algorithms for SMLM are density calculation, density thresholding, and cluster assignment of each localization. A common and simple segmentation approach is based on a rendered SMLM image. In the image, the intensity value of each pixel relates to localization density. Usually, an intensity threshold is applied to define high density adjacent pixels, in which localizations are assigned as a cluster. However, the intensity value depends on user-defined settings for image rendering and does not necessitate a proper density readout. Therefore, I will focus on segmentation approaches that can be applied to coordinate data directly and thus avoiding image rendering. Two such approaches are DBSCAN (Density-Based Spatial Clustering of Applications with Noise; Endesfelder *et al.*, 2013) and ToMATo (Topological Mode Analysis Tool; Pike *et al.*, 2018). They define the number of other localizations within a user-specified distance from a single localization as its density. After the density calculation for all localizations, DBSCAN connects localizations, with a density higher than a user-defined threshold, within a user-defined spacing (iv in Figure 1.4b). In comparison, ToMATo instead connects a localization only to the neighbor that has the highest density within a user-defined spacing (v in Figure 1.4b). This iterative procedure starts from the localization with the highest density and forms candidate clusters or 'trees'. Finally, these trees go through a persistence-based merging across different density scales and form clusters. Although ToMATo can distinguish close clusters better (Pike *et al.*, 2018), both approaches suit clusters with different size and shapes. Certainly, different definitions of density, with corresponding threshold, can also be used for clustering. These definitions include the $L(r)$ function (Owen *et al.*, 2010) and the inverse of a polygon area in a Voronoi diagram (iii,vi in Figure 1.4b; Andronov *et al.*, 2016), for each localization.

Segmentation is not necessarily always based on density. For example, in k-means clustering, localizations are assigned to the nearest one of the k reference points, initially determined at random, and form k clusters. The centroids of the clusters are used as updated reference points for the next round of the assignment. This procedure iterates until convergence and yields the final clusters.

However, an optimal segmentation approach that suits all different biological structures does not exist. Simple and widely used approaches such as DBSCAN or k-means clustering can be a good start. In the case when they fail to properly identify clusters, other approaches can be further explored.

1.2.3 Analysis of single clusters

Although biological structures in SMLM data can be seen as clusters, many of them contain substructures that cannot be represented simply by cluster size or density. To better understand complex biological structures, further analysis is necessary. I will discuss some possible options (Figure 1.3c) in this section.

1.2.3.1 Geometric Analyses

In many cases, the structure of interest can be approximated by a certain underlying geometry (e.g., rings, disks, stripes, spheres, tubes, and their derivatives). A parametrized model derived from the postulated geometry can then be used to analyze the structure, usually through model fitting. The fitting can be executed in different dimensionalities, with or without dimension reduction. The most common approach is based on the line profile (Figure 1.5a), a histogram showing the density of localizations projected along a user-defined line or axis. This process reduces the data to 1D and enables description of the structure using a simpler geometric model when applicable. For example, the line profile along an actin filament (Xu *et al.*, 2012) or microtubule (Dempsey *et al.*, 2011) can be fitted by a Gaussian or double Gaussian to quantify the size or diameter. Similarly, the distance between peaks in the line profile of actin rings that are distributed repetitively along the axon axis can be quantified as the spacing between the rings (Xu *et al.*, 2013). However, this approach has some drawbacks. First, the user-defined axes can lead to a selection bias. Second, annotating user-defined axes can be laborious and therefore hampers the throughput. Furthermore, the dimension reduction causes loss of information and can convolute the interpretation of data, especially when the shape is complex.

These issues can be prevented by analyzing the data in its original dimensionality. However, the available options are quite limited, usually to a ring structure. For example, the Hough transform can extract the diameters and centers of rings such as the viral particles in rendered SMLM images of 2D projections (Laine *et al.*, 2015). The same purpose can be achieved by fitting a ring model directly to the localization coordinates, for example, to the top-view projections of the NPC (Szymborska *et al.*, 2013; Thevathasan *et al.*, 2019) or cilium (Shi *et al.*, 2017; Figure 1.5b). Although these measurements were conducted in 2D, the original data dimensionality, it is not the real dimensionality of the structures, which is 3D. Even in 2D, rings are still a special case despite a common shape in biology. A single particle (cluster) analysis for fitting an arbitrary model to the data in its original dimensionality is still missing.

1.2.3.2 Classification

Clusters containing heterogeneous structures can be classified based on machine learning (ML) or topological features. The identified classes can then guide further analysis, for example, by suggesting the geometry to the model fitting discussed earlier.

In the routine of the ML-based classification, the user has to first decide the ML model and descriptors to use. Then the model has to be trained by the user using single particles with their classes annotated. The trained model has to be validated, usually based on simulated particles where the ground-truth classes are known, before it can be used to classify experimental data. This workflow can be performed

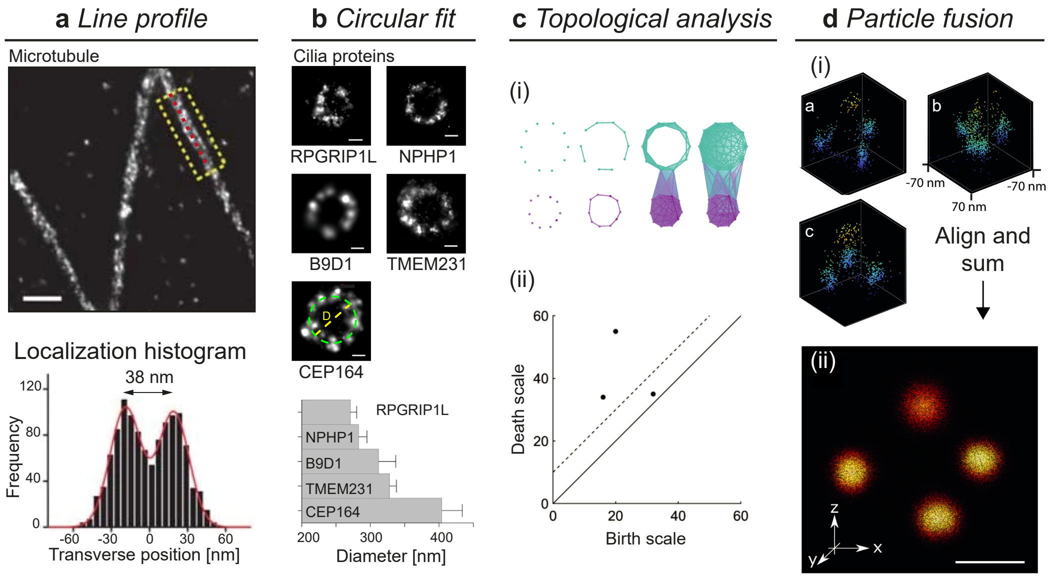

Figure 1.5 | Geometric analyses in SMLM. (**a**) The line profile of the structure of interest, e.g., a microtubule, can be used to extract specific parameters, like the diameter, by performing a double Gaussian fit. (**b**) A circular fit can be used to quantify the diameter of ring structures such as cilia components. (**c**) Topological analysis identifies features (in this case two holes; i) based on their birth and death scales (dots: smaller purple ring) shown in a persistence diagram (ii). Features below the persistence threshold (dotted line in ii) are considered as not meaningful (here is a random hole formed by connections between the rings). In i, connections between localizations at three various length scales are shown. (**d**) With particle fusion, single copies (i) of the identical structure (here the 3D tetrahedron-shaped DNA-origami nanostructure) can be fused by alignment to yield a high contrast average (ii; based on 256 copies). Scale bars: 250 nm (a), 100 nm (b), 50 nm (d). *Adapted from Wu* et al.*, 2020, on which I am the co-first author, with permission. Components have been adapted from Dempsey* et al.*, 2011; Pike* et al.*, 2020; Heydarian* et al.*, 2021; Shi* et al.*, 2017, with permission.*

in, e.g., ASAP (Automated Structures Analysis Program; Danial and Garcia-Saez, 2019).

Topological data analyses, on the other hand, classify the structures according to topological shapes such as connected components, holes, and, in 3D, enclosed voids (Figure 1.5c). These shapes are more abstract but can provide insights into the functions of the classified structures. Recently, a persistent homology-based topological data analysis was introduced to SMLM (Pike *et al.*, 2020). It classifies structures based on the identified topological shapes that are persistent across different length scales. The persistence is determined by the graph showing the length scales where the shapes appear (so-called birth scale) and disappear (death scale).

Topological data analyses and geometric shape classification are not exclusive to each other. For example, topological single holes in 2D could imply a geometric ring shape.

1.2.3.3 Particle Fusion

Interpreting the underlying structures based on single particles alone is usually hard because of the insufficient accuracy, which is determined by the data quality. The quality is limited by some key factors including localization precision, label displacement, and incomplete labeling (Thevathasan *et al.*, 2019). Nevertheless, single particles can be seen as resulting from imperfect sampling of the underlying structures. When single particles share the same underlying structure, it can be reconstructed by registering and fusing the particles, improving the contrast and labeling efficiency and thus resolution (Figure 1.5d). This concept originates from electron microscopy where many images of the same protein complex are aligned to solve its structure. Although the methods in EM can be directly applied to rendered images of particles in SMLM (Sieben *et al.*, 2018), a coordinate-based adaption was made to take the sparsity of SMLM data and localization precision into account (Heydarian *et al.*, 2018; Schnitzbauer *et al.*, 2018). The adaption was shown to enhance data sampling of synthetic structures and to reconstruct the underlying structure of the NPC (Heydarian *et al.*, 2018; Heydarian *et al.*, 2021).

1.3 The nuclear pore complex (NPC)

The NPC is a common test sample for microscopy and was also used in this work. This complex is a channel spanning the nuclear envelope for transporting substances across the nuclear membrane in both directions. Many copies of the complex are distributed in the nuclear membrane (Figure 1.6a, where the nucleoporin labeling identifies the nuclear envelop). Here, I will discuss the NPC in human cells. The NPC is formed by ~30 proteins, called nucleoporins (Nups). The complex has a size of 120 MDa (Reichelt *et al.*, 1990), a diameter of approximately 110 nm, and a total height of ~80 nm (Schwartz, 2016). Small molecules can passively diffuse through the pore. The classical active import/export pathways for larger molecules involve nuclear transport receptors (importins and exportins) and the small GTPase RAN in an energy-dependent manner (Görlich and Kutay, 1999).

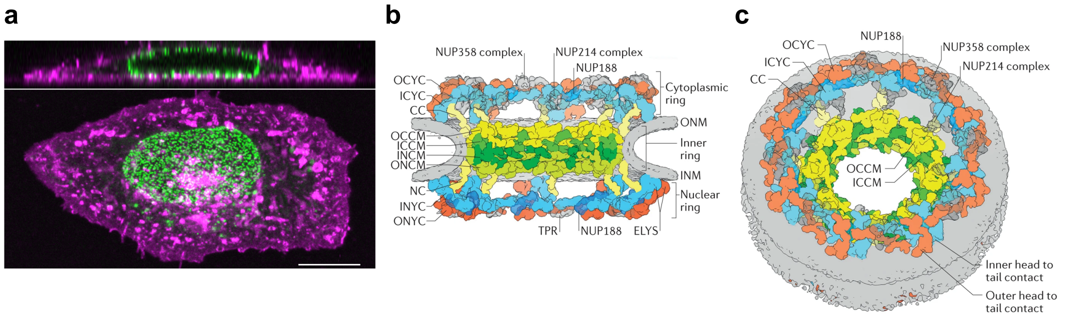

Figure 1.6 | The nuclear pore complex. (**a**) Example side-view and top-view confocal images of a U2OS cell with endogenous Nup96 tagged with GFP (green) and membranes stained with DiD (magenta). (**b-c**) the nuclear pore complex (NPC) scaffold. The cross-section (b) and the view seen from the cytoplasm (c) are shown. ONM: outer nuclear membrane; INM: inner nuclear membrane; ONYC: outer nuclear Y-complex; OCYC: outer cytoplasmic Y-complex; INYC: inner nuclear Y-complex; ICYC: inner cytoplasmic Y-complex; CC: cytoplasmic connector; NC: nuclear connector; ONCM: outer nuclear core module; INCM: inner nuclear core module; OCCM: outer cytoplasmic core module; ICCM: inner cytoplasmic core module. Scale bar: 10 µm. *Panel a has been adapted from Thevathasan* et al.*, 2019, on which I am a co-author. Panels b & c have been adapted from Beck and Hurt, 2017 with permission.*

1.3.1 The structure of the NPC

The NPC shows an eight-fold rotational symmetrical arrangement of subunits. It can be divided into sub-structures including cytoplasmic filaments, a cytoplasmic ring, an inner pore ring, a nucleoplasmic ring, and a nuclear basket (Figure 1.6b,c; Beck and Hurt, 2017). The channel between the inner and outer nuclear membrane is formed by the inner pore ring, which anchores the cytoplasmic and nucleoplasmic rings as a whole. The cytoplasmic filaments and the nuclear basket extend from the cytoplasmic and nucleoplasmic rings into the cytoplasm and nucleoplasm, respectively.

Nups can be classified into two groups: scaffold Nups and FG-Nups, although FG-Nups also have scaffolding functions (Beck and Hurt, 2017). Scaffold Nups are characterized by folded domains and contribute to the NPC architecture. These Nups form stable subcomplexes, the building blocks of the complex. They comprise the Y-complex, the NUP214 complex, the NUP62 complex, and the inner ring complex. In contrast, FG-Nups contains intrinsically disordered domains. FG-Nups have been given their name because they are rich in phenylalanine (F) and glycine (G) repeats. Most of FG-Nups form the central channel and create a protein meshwork, which contributes to the permeability barrier of the pore (Li *et al.*, 2016). The nuclear transport receptors interact with FG-repeats of FG-Nups when passing through the channel.

1.3.2 The Y-complex

The most well-studied subcomplex, the Y-complex, has seven conserved subunits: Nup96, Nup160, Nup133, Nup85, Nup107, Seh1, and Sec13 (Bui *et al.*, 2013). These sub-units together form a Y-shaped architecture (Figure 1.7a), hence the name 'Y'-complex. Three additional sub-units Nup43, Nup37 and Elys further bind to the subcomplex in a species-specific manner (all three in vertebrates; Nup37 and ELYS present in some fungi). A dimer of two Y-complex copies that are rotationally shifted can be seen as the basic structural unit in mammals (Figure 1.7b). Eight copies of the dimer concentrically are distributed in each of the cytoplasmic and nucleoplasmic rings in a head-to-tail manner, with opposite orientations in the different rings. The subcomplex has 32 copies in total which is also the case for all of its subunits, except for ELYS, which only binds to the nucleoplasmic ring (Beck and Hurt, 2017) and hence has only 16 copies.

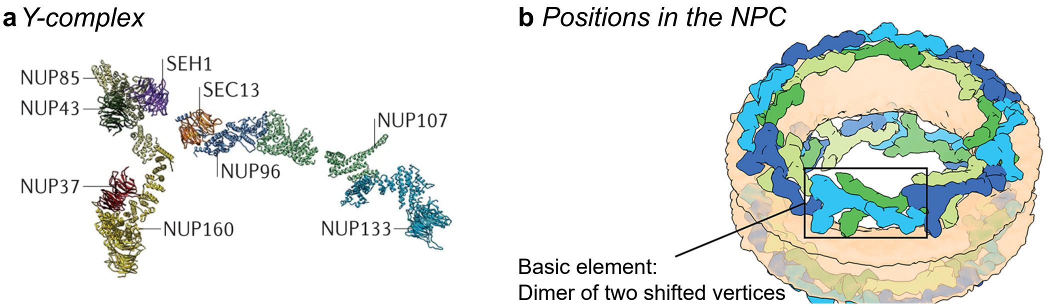

Figure 1.7 | Y-complex substructure. (**a**) The distribution of nucleoporins forming a Y-complex substructure. (**b**) In the nuclear pore complex (NPC), 2 copies of shifted Y-complex vertices form a dimer, which is the basic building block. Eight dimers together form one of the cytoplasmic and nucleoplasmic rings, resulting in 32 copies of the substructure per NPC. *Both panels have been adapted from Beck and Hurt, 2017; Bui* et al., *2013 with permission.*

1.4 Clathrin-mediated endocytosis

In this work, I used CME as a representative dynamic structure. Clathrin-mediated endocytosis (CME) is one, arguably the most well-known one, of the multiple pathways of endocytosis, which is an essential process that a eukaryotic cell uses to internalize substances, or cargoes, from the cell surface. Endocytosis is involved in many physiological functions, including nutrient uptake, receptor signaling, membrane remodeling, pathogen entry, neurotransmission, etc.

During CME, cargoes are loaded to an endocytic site. The plasma membrane of the site undergoes bending and invagination, and then is 'pinched off' by scission, forming a separate vesicle (McMahon and Boucrot, 2011). This process includes a gradual and dynamic coat formation. More than 50 endocytic proteins, including the key component clathrin, are recruited subsequently and form the endocytic machinery to drive the bending and invagination of the plasma membrane. These proteins are modular in terms of their functions and are highly conserved among eukaryotes, across yeast and mammalian cells. In mammals and yeasts, most endocytic proteins have homologues, at least functional homologues, with only a handful exceptions.

In this study, we use both mammalian cells and yeast cells as models, as they are commonly used for studying CME. We used clathrin coats in mammalian cells for a pioneer method development and extended the analysis to multiple endocytic proteins in yeast, covering different functional modules. Therefore, I will only briefly summarize CME in mammalian cells and discuss its yeast counterpart more in depth.

1.4.1 CME in mammalian cells

1.4.1.1 Endocytic machinery

Here, I will provide a brief overview of CME in mammalian cells and focus on the debate of how clathrin drives membrane bending. The machinery that drives CME assembles at the plasma membrane by sequentially recruiting endocytic proteins that are functionally modular, with the key signature—the clathrin coat. The coat is formed by clathrin and other proteins such as clathrin adaptors and scaffold proteins. Clathrin itself does not bind to the plasma membrane, therefore its link to the membrane has to be mediated by clathrin adaptors, which bind to cargo and specific lipids in the membrane. These adaptors can be heterotetrameric, e.g., AP2 complex, or monomeric ,e.g., members of the CALM (clathrin assembly lymphoid myeloid leukaemia protein) family and epsins (Ford *et al.*, 2002; Cocucci *et al.*, 2012; Kelly *et al.*, 2014; Messa *et al.*, 2014; Miller *et al.*, 2015; Kadlecova *et al.*, 2016). The coat components are held together by scaffold proteins, which interact with each other and the adaptors. The scaffolds include clathrin, epidermal growth factor receptor substrate 15 (EPS15), epidermal growth factor receptor substrate 15-like 1 (EPS15R), and intersectins (Henne *et al.*, 2010; Umasankar *et al.*, 2012; Ma *et al.*, 2016). An endocytic event has been proposed to be coordinatively initiated by some or all proteins that form the ’pioneer module’. The pioneer module includes the BAR domain proteins F-BAR domain only protein 1 (FCHO1), AP2, EPS15, EPS15R, and intersectins 1 and 2 (Henne *et al.*, 2010; Taylor *et al.*, 2011; Cocucci *et al.*, 2012; Umasankar *et al.*, 2012; Brach *et al.*, 2014; Ma *et al.*, 2016).

After the coat has assembled, proteins of the actin module are recruited to the endocytic site to form an actin network that potentially generates force for membrane bending. The members in this module are the actin network building blocks and regulatory components. Examples of these regulatory components are members of the Wiskott–Aldrich syndrome protein (WASP) family, which are nucleation promoting factors (NPFs) of actin filament (F-actin) polymerization, myosin motor proteins, and dynamin (Taylor *et al.*, 2011). Apart from actin itself, the network is built up by many actin-binding partners such as the Arp2/3 complex (formed by actin-related protein 2 (ARP2) and ARP3 (Merrifield *et al.*, 2004; Kaksonen *et al.*, 2006), which mediates actin nucleation. However, the requirement of actin polymerization for CME in mammalian cells is inconclusive, but has been shown to depend on the surrounding environment, e.g., high transmembrane pressure or tight cell contact, according to an increasing number of studies (Pontes *et al.*, 2017; Djakbarova *et al.*, 2021; Kaplan *et al.*, 2021).

The invagination has to be separated from the plasma membrane to form a vesicle toward the end of the process. This separation is mediated by members of the scission module, which includes BAR domain proteins (e.g., endophilins and amphiphysins) and the GTPase dynamin. The membrane-binding BAR domains have been characterized as curvature sensors. BAR domain proteins with different preferred membrane curvature have been proposed to be recruited to an endocytic site subsequently to increase of the curvature (Daumke *et al.*, 2014). Dynamin is then recruited, forming an oligomer and mediates further constriction and scission in a GTP-dependent manner (Antonny *et al.*, 2016).

Finally, the disassembly of the endocytic machinery is driven by proteins of the uncoating module, including chaperones, protein kinases, and lipid phosphatases (Massol *et al.*, 2006; Taylor *et al.*, 2011).

1.4.1.2 Clathrin coat formation

The coat has been considered as the main driving force of membrane bending, where clathrin triskelia have been shown to be key. During coat formation, ordered lattices of clathrin are organized into hexagons and pentagons, forming both flat and curved structures. Currently, there are two contradictory models of coat formation: the constant area model and the constant curvature model (Figure 1.8). The constant area model suggests that the coat remains flat until it grows to its final surface area and thereafter continuously acquires curvature until the vesicle is formed (Figure 1.8a). The first supporting evidence is that in EM micrographs, the coats have been found with different curvatures, assuming a growth continuum formed by all imaged clathrin structures. (Heuser, 1980). Later, flat clathrin lattices have been shown to be mostly hexagonal, which has been considered as topologically stable. In this case, the transition to the spherical geometry requires a dynamically difficult and energetically costly rearrangement of the clathrin lattice which is unlikely to happen (Kirchhausen and Toyoda, 1993). Therefore, the constant curvature model has been proposed, which assumes that the clathrin coat maintains the constant curvature of the final vesicle throughout the process and continuously grows in surface area over time to generate a complete sphere (Figure 1.8b). Flat clathrin structures are not considered as endocytic precursors and thus not included in the model.

However, recent studies have again reported that the curvature of flat clathrin coats can change during endocytosis (Doyon *et al.*, 2011; Aguet *et al.*, 2013; Avinoam *et al.*,

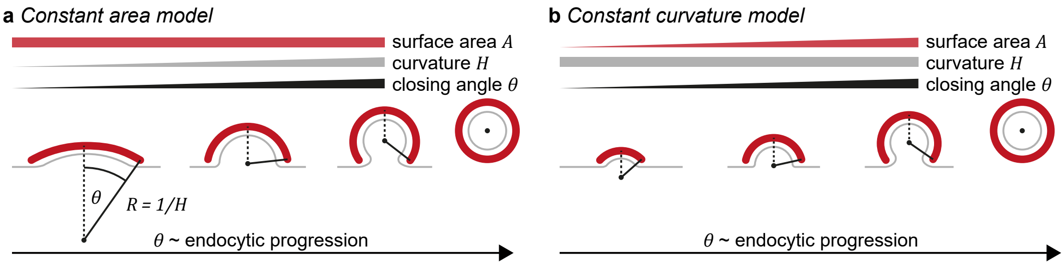

Figure 1.8 | Current models of clathrin coat formation. One of the two current models of clathrin coat formation is the constant area model (**a**), which assumes that the the coat gains its final area on the flat membrane, followed by increasing curvature via coat remodeling. Another model is the constant curvature model, which hypothesizes that the coat maintains the same curvature throughout the biological process and the coat grows by increasing its surface area. *Adapted from Mund* et al.*, 2022, on which I am a co-author.*

2015; Kaplan *et al.*, 2021). As a result, clathrin remodeling has regained the field's attention recently (Kaksonen and Roux, 2018; Sochacki and Taraska, 2019; Chen and Schmid, 2020). Interestingly, studies based on different methods supported either the constant area model (Avinoam *et al.*, 2015; Sochacki *et al.*, 2021), the constant curvature model (Willy *et al.*, 2021). Even a combination (Bucher *et al.*, 2018; Yoshida *et al.*, 2018; Tagiltsev *et al.*, 2021) and the co-existence (Scott *et al.*, 2018) of both models have also been reported. Therefore, the underlying model of coat formation is still inconclusive.

1.4.2 CME in *Saccharomyces cerevisiae*

Despite the high similarity, there are some major differences of CME in mammals and yeasts. These differences are mostly for overcoming forces (higher than 1,000 pN) that are exerted on the membrane invagination by turgor pressure during endocytosis in yeast (Dmitrieff and Nédélec, 2015; Ma and Berro, 2021). The pressure, which is only present in walled cells, is caused by the fluid stored in the cells pushing the plasma membrane to the cell wall.

The first main difference is in the geometry of invagination. In mammalian cells, the plasma membrane invaginates into a round, spherical geometry (McMahon and Boucrot, 2011), whereas the shape is much more elongated in yeast cells (Figure 1.9; Kukulski *et al.*, 2012). Second, the timing of membrane bending differs despite the similar overall lifetime. In mammalian cells, the bending begins shortly after the coat assembly starts, whereas in yeast cells the bending initiation roughly coincides with the beginning of actin polymerization. Lastly, the driving force of the membrane bending is different. In mammals, the coat has a major contribution to bending, in contrast to the strictly required involvement of actin polymerization in yeasts. In mammals, the involvement of actin polymerization in bending is still debated, probably it is required in a membrane tension-dependent manner (Kaplan *et al.*, 2021).

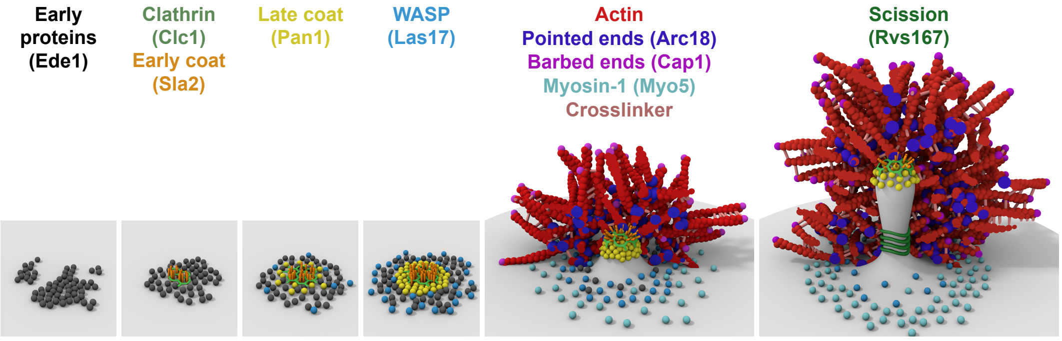

Figure 1.9 | Schematic model of clathrin-mediated endocytosis in budding yeast. On the flat membrane, early proteins are recruited followed by the arrival of other coat proteins at the endocytic site. The late coat then recruits the yeast WASP protein Las17, which at membrane forms a ring that patterns the nucleation of the actin polymerization. Membrane invagination starts during the initiation of the network. Later, proteins mediating membrane scission are recruited to the neck of the invagination. As shown in the schematic, endocytic proteins in the same functional modules have similar radial distributions. The size of the distributions correlates with the time when the proteins are recruited to the endocytic sites before the arrivals of the scission proteins, with the early proteins being recruited in the center and later proteins toward the periphery. Note that half of the actin network is not shown for clarity. *Adapted from Mund* et al., *2018 under the CC BY 4.0 license.*

1.4.2.1 The early module

CME is initiated at a flat membrane. In budding yeast, the process starts with a long-lasting but dispensable early phase (Brach *et al.*, 2014), which is temporally variable. Ede1 (yeast homolog of mammalian Eps15) and Syp1 (yeast homolog of mammalian FCHO1/2) are the two earliest proteins that arrive at the endocytic site. These proteins, which physically bind to each other (Reider *et al.*, 2009), enhance the initiation of CME and participate in cargo recognition (Stimpson *et al.*, 2009). Syp1 has a membrane-binding F-BAR domain, which was shown to regulate lipid dynamics within membranes (Zhao *et al.*, 2013). Recently, the phase separation property of Ede1 has been suggested to contribute to the initiation of CME (Kozak and Kaksonen, 2019). However, deletions of both proteins and even additional 5 earliest-arriving proteins do not entirely abolish endocytosis in cells (Brach *et al.*, 2014). Other initiator candidates are clustered cargo and PIP_2. However, Ede1 arrives before α-factor that binds to its receptor Ste2 accumulates (Toshima *et al.*, 2006). Formation of actin patches, a signature of the late phase of CME, is not reduced when PIP_2 levels are reduced (Homma *et al.*, 1998). Therefore, up to date, how endocytic events initiate in budding yeast, is still not fully understood.

1.4.2.2 The coat module

The early coat Following the early module, coat proteins which arrive early are clathrin, AP2, and the two paralogs Yap1801/2 (yeast homolog of mammalian Picalm). The clathrin heavy chain and light chain are coded for by genes CHC1 and CLC1, respectively. Compared to mammalian cells, clathrin and AP2 are not essential for CME in yeast and clathrin does not bind to AP2 (Yeung *et al.*, 1999).

Although the deletion of the clathrin heavy chain reduces the number of endocytic events in yeast cells, the events progress regularly except for much more variable vesicle size and scission time, compared to wild type cells (Kukulski *et al.*, 2016). The clathrin adaptors Yap1801/2 interact with clathrin through their C-terminal clathrin-binding motif (CBM). They also contain an N-terminal membrane-binding ANTH domain that binds to PIP_2 and multiple Asn-Pro-Phe tripeptide motifs, which is a ligand of EH (Eps15-homology) domains that are found in many endocytic proteins. The single and double deletions of YAP1801 and YAP1802 show that they have a cargo-specific role but do not affect the internalization of most cargoes tested (Burston *et al.*, 2009).

The intermediate coat At this stage, CME transitions from the long, variable early phase to the late phase that is more regular when invagination occurs. The next recruited coat proteins are Sla2 (yeast homolog of mammalian Hip1R) and two paralogs Ent1/2 (yeast homolog of mammalian epsin-like proteins). Sla2, which is key to the transition, binds to the membrane (PIP_2) and F-actin through its ANTH and THATCH (talin-HIP1/R/Sla2p actin-tethering C-terminal homology) domains, respectively. These connections link the endocytic coat to F-actin and transmit the force generated by actin polymerization to membrane invagination (see 1.4.2.4). Ent1/2 contain an ENTH (Epsin N-terminal homology) domain that binds PIP_2, cargo-binding ubiquitin-interacting motifs (UIMs), Asn-Pro-Phe motif, a variant clathrin box motif that binds clathrin, and an actin-binding domain. At the end of this stage, endocytic events are stalled until the presence of cargo to get through the 'cargo checkpoint' that has been proposed recently (Pedersen *et al.*, 2020).

The late coat This stage is the beginning of the mobile late phase. The major late coat proteins are Pan1, End3, and Sla1, which together form an intersectin-like complex (Tang *et al.*, 2000). Sla1 recruitment, mediated by Pan1 along with End3 and cargo peptide motifs, (Tang *et al.*, 2000; Tolsma *et al.*, 2020) can predict whether an endocytic event will undergo internalization (Newpher and Lemmon, 2006), in line with the aforementioned checkpoint. Sla1 has three PR (proline-rich) region-binding SH3 (SRC homology 3) domains, two cargo-interacting Sla1 homology domains, and a clathrin-binding motif. Phosphorylation sites on its C-terminus contribute to uncoating after vesicle scission (Warren *et al.*, 2002). Sla1 recruits Las17 (Sun *et al.*, 2006), a component of the actin assembly machinery. Pan1 has Yap1801/2 interacting EH domains and is the only essential coat protein. It can stimulate actin nucleation by Arp2/3, and activate the type-I myosins Myo3/5 (Duncan *et al.*, 2001; Barker *et al.*, 2007).

1.4.2.3 The WASP/Myo module

A highly branched network of short F-actin encloses the invagination and provides the pulling force that drives invagination. This force is for counteracting the turgor pressure that, pushing the plasma membrane to the cell wall, is caused by osmosis. Such a network does not form spontaneously but requires nucleation of F-actin by its nucleator Arp2/3 complex activated by NPFs in the WASP/Myo module. The key NPFs are Las17 (yeast homolog of mammalian WASP/N-WASP) and type I myosins (yeast homolog of mammalian myosin I) Myo3/5 (yeast homolog of mammalian myosin-1E). Las17 has a WH1 (WASP homology 1) domain and a SH3-interacting PR region. This protein also has a C-terminal WCA domain that are formed by a G-actin (globular actin)-binding WASP homology 2 (WH2), a central, and a Arp2/3-interacting acidic subdomains (Winter *et al.*, 1999). The WCA domain is therefore in charge of supplying G-actin to Arp2/3 nucleated F-actin. Myo3/5 have a motor domain, one membrane-binding tail homology (TH) domain, one actin-binding TH domain, an SH3 domain, and an acidic patch. Through its SH3 domain, myosin I interacts with the F-actin binding protein Vrp1, and the two proteins together form an functional WCA domain equivalent, which has NPF activity. Myo3 and Myo5 are functionally redundant in endocytosis, only double mutants show pronounced defects (Geli and Riezman, 1996). Their motors are oriented toward the center of the site (Mund *et al.*, 2018), possibly involved in translocation of F-actin to assist endocytosis, independent of their NPF activity (Lewellyn *et al.*, 2015; Manenschijn *et al.*, 2019). The endocytic function of myosin I requires its motor and NPF activities.

Actin polymerization starts about 20 s later than the arrival of Las17 at the endocytic site. Such a delay must be mediated by other inhibitors because Las17 has no autoinhibition function (Rodal *et al.*, 2003). The known inhibitors are the early protein Syp1, the coat protein Sla1, and Bbc1 from the WASP/Myo module. Sla1, Las17, and Bbc1 distribute radially at the endocytic site with increasing radius (Mund *et al.*, 2018). Sla1 and Bbc1 potentially define the inner and outer boundaries of the Las17 ring, creating patterned Arp2/3 activity (Mund *et al.*, 2018). Bzz1 (yeast homolog of mammalian syndapin), a F-BAR protein that arrives after the departure of another F-BAR protein Syp1, has been suggested to be recruited by Syp1-induced membrane curvature. The recruited Bzz1 releases Las17 from the inhibition by Sla1, potentially by competing with the Las17 binding of Sla1 through the PR region of Las17 (Soulard *et al.*, 2005; Boettner *et al.*, 2009).

The proteins of the WASP/Myo module stay at the membrane base of the endocytic site throughout the invagination, whereas the coat proteins are internalized. However, Myo5 and Las17 have been shown to locate at the tip and the side of invagination, respectively (Idrissi *et al.*, 2008).

1.4.2.4 The actin module

When NPFs in the WASP/Myo module have assembled, the nucleator Arp2/3 complex is then recruited, followed by actin polymerization, leading to a dynamic branched actin network that encloses and drives the invagination. F-actin is a polarized structure and grows in a directed manner. After nucleation, ATP bound

G-actin monomers are added to the barbed end and ATP soon gets hydrolyzed to ADP and inorganic phosphate (ATP → ADP + P_i) after G-actin binding. P_i is then disassociated in a rather slow manner. Association of a monomer with different forms of nucleotide and P_i corresponds to three different conformations of the actin monomer, representing an aging process. These distinct states of actin are associated with different dynamics, interacting partners, and mechanical properties of the entire or part of the actin filament (Dominguez and Holmes, 2011).

The barbed end quickly gets capped by capping complexes to ensure a shorter length (around 100 nm) of the filament by preventing further addition of monomers. The capping complex includes a Cap1/Cap2 heterodimer (capping protein, CP), which binds to newly formed free barbed ends, Aip1/Cofilin, which binds to old ADP-actin barbed end, and Abp1/Aim3, which binds to both.

Meanwhile, cross-linkers bind to F-actin in the network and bridge branched filaments, increasing the rigidity of the network. The main cross-linkers here are Sac6 and Scp1. Sac6 has two actin-binding domains, each containing two calponin homology (CH) domains (Klein *et al.*, 2004). Scp1 has an N-terminal CH domain and a C-terminal calponin-like repeat (CLR). Unlike Sac6, actin binding by Scp1 is not mediated by its CH domain but by two different regions in its PR motif and CLR, respectively (Gheorghe *et al.*, 2008).

Sac6 has a dominant role in actin network rigidity (Planade *et al.*, 2019) and has been reported to be important for membrane bending (Picco *et al.*, 2018). Sac6 deletion has a stronger defect than deletion of Scp1 (Gheorghe *et al.*, 2008). Turnover of the actin network occurs constantly, starting within seconds of the initial polymerization. Filaments are debranched, severed, and depolymerized (Goode *et al.*, 2015), releasing actin monomers that can be reused. During an endocytic event, the whole actin network is turned over 3 to 5 times (Kaksonen *et al.*, 2003; Lacy *et al.*, 2019). The turnover allows the plasticity of the network to adapt to shape change while maintaining the pulling force. Contributing factors include Aim7 (yeast homolog of mammalian GMF), Cof1 (cofilin), and crn1 (coronin). By binding to Arp2/3 complexes, Aim7 promotes filament debranching of the network and inhibits nucleation at the bound site (Gandhi *et al.*, 2010; Boczkowska *et al.*, 2013). Upon binding to ADP-actin, Cof1 causes twisting and thus severing of the actin filament. This Cof1 binding and severing are enhanced by Crn1 (Mikati *et al.*, 2015).

Abp1 has been shown to bind dynamically to sides of F-actin, and to associate stably with Arp2/3 branch junctions. Abp1 protects the junctions from Aim7-induced debranching. These findings suggest that Abp1 can mediate actin nucleation at filament sides and contribute to the turnover (Guo *et al.*, 2018).

1.4.2.5 The scission module

In this stage, a newly formed vesicle is released through scission of the invaginated membrane. In contrast to the requirement of the GTPase dynamin for scission in mammalian cells, Vps1 (yeast homolog of mammalian dynamin) is not necessary for this process in yeast (Nannapaneni *et al.*, 2010). Instead, scission in yeast is mediated by a heterodimer of BAR domain proteins Rvs161/167 (yeast homologs of mammalian endophilin/amphiphysin; Friesen *et al.*, 2006). Although the dimer has been reported to form a scaffold that binds to the tubular part of the invagination, it is still not fully understood how these proteins contribute to scission (Idrissi *et al.*, 2008). The binding has been proposed to impose friction at the narrow neck by limiting lipid diffusion, and in turn leads to membrane fission under the pulling force provided by the actin network (Kaksonen and Roux, 2018).

Once the new vesicle is formed, uncoating occurs rapidly so that the vesicle and fuse with its target endosome and proteins can be released for new endocytic events. Proteins with different functions have to orchestrate to disassemble the coat entirely from the membrane and from each other. For example, the coat proteins have to be phosphorylated by protein kinases including Ark1 and Prk1 (yeast homolog of mammalian AAK1) before disassembly. PI(4,5)P_2 has to be converted to PI(4)P through dephosphorylation by lipid phosphatases Inp51/52/53 (yeast homologs of mammalian synaptojanin) to weaken the interactions between coat proteins and the membrane (Toret *et al.*, 2008; Goode *et al.*, 2015).

1.4.2.6 Systematic investigation of endocytosis at the nanoscale

In a previous work of our group, Mund *et al.*, 2018 have systematically studied the average radial distributions of 23 different endocytic proteins in budding yeast (Figure 1.10). Here, I will summarize some main findings. First, these proteins, covering all functional modules, form well-defined structures such as patches or rings at the endocytic sites, except for the proteins in the early module. Second, the size of the distributions positively correlates with the temporal recruiting order of the proteins at the endocytic sites, implying a center-to-periphery expansion determined by the progression of recruitment. Furthermore, Las17 has been reported to form a ring-like nano-template on the plasma membrane and to pattern actin nucleation. According to a modeling analysis, this pattern controls the force generation via actin and is important for efficient vesicle formation.

The same study also demonstrated that the dynamics of endocytosis can be reconstructed from super-resolution snapshots (Figure 1.11), based on the prior knowledge of the continuous inward movement of Abp1 centroid and the stable positioning of Las17 at the invagination base during endocytosis, reported by a live-cell study (Picco *et al.*, 2015). Specifically, the centroid positions of Abp1 in the side-view snapshots are quantified with respect to Las17, providing temporal clues for sorting

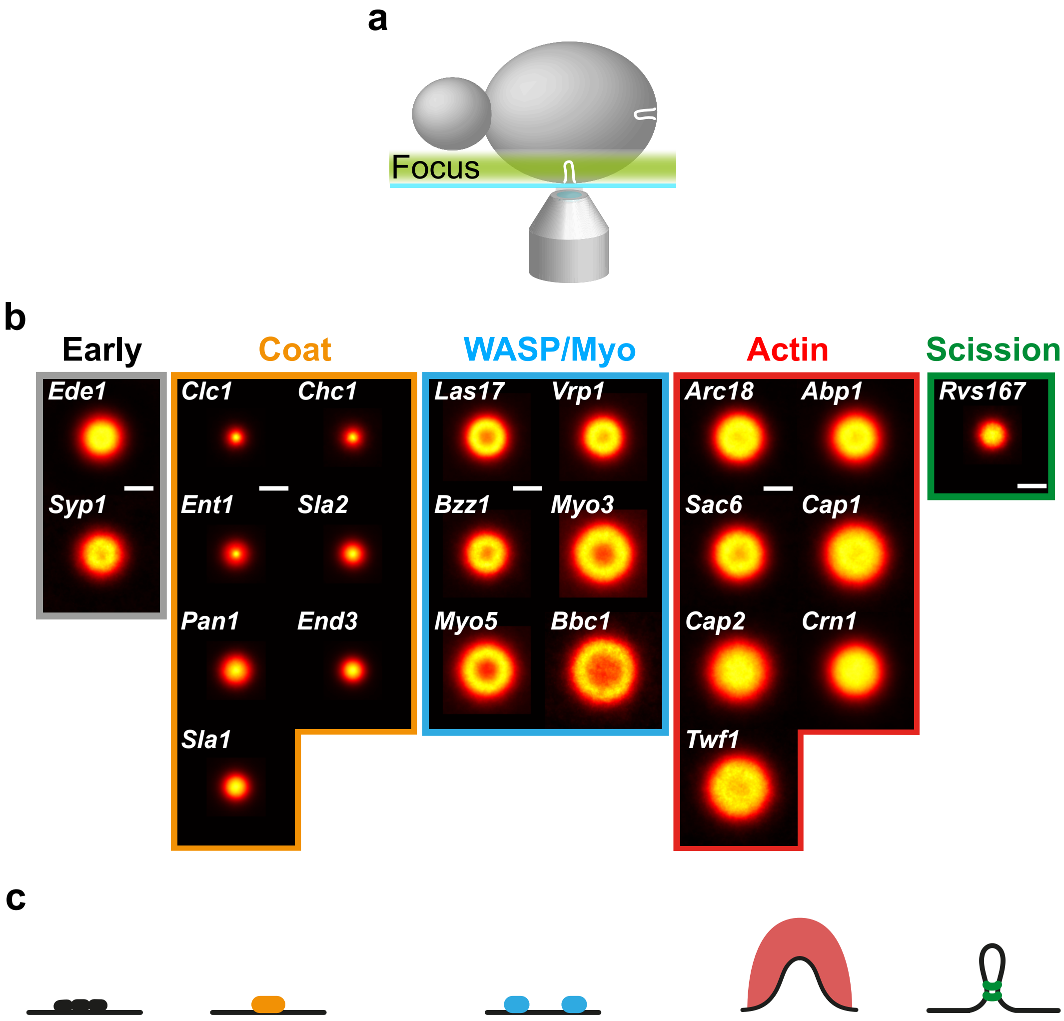

Figure 1.10 | Average radial distributions of 23 different endocytic proteins in budding yeast. Using single molecule localization microscopy (SMLM), by focusing on the bottom of yeast cells (**a**), thousands of endocytic sites in the bottom view have been acquired and yielded the average radial distributions (**b**) of the 23 endocytic proteins. The proteins in the same functional modules (**c**) have similar distributions. Proteins in the early model form more irregular distributions, whereas proteins in other modules form either patches (e.g., all coat proteins) or rings (e.g., proteins in the WASP/Myo module). Starting from the beginning of coat maturation, the temporal order of proteins arriving at the sites coincide with their size of distribution, except for the latest arriving Rvs167, which forms a smaller distribution due to its localization at the neck of invagination. Scale bar: 100 nm. *Adapted from Mund* et al., *2018 under the CC BY 4.0 license.*

the snapshots. However, in the reconstruction, the snapshots were registered by manual alignment, which limited the registration precision and analysis throughput. These limitations can be overcome by the approach presented in this work (see Section 3.1).

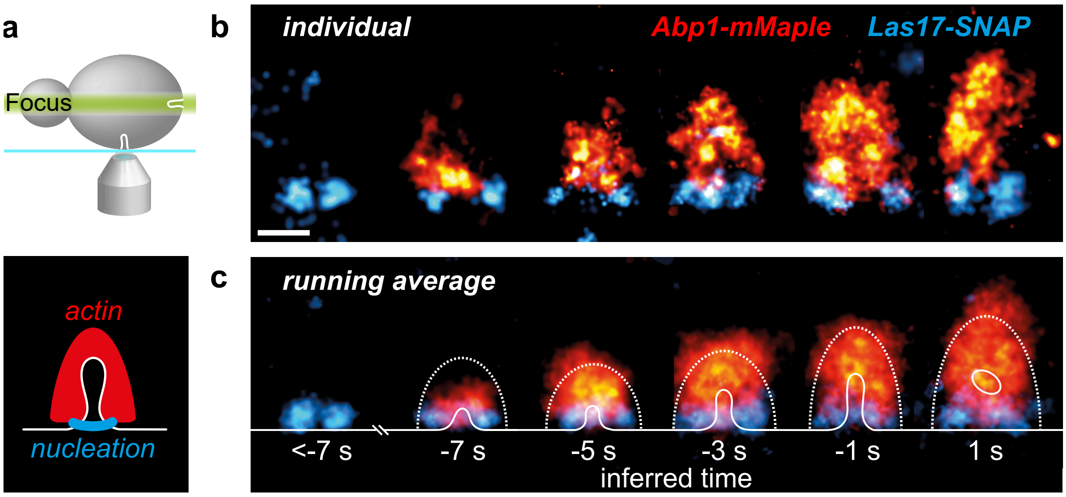

Figure 1.11 | Reconstructed dynamics of endocytosis in budding yeast. In this experiment, side-view super-resolution snapshots of endocytic sites were acquired by focusing on the equator of yeast cells (**a**). In the cells, Abp1 and Las17 were labeled with different fluorophores, which are members of the actin module and the WASP/Myo module, respectively. Each individual structure (**b**) was aligned manually by rotating the site to be pointing upward, followed by centering it at the bottom based on the Las17 distribution. The sites were then sorted based on the measured distance between the centroids of Abp1 and Las17. Finally, a running average was applied to obtain a smooth representation of the dynamics (**c**). Here, the CLEM-based average outer boundaries of the actin network (dotted lines) and plasma membrane profiles (solid line) reported by Kukulski *et al.*, 2012 are shown to provide the context. Scale bar: 100 nm. *Adapted from Mund* et al., *2018 under the CC BY 4.0 license.*

2 | Aims of the study

2.1 Development of a general model fitting framework for SMLM

Despite the recent development of data analysis approaches for SMLM (Section 1.2), the most common task of SMLM data analysis is not supported by either of the aforementioned approaches: extracting structural parameters using the most likely geometric model, of the ones postulated, to describe the structure of interest. Usually, such geometric models can be built based on visual data inspection or prior knowledge. Explicitly speaking, this task can be split into two steps. First, the geometry to best describe the structure has to be selected from the postulated models. Second, the precise structural parameters of the geometry are then extracted. This task is done at the scale of individual structures and therefore enables the quantification of biological and functional heterogeneities.

The first goal of this work is to develop a software tool that supports this task. The aims of this part are:

1. Development of a general framework.
2. Validation of the framework.
3. Exploring applications of the framework.

2.2 Dynamic reconstruction of the endocytic machinery

Nanoscale biological processes can be resolved by cryo-electron microscopy *in situ* with high contrast and high resolution, although in fixed samples and without molecular specificity. SMLM can complementarily provide molecular specificity but the dynamics are usually not directly observable. The second goal of this work is to exploit the combination of high quality SMLM and LocMoFit for reconstructing the dynamics of a biological process from its super-resolved snapshots. We developed an approach employing 'reference structures' simultaneously imaged with target proteins to map the snapshots in space and time.

To demonstrate this approach, we show how to reconstruct the dynamics of CME, a fast (an event finishes in approximately 20 s) and small (200 to 300 nm) process, in mammalian and yeast cells. The aims of this part are:

1. Development of an automated analysis to pre-process the high-throughput SMLM data.
2. Applying LocMoFit to reconstruct dynamics of CME.
3. Validations of the application.

3 | Results

To fill the gap of the missing approach that can extract complex parameters from individual structures, I developed **Loc**alization **Mo**del **Fit** (LocMoFit, Figure 3.1), a general framework for fitting an arbitrary geometric model directly to SMLM coordinate data. LocMoFit provides a basis for selecting the most likely model from alike that describes the structure of interest. Subsequently, given the best model, LocMoFit precisely estimates the model parameters that best describe the structure. If the underlying geometry can not be postulated, LocMoFit can perform model-free particle averaging and yields an average representation of the particles, assuming the variation among them is small. For efficient validation and quality control, LocMoFit is equipped with visualization tools and a simulation engine. Besides its stand-alone implementation, LocMoFit has been integrated as part of the open-source analysis platform SMAP (Ries, 2020) to gain access to tools for downstream analyses such as summary statistics of all analyzed particles and visualization of associations between parameters. LocMoFit, a MATLAB-based software, provides an API for code integration and incorporating user-defined models.

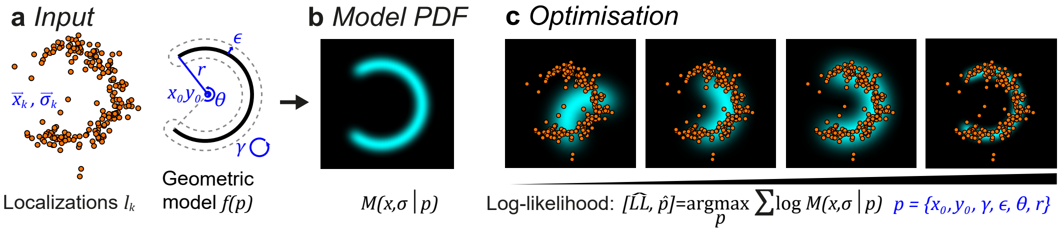

Figure 3.1 | LocMoFit. (**a**) Inputs of the LocMoFit framework. It requires 1) localization data l_k, containing spatial localization coordinates $\vec{x}_k$ and their precision $\vec{\sigma}_k$ from a structure and 2) a geometric model describing the structure. (**b**) The model is first converted to a probability density function (PDF) $M(x, \sigma \mid p)$, required by maximum likelihood estimation (MLE). (**c**) The PDF is then fitted to the localization data by searching in the parameter space to find estimates $\hat{p}$ of the parameters p that maximize the log-likelihood function $\hat{LL}$. To illustrate, here I fit a 2D arc model (cyan) to the localization coordinate data (orange dots). The model is parametrized by positions x_0, y_0, rotational angle γ, linkage error ϵ, arc opening angle θ, and radius r. *Adapted from Wu* et al.*, 2021, on which I am the first author.*

3.1 LocMoFit

In this section, I will briefly discuss the mathematical theory behind LocMoFit. I developed the theory with input from Jonas Ries.

3.1.1 LocMoFit and maximum likelihood estimation

The core of LocMoFit is estimating structural parameters by model fitting. With LocMoFit, a geometric model $f(p)$ can be fitted to K localizations $l_k = \{\vec{x}_k, \vec{\sigma}_k\}$ in a region of interest (ROI; Figure 3.1). Each ROI usually contains a single structure, so-called 'particle'. Context-wise, I also refer to a particle as a 'site'. As discussed in Sections 1.1.4.1 and 1.1.4.3, the localizations l_k are usually acquired by fitting a PSF to single emitters recorded in camera frames. l_k contains localization coordinates $\vec{x} = \{x, y\}$ and uncertainties $\vec{\sigma} = \{\sigma_x, \sigma_y\}$ for 2D data and $\vec{x} = \{x, y, z\}$ and $\vec{\sigma} = \{\sigma_x, \sigma_y, \sigma_z\}$ for 3D data. Our approach finds the set of parameter estimates $\hat{p}$ that best describes the set of localizations l_k using maximum likelihood estimation (MLE), given the model $f(p)$ (Figure 3.1c). To illustrate the workflow (Figure 3.1), I use synthetic localizations, of an arc structure, generated by the simulation engine of LocMoFit (Figure 3.2a; Section 6.2.2.2) as an example. Here, the geometric model $f(p)$ (an arc model in the example) parametrized by a set of parameters p is supplied. $f(p)$ is then converted to a probability density function (PDF) $M(\vec{x}, \vec{\sigma} \mid p)$, which describes the probability of acquiring a localization l at the position x at random, obeying the geometry $f(p)$, given the uncertainty σ. Assuming all localizations are independent, the joint likelihood to acquire the set of localizations l_k can be computed as the product of individual probabilities:

$$L(p) = \prod_k M\left(\vec{x}_k, \vec{\sigma}_k \mid p\right). \tag{3.1}$$

Accordingly, the procedure of maximum likelihood estimation can be expressed as

$$[\hat{L}, \hat{p}] = \underset{p}{\operatorname{argmax}}\, L(p). \tag{3.2}$$

Here, $\hat{L}$ denotes the maximum likelihood yielded by MLE. LocMoFit carries out this procedure using an optimization algorithm. In practice, the natural logarithm of the likelihood is used instead of the likelihood itself to avoid a small joint probability being rounded to zero. LocMoFit does not only output parameter estimates $\hat{p}$, but also optionally their 95 % confidence intervals.

The model $f(p)$ can be supplied in one of the forms: continuous, discrete, or image (Figure 3.2b). The continuous form describes the distribution of fluorophores in the shape of 1D lines (e.g., filaments or rings) or 2D surfaces (spheres and patches). By contrast, the discrete form directly describes the specific fluorophore positions.

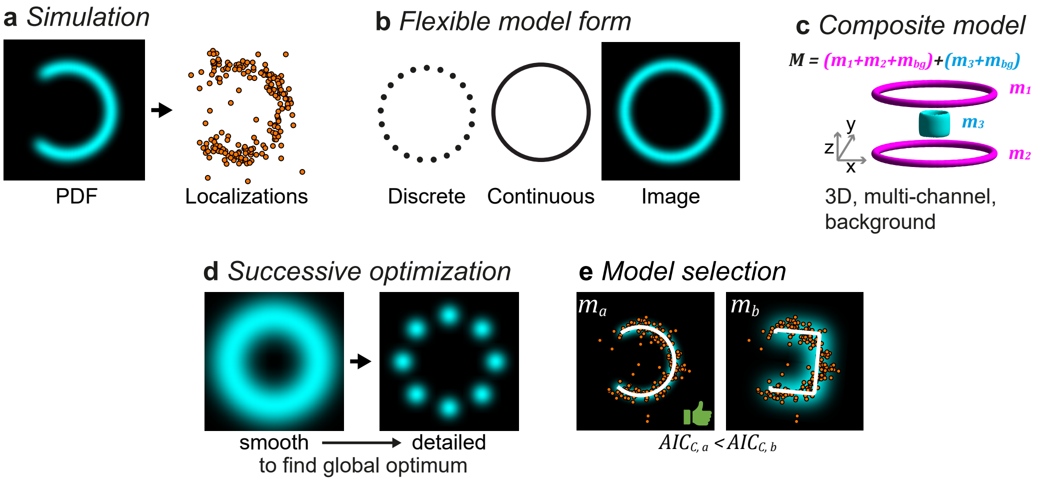

Figure 3.2 | Features of LocMoFit. (**a**) The *simulation* engine of LocMoFit simulates realistic localization data (orange dots) by sampling from the PDF (cyan; an arc model). (**b**) LocMoFit supports *flexible model forms* including the discrete, the continuous, and the image form. (**c**) LocMoFit can build a composite model by a linear combination of component models. For example, two identical rings fitted to one channel (magenta) and a cylinder fitted to another channel (cyan) are combined to form the composite model. Different channels have their own background models. This example also highlights that LocMoFit supports various data types, i.e., from 2D as shown in **a** to 3D and single to multiple channels. (**d**) LocMoFit supports *successive optimization* to avoid local optima. Different models, from smooth to detailed (from a continuous ring to eight-fold rotationally symmetric points in the example), can be fitted to the same site subsequently. The parameter estimates of smoother models are defined as the initial parameters of the more detailed models. (**e**) LocMoFit supports *model selection* by reporting the corrected version of the Akaike information criterion (AIC_C) as the basis for selecting the most likely model. Here, compared to the bucket model m_b, the arc model m_a has a smaller AIC_C, indicating m_a is a better model, given the example localizations. *Adapted from Wu* et al.*, 2021, on which I am the first author.*

First, I discuss the construction of $f(p)$ in the simplest case when $f(\vec{x}, p)$ describes the existence of a fluorophore at the position $\vec{x}$. In reality, the localizations we obtained from the experiments are not the exact fluorophore positions but with a random displacement scaling with the respective localization precisions $\vec{\sigma}$. To also consider this factor, we can use the mean precision $\langle\vec{\sigma}\rangle$ of all localizations as the standard deviations of a Gaussian function. We then convolve $f(\vec{x}, p)$ with the Gaussian to form a PDF ($\otimes$ denotes the convolution)

$$M(\vec{x}, \vec{\sigma} \mid p) = \left[\frac{f(\vec{x}, p)}{\iiint f(\vec{x}, p)\, dx\, dy\, dz}\right] \otimes G(\vec{x}, \langle\vec{\sigma}\rangle). \tag{3.3}$$

Next, we can move a step further to incorporate the lateral and axial localization precisions separately for each individual localization. For that, we can define the geometric model as $\vec{v}_j = f(p)$, where $f(p)$ outputs J fluorophore coordinates $\vec{v}_j$

defined by the model. Then the likelihood to obtain a single localization at the position $\vec{x}$ given the model $f(p)$ with parameters p is

$$M(\vec{x}, \vec{\sigma} \mid p) = \frac{1}{J} \sum_{j=1}^{J} (2\pi)^{-\frac{3}{2}} \det(\mathbf{\Sigma})^{-\frac{1}{2}} \exp\left(-\frac{1}{2} (\vec{x} - \vec{v}_j)^T \mathbf{\Sigma}^{-1} (\vec{x} - \vec{v}_j)\right). \tag{3.4}$$

Here $\mathbf{\Sigma} = \operatorname{diag}\left(\sigma_x^2, \sigma_y^2, \sigma_z^2\right)$ is the diagonal matrix of the localization precisions squared in respective spatial dimensions and $det(\mathbf{\Sigma})$ is the determinant of the matrix $\mathbf{\Sigma}$.

3.1.2 Model parameters

In LocMoFit, individual parameters fall into either of the two groups: intrinsic parameters p^i or extrinsic p^e. As indicated by their names, p^i are model-dependent and determine the shape of the model, whereas p^e are model-independent and determine the transformation of the model. Accordingly, the extrinsic parameters $p^e = \left\{\vec{x}_0, \vec{\alpha}, \vec{S}, w_{bg}, \epsilon\right\}$ are pre-defined for all models. $\vec{x}_0$ defines the position of the model, $\vec{\alpha}$ the orientation (elements of $\vec{\alpha}$ are angles of rotations about respective coordinate axes), and $\vec{S}$ the scaling. The background weight w_{bg} determines the proportion of background localizations (e.g., unspecific labeling). The extra uncertainty ϵ defines the uncertainties that cannot be represented by the localization precision. These uncertainties could originate from linkage errors (spacing between a fluorophore and its labeled molecule; described in Section 1.1.4.5), local structural deformations that are not described by the model, and residual instabilities (e.g., vibrations and drift) of the microscope. The inclusion of the extra uncertainty ϵ and the background weight w_{bg} can improve the robustness of fitting. When extrinsic parameters p^e are applied, LocMoFit substitutes $\boldsymbol{R}\vec{v}_j + \vec{x}_0$ for the fluorophore positions $\vec{v}_j$, $\sqrt{\vec{\sigma}_k^2 + \epsilon^2}$ for the uncertainty $\vec{\sigma}$, and $(1 - w_{bg})\, M\left(\vec{x}_k, \vec{\sigma}_k \mid p\right) + w_{bg} M_{bg}$ for the PDF $M(\vec{x}, \vec{\sigma} \mid p)$. Here $\boldsymbol{R}$ is a rotation matrix defined by the angles $\vec{\alpha}$.

3.1.3 The composite model

So far I only discussed the details of a one-component model. When necessary, multiple component models can be merged to form a composite model PDF M_c through linear summation (Figure 3.2c):

$$M_c(\vec{x}, \vec{\sigma} \mid p) = \sum_m w_m M_m\left(\vec{x}, \vec{\sigma} \mid p_m\right) + w_{bg} M_{bg}. \tag{3.5}$$

M_m is the model of the m^{th} component, with its parameters p_m, of N component models in total. Here, the set of parameters $p = \{p_m, m = 1 \dots N\}$. The total weight $\sum_m w_m + w_{bg} = 1$ is imposed to ensure that M_c is a proper PDF.

For multi-channel data, the PDF can be further extended as

$$M_{mc}\left(\vec{x}_k^c, \vec{\sigma}_k^c \mid p^{mc}\right) = \sum_c M_c\left(\vec{x}_k^c, \vec{\sigma}_k^c \mid p^c\right)^{w_c}. \tag{3.6}$$

In addition to its position and precision, a localization has one more property channel c. When a localization is localized in the corresponding channel c, the single-color PDF $M_c\left(\vec{x}_k^c, \vec{\sigma}_k^c \mid p^c\right)$ outputs the computed value, otherwise a value of zero. The weight W_c of the single-channel PDF M_c is set to 1 by default. When K_c, the number of localizations in channel c, are very different across channels, the weight can be set to the inverse of the fraction of localizations in the respective channel $W_c = K_c^{-1} \sum_c K_c$. This assignment is to cancel the dependence of the likelihood function on K_c, which scales with the number of multiplications contributed by each channel in Equation 3.1, where $K = \sum_c K_c$. Equation 3.6 represents the general form of the model PDF and covers various scenarios when fitting different biological structures.

3.1.4 Other key features

Successive optimization When the model is detailed, the landscape of the negative likelihood function is usually not smooth but with multiple valleys, called local optima. The optimization is oftentimes trapped in these valleys, especially in the initial phase, and fails to reach the global optimum. To prevent this, LocMoFit allows the stepwise optimization to transition from smoother models to the most detailed by transferring parameters subsequently across chained fitting steps (Figure 3.2d).

Model selection To serve as a basis for model selection, LocMoFit additionally computes the corrected version of the Akaike information criterion (AIC_C; Cavanaugh, 1997). Although the likelihood function itself is a measure of the goodness of fit, it potentially favors a higher number of free parameters, which can cause overfitting. By contrast, AIC_C, a likelihood derivative that penalizes the number of free parameters and rewards a larger sample size, discourages overfitting. When multiple candidate models are supplied, LocMoFit selects the best according to their AIC_C acquired by fitting the same data (Figure 3.2e).

3.1.5 Related metrics

LocMoFit performs MLE, therefore the metric has the nature of probabilistic likelihood $L(p)$. Its form is closely related to that of the cross-correlation used in other studies for determining the similarity between single particles (Schnitzbauer *et al.*, 2018; Huijben *et al.*, 2021). By replacing the multiplication of $L(p)$ with a summation, we get

$$L_{cc}(p) = \sum_k M\left(\vec{x}_k, \vec{\sigma}_k \mid p\right), \tag{3.7}$$

which is a special form of the general cross-correlation cost function (Schnitzbauer *et al.*, 2018; Huijben *et al.*, 2021) when assuming a constant localization uncertainty for the template. Another metric, the Bhattacharya cost function, which is also similar to the cross-correlation cost function, has been used to perform template-free particle fusion in SMLM recently (Heydarian *et al.*, 2018; Heydarian *et al.*, 2021).

3.1.6 Implementation

LocMoFit is implemented as a MATLAB-based toolkit that comprises of three major MATLAB classes *LocMoFit*, *SMLMModel*, and *geometricModel*, a library of models, and a couple of helper functions. The class *LocMoFit* corresponds to $M_c(x, \sigma \mid p)$ and $M_{mc}\left(x_k^c, \sigma_k^c \mid p^{mc}\right)$ for single-channel and multi-channel fits, respectively, and is the main class for controlling and performing fitting, and to summarize and visualize the result. To perform the fitting, the class *LocMoFit* has to be linked to at least one object of the class *SMLMModel* or its subclasses, which corresponds to a one-component PDF $M(x, \sigma \mid p)$. The class *SMLMModel* computes the PDF by converting from an object of a *geometricModel* subclass. The geometric model is coded in such a subclass, whose object corresponds to the geometric model $f(p)$. The default values of intrinsic parameter arguments for fitting are also defined in such a subclass.

3.2 Validation of LocMoFit

First, I wanted to validate LocMoFit and test its robustness for estimating parameters. For that, I produced synthetic localization data based on a specific geometric model with ground truth parameters using the simulation engine (Figure 3.2a). In the simulations, SMLM properties (see Section 6.2.2.2) were introduced by a realistic description of fluorophore blinking. Here, I evaluate the robustness based on estimation errors, i.e., the difference between parameter estimates output by LocMoFit and their ground truths. We suggest to always perform such an evaluation for a newly established pipeline before its application to experimental data.

Here, to systematically evaluate the robustness of LocMoFit, I simulated NPC particles based on an model derived from prior knowledge (Figure 3.3) and varied four factors contributing to the image quality: localization precision, labeling efficiency, background localizations (e.g., from unspecific labeling), and re-blinks (see Figure 3.4 for example particles).

This source model of the synthetic NPCs is a point model (Figure 3.3a) built according to the mapping of the nucleoporin Nup96 to the EM density of the NPC (Figure 3.3b). The model is composed of 32 coordinates, each corresponding to a copy of Nup96 per Y-complex subunit, as discussed in Section 1.3.2. Two copies of Nup96 form a symmetric unit that is repeated eight times rotationally on each of the nucleoplasmic and cytoplasmic rings, representing the eight-fold rotational

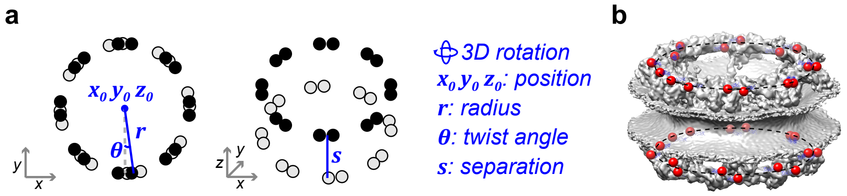

Figure 3.3 | The NPC model used for simulations and fitting. The NPC point model (**a**) is built based on the the positions of Nup96 mapped to the EM density (**b**; PDB ID: 5A9Q; von Appen *et al.*, 2015). In the model, two copies of Nup96 form a corner (unit) that presents itself eight times rotationally with an equal spacing to form a ring. Two copies of the ring, sharing the same radius r and having separation s in between, form the model. The twist angle θ determines the rotational displacement between the rings. To ensure the flexibility and generality, in each unit, the two Nup96 copies share the same distance to the central axis although a distance offset is known (von Appen *et al.*, 2015). *Adapted from Wu* et al.*, 2021, on which I am the first author.*

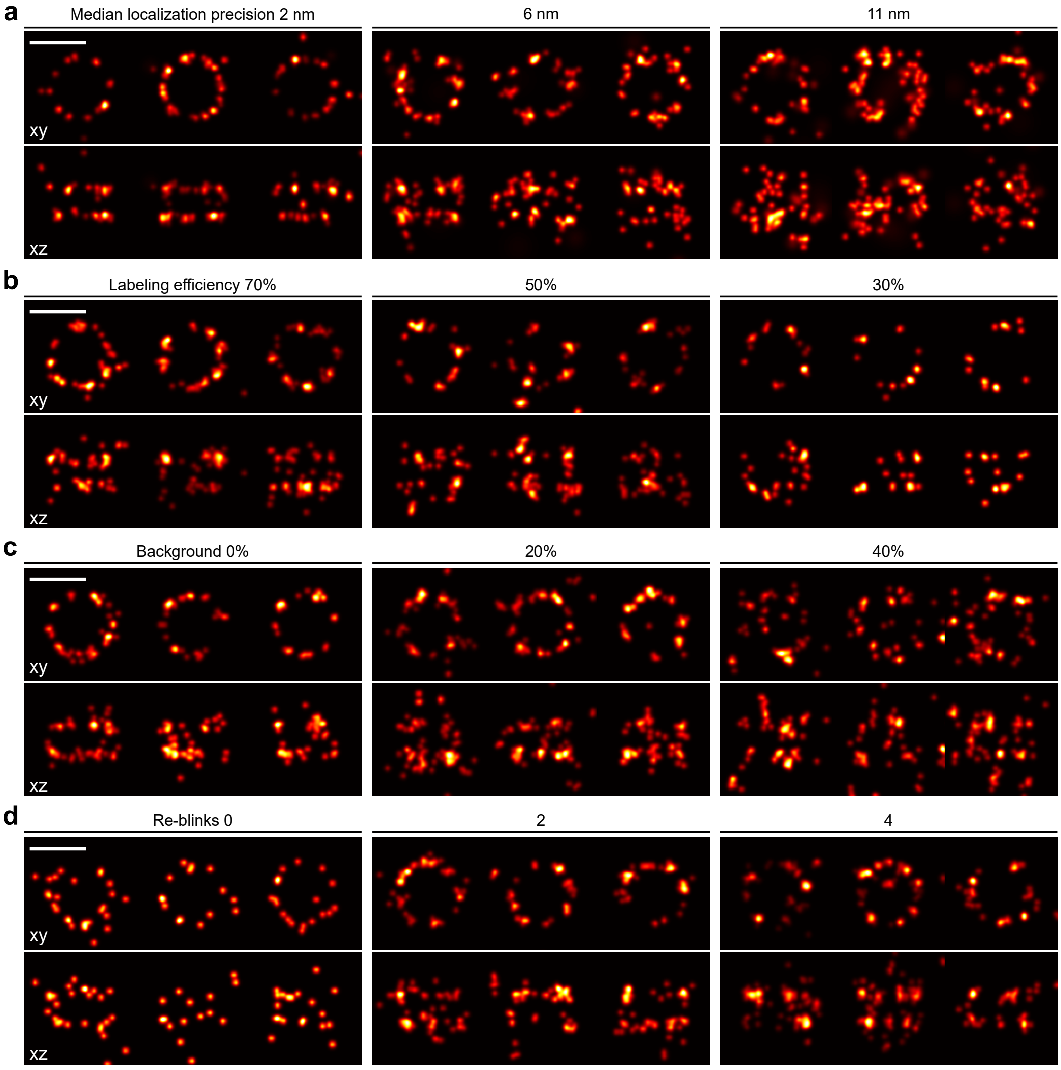

Figure 3.4 | Simulations of NPC particles across various conditions. Example particles of the simulations based on the model for different median localization precisions (**a**), labeling efficiencies (**b**), background localizations (**c**), and fluorophore re-blinks (**d**). 'xy' denotes the top view and 'xz' the side view. Scale bars: 100 nm. *Adapted from Wu* et al.*, 2021, on which I am the first author.*

symmetry. The shared *radius* r of the rings as well as the *twist angle* θ and *separation* s between the two rings are the intrinsic parameters of the model.

I fitted the model to the localization data of the synthetic NPC particles and quantified their structural parameters. As shown in Figure 3.5, overall the mean estimation errors are close to zero, indicating a bias-free parameter estimation. The only exception is the ring separation s, which has an increasing negative bias toward lower labeling efficiency. I visually inspected the simulated particles and found much more particles having their ring separations smaller than 30 nm when the labeling efficiency is low. These small ring separations are caused by the dual-ring approximation of one-ring NPCs arising from having one ring entirely unlabeled by chance. This is clearly shown when comparing 70 % labeling efficiency to 30 %, which has a long tail on the side of smaller ring separations (Figure 3.6). This issue might not be identified without a simulation, highlighting its importance for validating a pipeline. As expected, the spreads (uncertainties) of the errors positively correlate with worse data quality (increasing localization precision and background as well as decreasing labeling efficiency and re-blinks) in general, although LocMoFit is insensitive to re-blinks. In fact, the quality range that can be achieved in an imaging routine (e.g., localization precision 5 nm, labeling efficiency 65 %, background localizations 5 %, 2.5 re-blinks) yields unbiased errors with small uncertainty, presenting LocMoFit as a reliable quantitative tool.

3.3 Quantifying structural parameters

LocMoFit measures the interpretable parameters at the single-particle level requiring no averaging so that information on heterogeneity is retained after analysis. Potentially, this allows us to study the biological heterogeneity among individual particles. To demonstrate these merits, I applied LocMoFit to quantify the structural parameters of the NPC and microtubules, two ‘standard’ macromolecular complexes extensively used in SMLM as test structures.

3.3.1 Quantifying the NPC

Ulf Matti imaged endogenously SNAP-tagged Nup96 in a genome-edited U2OS cell line (Thevathasan *et al.*, 2019; Diekmann *et al.*, 2020). This cell line allowed us to obtain hundreds of NPC particles per field of view, as a large part of the cell’s nuclear envelope lies parallel in close proximity to the coverslip (Figure 3.7a). I fitted the single NPCs (Figure 3.7b) with a model of two continuous rings to roughly estimate the position and orientation of each particle as initial parameters for a subsequent fitting step. In the later step, I fitted the NPCs with the NPC model mentioned above (Figure 3.3a) to extract the three intrinsic parameters. I quantified the radius $r = 53.4 \pm 2.3\,\mathrm{nm}$ (median values ± standard, unless specified otherwise) and the twist angle $\theta = 8.8 \pm 9.0°$ (Figure 3.7c), which agree well with previously

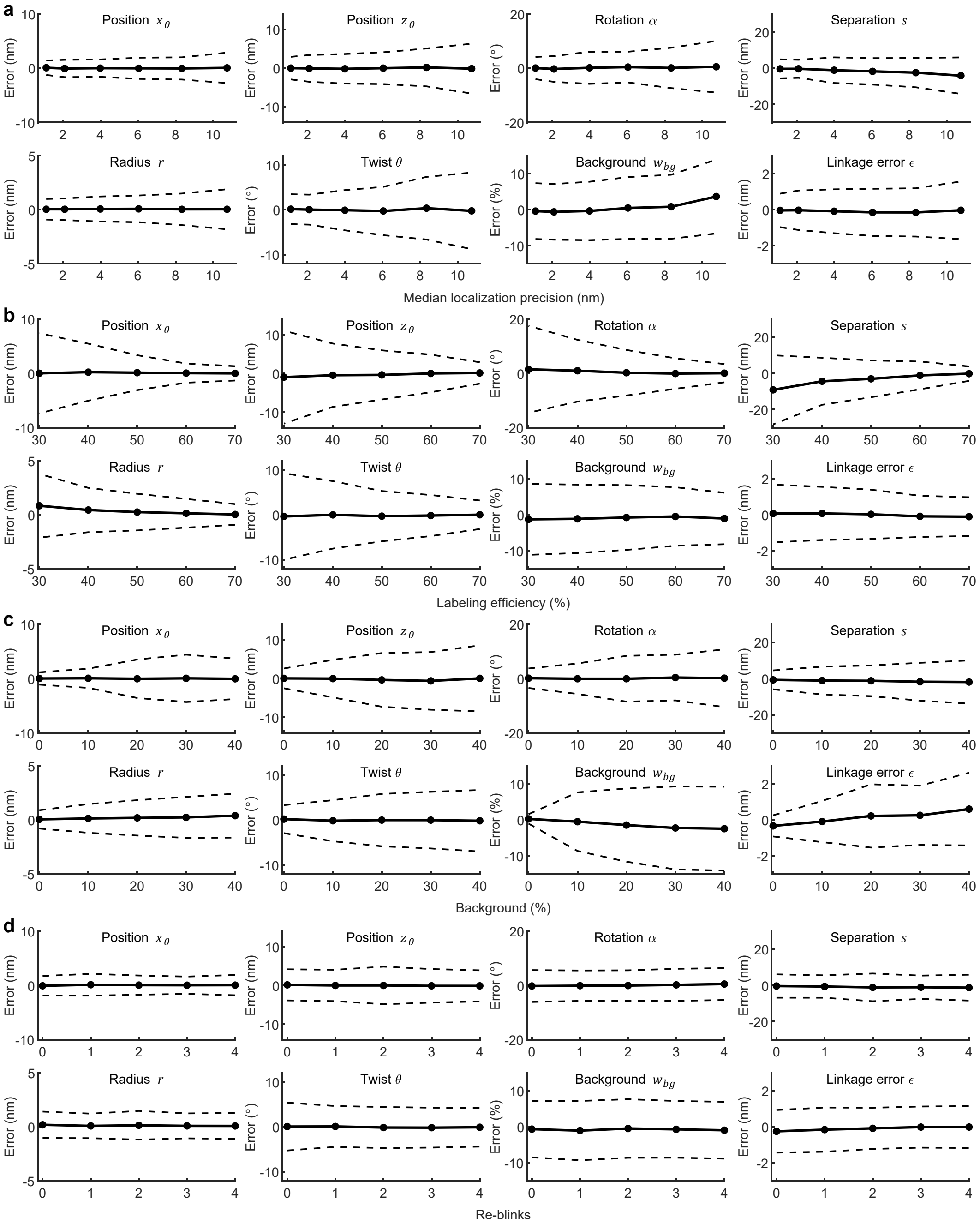

Figure 3.5 | Estimation errors in dependence on factors contributing to data quality in simulated NPC datasets. Based on the model shown in Figure 3.3, across different median localization precisions (**a**), labeling efficiencies (**b**), background localizations (**c**), and fluorophore re-blinks (**d**). Solid lines and dots indicate means, and dashed lines standard deviations. Example particles are shown in Figure 3.3. Sample size: 1,000 sites for each dot. *Adapted from Wu* et al.*, 2021, on which I am the first author.*

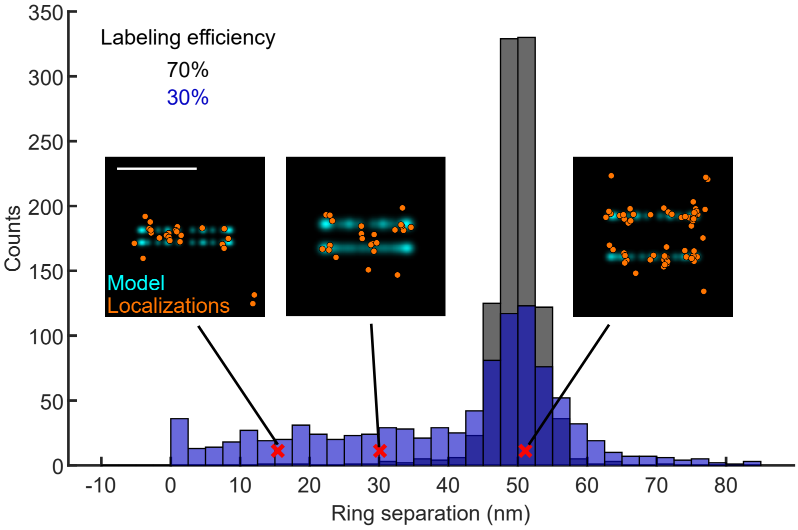

Figure 3.6 | Distributions of the measured ring separation of simulated NPCs with 30 % and 70 % labeling efficiency. Red crosses indicates the measured ring separations of three example NPCs shown in their side views. These three pores are all from the dataset with 30 % labeling efficiency. The data shown here have also been used in Figure 3.5. Sample size: 1,000 sites for each condition. Scale bar: 100 nm. *Adapted from Wu* et al.*, 2021, on which I am the first author.*

reported values (Thevathasan *et al.*, 2019). Because the unmatched refractive index causes a depth-dependent distortion along the z axis (Li *et al.*, 2019), the measured ring separation s of the NPC has an unwanted depth-dependent scaling (Figure 3.8). I corrected this experimental scaling factor (see Section 6.2.5.4) to obtain a mean value of 1, corresponding to the previously reported ring separation 49.3 nm (Thevathasan *et al.*, 2019). To investigate the source of variation, I compared the experimentally quantified parameters to the measurements of particles simulated using the experimental median parameters as the ground truths. The comparison shows even narrower distributions (Figure 3.7c, gray curves) for the simulations (see Figure 3.9), which represent technical variations, implying the presence of other sources of variation that were not considered in the model, potentially including biological heterogeneity.

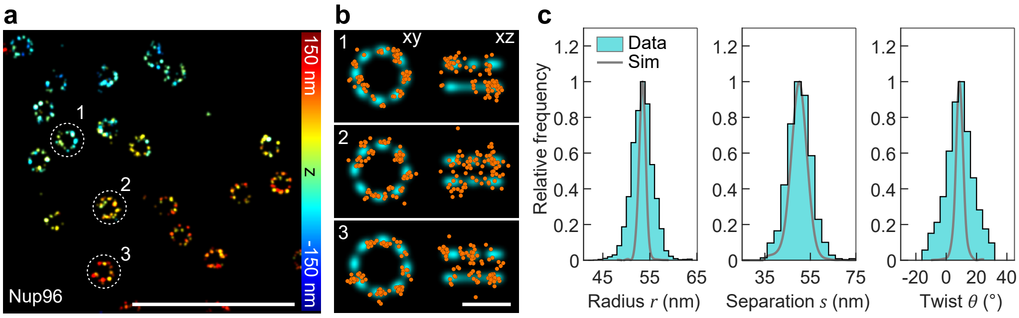

Figure 3.7 | Measuring structural parameters of single NPCs. (**a**) A top-view representative image of the Nup96-labeled nuclear pore complexes (NPCs, Nup96-SNAP-AF647) in the cell. (**b**) Example NPCs (localizations in orange) as numbered in **a** and their fitted model (cyan; see also Figure 3.3). (**c**) Distributions of three fitted parameters: radius $r = 53.4 \pm 2.3\,\mathrm{nm}$, separation $s = 50.2 \pm 5.6\,\mathrm{nm}$, and twist $\theta = 8.8 \pm 9.0°$. 'Sim' stands for 'simulation' (gray; see also Figure 3.9). Sample size: 3,517 sites, 5 cells. Scale bars: 1 µm (**a**), 100 nm (**b**). Ulf Matti acquired all the localization data. *Adapted from Wu* et al.*, 2021, on which I am the first author.*

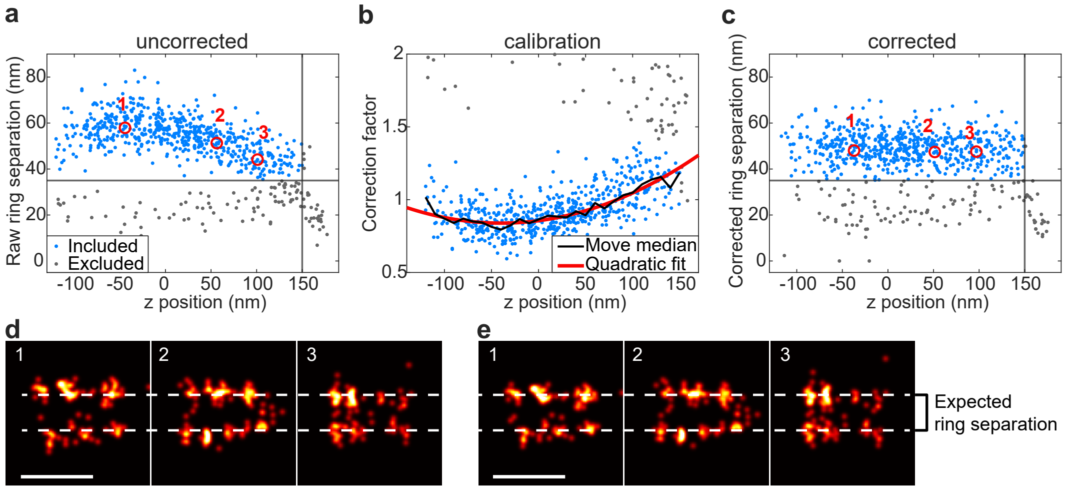

Figure 3.8 | Correction of z-dependent distortion. (**a**) The raw ring separation of the nuclear pore complex (NPC) depends on its z position in the acquired dataset. (**b**) a quadratic fit can well approximate the trend (median) of the correction factor over the z position. (**c**) The ring separation over the z position of each pore after the correction applied to all localizations. NPCs with ring separations smaller than 35 nm (gray horizontal lines, to exclude NPCs with only one ring labeled) and with z positions further than 150 nm away from the focus (gray vertical lines, to exclude out-of-focus pores) were excluded from the curve fit. Each point represents one NPC. **a**-**c** are based on the same pores. Side views of example sites at different z positions before (**d**) and after (**e**) the correction, as indicated by the numbered red circles in **a** and **c**. Scale bars: 100 nm. Ulf Matti acquired all the localization data. *Adapted from Wu* et al.*, 2021, on which I am the first author.*

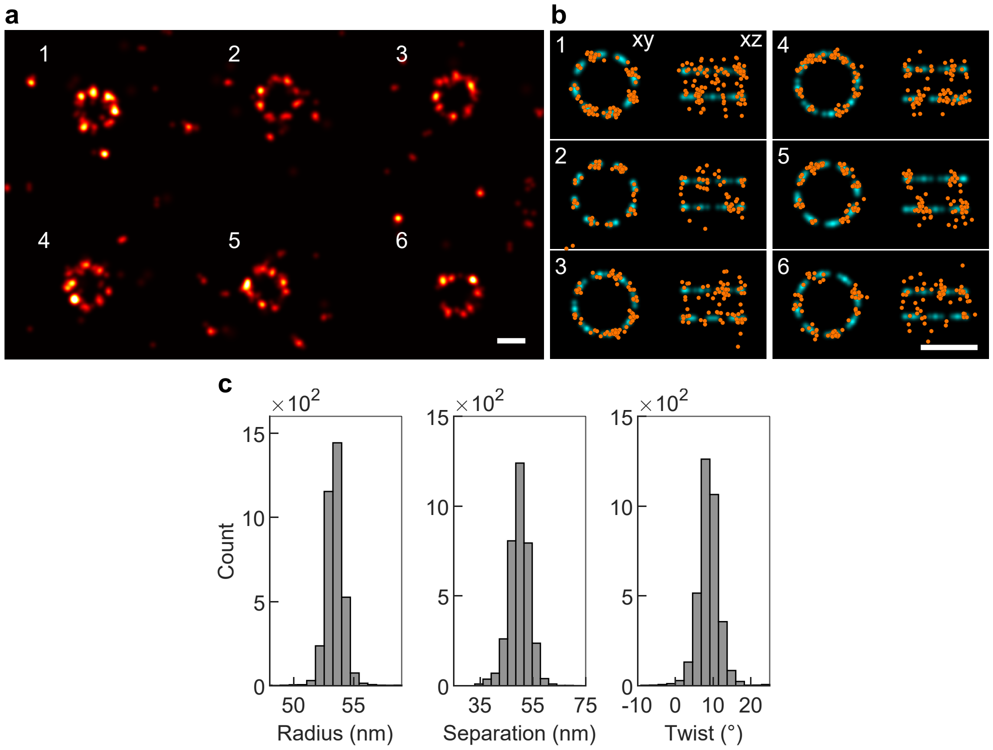

Figure 3.9 | Simulations based on experimental parameters. (**a**) The top view of six example nuclear pores. (**b**) The localizations (orange) of the nuclear pores in **a** displayed alongside the NPC point model (see Figure 3.3). xy: top view; xz: side view. (**c**) Distributions of the three fitted intrinsic parameters: radius $r = 53.4 \pm 0.8\,\mathrm{nm}$, separation $s = 49.8 \pm 3.8\,\mathrm{nm}$, and twist $\theta = 8.8 \pm 3.0°$. Sample size: 3,511 sites. Scale bars: 100 nm. *Adapted from Wu* et al.*, 2021, on which I am the first author.*

3.3.2 Quantifying microtubules

Previously, the diameter of microtubules was usually measured by performing a curve fit on a cross-sectional profile. Such an analysis is limited to short segments, usually less than 500 nm long, assuming approximately a linear geometry, which is required for a precise measurement in the the cross-section. The low sampling rate and residual curvature pose a risk of introducing a bias. In comparison, LocMoFit does not require short segments because it is independent of the linear, or in principle, any geometry. Here we approximated microtubules by the model of a 3D cubic-spline tube (Figure 3.10c), which can trace the curvature along the microtubule axes. By fitting micrometer-long immunolabeled microtubules with the model, we quantified the apparent tubular radius r as 24.1 ± 3.4 nm (Figure 3.10d). This value is 11.6 nm larger than the reported outer radius (12.5 nm) of microtubules alone, in line with the reported mean radius of indirectly immunolabeled microtubules (Früh *et al.*, 2021). This is a good reminder that in fluorescence microscopy images, fluorescent labels are visualized instead of the tagged targets themselves. With the resolution provided by SMLM, the effect of the linkage error has to be considered (see Section 4.4).

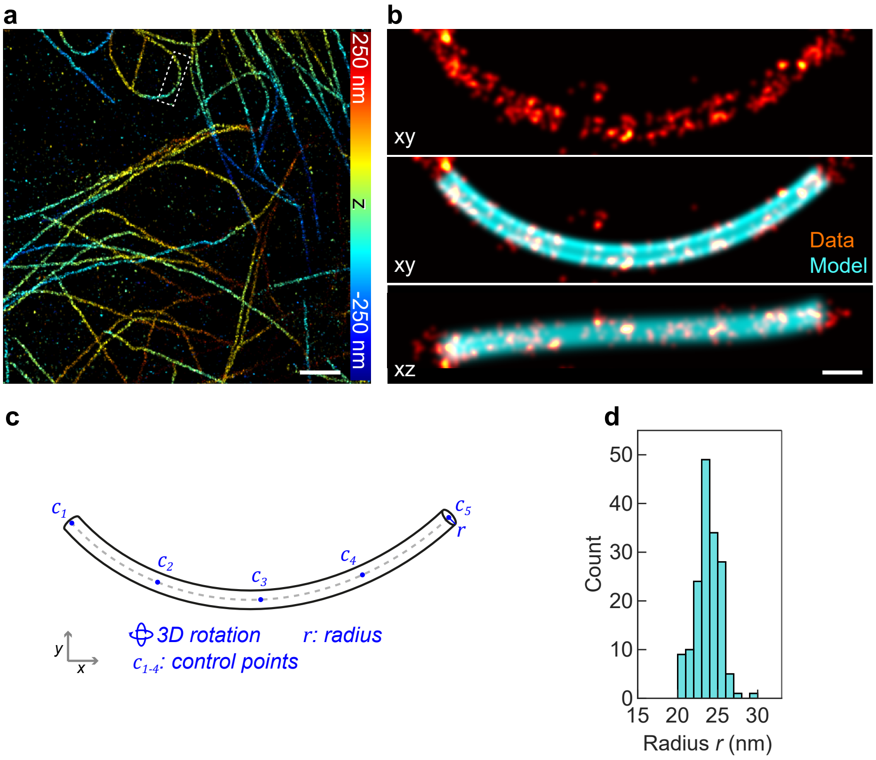

Figure 3.10 | Measuring structural parameters of microtubules. (**a**) A top-view representative image of immunolabeled microtubules in the cell. (**b**) An micrometer-long microtubule segment as boxed in **a**, along with the microtubule model in **c** with fitted parameters. (**c**) The microtubule model has a backbone described by a c-spline with fit parameters listed (blue). xy: top view; xz: side view. (**d**) The distribution of the tubular radius of the microtubule segments. Sample size: 161 segments. Scale bars: 1 µm (**a**), 100 nm (**b**). The localization data was published in Speiser *et al.*, 2021. *Adapted from Wu* et al.*, 2021, on which I am the first author.*

3.4 Model selection

The key to measuring meaningful parameters by LocMoFit is to incorporate a model that well describes the structure of interest. To enable the selection of such a model, LocMoFit reports AIC_C after fitting. AIC_C is a score that indicates the most likely model out of the models that are fitted. AIC_C is a log-likelihood (LL) derivative that further considers the number of free parameters P and the sample size K:

$$AIC_C = AIC + \left(2P^2 + 2P\right) / (K - P - 1). \tag{3.8}$$

Here $AIC = 2P - 2\ln \hat{L}$, where $\hat{L}$ is the maximum likelihood value reported by equation 3.2 after fitting. In LocMoFit, K is the number of localizations. By definition, AIC_C discourages high P and encourages larger K to prevent overfitting. The lowest AIC_C corresponds to the best model and should be the model of choice. This choice reflects our preference of a model that yields higher maximum likelihood with fewer free parameters. To validate this idea, I tested whether LocMoFit is able to reveal the known rotational symmetry of the NPC. I fitted each NPC in the Nup96 data set (Figure 3.7a,b) with models of different rotational symmetries ranging from 6 to 10-fold (see insets in Figure 3.11a). The cumulative distributions of AIC_C clearly show that the 8-fold symmetric model has the highest AIC_C overall (Figure 3.11a) and is therefore the best model, recapitulating the known symmetry of the NPC. We also simulated NPCs with different rotational symmetries and fitted the pores with these models. In the result (Figure 3.12), the overall AIC_C is the highest when the symmetries of the particles and that of the fitted model match, again validating the model selection.

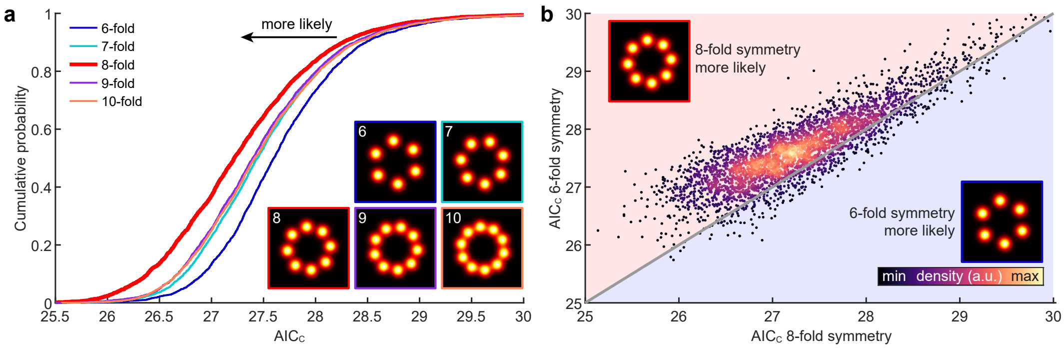

Figure 3.11 | Model selection by LocMoFit. (**a**) Cumulative distributions of the normalized AIC_C obtained by fitting the same experimental nuclear pore complexes (NPCs) with models having different rotational symmetries. (**b**) The normalized AIC_C obtained by fitting each NPC (dots) with the model having the 6-fold rotational symmetry against that of the 8-fold symmetry. The SMLM data is the same as in figure 3.7. Sample size: 3,517 sites, 5 cells. Ulf Matti acquired all localization data. *Adapted from Wu* et al.*, 2021, on which I am the first author.*

Interestingly, when I further investigated the scatter plot showing the pairwise comparison (Figure 3.11b) of fitted experimental AIC_C between 6 and 8-fold symmetric

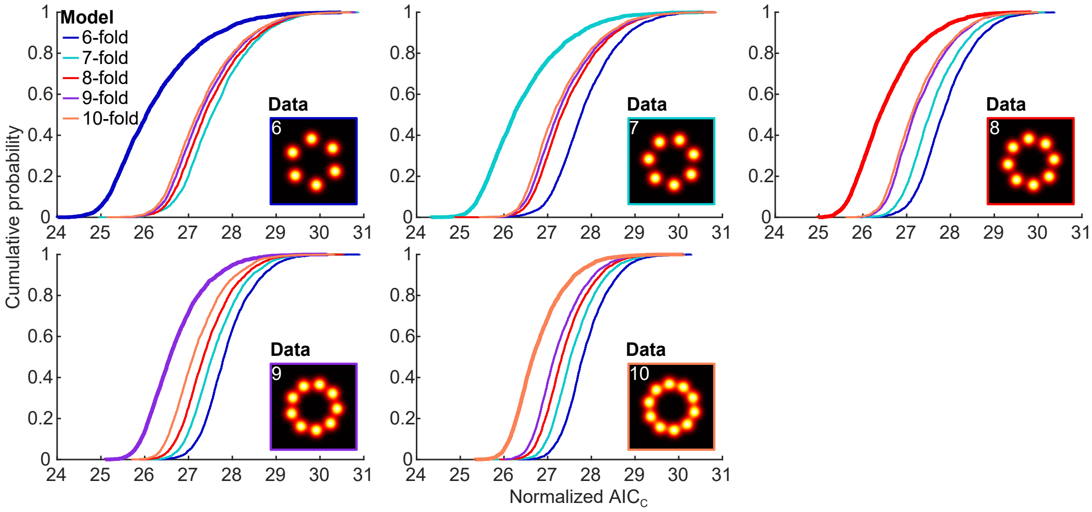

Figure 3.12 | The model selection applied to simulated NPCs. These cumulative probability distributions of the normalized AIC_C were acquired by fitting the same simulated nuclear pore complexes (NPCs) with models of different symmertries. The NPCs were simulated based on models having different rotational symmetries (shown by insets with symmetries displayed). Fitted models are indicated by different colors. Sample size: 3,000 sites for each panel. *Adapted from Wu* et al.*, 2021, on which I am the first author.*

models, I found that some particles have higher AIC_C for the 6-fold symmetry. However, the symmetry is not evident when visually inspecting single particles. To know whether the model selection is effective at the single-particle level, I revisited the simulated data and found a wrong model can still yield higher AIC_C than the correct one by chance, as shown in Figure 3.13a,b. This trend is more clear when the extra uncertainty is higher (i.e., $\epsilon = 6.3\,\mathrm{nm}$, corresponding to the experimental ϵ, compared to $\epsilon = 3\,\mathrm{nm}$, representing a technical uncertainty in an ideal case). With $\epsilon = 6.3\,\mathrm{nm}$, a small yet noticeable fraction (4 %) of 8-fold symmetric particles have a lower AIC_C when fitted with a 6-fold symmetric model (Figure 3.13c,d). Therefore, I do not recommend the interpretation of the model selection at the level of single particles.

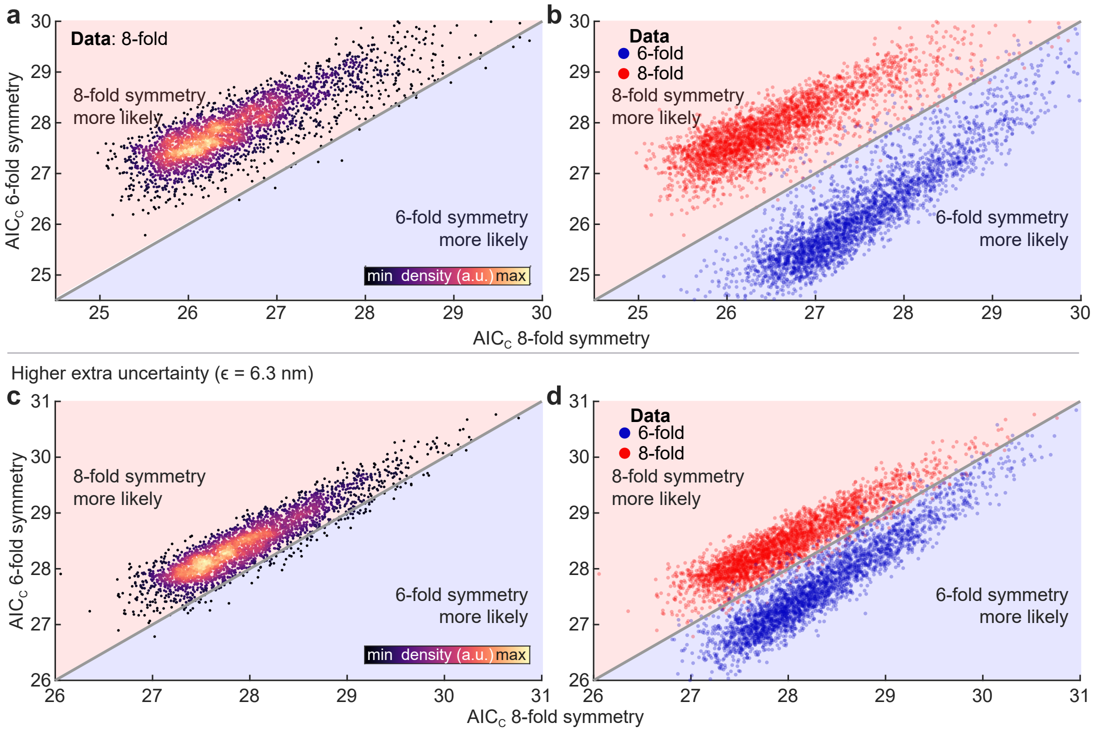

Figure 3.13 | Single-site AIC_C of simulated NPCs. (**a-b**) The normalized AIC_C reported by fitting each simulated nuclear pore complex (NPC; dots) with the model having the 6-fold rotational symmetry against that of the 8-fold. Either the 8-fold symmetric NPCs alone (a) or together with the 6-fold (b) are shown. The SMLM data used here are the same as in Figure 3.12, with extra uncertainty added $\epsilon = 3\,\mathrm{nm}$. (**c-d**) The same plots as in **a** and **b** but the NPCs simulated with higher extra uncertainty ($\epsilon = 6.3\,\mathrm{nm}$) are shown instead. Sample size: 3,000 sites for each rotational symmetry of the data. Data shown in **a**,**c** are also used in **b**,**d**. *Adapted from Wu* et al.*, 2021, on which I am the first author.*

3.5 Multi-color static protein distribution maps

In this section, I will discuss the application of LocMoFit to multi-color SMLM data. Multi-color microscopy can inform on spatial relations between different labeled targets, for example, how components of the same protein complex are distributed with respect to each other. However, labeling of multiple biological targets in parallel is limited by the maximum number of simultaneous labels that can be applied in the same sample. This is especially true in SMLM because the possible combinations are constrained by e.g., fluorophores' spectra and imaging conditions, practically limiting the number of colors in routine multi-color SMLM to three.

In LocMoFit, I applied the concept of a reference structure to generate protein distribution maps of target proteins that have unknown distributions. To perform the analysis, a target protein has to be co-labled with the reference structure, which can be described by a template (a rigid geometric model). Individual particles can then be registered by fitting solely the reference structure. Fusing the registered particles then yields an average distribution map of both the reference and the target. The same procedure can be applied to multiple pairs of different target proteins co-labled with the same reference structure. Since this target proteins share the same reference, they can be mapped to the same coordinate system to form a multi-color static protein distribution map.

To illustrate this concept, I used Nup96, which acts as a reference structure, to reconstruct the underlying distributions of other NPC components. In the Nup96-labeled cells, Ulf Matti co-labeled one of the target proteins Elys, Nup133, Nup62, or Nup153 using immunostaining or the inner channel of the NPC using wheat germ agglutinin (WGA) staining, respectively. By this, I obtained multiple dual-color datasets, where single NPCs were then fitted with a template in the Nup96 channel. The template was the point model (Figure 3.3a) with intrinsic parameters fixed to the previously quantified median values (Figure 3.7c). Importantly, the targets covered various labeling efficiencies: e.g., high for Elys (Figure 3.14a) and low for Nup133 (Figure 3.14b).

In the resulting averages (Figure 3.14c), the underlying distributions of the targets formed with improved contrast and labeling efficiency, regardless of the original labeling efficiency. Based on the shared reference, combining the individual dual-color averages to a multi-color protein density map was simply a superposition of all averages (Figure 3.14d).

For such an analysis, I would suggest not to overinterpret the average of the reference structure (e.g., Nup96 in the section above) because of the potential template bias. This term describes the patterns not in the original data but arising artificially from the fitting template during averaging (also discussed in Paragraph *Template bias* in Section 4.2.1). The target proteins are intrinsically free from the template bias because their information was not used in the registration.

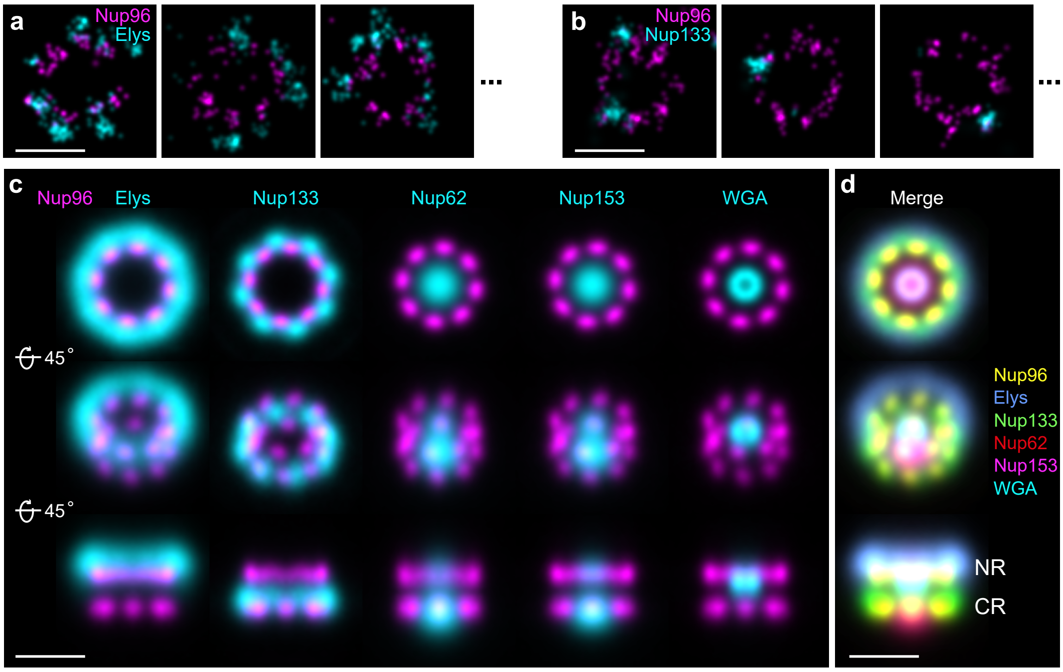

Figure 3.14 | Reconstructed protein distribution maps of the nuclear pore complex. Individual exemplary particles of Nup96-SNAP-AF647 with immunolabeled Elys-CF680 (**a**) or Nup133-CF680 (**b**). (**c**) The averages, hence the reconstructed protein distribution maps, of NPC particles of Nup96-SNAP-AF647 (magenta) with different targets (cyan) co-labeled. By mapping single particles to the common coordinate system based on the template fitting of Nup96, the individual averages (**c**) and the multi-color average were formed (**d**). NR denotes nucleoplasmic ring and CR cytoplasmic ring. Note that the immunolabeled structures may not entirely represent the true structures in the cell because of high linkage error and potentially biased labeling. Sample sizes: Elys: 1,875 sites; Nup133: 1,739 sites; Nup62: 2,263 sites; Nup153: 2,159 sites; WGA: 1,778 sites. 3 cells for all. Scale bars: 100 nm. Ulf Matti acquired all the localization data. *Adapted from Wu* et al.*, 2021, on which I am the first author.*

3.6 Model-free particle fusion

In the case when an appropriate reference structure is absent, LocMoFit can still reveal the underlying structure of a protein distribution through a model-free averaging independent of other proteins. As discussed in Section 1.2.3.3, the basic concept of a model-free averaging is to register sites to each other based on similarity, determined by e.g., cross-correlation (see also Section 3.1.5). The premise is that the component particles of the average share the same underlying structure. A recent successful model-free averaging for SMLM was implemented based on a redundant pairwise particle-to-particle registration of all particles (Heydarian *et al.*, 2018; Heydarian *et al.*, 2021). In LocMoFit, I implemented the model-free averaging differently in two aspects. First, LocMoFit uses the LL, or log-likelihood, as the similarity measure. Second, the pairwise registrations are applied to only a subset of particles, reducing the computational cost. The workflow of the model-free averaging in LocMoFit consists of five steps:

1. Calculating the sum of LL of each particle in a small subset based on the pairwise similarity (Figure 3.15a and b).
2. Building the initial data-driven template in the descending order of the sum of LL (Figure 3.15c).
3. Registering and fusing all particles to the template to form an average (Figure 3.15d).
4. Defining the resulting average as the new template (Figure 3.15d).
5. Repeating steps 3 and 4, usually less than 15 rounds, until the averages converge (Figure 3.15e).

The average with the highest sum of LL in step 5 is then defined as the final average.

Here, I would like to explain the first two steps in more detail. First, the sum of LL indicates how well a particle can describe other particles. This value for each particle is obtained by a pairwise registration of a small subset of particles. Next, the initial template is created by cumulative registration and fusion of particles in the descending order of the sum of LL.

I applied this approach to NPCs in one of the analyzed cells contributing to Figure 3.7c. I randomly selected a subset of 50 particles from the total 1,312 NPCs in the cell (see example particles in Figure 3.7a). The output final average (Figure 3.16a) recapitulates the mapping of Nup96 to the EM density (Figure 3.16b) without any structural assumption. The top view of the average clearly shows an 8-fold rotational symmetry and the side view shows two separate rings (Figure 3.16c). Strikingly, when I display the two rings separately (Figure 3.16c), each corner appears elongated and has an outward tilt. The tilt (Figure 3.16b) corresponds to slightly different distances of the two copies per corner to the central axis. In a previous work (Heydarian *et al.*, 2021), this characteristic tilt could not be resolved in template-free averages of another nucleoporin (Nup107) which is part of the same subcomplex as Nup96.

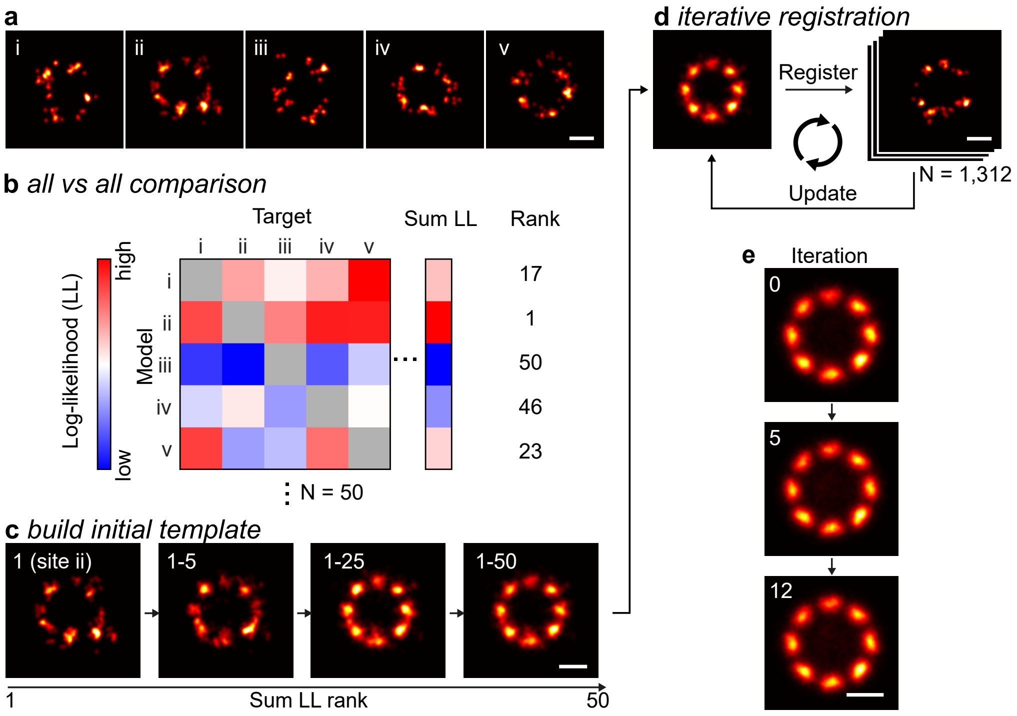

Figure 3.15 | The workflow of the model-free particle averaging. Example sites (**a**) from the initial subset of particles (50 particles in the example) randomly selected in the cell used for the all vs all comparison (**b**). This pair-wise comparison is to measure and to rank the the sum of log-likelihood (LL) of the particles. (**c**) To build the initial template, the particle on rank 1 is then used to register and fuse other pores in the subset cumulatively, in the order of the rank. To form the first average, the rest of particles in the same cell are then fused to the initial template after registration. (**d**) The new average is used as an updated template to register all the sites and create a new average. This registration is iterated until the average converges, yielding the final average (**e**). Sample size: 1,312 sites, 1 cell. Scale bars: 50 nm. Ulf Matti acquired all the localization data. *Adapted from Wu* et al.*, 2021, on which I am the first author.*

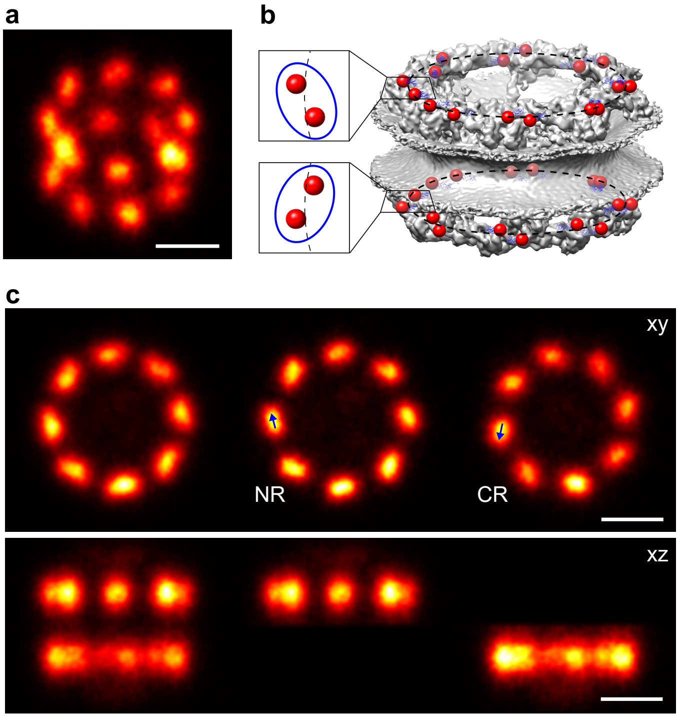

Figure 3.16 | The model-free average of the NPC. (**a**) The final average of the nuclear pore complexes (NPC) in the tilt view recapitulate the mapping of Nup96 C-termini to the EM density (PDB ID: 5A9Q; von Appen *et al.*, 2015) of the NPC (**b**). The average clearly shows two separate rings and the 8-fold symmetry, two features that were not included as known parameters in the analysis. (**c**) The top and side views of the average with both rings, only the nucleoplasmic ring (NR), and the cytoplasmic ring (CR) displayed. Sample size: 1,312 sites, 1 cell. Scale bars: 50 nm. Ulf Matti acquired all the localization data. *Adapted from Wu* et al.*, 2021, on which I am the first author.*

3.7 Dynamic protein density maps

Live-cell incompatibility of most techniques for *in situ* structural biology hindered their application to directly measure dynamic structural changes on the nanoscale. This issue also applies to SMLM so that its resulting data are usually snapshots of a dynamic biological process taken in fixed cells. However, LocMoFit overcomes the limit by extracting temporal information from the snapshots based on a quantifed structural parameter that changes overtime. More specifically, such a parameter is used as the basis for sorting the snapshots along the progression of the process. In this section, I will demonstrate this concept using clathrin-mediated endocytosis in both mammalian cells and budding yeast as examples.

3.7.1 Dynamic reconstruction of clathrin coat remodeling in mammalian cells

Here, I highlight the capability of LocMoFit to extract dynamic information based on the example of mammalian clathrin mediated endocytosis. For showcasing this particular example, I teamed up with Makus Mund and Aline Tschanz. Together with Johanna L. Mehl, they imaged immunolabeled clathrin at endocytic sites in fixed SK-MEL2 cells in 3D (Fig. 3.17a). This resulted in snapshots of super-resolved clathrin coats fixed at random time points during the endocytic process (Figure 3.17b). By visually inspecting single sites, we found that the top-view projections of most clathrin coats are round structures with different sizes. By further exploring the data in 3D, we found different shapes that have been reported previously (Bucher *et al.*, 2018), including flat, curved, dome-like, and spherical structures. To quantitatively describe these structures, I built a model of a spherical cap that can approximate all these shapes (Figure 3.17c). This model is parametrized by a radius R and a closing angle θ, where $\theta = 0°$ defines a flat structure and $\theta = 180°$ a complete vesicle. Because endocytosis generates a closed vesicle from the plasma membrane, the closing angle θ increases monotonically over time and therefore encodes information about the endocytic progression.

Although the above-mentioned parameterization is straightforward, it is not efficient. In the data, endocytic sites have a defined range of surface area determined by the number and density of clustered clathrin. However, fitting R without considering the surface area can lead to unnecessary large model coats for structures that are flat and makes the evaluation of the optimization computationally costly. Furthermore, the unconstrained surface area causes an exploration in the unreasonable range of the parameter space, often leading to failed optimization. I solved this issue by replacing r and θ with the surface area $A = 2\pi R^2(1 - cos\theta)$ and θ as fitting parameters, allowing a constraint of the surface area and significantly improving the efficiency and robustness of fitting. With this parameterization, the radius R and thus the curvature $H = 1/R$ can still be obtained through simple calculation.

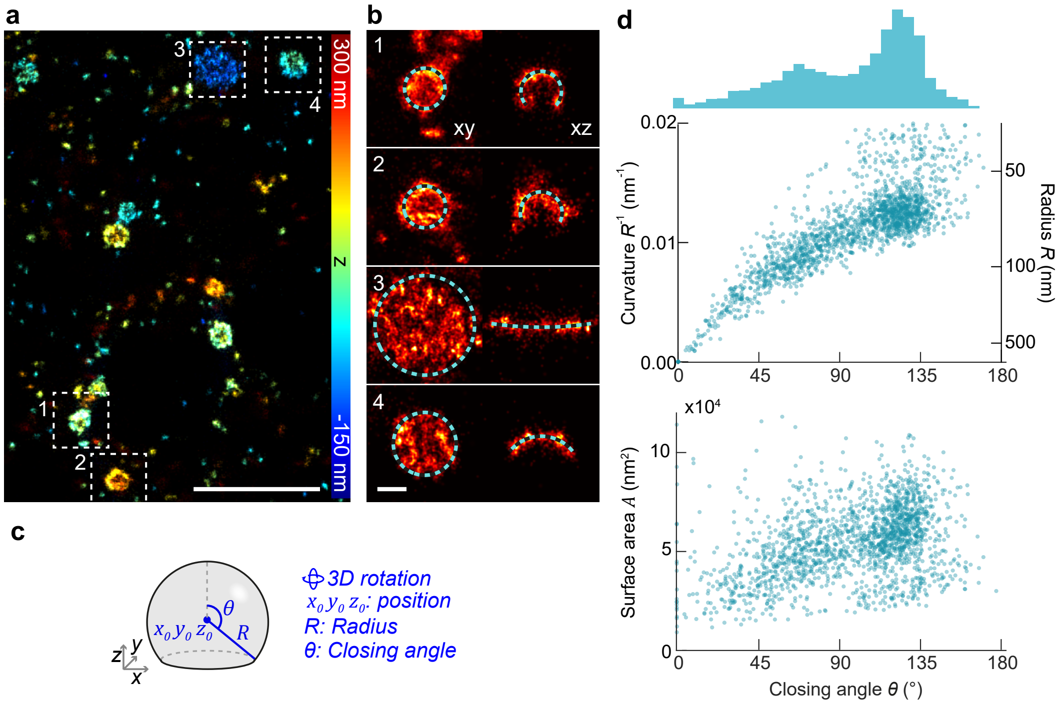

Figure 3.17 | Quantification of mammalian clathrin coats. (**a**) An example top-view image of sub-region of a clathrin-immunolabeled SK-MEL-2 cell. (**b**) Zoom in of the example clathrin coats indicated by numbered boxes in **a**. (**c**) The geometric model of a spherical cap we built for describing the coats. Fitted parameters are listed in blue. (**d**) Scatter plots showing the curvature $H = R^{-1}$ (middle panel) and the surface area A (lower panel) against the closing angle θ. The top panel shows the distribution of θ. Sample size: 1,798 sites, 13 cells. Scale bars: 1 µm (**a**), 100 nm (**b**,**e**). Markus Mund, Aline Tschanz, and Johanna L. Mehl acquired the data. Aline Tschanz and I performed the analyses jointly. *Created based on data published in Mund* et al.*, 2022, on which I am a co-author.*

To extract the structural parameters with LocMoFit, we fitted the model to all the 1,798 sites we acquired. In the extracted parameters, we found a clear trajectory of curvature H increament over θ, which is ranging from 0° to almost 180° (Figure 3.17d, middle panel). The increment slows down toward larger θ. Interestingly, barely any site is an entirely closed vesicle, which corresponds to $\theta = 180°$, and only a small portion of the sites is flat. The distribution of the closing angle has two peaks, one at around 70° and one at 130° (Figure 3.17d, top panel). Each of the peaks reflects an enriched structural intermediate in the investigated cells. The curvature H ranges from 0 nm^{-1} to 0.022 nm^{-1} with a median of 0.011 nm^{-1}, corresponding to a median radius of 87 nm. The surface area A ranges from 9,000 nm^2 to 140,000 nm^2, with a median of 54,000 nm^2 (Figure 3.17d, bottom panel).

The highly quantitative measurements opened the gate to develop a data-driven model that describes the relation between the structural parameters. For the development of such a model, we teamed up with Felix Frey and Ulrich S. Schwarz, who developed the *cooperative curvature model*. This model is based on two main assumptions that 1) the growth of the coat is determined by the addition of triskelia to the rim with a constant rate (Figure 3.18a) and 2) the coat curvature increase toward a preferred value H_0 determined by individual triskelia and their overall interactions. In this model, the preferred curvature and the cooperative effects of individual triskelia in the coat combinatorially determine the rate of curvature generation. We can solve this model to obtain curvature H as a function of the closing angle θ (see Mund *et al.*, 2022 for the full description of the model and its detailed derivation):

$$H(\theta) = H_0 \tanh\left(\frac{\gamma\theta}{H_0}\right). \tag{3.9}$$

Here γ denotes the initial rate of curvature increase.

Based on Equation 3.9, we also can describe the surface area $A(\theta)$ as a function of θ, given that $A(\theta) = 2\pi r^2(1 - cos\theta)$. We fitted this new model and the current models to H over θ and then converted the fitted models to A as a functions of θ (Figure 3.18b,c). The fit and derivatives show a monotonical increase of H and A over θ. These trends agree well with the data, as shown by the overlap of the running median of the two parameters, showing that our cooperative curvature model describes the experimental data the best. The fit also provides some key information: the invagination does not occur until around half of the final coat size has grown [$A(\theta = 0.01)/A(\theta = \pi) = 51\,\%$], the coat curvature grows with the initial rate $\gamma = 0.009\,\mathrm{nm}^{-1}$, and the preferred curvature of a clathrin coat is $H_0 = 0.014\,\mathrm{nm}^{-1}$, corresponding to a radius of $r_0 = 72\,\mathrm{nm}$.

The sites were fixed at random time points as snapshots of the endocytic process and thus can be seen as the outcome of random temporal sampling. Thanks to the data curation by Aline Tschanz after a systematical site segmentation, we have a high-quality dataset of homogenously sampled snapshots over the progression.

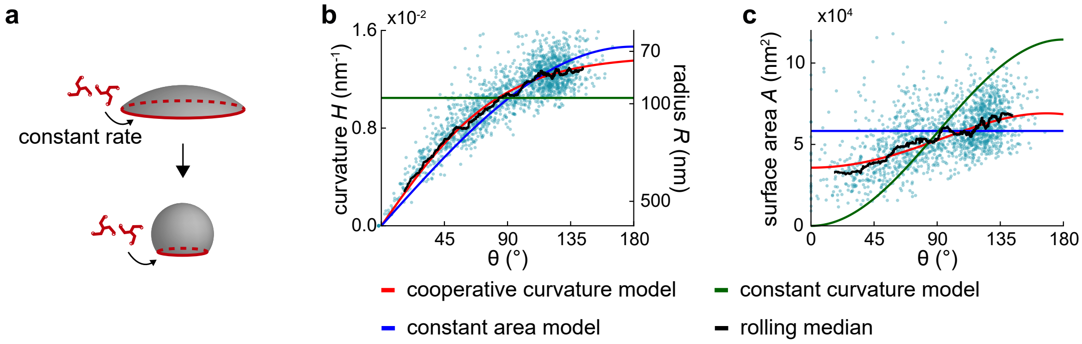

Figure 3.18 | The relations between different parameters and the closing angle θ fitted by various models. (**a**) A schematic shows the cooperative curvature model we proposed. This model assumes the coat is remodeled to approach a preferred curvature over time and the addition of clathrin triskelia happens at the edge of the coat with a constant rate. The three models, shown as curves, were fitted to curvature H (**b**) mapped to surface area A (**c**). The sites with curvature higher than 0.015 nm^{-1} (see Figure 3.17d) were considered as structures not originated from the plasma membrane and thus excluded from the analysis. Sample size: $n_s = 1{,}645$, $n_c = 13$. Markus Mund, Aline Tschanz, and Johanna L. Mehl acquired the data. Felix Frey, Aline Tschanz and I performed the analyses. Aline Tschanz and I created the figure jointly. *Adapted from Mund* et al.*, 2022, on which I am a co-author.*

Although we are not able to "record" the biological process over time directly, we can still extract temporal information from the snapshots based on a parameter that changes monotonically over time. As all current models suggest an increasing θ throughout CME, θ fulfills the requirement for such a parameter and thus is used in this work. In our case, the distribution of the quantified θ represents the rate of transition between states (Figure 3.19a). The large sample size ($1{,}645$ individual structures) ensured high coverage of time points. Specifically, the overrepresented ranges of θ correspond to a slow transition, while underrepresented ranges are indicative of endocytic stage that proceeds faster. As a result, the rank of θ informs the relative time, ranging from 0 to 1 (pseudo-time; Figure 3.19b).

Accordingly, we reconstructed the endocytic dynamics by sorting all sites based on θ. This reconstruction reveals a strong correlation between H and θ and indicates clathrin coats gain curvature continuously over time (Figure 3.18c). The surface area also increased (Figure 3.18d), from 32,000 nm^2 (median of sites within top 5 % of θ) to 50,000 nm^2 (median of sites within bottom 5 % of θ), corresponding to decreased projected area from 31.000 nm^2 to 13,000 nm^2, similar to previous EM measurements (Bucher *et al.*, 2018). The median surface area of the sites within bottom 5 % of θ recapitulates a previous EM-based work (Avinoam *et al.*, 2015), where the vesicular coats were quantified to have a median surface of 54,500 nm^2.

These results show that both the curvature and the surface area are not constant during endocytosis, disagreeing with the current models, which assume either the curvature or surface area is constant throughout most of the process (see also Figure 1.8 and Section 1.4.1.2).

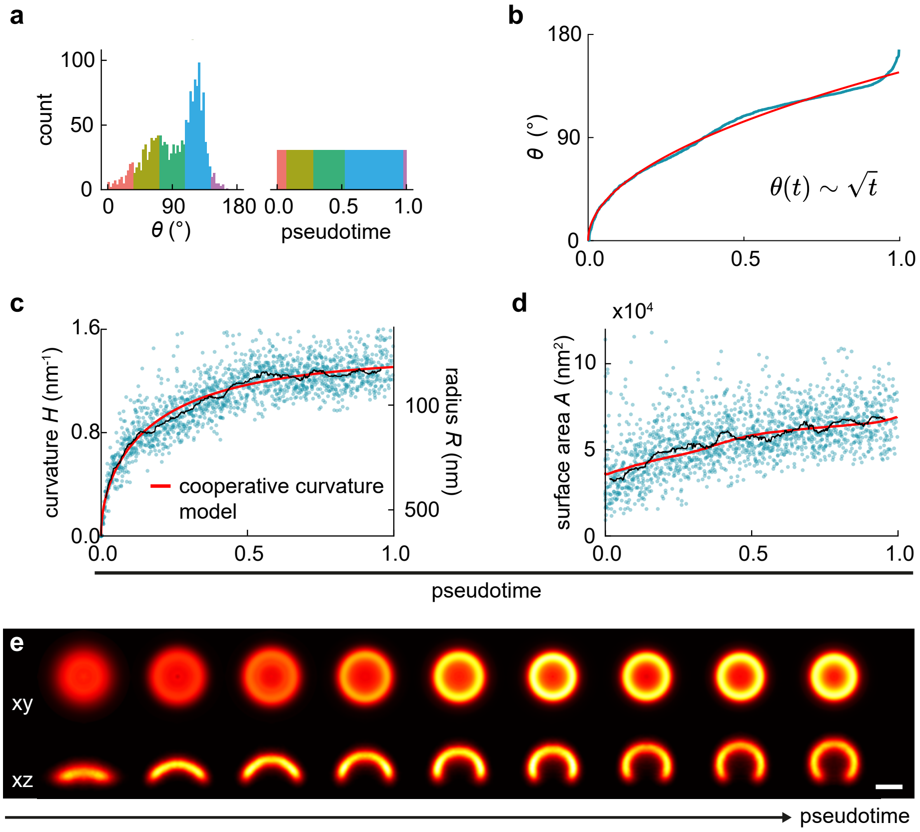

Figure 3.19 | Dynamic reconstruction of clathrin coat remodeling during endocytosis. (**a**) Histograms showing the distribution of the closing angle θ informs about temporal information (pseudotime). (**b**) The relation between the closing angle θ and pseudotime. The parameters of curvature H (**c**) and surface area A (**d**) plotted over pseudotime. The fitted cooperative curvature model is shown in red and the moving median black. (**e**) The reconstructed dynamics shown as temporally sorted bins. Rotational symmetry was imposed on bin, which contains 182 sites. xy: top view; xz: side view. Sample size: 1,645 sites, 13 cells. Scale bar: 100 nm. Markus Mund, Aline Tschanz, and Johanna L. Mehl acquired the data. Felix Frey, Aline Tschanz and I performed the analyses. Aline Tschanz and I created the figure jointly. *Adapted from Mund* et al., *2022, on which I am a co-author.*

We also derived θ as a function of time according to the assumption that the addition of triskelia to the rim determines the growth of the coat with a constant rate (see Mund *et al.*, 2022 for details). The derivation predicts θ has a square root dependence of time $\theta(t) \sim \sqrt{t}$, implying that the curvature generation is expected to slow down throughout the process.

The curve fit in Figure 3.19b shows that the square root dependence describes the data quite well, matching the characteristic of the cooperative curvature model. However, small deviations of the fitted model from the pseudotime-resolved data in the intermediate phase and when the pseudotime is approaching 1 (Figure 3.19b), suggesting that there are contributing factors that are not considered in the model. We also derived the curvature $H(t)$ as a function of time based on the cooperative curvature model and the square root dependence. The fitted function $H(t)$ and its mapping to the surface area both describe the pseudotime-resolved data well (Figure 3.19c,d), again validating the cooperative curvature model.

3.7.2 Dynamic reconstruction of the endocytic machinery in *Saccharomyces cerevisiae*

The previous section shows a promising result of CME dynamic reconstruction in mammalian cells. Our final goal is to extend the reconstruction to most of the endocytic proteins. Although we are progressing, this goal remains challenging in mammalian cells because of limited labeling strategies. First of all, primary antibodies, even the commercially available ones, require extensive validation and protocol optimization for SMLM. Second, genetic engineering for endogenous tagging is still challenging compared to that of, e.g., budding yeast *Saccharomyces cerevisiae*. On the other hand, yeast and mammalian cells have many functional homologues of endocytic proteins. These factors render budding yeast an ideal and widely used model for studying endocytosis. Therefore, we also extended the dynamic reconstructions to budding yeast. To that end, I teamed up with Philipp Hoess and Markus Mund. Philipp Hoess contributed to experiment design, strain generation, protocol optimization, and data acquisition. Markus Mund initiated SMLM of endocytic proteins in budding yeast (Mund *et al.*, 2018) and shared knowledge and materials. I contributed mainly to data analysis but also experiment design, strain generation, and data acquisition.

According to pioneer attempts (Mund, 2016), 3D SMLM compromised the xy resolution and the z-resolution is too low to reveal meaningful details of yeast endocytic sites in the z-direction, thus we only performed 2D imaging. Considering that yeast cells are shaped ovally and endocytic sites invaginate perpendicular to the plasma membrane (Picco *et al.*, 2015), focusing on distinct parts of the cells yields views of endocytic sites from different orientations. In a previous study, the nanoscale radial distribution of proteins at endocytic sites was determined by focusing on the bottom part (close to the coverslip) of the yeast cells (Mund *et al.*, 2018). In this study, to capture time-associated structural changes along the axis of invagination, we acquired side view images of endocytic sites by focusing on the equator of the yeast cells (Figure 1.11a).

3.7.2.1 A proof-of-principle example

In the previous work (Mund *et al.*, 2018), our group already demonstrated a dynamic reconstruction of endocytosis in budding yeast, where Abp1 (an actin binding protein localized at endocytic sites) and Las17 (an actin nucleation promoting factor) were labeled (Mund *et al.*, 2018). However, the reconstruction involved manual alignment, which limited the throughput of the analysis. To first demonstrate that LocMoFit can perform the same task, I analyzed a similar dataset having the same labeled proteins, acquired by Philipp Hoess (Figure 3.20a,b). Here, a model that includes a time-associated parameter is required to describe the distributions of these two proteins and to inform temporal information. A live cell microscopy study (Picco *et al.*, 2015) provides a hint in defining such a parameter: the centroid of Abp1 moved inward away from the plasma membrane over the endocytic progression, whereas that of Las17 stayed at the base of endocytic sites throughout. Along with that, we inferred that Abp1 forms a dome-shaped distribution around the endocytic membrane invagination. This inference is according to an EM study (Kukulski *et al.*, 2012), where a dome-shaped ribosome-free zone that is occupied by the dense actin network around the invagination has been reported. Based on these priors, we interpret the centroid movement as a result of increasing axial length of the distribution during endocytosis. Accordingly, the axial length encodes temporal information and is used as the time-associated parameter for the dynamic reconstruction. Along with my visual inspection over more than a hundred of sites in our dataset, I built a composite model having two components to describe the two proteins (Figure 3.20c). Specifically, the two models are a semi-ellipsoid for describing Abp1 and a thick ring for Las17, both as 2D projections (Figure 3.20d). Figure 3.20b shows that example endocytic sites at different stages can be well approximated by the model with fitted parameters, showing a faithful measurement of the axial length. I then aligned the endocytic sites to the center position of Las17 and sorted them by the measured axial length (Figure 3.20e).

Finally, I applied a moving average to the sorted sites along the increasing axial length, generating a dynamic reconstruction of endocytosis (Figure 3.20f). The result reproduces the earlier results obtained by manual alignment, proving the concept of using LocMoFit for a dynamic reconstruction of CME in yeast.

3.7.2.2 Reference structure

With the approach described above, in theory, we can dynamically reconstruct the whole endocytic machinery by simply increasing the number of channels (labels) and imaging many proteins simultaneously. However, this is technically challenging,

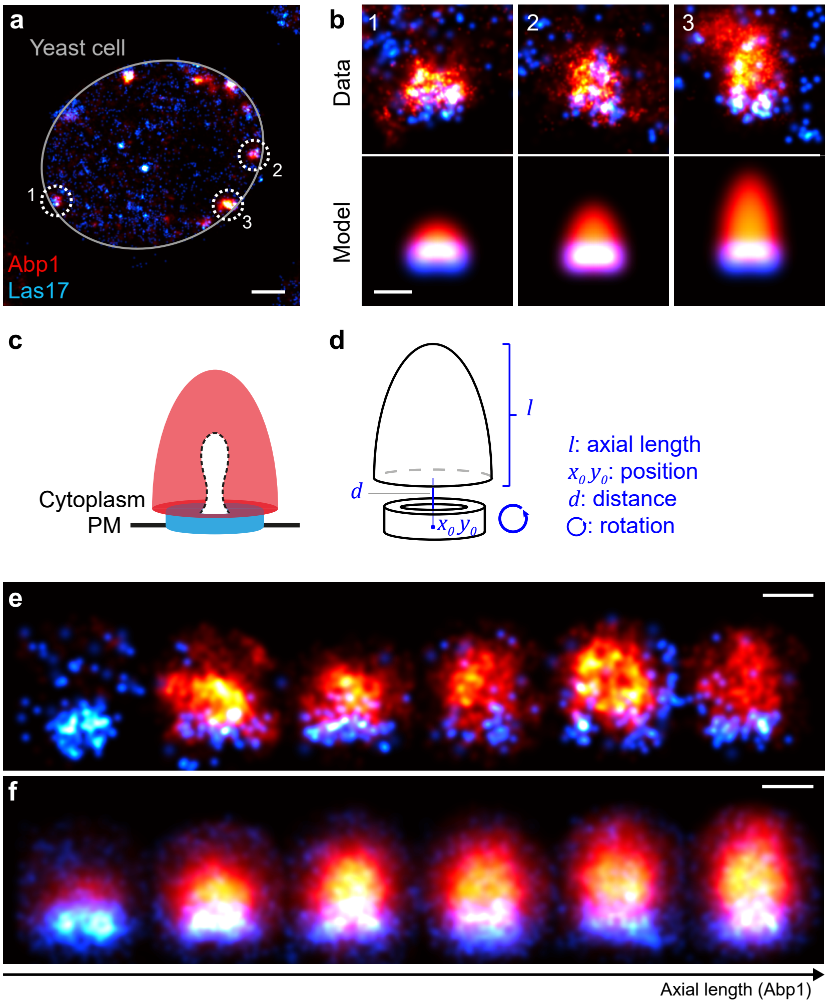

Figure 3.20 | Dual-color dynamic reconstruction of endocytosis in yeast. (**a**) An example image of an Abp1/Las17 co-labeled yeast cell acquired by focusing on the equator of the cells. (**b**) Rendered images of three example endocytic sites, indicated by numbered circles in **a**, and the models with fitted parameters of corresponding sites. Based on the prior that Abp1 is distributed in a dome-like shape, and Las17 as a thick ring (**c**), we build the composite model by merging a projected hemisphere and thick ring (**d**). Fitted parameters are listed in blue. 'PM' stands for 'plasma membrane'. (**e-f**) The dynamic reconstruction of endocytosis based on the two proteins. Examples of single sites (**e**) sorted by the time-associated parameter: the axial length of the Abp1 distribution. Based on the parameter, single sites were classified into time bins and then averaged per bin (each contains 21 sites). Sample size: 126 sites, 51 cells. Scale bars: 500 µm (**a**), 100 nm (**b**,**e**,**f**). Philipp Hoess acquired all the localization data, we performed the analyses jointly. *Adapted from Wu* et al.*, 2021, on which I am the first author.*

as discussed above in Section 3.5. Especially in yeast, enzymatic digestion of the ~100 nm thick cell wall is required for post-fixation immunolabeling and can largely disturb sample integrity. This requirement limits the use of a ratiometric approach, which usually relies on labeling the targets with antibodies conjugated with organic dyes and can potentially enable up to 4-color imaging (Li *et al.*, 2021). Also, targeting too many proteins involved in the same machinery endogenously can interfere with their function/assembly and create an unwanted phenotype, impeding a faithful interpretation of the experimental results. Therefore, we performed dual-color localization microscopy in yeast with the experimental protocol optimized by Philipp Hoess to achieve the optimal imaging quality (Höß, 2021). More specifically, we used the combination of spectrally different fluorophores—mMaple/mMaple3 (McEvoy *et al.*, 2012; Wang *et al.*, 2014), which are photoconvertible fluorescent proteins, and AF647 covalently linked to the SNAP-tag (Keppler *et al.*, 2003)—to label two distinct proteins.

Although we are limited to dual-color imaging, a suitable reference structure enables us to realize a multi-color reconstruction, as demonstrated in Section 3.5. However, for endocytosis in yeast, we did not find any single protein that can serve as a good reference structure. A single protein alone can only provide either sufficient spatial or temporal information in the best case. For example, Abp1 reflects the endocytic progression but the spacing between Abp1 distribution and the plasma membrane can vary, especially toward vesicle scission, rendering the spatial registration inaccurate. On the other hand, distributions of proteins such as Las17 are not sensitive to the progression of endocytosis because they stay near the plasma membrane throughout endocytosis, but therefore serve as a good spatial reference.

Instead of one protein, we then decided to use a pair of proteins to retain the advantages of both, thereby having a better reference. For the pair, we adopted one protein from the WASP/Myo module plus another from the coat module (see Figure 1.10b). This combination approximates both the tip and base positions of the invagination so that the invagination depth can be estimated as a sensitive time-associated readout. To use a protein pair as the reference and yet spare a channel for a target protein, we labeled both proteins in the reference structure with the same fluorophore and imaged them in the same channel. We then acquire data from different yeast strains, where in each strain the reference structure is co-labeled with a protein of interest (target protein) in the second channel. This will allow us to build a multi-color protein distribution map, similar as described in Section 3.5.

3.7.2.3 High-throughput SMLM and automated analysis

Our strategy for reconstructing a multi-color protein distribution map requires one strain for each target protein. Accordingly, imaging of tens of strains is expected as we are aiming to incorporate most, if not all, of the proteins in the dynamic reconstruction. Strain generation, however, is not a limiting factor because endogenous tagging can be easily achieved by homologous recombination in haploid yeast cells.

To achieve a reconstruction with high temporal and spatial resolution, hundreds of snapshots for each targeted endocytic protein are required. On the imaging end, the throughput is not a bottle neck thanks to the automated high-throughput SMLM established in our lab by Joran Deschamps and Markus Mund (Deschamps, 2017; Mund *et al.*, 2018; Deschamps and Ries, 2020). The automated SMLM allows collecting more than 20 fields of view overnight, each containing ~30 cells (around 0 to 5 sites per cell) and therefore ensures high statistical power.

On the data analysis end, to deal with the potentially high amount of data, I developed an automated workflow for segmenting cells and endocytic sites (Figure 3.21). Specifically, cells in an SMLM image were identified and segmented using intensity-based masks. Within each mask, a spline is fitted to describe the cell boundary (Figure 3.21a). By scanning through the intracellular proximity of the fitted boundary, the density peaks in the polar coordinate system are then identified as endocytic sites (Figure 3.21b). Each site is then rotated so that its tangent line on the fitted boundary is horizontal and below the site after rotation (Figure 3.21c). The rotation ensures the same upward orientation of sites. Afterward, quality controls are applied at the levels of cells and sites. First, non-round and small cells are discarded. Next, cells located at the edge of the field of view are usually with incomplete boundaries and therefore removed. Endocytic sites located at cell contacts, where the fitted boundaries may be imprecise, are also discarded. Finally, wide sites are discarded as they might be multiple sites that cannot be separated during the analysis (Figure 3.21d).

3.7.2.4 Validation of the reference structure

To validate the use of a merged reference structure (see Section 3.7.2.2), we began with the combination of Sla2 and Las17 from the coat and WASP/Myo modules, respectively. To test whether LocMoFit can recognize different proteins based on their spatial arrangement independently of the channels, we first performed dual-color imaging of the reference structure (Sla2-SNAP-AF647 and Las17-mMaple) without a target protein to retain the colors as the ground truth.

For describing the protein distributions, we built a model based on prior knowledge. First, based on the shape of the invagination reported by an EM study (Kukulski *et al.*, 2012), we inferred that the coat proteins, which are distributed around the tip of the invagination, have a cap-shaped distribution. In contrast, we inferred proteins in the WASP/Myo module, which are localized around the base of the invagination, to have a thick-ring distribution (Mund *et al.*, 2018). Accordingly, I implemented the model as a hemisphere for a coat protein and a thick ring for the

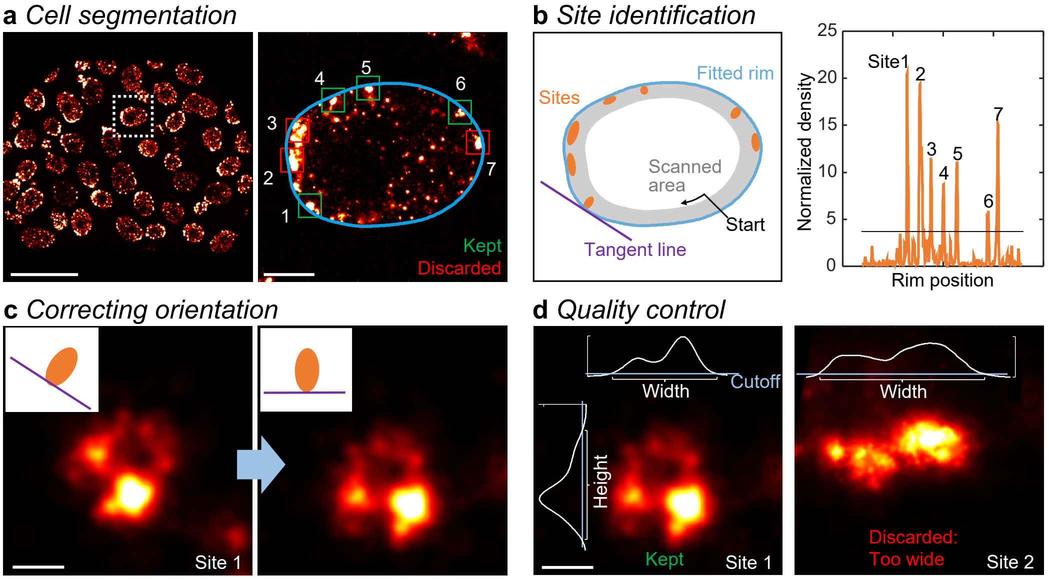

Figure 3.21 | Automated cell and site segmentation. (**a**) A segmented yeast cell with endocytic sites labeled (right) from the field of view on the left. (**b**) A schematic showing how sites were identified by scanning the intracellular area around the cell boundary. The start of the scanning is indicated by the arrowhead. The right panel shows the result of the scanning in the polar coordinate system. (**c**) Rotation of the site based on the slope of the tangent line also shown in **b**. (**d**) Measurements of the width and height of the sites based on their x and z profiles. In this example, site 2 is considered as multiple sites according to its width and thus discarded. Scale bars: 10 µm (a, left), 500 nm (a, right), 100 nm (c,d).

second protein (Figure 3.22b, left), hence a 'ring-cap' model, in LocMoFit. Last, based on the average radial arrangements of the corresponding proteins in the SMLM study (Mund *et al.*, 2018; Figure 1.10b), I determined and fixed the size (radii) of the two shapes, resulting in the final model (Figure 3.22a).

To reconstruct the dynamics, I then performed the fitting in LocMoFit to acquire the distance between the two parts of the composite model, which was used as a pseudotime. I removed color information from the localizations before loading them into LocMoFit. After fitting through all sites, the same procedure as described in Section 3.7.2.1 was applied except that the pseudotime is based on the ring-cap distance, resulting in the reconstructed dynamics (Figure 3.22d). For verifying the reconstruction, I mapped the colors back to the localizations. The reconstruction exhibits the expected distributions for both proteins (Figure 3.22e), confirming that LocMoFit can extract the ring-cap distance precisely with even only one channel and thus validate the use of the composite reference structure.

Next, I will demonstrate how to reconstruct the dynamics of target proteins based on the reference structure. For that, we tagged the target protein pan1, another coat protein, with SNAP in addition to the reference structure tagged with mMaple and performed dual-color SMLM. Note that here the reference structure was modified: we replaced Las17 with Myo5, which is another protein in the same functional module but has more protein copies and a wider radial distribution, thereby providing

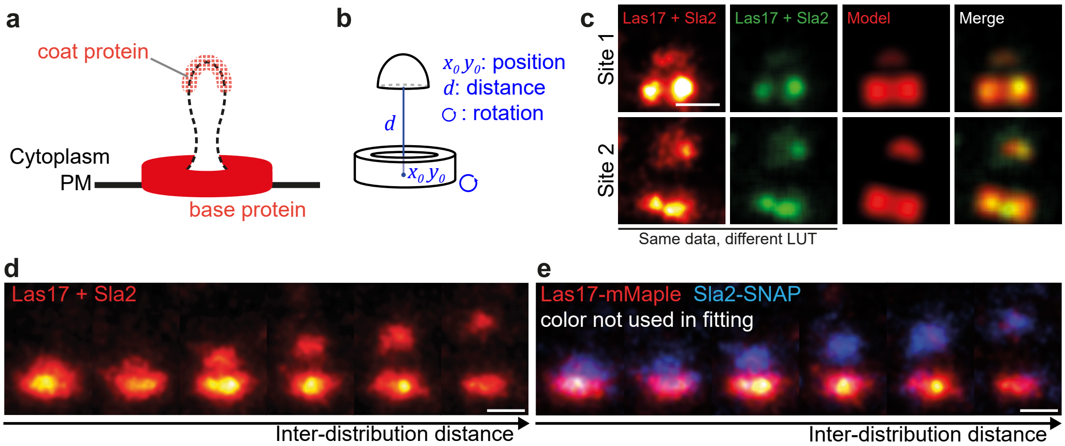

Figure 3.22 | Composite reference structure. (**a**) A schematic showing the reference structure: a combination of the two proteins Sla2 (coat) and Las17 (base). The ring-cap distance d increases during the endocytic progression. (**b**) A hemisphere and a thick ring were used to build the joint model describing the protein distributions. (**c**) Two example sites with the corresponding fitted model. (**d-e**) Reconstructed dynamics based on the two proteins after fitting. The color information was hidden during fitting (**d**) and is only shown here for visualization (**e**). Each time bin, containing 15 sites, is a frame of a running average movie consisted of 1,040 sites. Scale bars: 100 nm.

higher structural sampling and sensitivity to rotation. In the resulting reconstruction, the target Pan1 shows dynamics similar to that of the coat protein Sla2 (Figure 3.23b), indicating a promising reconstruction and validating the proposed approach. Interestingly, I found a linear increase of the sorted measured ring-cap distance in the range where the temporal information can be more faithfully inferred. This range is from 15 nm, the minimum distance determined by the settings for fitting (this minimum was further reduced to zero in the analysis described in Figure 3.24), to 108 nm, the ring-cap distance corresponding to membrane scission (Picco *et al.*, 2015). After scission, the ring-cap distance has been shown to be much more variable (Picco *et al.*, 2015), thus the pseudotiming is expected to be less meaningful. This linearity has also been observed in the live-cell study by Picco *et al.*, 2015, again supporting my reconstruction approach. Furthermore, with a linear interpolation based on the two points $[15\,\mathrm{nm}, -4.9\,\mathrm{sec}]$ and $[108\,\mathrm{nm}, 0\,\mathrm{sec}]$, reported by Picco *et al.*, 2015 (Figure 3.23b), I was able to assign absolute time to the time bins of the reconstruction (Figure 3.23a).

3.7.2.5 Dynamic protein distribution maps

Finally, we are working on expanding this approach to all endocytic proteins. To provide an overview of the future reconstruction of the whole machinery, we first reconstructed the dynamics of one protein for each of the modules (Figure 1.10b). These proteins are the coat protein End3, the yeast WASP Las17, the actin crosslinker Sac6, and Rvs167 from the scission module. For the reconstruction, Philipp Hoess acquired for each of the proteins one dataset, where he manually picked 203 sites and rotated them to have upward-pointing invagination after rotation. I

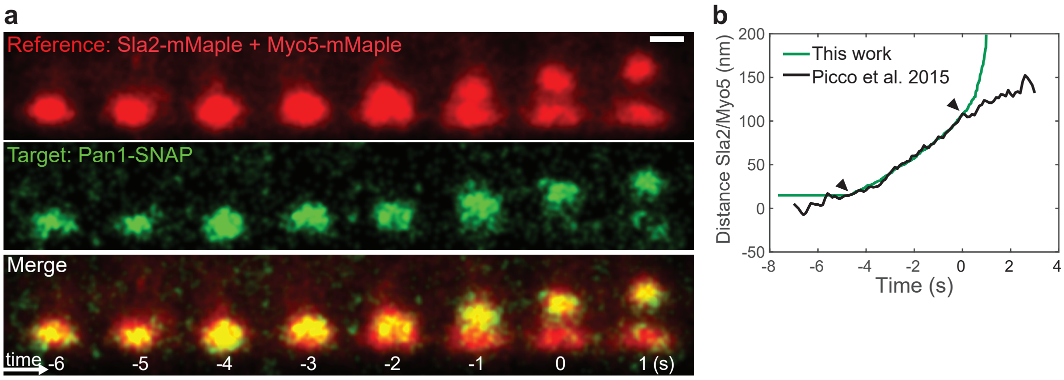

Figure 3.23 | Composite reference structure. (**a**) The dynamic reconstruction of Pan1 based on the composite reference structure. Each time bin contains 20 sites. The time points were assigned by a linear interpolation based on the two points $[15\,\mathrm{nm}, -4.9\,\mathrm{sec}]$ and $[108\,\mathrm{nm}, 0\,\mathrm{sec}]$. These two points were determined based on the values reported by Picco *et al.*, 2015. (**b**) The trajectory of the measured ring-cap distance mapped to the corresponding trajectory overtime reported by Picco *et al.*, 2015. Arrowheads indicate the start and end of the linear range. Sample size: 651 sites, 310 cells, 20 experiments. Scale bar: 100 nm.

then fitted the reference structure in LocMoFit and applied the workflow of the dynamic reconstruction. I found that in some sites, only one component of the reference structure was detected (model weight $< 5\,\%$). These sites were considered as having only the coat and thus placed at the beginning of the list (see Paragraph 4.7.2 for a discussion in depth). In the reconstructed dynamics, co-localization of End3 with both reference components (Figure 3.24a) is evident, particularly in the late time points. Throughout the endocytic progression, Las17 stays at the base of the endocytic invagination, with a more diffuse distribution along the axis of invagination found at late time points (Figure 3.24b). The distribution of Sac6 is located around the reference and expanded over time (Figure 3.24c). Rvs167 has increasing intensity toward the end, although the Rvs167 signal was also high in the first bin (Figure 3.24d). Finally, we show the last time bin of the four-color reconstructed protein distribution map created based on the shared reference (Figure 3.24e). This promising preliminary result supports the idea of a more extensive reconstruction.

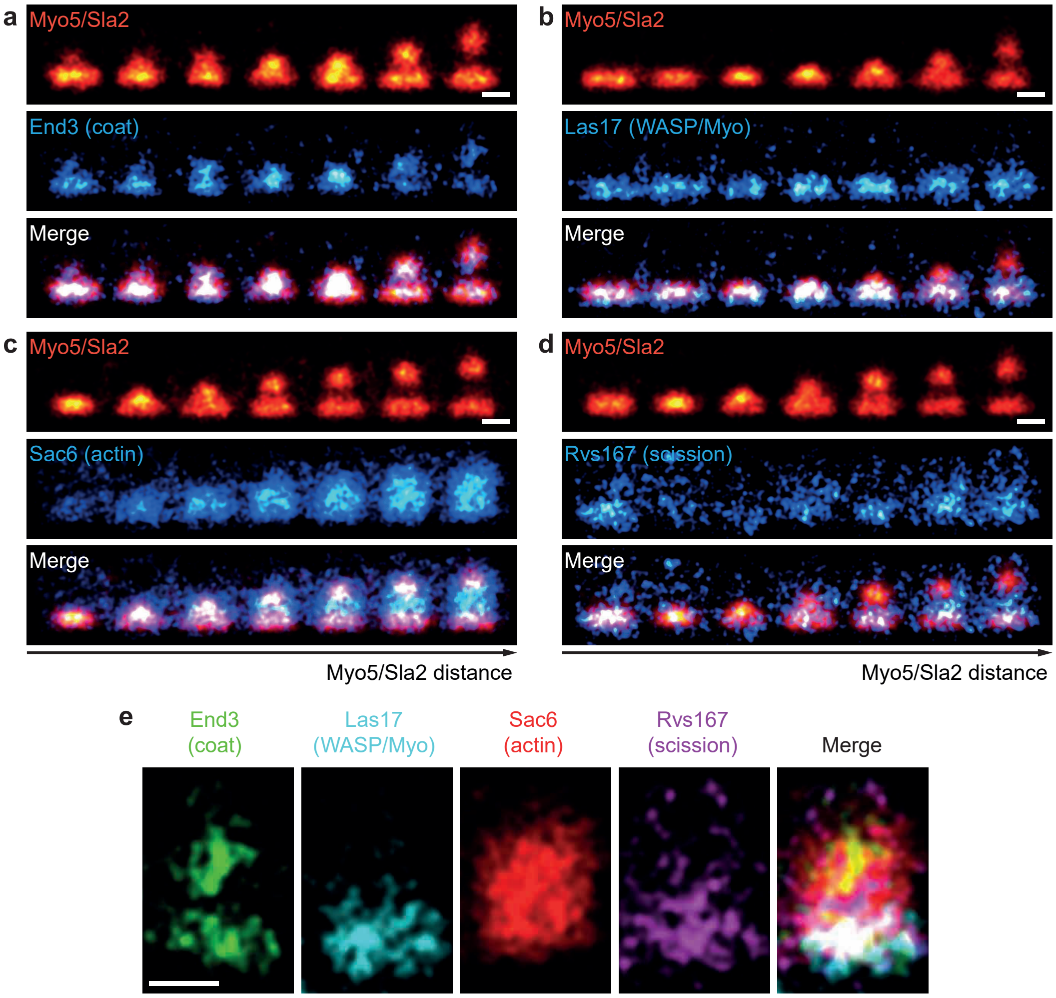

Figure 3.24 | Multi-color dynamic protein distribution map of four endocytic proteins in yeast. (**a-d**) Dynamic reconstructions of the four target proteins End3 (**a**), Las17 (**b**), Sac6 (**c**), and Rvs167 (**d**) based on the composite reference structure formed by Myo5 and Sla2. Each time bin contains 29 sites. (**e**) The last time bin of each target protein and merge. Sample size: 203 sites for each target protein. Philipp Hoess acquired all the localization data, we performed the analyses and created the figure jointly. Scale bar: 100 nm.

4 | Discussion

4.1 Analyzing individual structures

In this work, I presented the powerful and general analysis framework LocMoFit for extracting quantitative descriptors of macromolecular structures by fitting an arbitrary, parameterized model to individual structures in SMLM data (i.e., Figures 3.7, 3.10, and 3.17). In general, extracting quantitative descriptors with other high-resolution techniques is difficult. For example, electron microscopy typically relies on forming an average of many copies of identical structures to reach sufficient signal-to-noise ratios. LocMoFit does not require averaging and thus allows for the investigation of cellular structures that are heterogeneous and complex, making SMLM an important complementary method for *in situ* structural biology.

4.1.1 Comparison of LocMoFit and PERPL

Apart from LocMoFit, PERPL is the only analysis that can extract complex parameters from SMLM data among all relevant algorithms. Similar to LocMoFit, PERPL extracts parameters by fitting a parameterized model and has been applied to quantify the size and ring separation of the NPC (Curd *et al.*, 2021). The main advantage of PERPL is that it does not require segmentation and registration of the structures prior to the analysis. However, instead of the 2D or 3D coordinates, it uses a 1D representation, the relative position distribution (RPD), for fitting. Although it is based on spatial statistics such as pair-correlation analysis, which is usually applied to a larger field of view containing many structures, PERPL has also been used to analyze and classify individual structures. Thus, I directly compared the performance of PERPL and LocMoFit on simulated individual structures. First, I attempted to use 3D clathrin coats (Figure 3.17c) as test structures that are not identical but contain many closing angles and curvatures to represent a situation in which a bulk analysis is not applicable. This attempt was not feasible with PERPL because of the extremely long runtime (more than 8 h compared to tens of seconds for LocMoFit per site) resulting from the computationally expensive calculation of an RPD model for the continuous geometry. Therefore, I used arcs (Figure 4.1a,b) instead, which can be seen as 2D cross-sections of the clathrin-coated pits described in Figure 3.17c. The parameter estimates reported by PERPL have a strong variability and bias, and many fits even failed to converge to the global optimum (Figure 4.1c). This issue is likely to arise from the indistinguishable RPDs produced by visually different geometries, given the noise in the data (Figure 4.1d-f). The similarity of RPDs results from the loss of information caused by the dimensionality reduction, which renders the RPD a quite abstract representation of the underlying data. In contrast, LocMoFit yields much more robust and accurate parameter estimates thanks to its direct fitting to coordinates.

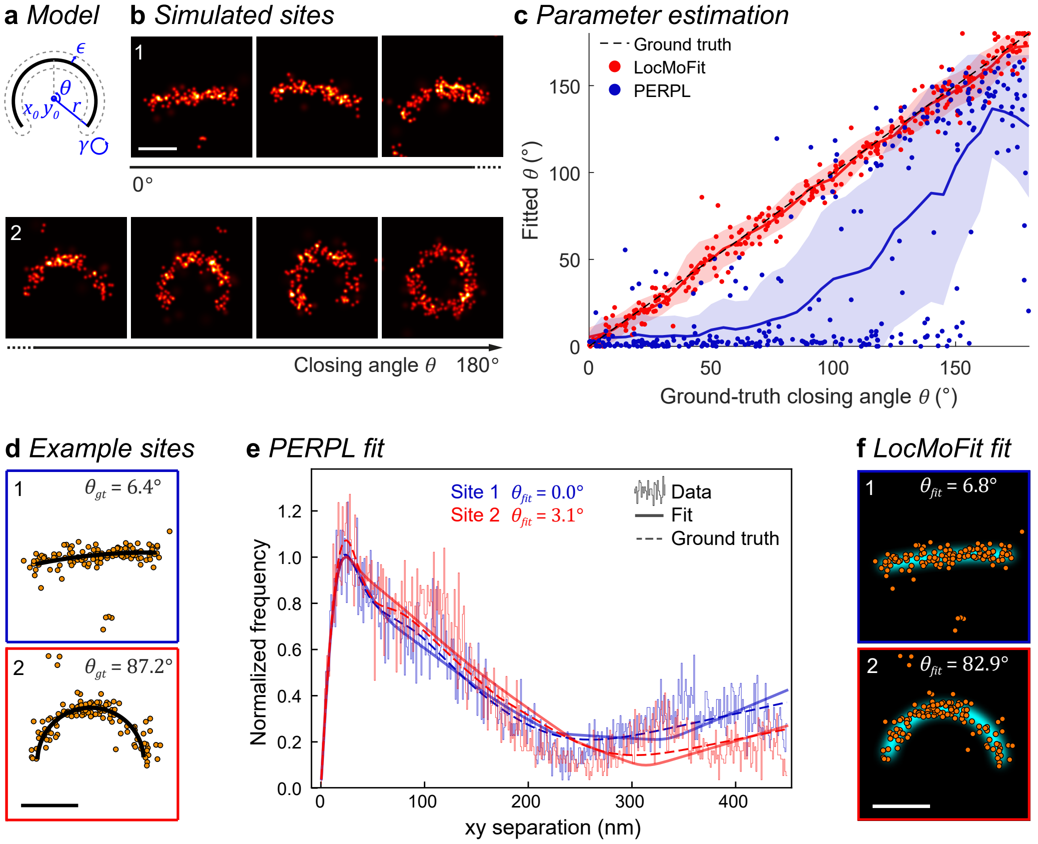

Figure 4.1 | Comparison between LocMoFit and PERPL. (**a**) The arc model used for simulating single structures with different closing angles θ (**b**). Other parameters are position x_0, y_0, rotational angle γ, linkage error ϵ, and radius r. (**c**) The fitted closing angle θ reported by LocMoFit and PERPL in comparison to the corresponding ground truth (dashed lines). Solid lines are rolling means and shades are standard deviations. Two different geometries (**d**) yield similar relative position distributions (RPDs; **e**), which account for the ambiguous fit result. (**e**) LocMoFit performs the fitting on the coordinates directly and therefore dose not suffer from this issue. Simulation parameters are summarized in Table 6.13. Sample size: 300 sites. Scale bars: 100 nm.

The same trend was also evident for another test structure, NPCs simulated with constant parameters (Figure 4.2). Here, LocMoFit yielded unimodal parameter distributions that reflect the constant ground truth values, which PERPL failed to reveal.

To sum up, PERPL is powerful because it enables bulk analysis of complex structures when they share the identical underlying structures (Curd *et al.*, 2021). However,

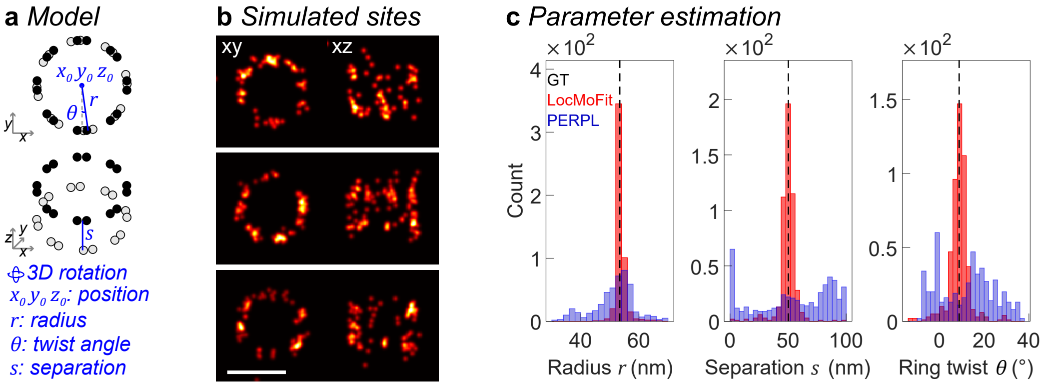

Figure 4.2 | Comparison between LocMoFit and PERPL based on simulated NPCs. (**a**) The NPC (nuclear pore complex) model used for simulating single NPCs (**b**). (**c**) Fitted parameter values reported by LocMoFit ($r = 53.7 \pm 2.7\,\mathrm{nm}$, $s = 49.7 \pm 7.7\,\mathrm{nm}$, $\theta = 8.8 \pm 4.6°$) and PERPL ($r = 53.2 \pm 10.4\,\mathrm{nm}$, $s = 54.9 \pm 32.7\,\mathrm{nm}$, $\theta = 12.0 \pm 12.1°$). Ground truth (GT) values are $r = 53.4\,\mathrm{nm}$, $s = 50.2\,\mathrm{nm}$, and $\theta = 8.8°$. Simulation parameters are summarized in Table 6.13. Sample size: 500 sites. Scale bar: 100 nm.

PERPL relies on dimensionality reduction, which is sensitive to differences in labeling efficiency and background, although their effects are diluted in bulk analysis where the information of many particles is pooled. This advantage of PERPL is not applicable to single particle analysis, where LocMoFit is much more robust because it directly analyzes localization data in their original dimensionality. Therefore, LocMoFit is more suitable for analyzing single particles, compared to PERPL.

4.2 Protein distribution maps

The distribution of a protein relative to the complex it belongs to is often related to its biological function. Knowing a protein distribution and statistical analysis of individual structures are both important. Retrieving such a distribution precisely from a single particle is typically impossible because of imperfect localization precision and labeling efficiency. Nevertheless, when many copies of the identical structure can be obtained, the protein distribution can be mapped as an average of these copies. The resulting distribution map is beneficial for improved contrast and labeling efficiency, compared to single particles. In LocMoFit, such a map can be created with or without a reference structure. With the intention of using a reference, dual-color SMLM has to be performed to image a target protein simultaneously with the reference structure in the same protein complex in different channels. The reference structure is then fitted with a corresponding model in LocMoFit to register single particles.

In the case when the model is defined as a fixed template, the distribution map of the target protein can then be simply generated by superpositioning the registered particles. When different target proteins are imaged with the same reference, these proteins can be mapped to the same coordinate system by applying the same procedure, resulting in a multi-color protein distribution map (Figure 3.14). In another case when a parameter, which increases monotonically over time, can be defined in the model describing the reference structure, the structure can be dynamically reconstructed by sorting the individual super-resolution snapshots by this parameter. For example, as shown in Figures 3.18 and 3.19, we were able to help resolve a long-standing dispute about the mechanism of endocytic coat remodeling in mammalian cells and visualize the corresponding structural dynamics. This application of LocMoFit enables assigning temporal information to fixed snapshots of a fast dynamic biological process, which is necessary as SMLM is often too slow to investigate these processes in living cells.

If the underlying structure cannot be obtained beforehand, a protein distribution map can still be generated without a reference structure. This analysis, called model-free particle averaging, assumes that all particles share an identical underlying structure. In LocMoFit, this analysis (see Figure 3.15 for the entire workflow) is performed by first generating a data-driven template based on the similarity across a subset of particles. The template is then used to iteratively register and fuse all particles in the same dataset, updating the template in each round. An average representation, or the protein distribution map, of the structure can be obtained when the template update converges. Using this approach, I generated a 3D protein distribution map of the NPC with remarkable quality. This map of Nup96 shows that each of the eight corners per NPC ring is elongated and tilted outward, reflecting the presence of two individual proteins per corner (Figure 3.16). This feature was invisible in the average of a similar nucleoporin Nup107 obtained by a recently published approach (Heydarian *et al.*, 2021), but was observed at small subsets of individual NPCs using DNA-PAINT (Schlichthaerle *et al.*, 2019).

4.2.1 Potential biases caused by averaging

Here, I will discuss the biases to be considered when generating a protein distribution map using LocMoFit.

4.2.1.1 Template bias

The so-called ‘template bias’ refers to the fact that the average derived from a template-based registration can be biased toward the template. This bias can cause the features that are present in the model but not the data to appear in the average, resulting in a wrong interpretation. Therefore, interpreting the averages of the reference structures (e.g., Nup96 in Figure 3.14) should be done carefully. For example, before concluding any novel feature based on the average, one should always make sure that the feature is not a prior used in the model. However, target structures should be free of this bias when the registration is solely based on the co-labeled reference structure.

4.2.1.2 Bias to a sub-population

Model-free averaging does not suffer from template bias because no template is used. However, variability including different structural conformations is expected in most biological samples. The resulting averages can be biased toward a certain sub-population that is usually the most dominant among the single particles (Henderson, 2013). To avoid this bias, a classification prior to averaging might be necessary, as demonstrated in a recent study where different ellipticities of the NPC can only be retained in the final averages when they are pre-classified (Huijben *et al.*, 2021).

4.3 Key factors to reliable analysis

A reliable image analysis pipeline incorporating LocMoFit necessitates good data quality, a proper workflow, and choosing correct priors. I will discuss these factors in the following paragraphs.

4.3.1 Priors

Choosing correct models is the key to performing a meaningful analysis in LocMoFit. One has to keep in mind that any model always yields certain parameters. However, these parameters can be difficult to interpret or meaningless if the model is wrong. Therefore, the construction of a meaningful model should be based on prior knowledge acquired by other techniques, visual inspection of the data, and/or model-free particle averaging. The latter two points are supported by many functions implemented in LocMoFit.

To avoid bias, I recommend to parametrize the model in a more general way so that the same parameters can describe structures of different classes. For example, the models used in this study for estimating parameters are not defined as rigid templates. Therefore, the models can explore different sizes and shapes during optimization. In general, simple models with few free parameters have a lower risk of over-fitting, in comparison to complex models. When multiple possible models exist, LocMoFit provides AIC_C to help identify the most suitable one given the localization data, taking the sample size and the number of free parameters into account (Cavanaugh, 1997).

4.3.2 Data quality

To provide precise parameter estimation and to avoid over-fitting, sufficient data quality is required. Data quality is determined by SMLM properties including labeling density, localization errors, re-blinks, etc. The required quality also depends on the complexity of the structures being analyzed and is difficult to assess without knowing the underlying structure and parameters of the ‘ground truth’ (Venkataramani *et al.*, 2016; Griffié *et al.*, 2020). Therefore, LocMoFit employs a simulation engine that allows the user to generate realistic test datasets based on the ground truth, across different ranges of SMLM properties that correspond to various data qualities. When comparing the parameters estimated by LocMoFit with the ground truth values, the estimation errors of the parameters can be evaluated. According to the errors that can be tolerated, the user can estimate the data quality necessary for a reliable quantification.

4.3.3 Workflow

A plausible and robust analysis workflow has to be established corresponding to the supplied model and data. A robust workflow relies on the choice of the parameters' starting values and search ranges, both of which can be defined flexibly in LocMoFit. LocMoFit even allows users to define specific rules for assigning the starting values. Optimization during the fitting is also an important part of the workflow. For that, LocMoFit supports different optimizers, including gradient-based optimization (Waltz *et al.*, 2006) and alternatives that perform a parameter search over defined intervals (simplex-based optimization; Lagarias *et al.*, 1998) or more globally (particle swarm optimization; Kennedy and Eberhart, 1995). Even when a proper model and optimizer are used, the convergence of the fitting procedure to the global optimum can still fail due to the complexity of the model. When this happens, I would recommend using the step-wise optimization, also supported by LocMoFit, to roughly estimate the key parameters by first fitting a simpler version of the model to the data and then transferring the fitted information to aid the following fitting steps.

For evaluating the workflow, the aforementioned simulation functionality implemented in LocMoFit can provide realistic test datasets. Visualization tools that enable users to visually inspect the fit results are also provided to check the reliability of the workflow and avoid result misinterpretation.

4.4 Linkage errors and biased labeling

I still would like to underline the effect of the linkage error, although it is introduced by the labeling strategy and not the data analysis. In fluorescence microscopy, one does not observe the protein of interest but fluorophores attached to it. The attachment can be either covalent (e.g., tagging with GFP) or mediated by molecular interactions (e.g., immunolabeling). With the resolution provided by SMLM, the effect of the linkage error has to be considered. The distribution visualized by SMLM is more representative to the distribution of the protein of interest when the linkage error is small. Therefore, when immunolabeling is applied, which introduces a relatively large linkage error compared to most other labeling strategies (Früh *et al.*, 2021), the protein distribution has to be interpreted with care. Additionally, limited epitope accessibility and/or high local molecular crowdedness can cause biased labeling, e.g., only a particular subset of the protein's copies is labeled, or the displacement of the fluorophore has a preferred orientation. This biased labeling can cause inaccuracies in the reconstructed protein map. Linkage error and biased labeling can be reduced or avoided by using different labeling strategies (described in Section 1.1.4.5), which have to be chosen based on the balance between their ease of use and the intended accuracy per sample.

4.5 General concept of dynamic reconstruction

Because of its long acquisition time, SMLM cannot directly acquire the time series of a fast and dynamic biological process. However, as I demonstrated in this work (Section 3.7), the dynamics of the procedure can be reconstructed from super-resolution snapshots that are fixed at random time points in the biological process. Here, I will discuss the general concept of such a reconstruction.

4.5.1 Extraction of temporal information encoded in snapshots

Dynamic reconstruction is based on temporal information encoded in static snapshots. The temporal information can be obtained based on single or multiple time-associated parameters. Although all dynamic reconstruction examples shown in this work are based on single parameters, I will also discuss the possible use of multiple parameters in the future.

Based on single parameter Monotonic changes of such parameters over time are required; otherwise, the temporal assignment is not unambiguous, i.e., the same parameter value corresponds to multiple time points. However, the linearity of the correlation between time and a time-associated parameter is not mandatory. When describing the parameter values as a function of time, the slow and fast transitions of the parameter over time (or higher and lower slopes in the function's curve) are translated to over- and under-represented parts of the parameter distribution. This is how we obtained the transition speed over the progression of mammalian CME, as shown in Figure 3.19.

Based on multiple parameters The inference of time can be based on multiple time-associated parameters. This concept has been demonstrated in many single-cell studies, where multiple or even thousands of parameters have been used in pseudotime analysis to reconstruct or infer single-cell trajectories across certain dynamic biological processes such as cell differentiation (Saelens *et al.*, 2019). When multiple parameters are used together in the right combination, individual parameters are not strictly required to have a monotonic trend over time if a temporal trajectory can form in the multi-dimensional parameter space.

In the case of the dynamic reconstruction of CME in yeast (see Section 3.7.2), I propose to use the ratio of localization counts between the two components (e.g., myosin Myo5 and the coat protein Sla2, as shown in Figure 3.20a) of the reference structure as a second time-associated parameter. At endocytic sites, the copy number of Myo5 changes during endocytic progression, while the copy number of Sla2 is more consistent throughout the informative time frame (Picco *et al.*, 2018; see Paragraph *Informative time frame* below for more details). The choice of the ratio instead of copy numbers provides an internal calibration that in theory eliminates the variation across different experiments (e.g., different blinking characteristics caused by changes in laser powers). The ratio of the two model parts is already a fit parameter in the current workflow to improve the robustness by considering the different molecules of the two parts and is therefore readily available.

4.5.2 Factors that may affect the inference of the reconstructed dynamics

In this section, I will discuss the factors that have to be considered when inferring the reconstructed dynamics.

Variability over time A dynamic process with small variability such as CME in yeast can be well described by representative dynamic trajectories (usually averages) of parameters. Because the variability is non-zero in most dynamic processes, their individual events do not exactly follow the trajectories. The parameters quantified in snapshots are therefore typically not exactly on the trajectories but with certain deviations. The consistency of the variability over time then determines whether these deviations may interfere with the dynamic reconstruction. When the parameter measurements are sorted to form a temporal trajectory, they spread out from their original time points because of these deviations. A constant variability over time then ensures that the degree of spread at each time point is equivalent on average, assuring that the trajectory represents the average curve obtained in live-cell measurements.

However, when the variability over time is inconsistent, the representability is not guaranteed. One example is that the centroid position of Myo5 becomes more variable after scission in yeast endocytosis. This increase in variation led to the inconsistency between the reconstructed trajectory and similar information retrieved from a live cell study (Picco *et al.*, 2018) at late time points where LocMoFit reported a faster movement (Figure 3.23b). Since the variation is quantified in Picco *et al.*, 2018, it can be incorporated to revise the dynamic reconstruction in the future. If multiple parameters are used for the dynamic reconstruction, they may form a temporal trajectory in the multi-dimensional parameter space, as discussed earlier. Unlike the 1D trajectory generated based on sorting, parameter measurements are allowed to deviate from the multidimensional temporal trajectory, which may serve as a timing index that tolerates inconsistent variability better.

Co-existence of multiple paths The same biological process can undergo different paths in the cell at the same time or depending on the cellular context. For example, CME in mammalian cells has been suggested to proceed through different models, including constant curvature and constant area models, depending on different factors such as the local environment (Chen and Schmid, 2020). Each model should correspond to a trajectory in the parameter space of curvature of the coats and their closing angles. In this study, we only observed a single trajectory (Figure 3.17) based on our data and given the data quality/resolution. This implies a single path of CME, at least in the cell line we used under standard cell culture conditions.

In yeast, no alternative path has been reported and the dynamics of the endocytic proteins have highly stereotypical average trajectories during CME (Kaksonen *et al.*, 2003; Mooren *et al.*, 2012; Picco *et al.*, 2015). Therefore, the dynamics we reconstructed should still represent the average trajectories when the parameter variation is constant over the time analyzed. Nevertheless, adding a second time-associated parameter will allow multiple trajectories to exist and thus the investigation of different paths.

Examples for multiple paths Biological events can stop on their trajectory or even pass through it in reverse order after stalling. These events can interfere with inferring the reconstructed dynamics by causing certain stages to appear more prolonged. In this work, no information can be used to distinguish these events from the productive events because they share the same trajectories in the parameter space and we neither have information about their history nor their future. In the following, I will discuss why we think that these events can be ignored in our analyses.

In mammalian CME, two populations of abortive or stalled events have been reported. The early abortive events have been considered as a result of failed clathrin-coated pit nucleation and have a lifetime of seconds (Loerke *et al.*, 2009; Cocucci *et al.*, 2012). In these events, very few (< 6) clathrin triskelia are recruited (Cocucci *et al.*, 2012) and should not be able to form an recognizable geometry in our analysis. The late abortive events (Ehrlich *et al.*, 2004; Taylor *et al.*, 2011; Kadlecova *et al.*, 2016) have been proposed to be controlled by a putative endocytic checkpoint (Kadlecova *et al.*, 2016) that monitors the maturation of the clathrin-coated pits. These events should correspond to flat structures (Kadlecova *et al.*, 2016), which are rare in our data set, hinting at rare detectable abortive events in the cells we analyzed. Therefore, abortive events have a mild or no effect on our inference of the dynamics.

In wild-type budding yeast, endocytic events in the immobile phase have been reported to be stalled instead of abortive (Pedersen *et al.*, 2020). Nonetheless, the stalling happens either before or at the beginning of the time frame we investigated as the components forming the reference structure are only recruited to the endocytic site relatively late in the immobile phase, thereby having a limited effect on our analyses. Retracting events during the mobile phase exist but are rare (0.7 %; Kaksonen *et al.*, 2005), hence can be also ignored in our analyses.

4.6 Dynamic reconstruction of mammalian CME sheds light on its structural mechanism

In the field, there are two competing models of CME, as described in Section 1.4.1.2. Briefly, the constant curvature model assumes that the curvature of the clathrin coat stays the same over the entire endocytic progression. The growth of the coat has been seen as the completion of the closed vesicle via increase of the closing angle. The constant area model suggests that, already on the flat membrane, the coat rapidly obtains its final surface area, which remains constant until the vesicle forms. There is no consensus on the correct model because contradictory conclusions have been suggested to support either of the models, their co-existence, or alternative models.

In this work, jointly with others, I applied LocMoFit to quantitatively describe the clathrin coats in SMLM snapshots and to extract parameters, including the closing angle θ, which is a parameter representing endocytic progression. Based on θ, we were able to assign temporal information to the static snapshots for studying the mechanism of CME and to reconstruct a dynamic movie showing the structural rearrangement of the clathrin coat during endocytic progression. Our results disagree with both competing models.

4.6.1 Quantitative description of single clathrin coats

Most approaches in *in situ* structure biology are not live-cell compatible. Therefore, the investigation of the dynamics of CME in cells relies on acquiring many 3D snapshots of the process fixed at random time points. The previous approaches based on EM either provide limited throughput (Avinoam *et al.*, 2015) or suffer from indirect 3D information (Bucher *et al.*, 2018; Sochacki and Taraska, 2019; Sochacki *et al.*, 2021). A recent work (Willy *et al.*, 2021) studied the dynamics in live cells with also indirect 3D information using SIM, which provides limited resolution compared to other super-resolution techniques. Here, we overcame these limitations by using SMLM to obtain high-quality super-resolution 3D snapshots of clathrin coats *in situ* with higher throughput (more than 1,000 sites). I then applied LocMoFit to extract the temporal information encoded in the snapshots and reconstructed the dynamics of CME.

In LocMoFit, I translated the concept of spherical geometry into an applicable quantitative model for probing the geometry of CME at the single site level. The model can successfully describe the main geometries that have been used to characterize the coat's shapes, including flat, dome-shaped, and spherical structures (Avinoam *et al.*, 2015). The single-structure quantification led to the discovery of a trajectory of curvature changing over pseudotime, which is encoded in the distribution of the closing angle.

4.6.2 Curvature over the closing angle

In the trajectory, only a few flat clathrin lattices were found, indicating they are transient in the beginning of endocytosis. During the first 10 % of the progression, the shallow curvature $H = 0.007\,\mathrm{nm}^{-1}$ (cooresponding to $r = 134\,\mathrm{nm}$) of the clathrin coat is quickly established. The bending slows down and continues until ~60 % of the progression, reaching an average curvature of 0.012 nm^{-1} ($r = 83\,\mathrm{nm}$). In the last ~40 % of the progression, the curvature increases much slower than before, and finally reaches its maximum at/just before vesicle scission. Furthermore, the fit result shows that the earliest sites (with $\theta = 0.01$) already gain ~50 % of the final vesicle surface area.

The rapid transition from a flat to a dome-shaped structure reflects a strong tendency to bend in the beginning of the process. Moreover, the high surface area of the earliest sites either reflects a rapid formation of the initial clathrin coats, or the possibility of even smaller earlier sites being below our detection limit.

We concluded from the trends of curvature and surface area over time (Figure 3.18b,c) that neither of them stays constant over the endocytic progression, disagreeing with the main current models (see Figure 3.19c,d). The highly quantitative data allowed us to further derive the alternative cooperative-curvature model (Figure 3.18a).

4.6.3 Cooperative-curvature model for CME

Based on the observation that the surface area increases during endocytosis (Bucher *et al.*, 2018), we assumed that the addition of triskelia to the rim with a constant rate is the main source of the net growth of the coat (Figure 1.8a). This assumption does not preclude the reported exchange of triskelia within the coat (Avinoam *et al.*, 2015). The curvature increase slowed down over the endocytic progression, leading to the hypothesis of a preferred curvature in the model. The presence of a preferred curvature is also supported by structures formed by purified clathrin *in vitro* (Fotin *et al.*, 2004; Saleem *et al.*, 2015). A nonlinear relation between the rates of curvature increase and curvature is introduced to reflect the cooperativity in the lattice, supported by recent studies (Sochacki *et al.*, 2021; Zeno *et al.*, 2021). This assumption of cooperativity is crucial for the consistency between the model and the data and is, for example, exemplified in rearrangements of neighboring triskelia. The cooperativity is also reflected by the predicted square root law of curvature versus pseudotime (Figure 3.19c).

However, for simplicity, factors other than the clathrin coat itself are not considered in the cooperative-curvature model. The deviation of the model from the data in the trajectories of closing angle θ over time (Figure 3.19b) related to the stalling at 70° and 130° in the data (corresponding to the two peaks in Figure 3.19a) also indicates the involvement of other factors. These factors include a vast number of proteins such as several BAR domain proteins that mediate the temporal change of membrane curvature at the endocytic site (Kaksonen and Roux, 2018). In addition, the clathrin coat properties described in the model were all treated as constants, although they can be variable.

Overall, the uncovered trajectory of mammalian CME clearly demonstrates the potential of LocMoFit in answering important biological questions. Despite the presence of shapes that are more complicated than the supplied standard geometrical model (e.g., asymmetric, ellipsoidal, or more irregular sites), it still well approximates the overall shapes. These asymmetric features are averaged out in the dynamic reconstruction because of the rotational symmetry assumed by the model. However, U-shaped structures, which deviate from the model along the axis of the rotational symmetry, can be retained in the reconstruction (Figure 4.3).

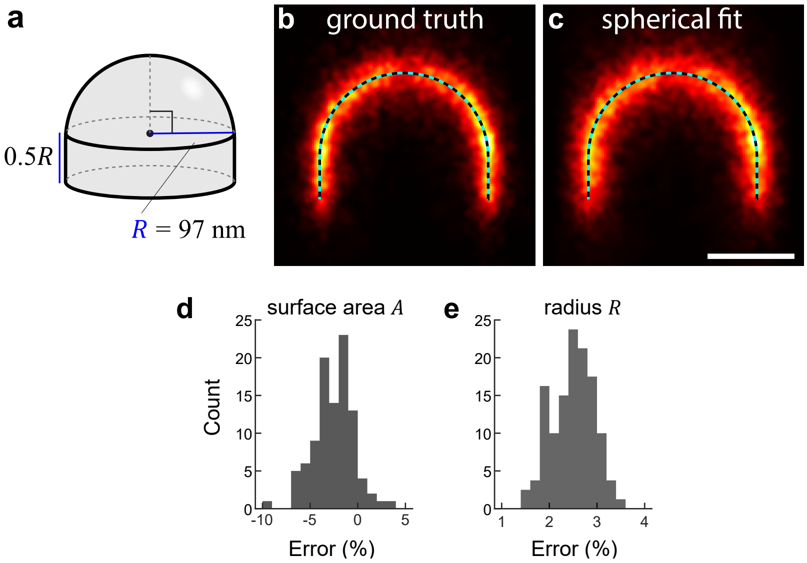

Figure 4.3 | Fitting simulated U-shaped structures with the spherical model. I simulated U-shaped structures with the model (**a**) that are formed compositely by a hemisphere on top of a cylinder. The radius R of the hemisphere and the cylinder is fixed at 97 nm, according to the average radius of structures that have closing angles slightly beyond 90°. The height of the cylinder is fixed at half of R. Simulated structures were averaged based on the ground truth or the spherical fit. 20-nanometer cross-sections of the averages are shown (**b,c**). The averages are overlaid with the outline (dashed line) of the ground truth. The normalized errors of the fitted surface area A (**d**) and radius R (**e**) are shown in the histograms. Sample size: 100 sites. Scale bar: 50 nm. Aline Tschanz and I created the figure jointly. *Adapted from Mund* et al.*, 2022, on which I am a co-author.*

If necessary, more complex geometric models can be implemented to analyze these structures, e.g., for quantifying different curvatures in asymmetric structures. However, using a more complex model can suffer from over-fitting or failed fits. These shortcomings can be assessed or avoided by comparison with the spherical model based on AIC_C or a step-wise optimization, which are supported by LocMoFit.

4.7 Systematically studying the dynamics of CME in budding yeast

In this work, jointly with Philipp Hoess and Jonas Ries, I developed the concept of using a composite reference structure to reconstruct the dynamics of endocytosis in yeast. We have demonstrated that the geometric features of protein distributions are sufficient for identifying specific proteins in the reference structure (Figure 3.22). The features also allowed a precise estimation of the time-associated ring-cap distance based on only one label. The inward movement of the coat protein Pan1 (Picco *et al.*, 2015) can be recapitulated (Figure 3.20) by the dynamic reconstruction based on the ring-cap distance, showing that the distance indeed encodes temporal information. I developed an automatic analysis pipeline to process high-throughput data which contain thousands of sites per overnight acquisition. Thanks to the easy-to-manipulate genome of budding yeast, we were able to apply the reconstruction systematically to multiple endocytic proteins (Figure 3.24) in a preliminary data set.

4.7.1 Automatic analysis pipeline for processing high-throughput data

To process the large amount of data (hundreds or thousands of sites per target protein), an automated analysis pipeline is necessary. This requires the automation of data pre-processing and LocMoFit fitting. I developed an additional pre-processing pipeline (Figure 3.21) in SMAP that can be applied prior to LocMoFit. This fully automated pipeline segments cells and endocytic sites, filters cells by shape and size, removes overlapping sites, and thus ensures that good-quality sites are selectively retained. These sites are either rotated to be pointing upward or removed if their orientation cannot be faithfully determined. At this stage, the sites are ready for the LocMoFit fitting, which can be executed across all segmented sites without user intervention in SMAP once the fitting settings are pre-defined. The throughput of the entire workflow is demonstrated by analyzing the dataset with 651 sites and 310 cells (Figure 3.23).

4.7.2 A step toward the dynamic reconstruction of the entire endocytic machinery

CME in yeast involves more than 50 proteins that arrive at and leave from the endcoytic site in a highly coordinated manner. To finish the entire process, an endocytic site has to undergo a long and variable (from $\sim 30\,\mathrm{s}$ to $4\,\mathrm{min}$) immobile phase and a short ($\sim 30\,\mathrm{s}$) mobile phase, where the proteins dynamically rearrange to drive the membrane invagination. One of our main goals is to extend the dynamic reconstruction to the entire endocytic machinery to understand how these proteins orchestrate. This goal requires analyses of individual target proteins, followed by dataset merging. At the time I wrote up this work, we were still working on extending the data set with more proteins of interest. The preliminary results based on the proteins representing each endocytic module (Figure 3.24) show features that agree well with prior findings but there are also features that are unexpected or previously unknown. We found the coat protein End3 is localized in the coat but also curiously at the base of the endocytic sites (Figure 3.24a). This pattern is also present at a single site level, excluding an artifact caused by averaging. A potential artifact caused by tagging the three proteins in the same cell has to be further investigated. Although being an interesting finding, we still have to further validate this pattern with higher sampling rate in the mobile phase with a larger sample size. According to the last three time bins shown in Figure 3.24b, the yeast homolog of the mammalian WASP Las17 is distributed more diffusely toward the end of endocytic progression. This agrees with the reported localization of Las17 at the invagination's neck by immunoelectron microscopy (Idrissi *et al.*, 2008) and the slight inward movement of the Las17 centroid by live-cell fluorescence microscopy (Picco *et al.*, 2018). The dynamic reconstruction of the actin-crosslinker Sac6 shows an expected dome-shaped distribution that expands inward over time (Figure 3.24c). We found a denser part of the distribution sandwiched by the two parts of the reference structure, having the upper and lower boundaries slightly overlapped with the coat and the base ring, respectively. This finding of the denser part, which in principle marks the sub-region of the actin network that has higher rigidity, may potentially provide insight into the force generation if we can relate more members of the actin network. However, I cannot exclude that the denser part is an effect of projection. This possibility will be able to investigate with 3D imaging by 4Pi-SMS, which provides isotropic resolution. In the mobile phase, Rvs167, a protein of the scission module, distributes diffusely around the endocytic site right before the separation of the coat from the base ring (bin 4 in Figure 3.23d). A denser part of the Rvs167 distribution forms at the location of the base ring (bin 5) and then moves slightly inward (bins 6 and 7) to the neck of the invagination.

Although being a preliminary result with only four target proteins and a small sample size, these reconstructions not only already present previously unknown features of protein rearrangements during endocytosis, but also provide useful guidance to further analyses. In the following, I will discuss the points that have to be considered in the further analyses.

Informative time frame As described in Section 3.7.2, the scope of this work is to investigate the dynamic rearrangements that are observable in the side view, where the change along the axis of endocytosis can be observed well. These rearrangements mainly happen during the mobile phase, which thus defines the informative time frame. The reference structure we used, i.e., Myo5/Sla2, has a ring-cap distance increasing throughout the mobile phase, perfectly suiting this time frame.

Sites outside of the time frame However, many of the sites that are not in the informative time frame were also obtained: the sites with only one component of the composite reference structure are detected, where the two components largely overlap. In this case, the ring-cap distance cannot be faithfully determined.

During the temporal sorting, I decided to place the sites whose reference structure contained only one component at the beginning of the list. The purpose was to retain sites with the reference structure containing only Sla2, which could be described not only by the cap model, but also solely by the ring model in some cases. These sites can occur if they were fixed in the small time frame between the arrivals of Sla2 and Myo5. However, we cannot exclude that Myo5 could appear alone in the reference structure, e.g., after scission, because Rvs167, a protein recruited right before scission, was present in the first time bin where the reference structure is flat (Figure 3.24d).

I also noticed a long immobile phase, characterized by the overlay of the coat and ring, in most of the reconstructions (Figure 3.24a,b,d). Although Myo5 was considered as detectable according to the fitted weight ($> 5\,\%$) of the ring structure, the coat geometry was still dominant in some of the time bins in the immobile phase (see Figure 3.24 for the examples: bin 3 in subpanel a, bins 3 and 4 in b, and bins 2 and 3 in d). This dominant geometry indicates that Myo5 might not have been recruited in some composite sites forming these bins.

The cases above either are in the immobile phase or are rare events in the mobile phase, therefore should be excluded from the future analysis.

Combining datasets One key step is to integrate several datasets so that different target proteins can be related spatially and temporally. If the same reference structure is used in all datasets, the seamless integration can be achieved by putting all datasets on top of each other based on the time bins. However, in our preliminary results, the immobile phase was observed at different frequencies in the different datasets (Figure 3.24a-d). The different frequencies could be explained by the variable lifetime of the mobile phase, ranging from $\sim 30\,\mathrm{s}$ to $4\,\mathrm{min}$ (Pedersen *et al.*, 2020). The variable lifetime depends on the local environment of the endocytic sites, e.g., in the growing bud or not, (Pedersen *et al.*, 2020) and can be more pronounced on different datasets given the small sample size of the preliminary result.

To sum up, these preliminary results clearly show that the dynamic reconstruction of the mobile phase of yeast endocytosis by using a reference works well. Therefore, it can be used to study the structural rearrangements of different target proteins. For a comprehensive study, we will increase the sampling and the number of target proteins.

4.8 LocMoFit software

To benefit more potential users, LocMoFit is published as an open-source tool (`https://github.com/jries/SMAP/tree/master/LocMoFit`) that has also been integrated as part of the SMLM software platform SMAP (Ries, 2020). This integration provides a graphical user interface for users to easily access LocMoFit for fitting their own data. Users can learn how to use LocMoFit through tutorials and example files I provide. For a more complex task, LocMoFit can be used as stand-alone tool with an API for integration into own software. All the models described in this work are readily usable and can be accessed by everyone via our Git repository. These models can be used as the building block to form complex composite models. Creation of new models is supported by template files and guides although basic programming expertise is required. For knowledge sharing, I would encourage users to deposit their own models to our Git repository.

The model fitting in LocMoFit is based on MLE, which is computationally expensive. In the current implementation of LocMoFit, fitting a single site requires seconds to minutes depending on the complexity of the model and the number of localizations of the site: 5 to 10 s for an NPC and CME site in yeast, tens of seconds to a few minutes for an CME site in a mammalian cell, 5 to 10 min for a micrometer-long microtubule. With this performance, hundreds of sites can be fitted in overnight runs on a standard CPU (e.g., Intel Core i5-4460).

I anticipate that LocMoFit will greatly increase the information that researchers can extract from their SMLM data. Integration of LocMoFit into data analysis workflows would allow them to handle more complex tasks that drive biological discovery.

5 | Future outlook

In this work, I presented LocMoFit, a model-fitting framework for single particle analysis in SMLM. I described the key functionalities of LoMoFit and demonstrated their applications in *in situ* structural biology and studying dynamic structures.

Although the current version of LoMoFit is already catholic, the software itself and its biological applications can still be extended in the future.

5.1 Extension of LocMoFit

LocMoFit uses sum log-likelihood as the objective function for the optimization and has achieved precise parameter estimation. However, I have not explored the distribution of log-likelihood values at single sites (i.e., log-likelihood of individual localizations in certain areas), which should carry additional information, e.g., the local discrepancy between the model and the data. I will further investigate the values' potential, e.g., to inform about heterogeneity.

I showed that classifying particles into time bins prior to particle averaging of heterogeneous and dynamic cellular structures is necessary. Therefore, I will include classification (Danial and Garcia-Saez, 2019; Pike *et al.*, 2020) as part of the standard particle averaging workflow in LocMoFit.

The current version of LocMoFit assumes that localizations are independent, although multiple localizations may be generated by the same fluorophore at non-consecutive time points so that they cannot be properly grouped. Assigning these localizations to originate from the same fluorophore, e.g., using a Bayesian framework that considers fluorophore blinking and non-stoichiometric labeling in a probabilistic manner, has been shown to improve the localization precision (Fazel *et al.*, 2019). Inclusion of such a model in LocMoFit could further improve its robustness and accuracy, but at the expense of runtime.

Although LocMoFit is already faster than PERPL, the tool I compared LocMoFit to, for the same tasks I tested, fitting a large number of structures is still time consuming. In the future version, the performance of LocMoFit can be further improved by supporting the use of clusters or deployment on GPUs.

5.2 Biological applications of LocMoFit

In this work, I quantified the key parameters of the NPC. However, I observed some features that can not be probed by the current model. We expect to extend the model to further quantify, for example, the ellipticity and local deformations of the NPC rings. This could help us better understand how the NPC interacts with its local environment or if different functional states which can be distinguished structurally exist.

Jointly with other members in the group, we are applying the spherical model of CME to study the coat rearrangement in different cell types and organisms. We are also working on introducing the concept of the reference structure to reconstruct the dynamics of other endocytic proteins, such as AP2 and dynamin, using clathrin as the reference.

Up until now, we only analyzed one protein for each module of endocytosis in yeast with a small sample size. We are working on increasing the sample size and extending the number of target proteins. With the advance of an algorithm for PSF fitting in 4Pi-SMS developed in the lab, it is possible to gain isotropic resolution in all spatial dimensions. We envision to image endocytosis in yeast with the 4Pi-SMS in the lab to obtain meaningful 3D information which improves the LocMoFit fitting result but also provides us with the target protein in 3D.

I expect LocMoFit will benefit more researchers and drive their studies forwards. Accordingly, for different structures of interest, models can be reused or newly created. For example, in an on-going work of our collaborator Ivana Čavka (from the Köhler group at EMBL), existing and new models are both applied to study the arrangement of components of the synaptonemal complex in the nematode *Caenorhabditis elegans* during meiosis. We will be maintaining a model library that users can also contribute to, e.g., by uploading their models to our Github repository, to support knowledge sharing.

6 | Materials & Methods

6.1 Materials

6.1.1 Chemicals

Table 6.1 | Simulation parameters.

Parameter	Value	Value
Adenine hemisulfate salt	Sigma-Aldrich, St. Louis, MO, USA	A3159
Ammonium chloride	Merck, Darmstadt, Germany	101145
Anti-clathrin heavy chain rabbit polyclonal antibody	Abcam, Cambridge, UK	ab21679
Anti-clathrin light chain rabbit polyclonal antibody	Santa Cruz Biotechnology, Dallas, TX, USA	sc-28276
Anti-Elys rabbit polyclonal antibody	Atlas Antibodies, Bromma, Sweden	HPA031658
Anti-mouse antibody, CF660C conjugated	Biotium, Fremont, CA, USA	20819
Anti-mouse antibody, CF680 conjugated	Biotium, Fremont, CA, USA	20815
Anti-Nup133 rabbit polyclonal antibody	Atlas Antibodies, Bromma, Sweden	HPA059767
Anti-Nup153 mouse monoclonal antibody	Abcam, Waltham, MA, USA	ab24700
Anti-Nup62 mouse monoclonal antibody	BD Biosciences, San Jose, CA, USA	610498
Anti-rabbit antibody, unconjugated	Jackson ImmunoResearch, West Grove, PA, USA	711-005-152
Anti-rabbit antibody, CF660C conjugated	Biotium, Fremont, CA, USA	20818
Anti-rabbit antibody, CF680 conjugated	Biotium, Fremont, CA, USA	20813
Bacto Agar	BD Biosciences, San Jose, CA, USA	214010
Bovine Serum Albumin	Sigma-Aldrich, St. Louis, MO, USA	A7030
Concanavalin A	Sigma-Aldrich, St. Louis, MO, USA	C2010
D(+)-Glucose monohydrate	Merck, Darmstadt, Germany	104074
Di-sodium hydrogen phosphate	Merck, Darmstadt, Germany	106586
Digitonin	Sigma-Aldrich, St. Louis, MO, USA	D141
DMEM (high-glucose, w/o phenol red)	Thermo Fisher, Waltham, MA, USA	11880-028
DMEM/F12	Thermo Fisher	10565018
DTT	Sigma-Aldrich, St. Louis, MO, USA	43819
Formaldehyde solution, about 37 %	Merck, Darmstadt, Germany	104003
Glucose-Oxidase	Carl Roth, Karlsruhe, Germany	6028.1
Glutamine	Sigma-Aldrich, St. Louis, MO, USA	P0380
HEPES	Biomol, Hamburg, Germany	5288
Image-iT™ FX Signal Enhancer	Thermo Fisher, Waltham, MA, USA	I36933
Non-essential amino acids (100$times$)	Thermo Fisher, Waltham, MA, USA	11140-035
Normal Goat Serum	Thermo Fisher, Waltham, MA, USA	PCN5000
Peptone	BD Biosciences, San Jose, CA, USA	211677
Potassium chloride	Merck, Darmstadt, Germany	104936
Potassium dihydrogen phosphate	Merck, Darmstadt, Germany	104873

Continued on the next page

Table 6.1 Continued from previous page

Parameter	Value	Value
SNAP-Surface® Alexa Fluor™ 647	New England Biolabs, Ipswich, MA, USA	S9136S
Sodium chloride	Merck, Darmstadt, Germany	106404
Sucrose	Sigma-Aldrich, St. Louis, MO, USA	S0389
Triton™ X-100	Sigma-Aldrich, St. Louis, MO, USA	X100
Yeast extract	BD Biosciences, San Jose, CA, USA	212750
ZellShield®	Minerva Biolabs, Berlin, Germany	13-0050

6.1.2 Buffers, solutions and media

Unless specified, all buffers, solutions, and media were prepared with Milli-Q® ultrapure water.

ConA solution

Concanavalin A	0.4 % [w/v]
in PBS	

Formaldehyde (FA) fixation solution

Formaldehyde (from 37 %, MeOH stabilized)	4 % [w/v]
Sucrose	2 % [w/v]
in PBS	

PBS

KCl	2.7 mM
KH_2PO_4	1.5 mM
Na_2HPO_4	8.1 mM
NaCl	137 mM

Quenching solution

Ammonium chloride	100 mM
in PBS	

Permeabilization and blocking solution

Image-iT™ FX Signal Enhancer	50 % [v/v]
Triton™ X-100	0.25 % [v/v]
in PBS	

Digitonin permeabilization solution

Digitonin	0.01 % [w/v]
in PBS	

SNAP-tag staining solution

SNAP Surface® Alexa Fluor 647™	1 µM
BSA	1 % [w/v]
Triton™ X-100	0.25 % [v/v]
DTT	1 mM
in PBS	

Blocking and antibody dilution buffer

Normal goat serum (NGS)	5 % [v/v]
in PBS	

Blocking buffer (CME)

BSA	1 % [w/v]
in PBS	

WGA staining buffer

WGA-CF680	400 [ng/mL]
Tris pH 8.0	100 mM
NaCl	40 mM

Blinking buffer

Tris/HCl pH 8	50 mM
NaCl	10 mM
D-glucose	10 % [w/v]
Glucose oxidase	$500\,\mu g\,mL^{-1}$
Catalase	$40\,\mu g\,mL^{-1}$
MEA	35 mM

SK-MEL-2 medium	
FBS	10 % [v/v]
ZellShield	
HEPES	30 mM
in DMEM/F12[i]	

[i] with GlutaMAX and phenol red

U2OS medium	
FBS	10 % [v/v]
L-glutamine	2 mM
Non-essential amino acids	1×
ZellShield	
in DMEM[i]	

[i] high-glucose, without phenol red

YPAD (Yeast extract Peptone Adenine Dextrose) medium (plates)	
Yeast extract	1 % [w/v]
Bacto peptone	2 % [w/v]
Adenine hemisulfate	0.004 % [w/v]
D-glucose	2 % [w/v]
Bacto agar (for plates)	2 % [w/v]

6.1.3 Yeast strains

Table 6.2 | Yeast Strains used in this work.

Strain number	Description	Genotype	Source
JRY0014	MKY0100 Las17-SNAP$_f$ (HIS) Abp1-mMaple (Hph) MATa	*MATa, his3Δ200, leu2-3,112, ura3-52, lys2-801, LAS17-SNAP$_f$::HIS3MX6, ABP1-mMaple::hphNT1*	Ries Lab (Mund *et al.*, 2018)
yPH069	MKY0100 Abp1-EGFP (HIS) Las17-mMaple (Hph) Sla2-SNAP$_f$ (Nat) MATa	*MATa, his3Δ200, leu2-3,112, ura3-52, lys2-801, ABP1-EGFP::HIS3MX6, LAS17-mMaple::hphNT1, SLA2-SNAP$_f$::natNT2*	Höß, 2021
yPH197	MKY0102 Sla2-mMaple (LEU) Pan1-SNAP$_f$ (Nat) Myo5-mMaple-HA (Kan) MATalpha	*MATα, his3Δ200, leu2-3,112, ura3-52, lys2-801, SLA2-mMaple::LEU2, PAN1-SNAP$_f$::natNT2, MYO5-mMaple-HA::kanMX4*	This work (generated by Philipp Hoess)
yPH245	MKY0100 Myo5-mMaple3 (Hph) Sla2-mMaple3 (LEU) End3-SNAP$_f$ (Nat) MATa	*MATa, his3Δ200, leu2-3,112, ura3-52, lys2-801, MYO5-mMaple3::hphNT1, SLA2-mMaple3::LEU2, END3-SNAP$_f$::natNT2*	Höß, 2021 (generated by me)
yPH246	MKY0100 Myo5-mMaple3 (Hph) Sla2-mMaple3 (LEU) Las17-SNAP$_f$ (Nat) MATa	*MATa, his3Δ200, leu2-3,112, ura3-52, lys2-801, MYO5-mMaple3::hphNT1, SLA2-mMaple3::LEU2, LAS17-SNAP$_f$::natNT2*	Höß, 2021 (generated by me)
yPH247	MKY0100 Myo5-mMaple3 (Hph) Sla2-mMaple3 (LEU) Rvs167-SNAP$_f$ (Nat) MATa	*MATa, his3Δ200, leu2-3,112, ura3-52, lys2-801, MYO5-mMaple3::hphNT1, SLA2-mMaple3::LEU2, RVS167-SNAP$_f$::natNT2*	Höß, 2021 (generated by me)
yPH249	MKY0100 Myo5-mMaple3 (Hph) Sla2-mMaple3 (LEU) Sac6-SNAP$_f$ (Nat) MATa	*MATa, his3Δ200, leu2-3,112, ura3-52, lys2-801, MYO5-mMaple3::hphNT1, SLA2-mMaple3::LEU2, SAC6-SNAP$_f$::natNT2*	Höß, 2021 (generated by me)

6.1.4 Cell lines

Table 6.3 | Cell lines used in this work.

Cell line	Description	Source
SK-MEL-2	SKMEL2 DNM2-GFP CLC-RFP	A kind gift from David Drubin, UC Berkeley (Doyon *et al.*, 2011)
U2OS	U-2 OS-CRISPR-NUP96-SNAP clone no.33	Thevathasan *et al.*, 2019

6.2 Methods

Tables and their footnotes in this chapter have been adapted from Wu *et al.*, 2021 and was originally written by myself.

6.2.1 LocMoFit framework

6.2.1.1 Model fitting in LocMoFit

Most text of this section has been adapted from Wu *et al.*, 2021 and was originally written by myself. In LocMoFit, MLE is used to fit a parameterized geometric model to localizations constituting a structure of interest, particles, or sites. For such a task, two inputs are required: 1) a geometric model $f(p)$, parameterized with a set of parameters p, that describes the distribution of fluorophores in the site, and 2) a set of K localizations $l_k = \{\vec{x}_k, \vec{\sigma}_k\}$ in the site to be approximated by the model. Here $\vec{x} = \{x, y, z\}$ are the localization coordinates with their uncertainties $\vec{\sigma} = \{\sigma_x, \sigma_y, \sigma_z\}$. $\vec{x}_k$ and $\vec{\sigma}_k$ are usually acquired from camera frames by fitting them with an experimental or Gaussian PSF model through MLE (Smith *et al.*, 2010; Li *et al.*, 2018).

In LocMoFit, a geometric model $f(p)$ is converted to a PDF $M(\vec{x}, \vec{\sigma} \mid p)$, which is required by the MLE theory. This allows the incorporation of localization uncertainties in the PDF. $M(\vec{x}, \vec{\sigma} \mid p)$ describes the probability of having a single localization l at the location $\vec{x}$ with an uncertainty $\vec{\sigma}$ given the model parameters p.

Here we assume that localizations in the set l_k are random and independent variable of the PDF. The likelihood of getting these localizations from the PDF equals to the product of individual probabilities as in Equation 3.1.

To get the set of parameter estimates $\hat{p}$ that best describe l_k given the PDF $M(P)$ and so as $f(p)$, we employ an optimization algorithm (see *Optimization procedure*) to maximize the likelihood, as described by equation 3.2.

6.2.1.2 Calculation of the probability density function

In this section, I will discuss how to convert a geometric model $f(p)$ to its PDF $M(\vec{x}, \vec{\sigma} \mid p)$. $f(p)$ be defined in either form of a *fluorophore density map*, *discrete fluorophore coordinates* or *a continuous fluorophore distribution*.

For the first form *fluorophore density map*, the outputs of the geometric model $d = f(\vec{x}, p)$ is the density d of the fluorophore at a position $\vec{x}$. $f(\vec{x}, p)$ does not need to be normalized when supplying it. If an arbitrary localization uncertainty has been defined in $f(p)$, its PDF can be calculated by merely normalization:

$$M(\vec{x} \mid p) = \frac{f(\vec{x}, p)}{\iiint f(\vec{x}, p) dx dy dz}. \tag{6.1}$$

Otherwise, the uncertainty is usually defined by the mean localization uncertainty $\langle\vec{\sigma}\rangle$ and is incorporated as the standard deviation of a Gaussian function convoluting $f(\vec{x}, p)$ (see equation 3.3). Practically, the model $f(p)$ can be supplied as either an image (2D fit), an image stack (3D fit), or directly as a function (regardless of the dimensionality).

For the second form *discrete fluorophore coordinates*, the geometric model $v_j = f(p)$ outputs coordinates of the fluorophores v_j. Taking an one-dimensional example, the corresponding PDF is defined as

$$M(x, \sigma \mid v) = \frac{1}{\sqrt{2\pi}\sigma} \exp\left(-\frac{(x-v)^2}{2\sigma^2}\right). \tag{6.2}$$

Here, I assume the data has only a single fluorophore, at position v with a localization precision σ, that is localized repeatedly. This yields localization coordinates x_k scattering around the position v following a Gaussian distribution having its standard deviation as σ. If we have J model fluorophore positions $\vec{v}_j$ the probability that they describe a single measured localization.

6.2.1.3 Optimization procedure

The text of this section has been adapted from Wu *et al.*, 2021 and was originally written by myself.

To find the set of parameters $\hat{p}$ that maximizes $L(p)$, the user can select either an evolutionary algorithm that searches parameters globally, a simplex-based derivative-free searching, or a gradient-descent optimizer. Before optimization, the user can define which parameters to fit and which to set to a constant value, and their initial values and boundaries. The initial parameters can be either pre-defined values, values derived from user-defined rules, or values inherited from a previous fitting step.

For fitting, we classify the parameters p into intrinsic parameters p^i that directly determine the shape of the model and extrinsic parameters $p^e = \left\{\vec{x}_0, \vec{\alpha}, \vec{S}, \epsilon, w_{bg}\right\}$ that describe the position of the model $\vec{x}_0$, the orientation, described by the rotation angles $\vec{\alpha}$ about the three axes, and optionally a global scaling factor $\vec{S}$, an uncertainty ϵ additional to the localization precision, and the weight w_{bg} of a constant background PDF M_{bg} to accommodate the localizations that cannot be described by the geometric PDF (see next section). Here the rotation angles $\vec{\alpha} = \{\alpha, \beta, \gamma\}$ about the *x*, *y*, and *z* axes, respectively, define the rotation matrix:

$$\boldsymbol{R} = \begin{bmatrix} \cos\beta\cos\gamma & -\cos\beta\sin\gamma & \sin\beta \\ \cos\alpha\sin\gamma + \cos\gamma\sin\alpha\sin\beta & \cos\alpha\cos\gamma - \sin\alpha\sin\beta\sin\gamma & -\cos\beta\sin\alpha \\ \sin\alpha\sin\gamma - \cos\alpha\cos\gamma\sin\beta & \cos\gamma\sin\alpha + \cos\alpha\sin\beta\sin\gamma & \cos\alpha\cos\beta \end{bmatrix}. \tag{6.3}$$

This parameterization of $\boldsymbol{R}$ corresponds to the rotations about z, y, and x axes subsequently. $\vec{S} = \{s_x, s_y, s_z\}$ contains the scaling factors of the three spatial axes, defining the scaling matrix $S = \text{diag}\left(\vec{S}\right)$. For a model in the continuous form, we use the extrinsic parameters p^e to reversely transform the localizations, which is computationally more efficient than to transform the model. Thus, during the optimization, we first transform the localization coordinates as

$$\vec{x}' = \boldsymbol{R}^{-1}\boldsymbol{S}^{-1}\left(\vec{x} - \vec{x}_0\right) \tag{6.4}$$

For a discrete model we translate and rotate the model instead to avoid computationally costly rotation of the anisotropic multidimensional Gaussian (Equation 3.4), particularly in 3D. In this case, the fluorophore positions of the model $\vec{v}$ are transformed during optimization as:

$$\vec{v}' = \boldsymbol{S}\boldsymbol{R}\vec{v} + \vec{x}_0 \tag{6.5}$$

As a result of maximizing the likelihood with respect to p^i and p^e, we obtain the parameter estimates $\hat{p}^i$ and $\hat{p}^e$ along with their 95% confidence intervals based on the Hessian matrix $\boldsymbol{H}$ estimated by fitting the log-likelihood function $LL\left(p\right)$ with a quadratic form $L_q\left(p\right)$ using random parameter values p around the parameter estimates $\hat{p}$ as samples (Verdier *et al.*, 2017), with a fitted constant a_0:

$$LL\left(p\right) \approx LL_q\left(p\right) = \left(p - \hat{p}\right)^T \boldsymbol{H}\left(p - \hat{p}\right) + a_0. \tag{6.6}$$

The b^{th} diagonal element of the inverse of $-\boldsymbol{H}$ are the estimated variance of the b^{th} fit parameters in $\hat{p}$:

$$\text{var}\left(\hat{p}_b\right) = \left[\left(-\boldsymbol{H}\right)^{-1}\right]_{b,b}. \tag{6.7}$$

The 95% confidence interval of parameter $\hat{p}_b$ is the given as $CI\left(\hat{p}_b\right) = \hat{p}_b \pm 1.96 \times \sqrt{\text{var}\left(\hat{p}_b\right)}$.

6.2.1.4 Background localizations and additional uncertainties

The text of this section has been adapted from Wu *et al.*, 2021 and was originally written by myself.

In real experiments, unspecific background fluorophores, localizations from neighboring structures or large localization errors lead to localizations that are not described by the model. This mismatch can introduce a bias in the parameter estimates. We accommodate these so-called 'background' localizations with an evenly distributed (constant) PDF M_{bg}:

$$M_b\left(\vec{x}, \vec{\sigma}|p\right) = \left(1 - w_{bg}\right) M\left(\vec{x}, \vec{\sigma}|p_m\right) + w_{bg}M_{bg}. \tag{6.8}$$

The set of parameters p_m contains all elements of p except for the background weight w_{bg}. $M_{bg} = d^{-D}$ where d is the length of a site and D is the dimension, so that the summed probability of M_{bg} over the site is one. w_{bg} is the background weight that represents the fraction of localizations that are considered background. The total number K_{bg} and density ρ_{bg} of background localizations can be obtained as $K_{bg} = K \cdot w_{bg}$ and $\rho_{bg} = K_{bg}/d^2$. In LocMoFit the user can choose if to use the density ρ_{bg} or the weight w_b as the fitting parameter. The difference between the total number of localizations K and K_{bg} is then the total number of localizations described by the model $K_m = K - K_{bg}$.

The localization precision σ often underestimates the true spread of localizations in real experiments. The reason can be instabilities like thermal drifts or vibrations during the experiment, the size of the label that displaces the fluorophore from the target structure (linkage error) or biological variability that leads to a spread of the fluorophores that is not described in the model. These additional uncertainties, quantified by the parameter ϵ, lead to an additional blurring (Equation 3.3) with $\langle\sigma\rangle^2 \rightarrow \langle\sigma\rangle^2 + \epsilon^2$. In Equation 3.4 we take ϵ into account with a modified covariance matrix:

$$\mathbf{\Sigma} = \text{diag}\left(\sigma_x^2 + \epsilon^2, \sigma_y^2 + \epsilon^2, \sigma_z^2 + \epsilon^2\right). \tag{6.9}$$

ϵ can be specified by the user or used as an additional free fitting parameter.

6.2.1.5 Composite models

The text of this section has been adapted from Wu *et al.*, 2021 and was originally written by myself.

LocMoFit allows the user to combine several simple models into a single one by adding up and re-normalizing the PDFs of each model (see Equation 3.5).

The sum of weights is 1: $\sum_m w_m + w_{bg} = 1$. w_m represents the proportion of the localizations that can be described by the component PDF M_m. With the weights we can estimate the number of localizations K_m coming from a specific component model M_m by K_m=$K \cdot w_m$.

Note that here we define the extrinsic parameters p_m^e (except for the model weight w_m) of the m^{th} component model ($m > 1$) with respect to the first component model, with a value zero indicating the same transformation as the first component model. That is, the rigid transformation of the first component model (according to p_1^e) is first applied to all component models, followed by the rigid transformation of the m^{th} component model (according to p_m^e) applied to only the m^{th} component model.

The user can select which parameters are fixed among the models and which are fitted independently. This greatly facilitates constructing complex models.

When fitting multi-color SMLM data, each localization is not only described by its coordinate and localization precision, but also its color c. In this case, we can define a separate model for each color channel and fit all models simultaneously, as shown in Equation 3.6.

The weight for each color channel w_c is introduced to minimize the effects of different numbers of localizations between different colors and can be assigned as $w_c = {K_c}^{-1} \sum_c K_c$, where K_c is the number of localizations with the color c. w_c is used as an exponent to normalize the different multiplications, which scales to the number of localizations, in Equation 3.1. When the effects of different numbers of localizations are preferred, weighting can be switched off by setting $w_c = 1$. Note that each single-color PDF $M_c\left(\vec{x}_k^c, \vec{\sigma}_k^c | p^c\right)$ (with the background PDF M_{bg}^c, as described by Equation 3.5 for an individual model or Equation 3.6 for a composite model) is evaluated only with the localizations of the corresponding color.

6.2.1.6 Chaining fitting steps for improved convergence

The text of this section has been adapted from Wu *et al.*, 2021 and was originally written by myself.

For complex models with many fitting parameters, optimizers are limited in scanning the entire parameter space to find a global optimum and might get stuck in a local maximum of the likelihood. Thus, LocMoFit allows the user to chain several fitting steps with different models and use the results of the previous step as the initial parameter for the next one. Note that the first step can employ user-defined rules/functions to provide initial parameter estimates. Then, the user can use a less complex model with strong blur (Equation 6.9), using a global optimizer before fine-tuning the fit with a simplex or gradient-descend optimizer on the precise model. In this way, LocMoFit efficiently finds the global maximum of the cost function $L\left(p\right)$.

6.2.1.7 The relation between likelihood and cross-correlation

The text of this section has been adapted from Wu *et al.*, 2021 and was originally written by myself.

The likelihood $L\left(p\right)$ can be seen as a metric that describes the similarity between model $f\left(p\right)$ and data l_k from the probabilistic aspect. By changing the multiplication in Equation 3.1 to summation, we get another metric that is regularly used for pattern matching and represents the cross-correlation between model and data (Equation 3.7). When using a model $f\left(p\right)$ in the discrete form, by plugging its PDF (as in Equation 3.4) into Equation 3.7, we get a similar form as the correlation between two sets of points derived in Schnitzbauer *et al.*, 2018, with the exception that we do not assign uncertainties to fluorophore coordinates in the model. Also, it is closely related to the Bhattacharya cost function and derivations that were previously used for particle fusion (Heydarian *et al.*, 2018; Heydarian *et al.*, 2021) and detecting structural heterogeneity (Huijben *et al.*, 2021) in SMLM. Therefore, the cross-correlation $L_{cc}(p)$ can also be used as the objective function in LocMoFit.

6.2.2 Data analysis

6.2.2.1 Model fitting

The text of this section has been adapted from Wu *et al.*, 2021 and was originally written by myself.

Model fitting requires segmented sites (see Section 6.2.5.3).

Nup96 We used three models to describe Nup96 in different fitting steps. The first model, *NPC*$_{m1}$, is a composite model of two identical rings, with a fixed radius, shifted along their common axis. The extrinsic parameters of the upper ring were fixed to those of the lower ring, except for the z position. This model was implemented as a fluorophore density map. The second model, *NPC*$_{m2}$, is a dual-ring model that has two identical parallel rings, parameterized by intrinsic parameters ring radius r and ring separation s. This model was implemented as a discretized continuous fluorophore distribution. The third model, *NPC*$_{m3}$, was built using the *NPC*$_{m2}$ as a backbone, having the continuous rings replaced by fluorophore positions (Figure 3.3a). Two of the fluorophores form a unit, which is evenly placed eight times on one ring rotationally and yield 32 positions in total. Since the rings are not continuous anymore, the twist θ between the two rings is also an intrinsic parameter in addition to the two parameters inherited from the second model.

For single-color NPC data (Figure 3.7), we chained these three fitting steps: 1) fitting with *NPC*$_{m1}$ to roughly measure the orientations, positions, and ring separations of the NPCs, 2) fitting with *NPC*$_{m2}$ to refine the previously measured parameters and to measure radii, and 3) fitting with the *NPC*$_{m3}$ to measure the ring twist, with the extra uncertainty ϵ a free parameter to allow exploring parameter space more during optimization. The initial parameters of a later step were inherited from the final parameters of the previous step. All parameter settings are summarized in Table 6.4. For a direct and unbiased comparison between LocMoFit and PERPL (Figure 4.2), we skipped the first step and used a different set of parameter settings Table 6.5.

Table 6.4 | Fitting settings used in this study for Nup96 in single color data.

Step	Model[i]	Parameter type[ii]	Internal parameter name	Free parameter	Relative[iii]		Absolute[iii]		Initial value[iv]	Unit	Symbol
					LB	UB	LB	UB			
1	1	e	x	yes	-50	50	-150	150	$\tilde{x}_k$	nm	x_0
1	1	e	y	yes	-50	50	-150	150	$\tilde{y}_k$	nm	y_0
1	1	e	z	yes	-100	20	-300	300	$\tilde{z}_k - 40$	nm	z_0
1	1	e	weight	no					1		w_1
1	1	e	xrot	yes	-30	30	-inf	inf	0	°	α

Continued on the next page

Table 6.4 Continued from previous page

Step	Model[i]	Parameter type[ii]	Internal parameter name	Free parameter	Relative[iii]		Absolute[iii]		Initial value[iv]	Unit	Symbol
					LB	UB	LB	UB			
1	1	e	yrot	yes	-30	30	-inf	inf	0	°	β
1	1	e	zrot	no					0	°	γ
1	1	e	xscale	no					1		s_x
1	1	e	yscale	no					1		s_y
1	1	e	zscale	no					1		s_z
1	1	e	variation	no					0	nm	ϵ
1	2	e	x	no					0	nm	x_0
1	2	e	y	no					0	nm	y_0
1	2	e	z	yes	-40	100	0	300	40	nm	$\hat{z}_0$
1	2	e	xrot	no					0	°	α
1	2	e	yrot	no					0	°	β
1	2	e	zrot	no					0	°	γ
1	2	e	variation	no					0	nm	ϵ
1	2	e	weight	no					1		w_1
1	2	e	xscale	no					0		s_x
1	2	e	yscale	no					0		s_y
1	2	e	zscale	no					0		s_z
1	L1	e	weight	yes	-1	1	0.001	0.999	0		w_{bg}
2	1	e	x	yes	-20	20	-150	150	$\hat{x}_0^{1,1} + \phi\left(\hat{z}_0^{1,2}\right)_{[1]}$	nm	x_0
2	1	e	y	yes	-20	20	-150	150	$\hat{y}_0^{1,1} + \phi\left(\hat{z}_0^{1,2}\right)_{[2]}$	nm	y_0
2	1	e	z	yes	-20	20	-300	300	$\hat{z}_0^{1,1} + \phi\left(\hat{z}_0^{1,2}\right)_{[3]}$	nm	z_0
2	1	e	xrot	yes	-15	15	-inf	inf	inherited	°	α
2	1	e	yrot	yes	-15	15	-inf	inf	inherited	°	β
2	1	e	zrot	no					0	°	γ
2	1	e	variation	yes	0	20	1	20	0	nm	ϵ
2	1	e	weight	no					1		w_1
2	1	e	xscale	no					0		s_x
2	1	e	yscale	no					0		s_y
2	1	e	zscale	no					0		s_z
2	1	i	azimuthalShift	no					0	°	θ
2	1	i	cornerDegree	no					12	°	ψ
2	1	i	ringDistance	yes	-10	10	0	100	inherited	nm	s
2	1	i	radius	yes	-10	10	30	70	inherited	nm	r
2	L1	e	weight	no					inherited		w_{bg}
3	1	e	x	no					inherited	nm	x_0
3	1	e	y	no					inherited	nm	y_0
3	1	e	z	no					inherited	nm	z_0
3	1	e	xrot	no					inherited	°	α
3	1	e	yrot	no					inherited	°	β
3	1	e	zrot	yes	-180	180	-inf	inf	0	°	r
3	1	e	variation	yes	-10	10	1	20	5	nm	ϵ
3	1	e	weight	no					inherited		w_1
3	1	e	xscale	no					inherited		s_x
3	1	e	yscale	no					inherited		s_y
3	1	e	zscale	no					inherited		s_z
3	1	i	ringDistance	no					inherited	nm	s
3	1	i	radius	no					inherited	nm	r
3	1	i	cornerDegree	no					12	°	ψ
3	1	i	azimuthalShift	yes	-180	180	-inf	inf	0	°	θ
3	L1	e	weight	yes	-1	1	0.001	0.999	inherited		w_{bg}

[i] L1 represents layer 1.

[ii] i and e represent intrinsic and extrinsic parameters, respectively.

[iii] LB/UB: lower/upper boundaries. Blanks indicate values not applicable.

[iv] A tilde operator represents a median value, a hat operator indicates a parameter estimate, and superscripts represent steps and models (e.g., $\hat{z}_0^{1,2}$ means the estimate of z_0 from model 2 in step 1). The function $\vec{z}'_{[k]} = \phi(z)_{[k]}$ outputs the k^th element of the vector $\vec{z}'$ derived from $\vec{z} = \begin{bmatrix} 0 & 0 & z \end{bmatrix}$ rotated by the rotation matrix constructed using $\left\{\hat{\alpha}^{1,1}, \hat{\beta}^{1,1}, \hat{r}^{1,1}\right\}$ as the angles $\{\alpha, \beta, \gamma\}$ in Equation 6.3. 'inherited' indicates that a value is inherited from its counterpart estimate in the previous step. Other symbols have the same meanings as in the main text.

Table 6.5 | LocMoFit fitting settings used in the comparison of LocMoFit and PERPL for the simulated NPCs.

Step	**Model**[i]	**Parameter type**[ii]	**Internal parameter name**	**Free parameter**	**Relative**[iii]		**Absolute**[iii]		**Initial value**[iv]	**Unit**	**Symbol**
					LB	**UB**	**LB**	**UB**			
1	1	e	x	yes	-50	50	-150	150	$\tilde{x}_k$	nm	x_0
1	1	e	y	yes	-50	50	-150	150	$\tilde{y}_k$	nm	y_0
1	1	e	z	yes	-50	50	-300	300	$\tilde{z}_k$	nm	z_0
1	1	e	xrot	yes	-15	15	-inf	inf	0	°	α
1	1	e	yrot	yes	-15	15	-inf	inf	0	°	β
1	1	e	zrot	no					0	°	γ
1	1	e	variation	yes	-inf	inf	1	20	10	nm	ϵ
1	1	e	weight	no					1		w_1
1	1	e	xscale	no					1		s_x
1	1	e	yscale	no					1		s_y
1	1	e	zscale	no					1		s_z
1	1	i	azimuthalShift	no					0	°	θ
1	1	i	cornerDegree	no					12	°	ψ
1	1	i	ringDistance	yes	-inf	inf	0	100	35	nm	s
1	1	i	radius	yes	-inf	inf	0	100	35	nm	r
1	L1	e	weight	yes	-1	1	0.001	0.999	0.1		w_{bg}
2	1	e	x	no					inherited	nm	x_0
2	1	e	y	no					inherited	nm	y_0
2	1	e	z	no					inherited	nm	z_0
2	1	e	xrot	no					inherited	°	α
2	1	e	yrot	no					inherited	°	β
2	1	e	zrot	yes	-180	180	-inf	inf	0	°	r
2	1	e	variation	yes	-10	10	1	20	5	nm	ϵ
2	1	e	weight	no					inherited		w_1
2	1	e	xscale	no					inherited		s_x
2	1	e	yscale	no					inherited		s_y
2	1	e	zscale	no					inherited		s_z
2	1	i	ringDistance	no					inherited	nm	s
2	1	i	radius	no					inherited	nm	r
2	1	i	cornerDegree	no					12	°	ψ
2	1	i	azimuthalShift	yes	-180	180	-inf	inf	0	°	θ
2	L1	e	weight	yes	-1	1	0.001	0.999	inherited		w_{bg}

[i] L1 represents layer 1.

[ii] i and e represent intrinsic and extrinsic parameters, respectively.

[iii] LB/UB: lower/upper boundaries. Blanks indicate values not applicable.

[iv] A tilde operator represents a median value. 'inherited' indicates that a value is inherited from its counterpart estimate in the previous step. Other symbols have the same meanings as in the main text.

For dual-color NPC data (Figure 3.14), Nup96 was fitted in two chained steps: 1) fitting with NPC_{m1} as for the single-color data, and 2) fitting with NPC_{m3}, having intrinsic parameters fixed to the mean parameter values that were extracted from the single-color data (Figure 3.7c). All parameter settings are summarized in Table 6.6.

Table 6.6 | Fitting settings used in this study for Nup96 in dual-color data.

Step	Model[i]	Parameter type[ii]	Internal parameter name	Free parameter	Relative[iii]		Absolute[iii]		Initial value[iv]	Unit	Symbol
					LB	UB	LB	UB			
1	1	e	x	yes	-50	50	-150	150	$\tilde{x}_k$	nm	x_0
1	1	e	y	yes	-50	50	-150	150	$\tilde{y}_k$	nm	y_0
1	1	e	z	yes	-100	20	-300	300	$\tilde{z}_k - 40$	nm	z_0
1	1	e	weight	no					1		w_1
1	1	e	xrot	yes	-30	30	-inf	inf	0	°	α
1	1	e	yrot	yes	-30	30	-inf	inf	0	°	β
1	1	e	zrot	no					0	°	γ
1	1	e	xscale	no					1		s_x
1	1	e	yscale	no					1		s_y
1	1	e	zscale	no					1		s_z
1	1	e	variation	no					0	nm	ϵ
1	2	e	x	no					0	nm	x_0
1	2	e	y	no					0	nm	y_0
1	2	e	z	yes	-30	100	0	300	40	nm	z_0
1	2	e	xrot	no					0	°	α
1	2	e	yrot	no					0	°	β
1	2	e	zrot	no					0	°	γ
1	2	e	variation	no					0	nm	ϵ
1	2	e	weight	no					1		w_1
1	2	e	xscale	no					0		s_x
1	2	e	yscale	no					0		s_y
1	2	e	zscale	no					0		s_z
1	L1	e	weight	yes	-1	1	0.001	0.999	0		w_{bg}
2	1	e	x	yes	-20	20	-150	150	$\hat{x}_0^{1,1} + \phi\left(\hat{z}_0^{1,2}\right)_{[1]}$	nm	x_0
2	1	e	y	yes	-20	20	-150	150	$\hat{y}_0^{1,1} + \phi\left(\hat{z}_0^{1,2}\right)_{[2]}$	nm	y_0
2	1	e	z	yes	-20	20	-300	300	$\hat{z}_0^{1,1} + \phi\left(\hat{z}_0^{1,2}\right)_{[3]}$	nm	z_0
2	1	e	xrot	yes	-10	10	-Inf	Inf	inherited	°	α
2	1	e	yrot	yes	-10	10	-Inf	Inf	inherited	°	β
2	1	e	zrot	yes	-180	180	-inf	inf	[1 360]	°	r
2	1	e	variation	yes	-10	10	1	20	5	nm	ϵ
2	1	e	weight	no					1		w_1
2	1	e	xscale	no					1		s_x
2	1	e	yscale	no					1		s_y
2	1	e	zscale	no					1		s_z
2	1	i	ringDistance	no					50.2	nm	s
2	1	i	radius	no					53.4	nm	r
2	1	i	cornerDegree	no					12	°	ψ
2	1	i	azimuthalShift	no					8.8	°	θ
2	L1	e	weight	yes	-1	1	0.001	0.999	inherited		w_{bg}

[i] L1 represents layer 1.

[ii] i and e represent intrinsic and extrinsic parameters, respectively.

[iii] LB/UB: lower/upper boundaries. Blanks indicate values not applicable.

[iv] A tilde operator represents a median value, a hat operator indicates a parameter estimate, and superscripts represent steps and models (e.g., $\hat{z}_0^{1,2}$ means the estimate of z_0 from model 2 in step 1). The function $\vec{z}'_{[k]} = \phi(z)_{[k]}$ outputs the kth element of the vector $\vec{z}'$ derived from $\vec{z} = \begin{bmatrix} 0 & 0 & z \end{bmatrix}$ rotated by the rotation matrix constructed using $\left\{\hat{\alpha}^{1,1}, \hat{\beta}^{1,1}, \hat{r}^{1,1}\right\}$ as the angles $\{\alpha, \beta, \gamma\}$ in Equation 6.3. 'inherited' indicates that a value is inherited from its counterpart estimate in the previous step. Other symbols have the same meanings as in the main text.

For the model selection, the fitting steps were the same as for single-color NPC data except that different rotational symmetries were used as specified.

Microtubules We used two models to describe microtubules. The first model, MT_{m1}, describes a cubic spline in 3D. In this model, the spline is defined as piecewise third-order polynomials that traverse through a set of odd number N of equidistant control points, in the order $q = 1$ to N. The middle point ($q = q_0 = (N+1)/2$) is defined as the reference position $\vec{x}_{\mathrm{mid}} = \{x_{\mathrm{mid}}, y_{\mathrm{mid}}, z_{\mathrm{mid}}\}$. Starting from the middle point, the rest of control points are defined in two directions, one from $q = q_0 - 1$ to 1 and the other from $q = q_0 + 1$ to N. Following these orders, the position of one control point ($q = q_n$) is defined by its distance d from the previous control point and the azimuth θ_q and elevation angle φ_q, defined relative to the previous control point. The second model, MT_{m2}, uses the first model as a backbone, rendering rings, centered at equidistant points on the backbone spline, perpendicular to the backbone (Figure 3.10c). Thus, the radius r of the rings is an intrinsic parameter in addition to the ones inherited from the first model. Both models were implemented as discretized continuous fluorophore distributions. In this study, we used the number of control points $N = 5$ and the distance between points $d = 250\,\mathrm{nm}$.

Microtubules (Figure 3.10) were fitted with two chained steps: 1) fitting with MT_{m1}, having a large free extra uncertainty ϵ to estimate the central line of microtubule segments, and 2) fitting with MT_{m2} to refine the path of the microtubules and to measure the radius. The initial parameters of the second step were inherited from the final parameters of the first step. All parameter settings are summarized in Table 6.7.

Table 6.7 | Fitting settings used in this study for microtubules.

Step	Model[i]	Parameter type[ii]	Internal parameter name	Free parameter	Relative[iii]		Absolute[iii]		Initial value[iv]	Unit	Symbol
					LB	UB	LB	UB			
1	1	e	x	no					$\tilde{x}_k$	nm	x_0
1	1	e	y	no					$\tilde{y}_k$	nm	y_0
1	1	e	z	no					$\tilde{z}_k$	nm	z_0
1	1	e	xrot	no					0	°	α
1	1	e	yrot	no					0	°	β
1	1	e	zrot	no					$\mathit{pcaRot}\left(\tilde{x}_k, \tilde{y}_k, \right)$	°	γ
1	1	e	variation	yes	-Inf	Inf	30	45	40	nm	ϵ
1	1	e	weight	no					1		w_1
1	1	e	xscale	no					1		s_x
1	1	e	yscale	no					1		s_y
1	1	e	zscale	no					1		s_z
1	1	i	xMid	yes	-Inf	Inf	-500	500	0	nm	x_q
1	1	i	yMid	yes	-Inf	Inf	-500	500	0	nm	y_q
1	1	i	zMid	yes	-Inf	Inf	-500	500	0	nm	z_q
1	1	i	dist	no					250	nm	q
1	1	i	rotAziL1	yes	-25	25	-Inf	Inf	0	°	θ_{L1}
1	1	i	rotEleL1	yes	-25	25	-Inf	Inf	0	°	φ_{L1}
1	1	i	rotAziR1	yes	-25	25	-Inf	Inf	0	°	θ_{R1}
1	1	i	rotEleR1	yes	-25	25	-Inf	Inf	0	°	φ_{R1}
1	1	i	rotAziL2	yes	-25	25	-Inf	Inf	0	°	θ_{L2}
1	1	i	rotEleL2	yes	-25	25	-Inf	Inf	0	°	φ_{L2}

Continued on the next page

Table 6.7 Continued from previous page

Step	Model[i]	Parameter type[ii]	Internal parameter name	Free parameter	Relative[iii]		Absolute[iii]		Initial value[iv]	Unit	Symbol
					LB	UB	LB	UB			
1	1	i	rotAziR2	yes	-25	25	-Inf	Inf	0	°	θ_{R1}
1	1	i	rotEleR2	yes	-25	25	-Inf	Inf	0	°	φ_{R1}
1	L1	e	weight	yes	-1	1	0.001	0.999	0.5		w_{bg}
2	1	e	x	no					inherited	nm	x_0
2	1	e	y	no					inherited	nm	y_0
2	1	e	z	no					inherited	nm	z_0
2	1	e	xrot	no					inherited	°	α
2	1	e	yrot	no					inherited	°	β
2	1	e	zrot	no					inherited	°	γ
2	1	e	variation	no					7	nm	ϵ
2	1	e	weight	no					inherited		w_1
2	1	e	xscale	no					inherited		s_x
2	1	e	yscale	no					inherited		s_y
2	1	e	zscale	no					inherited		s_z
2	1	i	xMid	yes	-30	30	-500	500	inherited	nm	x_q
2	1	i	yMid	yes	-30	30	-500	500	inherited	nm	y_q
2	1	i	zMid	yes	-30	30	-500	500	inherited	nm	z_q
2	1	i	r	yes	-Inf	Inf	10	60	30	nm	r
2	1	i	dist	no					inherited	nm	q
2	1	i	rotAziL1	yes	-Inf	Inf	-25	25	inherited	°	θ_{L1}
2	1	i	rotEleL1	yes	-Inf	Inf	-25	25	inherited	°	φ_{L1}
2	1	i	rotAziR1	yes	-Inf	Inf	-25	25	inherited	°	θ_{R1}
2	1	i	rotEleR1	yes	-Inf	Inf	-25	25	inherited	°	φ_{R1}
2	1	i	rotAziL2	yes	-Inf	Inf	-25	25	inherited	°	θ_{L2}
2	1	i	rotEleL2	yes	-Inf	Inf	-25	25	inherited	°	φ_{L2}
2	1	i	rotAziR2	yes	-Inf	Inf	-25	25	inherited	°	θ_{R1}
2	1	i	rotEleR2	yes	-Inf	Inf	-25	25	inherited	°	φ_{R1}
2	L1	e	weight	yes	-1	1	0.001	0.999	inherited		w_{bg}

[i] L1 represents layer 1.

[ii] i and e represent intrinsic and extrinsic parameters, respectively.

[iii] LB/UB: lower/upper boundaries. Blanks indicate values not applicable.

[iv] A tilde operator represents a median value. The function *pcaRot*$(x_k, y_k,)$ outputs the angle between the x-axis and the first component of the localizations in the x-y plane. 'inherited' indicates that a value is inherited from its counterpart estimate in the last step. Other symbols have the same meanings as in the main text.

Yeast endocytic structures For fitting endocytic sites in yeast cells where Las17 and Abp1 were labeled, we used a composite model formed by a two-element model: projections of a 3D hemiellipsoid and a thick ring onto the 2D imaging plane (Figure 3.20d). This model was implemented as a discretized continuous fluorophore distribution. In the imaging plane, the base of the hemispherical projection is limited to below the thick-ring projection. The hemispherical projection is parameterized by the half long and half short axes a and b of a hemiellipsoid. The thick-ring projection is parameterized by the thickness t and the inner/outer radii r and q of the ring. This model was fitted to the yeast endocytic sites in the dual-color dataset (Figure 3.20). The hemiellipsoid was only fitted to the localizations in the mMaple channel (Abp1) and the thick ring to the localizations in the AF647 channel (Las17), respectively. All parameters are summarized in Table 6.8.

Table 6.8 | Fitting settings used in this study for fitting two channels in yeast.

Step	Model[i]	Parameter type[ii]	Internal parameter name	Free parameter	Relative[iii]		Absolute[iii]		Initial value[iv]	Unit	Symbol
					LB	UB	LB	UB			
1	1	e	x	yes	-30	30	-150	150	0	nm	x_0
1	1	e	y	yes	-50	50	-150	150	$\tilde{y}_k$	nm	y_0
1	1	e	zrot	yes	-15	15	-Inf	Inf	0	°	γ
1	1	e	variation	no					0	nm	ϵ
1	1	e	weight	no					1		w_1
1	1	e	xscale	no					1		s_x
1	1	e	yscale	no					1		s_y
1	1	i	innerRadius	no					40	nm	r
1	1	i	outerRadius	no					70	nm	q
1	1	i	thickness	no					60	nm	t
1	2	e	x	no					0	nm	x_0
1	2	e	y	yes	-300	50	-200	200	0	nm	y_0
1	2	e	zrot	no					0	°	γ
1	2	e	variation	no					0	nm	ϵ
1	2	e	weight	no					1		w_1
1	2	e	xscale	no					0		s_x
1	2	e	yscale	no					0		s_y
1	2	i	a	no					85	nm	a
1	2	i	b	yes	0	250	1	270	0	nm	b
1	L1	e	weight	yes	-1	1	0.001	0.999	0		w_{bg}
1	L2	e	weight	yes	-1	1	0.001	0.999	0		w_{bg}

[i] L1 represents layer 1.

[ii] i and e represent intrinsic and extrinsic parameters, respectively.

[iii] LB/UB: lower/upper boundaries. Blanks indicate values not applicable.

[iv] A tilde operator represents a median value and superscripts represent channels (e.g., $\tilde{y}_k^1$ means the median of y_k, or y positions of localizations, in channel 1). Other symbols have the same meanings as in the main text.

For fitting endocytic sites in yeast cells where a reference structure was labeled, the above-mentioned composite model was used but the hemiellipsoid was replaced by a hemisphere. Accordingly, the parameters a and b were replaced by the spherical radius r. Both component models were fitted to the localizations of the reference structure. All parameters are summarized in Table 6.9 for the reference Las17/Sla2 and Table 6.10 for Myo5/Sla2.

Table 6.9 | Fitting settings used in this study for the reference structure Las17/Sla2 in yeast.

Step	Model[i]	Parameter type[ii]	Internal parameter name	Free parameter	Relative[iii]		Absolute[iii]		Initial value[iv]	Unit	Symbol
					LB	UB	LB	UB			
1	1	e	x	yes	-100	100	-150	150	0	nm	x_0
1	1	e	y	yes	80	120	-150	150	$\tilde{y}_k$	nm	y_0
1	1	e	zrot	yes	-15	15	-Inf	Inf	0	°	γ
1	1	e	variation	no					0	nm	ϵ
1	1	e	weight	no	-Inf	Inf	0	1	1		w_1
1	1	e	xscale	no					1		s_x
1	1	e	yscale	no					1		s_y
1	1	i	innerRadius	no					40	nm	r

Continued on the next page

Table 6.9 Continued from previous page

Step	Model[i]	Parameter type[ii]	Internal parameter name	Free parameter	Relative[iii]		Absolute[iii]		Initial value[iv]	Unit	Symbol
					LB	UB	LB	UB			
1	1	i	outerRadius	no					60	nm	q
1	1	i	thickness	no					70	nm	t
1	2	e	x	no					0	nm	x_0
1	2	e	y	yes	-200	0	-200	150	0	nm	y_0
1	2	e	zrot	no					0	°	γ
1	2	e	variation	no					0	nm	ϵ
1	2	e	weight	no	-Inf	Inf	0	1	1		w_1
1	2	e	xscale	no					0		s_x
1	2	e	yscale	no					0		s_y
1	2	i	radius	no					40	nm	r
1	L1	e	weight	yes	-1	1	0	0.99	0		w_{bg}

[i] L1 represents layer 1.

[ii] i and e represent intrinsic and extrinsic parameters, respectively.

[iii] LB/UB: lower/upper boundaries. Blanks indicate values not applicable.

[iv] A tilde operator represents a median value (e.g., $\tilde{y}_k$ means the median of y_k, or y positions of localizations). Other symbols have the same meanings as in the main text.

Table 6.10 | Fitting settings used in this study for the reference structure Myo5/Sla2 in yeast.

Step	Model[i]	Parameter type[ii]	Internal parameter name	Free parameter	Relative[iii]		Absolute[iii]		Initial value[iv]	Unit	Symbol
					LB	UB	LB	UB			
1	1	e	x	yes	-30	30	-150	150	0	nm	x_0
1	1	e	y	yes	0	120	-150	150	$\tilde{y}_k$	nm	y_0
1	1	e	zrot	yes	-25	25	-Inf	Inf	0	°	γ
1	1	e	variation	no					0	nm	ϵ
1	1	e	weight	no	-Inf	Inf	0.001	0.999	1		w_1
1	1	e	xscale	no					1		s_x
1	1	e	yscale	no					1		s_y
1	1	i	innerRadius	no					20	nm	r
1	1	i	outerRadius	no					90	nm	q
1	1	i	thickness	no					60	nm	t
1	2	e	x	no					0	nm	x_0
1	2	e	y	yes	-260	20[v]	-200	150	0	nm	y_0
1	2	e	zrot	no					0	°	γ
1	2	e	variation	no					0	nm	ϵ
1	2	e	weight	no	-Inf	Inf	0.001	0.999	1		w_1
1	2	e	xscale	no					0		s_x
1	2	e	yscale	no					0		s_y
1	2	i	radius	no					40	nm	r
1	L1	e	weight	yes	-1	1	0.001	0.999	0		w_{bg}

[i] L1 represents layer 1.

[ii] i and e represent intrinsic and extrinsic parameters, respectively.

[iii] LB/UB: lower/upper boundaries. Blanks indicate values not applicable.

[iv] A tilde operator represents a median value (e.g., $\tilde{y}_k$ means the median of y_k, or y positions of localizations). Other symbols have the same meanings as in the main text.

[v] The UB of 0 nm was used for the analysis described in Figure 3.23, corresponding to a minimum centroid distance of 15 nm

Clathrin coat The text of this section has been adapted from Mund *et al.*, 2022 and was originally written by myself. For fitting the clathrin coats in mammalian cells, we used an hollow spherical cap model (Figure 3.17a). This model was implemented as a discretized continuous fluorophore distribution. The spherical cap is parameterized by the surface area A and closing angle θ, where the radius $R = \sqrt{A/2\pi(1 - cos\theta)}$. θ is defined as the angle between the two vectors that point to the pole of the cap and to the rim, respectively, from the center of the sphere. All parameters are summarized in Table 6.11.

Table 6.11 | Fitting settings used in this study for clathrin coats in mammalian cells.

Step	Model[i]	Parameter type[ii]	Internal parameter name	Free parameter	Relative[iii]		Absolute[iii]		Initial value[iv]	Unit	Symbol
					LB	UB	LB	UB			
1	1	e	x	yes	-70	70	-250	250	$\tilde{x}_k$	nm	x_0
1	1	e	y	yes	-70	70	-250	250	$\tilde{y}_k$	nm	y_0
1	1	e	z	yes	-70	70	-300	300	$\tilde{z}_k$	nm	z_0
1	1	e	xrot	yes	-10	10	-inf	inf	0	°	α
1	1	e	yrot	yes	-10	10	-inf	inf	0	°	β
1	1	e	zrot	no					0	°	γ
1	1	e	variation	yes	-inf	inf	5	30	20	nm	ϵ
1	1	e	weight	no					1		w_1
1	1	e	xscale	no					1		s_x
1	1	e	yscale	no					1		s_y
1	1	e	zscale	no					1		s_z
1	1	i	surfaceArea	no	-inf	inf	0	20	3	$nm^2 \times 10^4$	A
1	1	i	closeAngle	no	-inf	inf	-135	135	90	°	θ
1	L1	e	weight	yes	-1	1	0.001	0.999	0.1		w_{bg}
2	1	e	x	yes	-30	30	-250	250	inherited	nm	x_0
2	1	e	y	yes	-30	30	-250	250	inherited	nm	y_0
2	1	e	z	yes	-30	30	-300	300	inherited	nm	z_0
2	1	e	xrot	yes	-10	10	-inf	inf	inherited	°	α
2	1	e	yrot	yes	-10	10	-inf	inf	inherited	°	β
2	1	e	zrot	no					inherited	°	γ
2	1	e	variation	yes	-inf	inf	5	30	inherited	nm	ϵ
2	1	e	weight	no					inherited		w_1
2	1	e	xscale	no					inherited		s_x
2	1	e	yscale	no					inherited		s_y
2	1	e	zscale	no					inherited		s_z
2	1	i	surfaceArea	no	-inf	inf	0	20	inherited	$nm^2 \times 10^4$	A
2	1	i	closeAngle	no	-inf	inf	-180	180	inherited	°	θ
2	L1	e	weight	yes	-1	1	0.001	0.999	inherited		w_{bg}

[i] L1 represents layer 1.

[ii] i and e represent intrinsic and extrinsic parameters, respectively.

[iii] LB/UB: lower/upper boundaries. Blanks indicate values not applicable.

[iv] A tilde operator represents a median value (e.g., $\tilde{y}_k$ means the median of y_k, or y positions of localizations). 'inherited' indicates that a value is inherited from its counterpart estimate in the previous step. Other symbols have the same meanings as in the main text.

Arc structures For fitting the simulated 2D arc particles, we used an arc model (Figure 4.1a). This model was implemented as a discretized continuous fluorophore distribution. The structure is defined as a circular arc parameterized by the arc length a and closing angle θ, where the radius $r = a/2\theta$. θ is defined as the angle between the two vectors that point to the midpoint of the arc and to the rim, respectively, from the center of the circle. This model was fitted to the simulated 2D arc particles in the comparison between LocMoFit and PERPL (Figure 4.1b). All parameters are summarized in Table 6.12.

Table 6.12 | LocMoFit fitting settings used in this study for the arc structure.

Step	Model[i]	Parameter type[ii]	Internal parameter name	Free parameter	Relative[iii]		Absolute[iii]		Initial value[iv]	Unit	Symbol
					LB	UB	LB	UB			
1	1	e	x	yes	-300	300	-450	450	$\tilde{x}_k$	nm	x_0
1	1	e	y	yes	-300	300	-450	450	$\tilde{y}_k$	nm	y_0
1	1	e	zrot	yes	-20	20	-Inf	Inf	0	°	γ
1	1	e	variation	yes	-inf	inf	1	30	20	nm	ϵ
1	1	e	weight	no					1		w_1
1	1	e	xscale	no					1		s_x
1	1	e	yscale	no					1		s_y
1	1	i	arcLength	yes	-inf	inf	100	500	100	nm	a
1	1	i	theta	yes	-inf	inf	0	180	60	nm	θ
1	L1	e	weight	yes	-1	1	0.001	0.999	0.01		w_{bg}

[i] L1 represents layer 1.

[ii] i and e represent intrinsic and extrinsic parameters, respectively.

[iii] LB/UB: lower/upper boundaries. Blanks indicate values not applicable.

[iv] A tilde operator represents a median value. Other symbols have the same meanings as in the main text.

6.2.2.2 Simulations

The simulation parameters are indicated in italics below and summarized in Table 6.13. To generate realistic simulated data, a bright/dark two-state fluorophore model considering bleaching was used to perform the simulations (Sage *et al.*, 2019). The workflow started with setting model parameters, which were defined as fixed values or random variables uniformly distributed within specified ranges. For each simulated particle, all proteins defined in the point model or a specific number of samples randomly drawn from a PDF with zero extra uncertainty were then assigned as protein positions. Only a subset of positions was retained according to the probability p_{label} of the protein position labeled by the fluorophore to represent the effect of labeling efficiency. Next, the retained positions were displaced independently in all dimensions with the displacements defined as random variables of a normal distribution, of which the variance corresponds to the *linkage error*. There were two modes of displacements: the *free* mode assumed free rotations of fluorophores in 3D between different blinks, and the *fixed* mode applied the same displacement across all blinks. Per blink, each label position was fluorescent for a course of time that was a random variable with an exponential distribution determined by the user-defined average time t_l. Unless it was bleached, each label could be reactivated with a probability p_{react} according to the user-specified average number of re-blinks. A random time point was then assigned to each localization. The brightness or *photon count* of a fluorophore during the *on time* was constant. Thus, the brightness in each frame was the portion of the total brightness divided by the amount of on time in the unit of frames. The emitted photons of the fluorophore in each frame were defined as a random Poisson variable, of which the mean value was set to the average brightness in that frame. To mimic the process of localizing, in each frame, the localization precision of the localization was assigned as the calculated CRLB (Cramér-Rao lower bound) in x, y, and z based on the theoretical Gaussian PSF

(Mortensen *et al.*, 2010) or a bead-calibrated 3D cspline PSF model (Li *et al.*, 2018), given the number of photons and the *background photons*. In each dimension, the corresponding localization precision was then defined as the variance of a normal distribution, whose random variable was added to the label position to yield a localization.

Table 6.13 | Simulation parameters.

Parameter	Value[i]	Unit	Symbol
Figures 3.4 & 3.5			
SMLM property			
photon count	5000[ii]		
background	100[ii]	photons/pixel/localization	
labelling efficiency	60	percent	
re-blinks	2		
lifetime	2	frame	
linkage error (fixed)	5	nm	
EM on	false		
number of frames	100,000		
NPC model parameter			
x	[-50, 50]	nm	x_0
y	[-50, 50]	nm	y_0
z	[-50, 50]	nm	z_0
xrot	[-15, 15]	°	α
yrot	[-15, 15]	°	β
zrot	[0, 360]	°	r
variation	0	nm	ϵ
weight	1		w_1
xscale	1		s_x
yscale	1		s_y
zscale	1		s_z
ringDistance	50	nm	s
radius	53.5	nm	r
cornerDegree	12	°	ψ
azimuthalShift	8.8	°	θ
background weight	0.1		w_{bg}
Simulations in Figures 3.7, 3.9, 3.12, & 4.2			
SMLM property			
photon count	12,000		
background	260	photons/pixel/localization	
labelling efficiency	67	percent	
re-activation	4.1		
lifetime	2	frame	
linkage error (free)	3	nm	
EM on	true		
number of frames	100,000		
NPC model parameter			
x	[-50, 50]	nm	x_0
y	[-50, 50]	nm	y_0
z	[-50, 50]	nm	z_0
xrot	[-15, 15]	°	α
yrot	[-15, 15]	°	β
zrot	[0, 360]	°	r
variation	0	nm	ϵ
weight	1		w_1
xscale	1		s_x
yscale	1		s_y

Continued on the next page

Table 6.13 Continued from previous page

Parameter	Value[i]	Unit	Symbol
zscale	1		s_z
ringDistance	50.2	nm	s
radius	53.4	nm	r
cornerDegree	12	°	ψ
azimuthalShift	8.8	°	θ
background density	20	μm^{-2}	ρ_{bg}
Simulations in Figure 4.1			
SMLM property			
photon count	9,200		
background	170	photons/pixel/localization	
labelling efficiency	60	percent	
re-activation	2		
lifetime	2	frame	
linkage error (free)	10	nm	
EM on	true		
number of frames	100,000		
Arc model parameter			
x	[-15, 15]	nm	x_0
y	[-15, 15]	nm	y_0
zrot	[-15, 15]	°	r
variation	0	nm	ϵ
weight	1		w_1
xscale	1		s_x
arcLength	$a(\theta)$[iii]	nm	a
theta	[0, 180]	°	θ
background density	20	μm^{-2}	ρ_{bg}
number of molecules	$\lfloor a/4nm \rceil$ [iv]		

[i] These values were used unless indicated otherwise.

[ii] Photon counts for getting different localization precisions (indicated in the parentheses) in Figure 3.4a: 370 (11 nm), 550 8 nm), 920 6 nm), 1,900 4 nm), 6,500 2 nm, 22,300 1 nm), with zero fluorescence background.

[iii] $a(\theta) = 0.2\pi\theta \times \tanh\left(3.76 \times 10^{-3}\pi\theta\right)$ derived from the cooperative curvature described in Mund *et al.*, 2022 is the arc length of the spherical coat cross-section.

[iv] $\lfloor x \rceil$ represents rounding to the nearest integer of the value x.

I then processed the simulated data with the same workflow as for the experimental data.

6.2.2.3 Reference-based averaging of multi-color data

The text of this section has been adapted from Wu *et al.*, 2021 and was originally written by myself.

To create the average density map of the nuclear pore complex, in each site only Nup96 localizations were fitted as described in Paragraph *Nup96* in Section 6.2.2.1. Each site was transformed to the orientation and position of the model so that all the sites were in the same coordinate system. The averages were reconstructed from the transformed localizations of all sites.

For the dynamic reconstruction of CME in yeast, all sites were sorted by the fitted length of the hemi-ellipsoid describing Abp1 localizations. The orientation of each site was aligned to the direction of the membrane invagination and the estimated position of the Las17 ring model defined the origin. Each time bin was then created from the localizations of 21 aligned sites.

6.2.2.4 Model selection

The text of this section has been adapted from Wu *et al.*, 2021 and was originally written by myself.

In LocMoFit, we provide the corrected Akaike information criterion (AIC_C; Cavanaugh, 1997) as the metric for performing model selection. In general, a model with more free parameters tends to fit better. Therefore, instead of using the maximum likelihood $\hat{L}$ as the metric, $AIC = 2P - 2\ln\hat{L}$ was suggested for penalizing the number of free parameters P (Cavanaugh, 1997). In practice, we would like to choose a model with fewer parameter and yet a larger maximum likelihood. Therefore, the smallest AIC indicate the best model when fitting the same data. To avoid overfitting caused by small sample size, the corrected AIC_C includes an additional penalty: $AIC_C = AIC + (2P^2 + 2P)/(K - P - 1)$, where K is sample size (Cavanaugh, 1997). When $K \to \infty$, the additional penalty term approaches zero so that AIC_C converges to AIC. In LocMoFit, the sample size K is the number of localizations. For visual comparison of the AIC_C, we normalize by the number of localizations K.

6.2.2.5 Model-free averaging

The text of this section has been adapted from Wu *et al.*, 2021 and was originally written by myself.

For model-free averaging of Nup96 particles, we generated an initial model from a subset of particles $P_1 \dots P_{50}$. To this end, we defined the localization coordinates of each particle as the fluorophore positions of a point model and fitted each model to all other particles in the 50-particle subset. Prior to that all-against-all pairwise fitting, we optionally set the initial parameters of positions and rotations according to the fit with a continuous dual-ring model. This step narrows the search range of rotations during the pairwise fitting and reduces bright 'hot spots' or overlaps of denser corners enhanced by a wide search range of rotations. Next, based on LL values acquired by all-against-all pairwise fitting, we then built a similarity matrix $\boldsymbol{M}$. Next, we cumulatively fused the particles in the order R of their total similarity: Each particle $P_{[R=i]}$ was registered to the fused particle $T_{[R=i-1]}$ starting with the highest-ranked particle $T_1 = P_{[R=1]}$. This initial model T that was used to register the remaining particles $P_{51} \dots P_k$ in the k-particle data set. The resulting average T was then used as the new initial template for the next round of registration. This step was iterated until convergence and yielded the final average T. See Algorithm 1 for the pseudocode.

6.2.2.6 PERPL analysis

We used PERPL (version 0.1), downloaded from `https://bitbucket.org/apcurd/perpl-python3/src/0.1/`. This version was used in the original work

Algorithm 1 Model-free averaging

```
Input: $k$ individual particles $\boldsymbol{P_1 P_2 \ldots P_k}$, each contains localization coordinates
  and uncertainties
Output: final average $\boldsymbol{T}$
  // all-against-all pairwise registration among a $\boldsymbol{n}$-sites subset of particles with
  $\boldsymbol{n < k}$
  // $\boldsymbol{k}$ is the total number of particles in the dataset
  for each pair $\{\boldsymbol{i}, \boldsymbol{j}\} \in \{\ \mathbf{1}\ \ \ldots\ \ \boldsymbol{n}\ \}$ do
      if $i \neq j$ then
          // $\mathrm{LocMoFit}\,(A, B)$ represents fitting $\boldsymbol{A}$ to $\boldsymbol{B}$ through $\boldsymbol{LocMoFit}$
          $\boldsymbol{M}[\boldsymbol{i}, \boldsymbol{j}] \leftarrow$ maximum log-likelihood of $\mathrm{LocMoFit}\,(P_i, P_j)$
      else
          $\boldsymbol{M}[\boldsymbol{i}, \boldsymbol{j}] \leftarrow 0$
   vector $\boldsymbol{R} \leftarrow \mathrm{rank}(\mathrm{rowsum}(\boldsymbol{M}))$

  // forming the first data-driven template
  $\boldsymbol{T} \leftarrow \boldsymbol{P}_{[\boldsymbol{R}=1]}$ // taking the particle with the highest total similarity as the seed
  for $\boldsymbol{i} = 2 \ldots \boldsymbol{n}$ do
      $P' \leftarrow P_{[R=i]}$ registered to $\boldsymbol{T}$ through $\mathrm{LocMoFit}\left(\boldsymbol{T}, \boldsymbol{P}_{[\boldsymbol{R}=\boldsymbol{i}]}\right)$ $\boldsymbol{T} \leftarrow \boldsymbol{P'} \cup \boldsymbol{T}$

  // iterative optimization of the average particle until no further improvement
  // the optimization stops when J unimproved iterations reached
  $\boldsymbol{S} \leftarrow -inf$ // initializing the current best score $\boldsymbol{S}$
  $\widetilde{\boldsymbol{T}} \leftarrow \boldsymbol{T}$ // use the current $\boldsymbol{T}$ as the initial template for the iterative registrations
  repeat
      for $\boldsymbol{i} = \mathbf{1} \ldots \boldsymbol{k}$ do
          $\boldsymbol{L_i} \leftarrow$ maximum log-likelihood of $\mathrm{LocMoFit}\left(\widetilde{\boldsymbol{T}}, \boldsymbol{P_i}\right)$
          $\boldsymbol{P}'_i \leftarrow \boldsymbol{P}_i$ registered registered to T through $\mathrm{LocMoFit}\left(\widetilde{\boldsymbol{T}}, \boldsymbol{P_i}\right)$
      $\widetilde{\boldsymbol{S}} \leftarrow \mathrm{sum}\,(\boldsymbol{L_1} \ldots \boldsymbol{L_k})$ // the current score
      $\widetilde{\boldsymbol{T}} \leftarrow \boldsymbol{P'_1} \cup \boldsymbol{P'_2} \ldots \boldsymbol{P'_k}$ // $\widetilde{T}$ is the template
      if $\widetilde{\boldsymbol{S}} > \boldsymbol{S}$ then // if there is an improvement
          $\boldsymbol{T} \leftarrow \widetilde{\boldsymbol{T}}$ // $\boldsymbol{T}$ is the current best average
          $\boldsymbol{S} \leftarrow \widetilde{\boldsymbol{S}}$
          $j \leftarrow \mathbf{0}$
      else// if there is no improvement
          $\boldsymbol{j} \leftarrow \boldsymbol{j} + \mathbf{1}$
  until $\boldsymbol{J} = \boldsymbol{J}$ // stops when no improvement for $\boldsymbol{J}$ consecutive times
  return $\boldsymbol{T}$ as the final average
```

of PERPL (Curd *et al.*, 2021). In PERPL, we implemented the geometric models of the arc structure and the 3D NPC model with the exact same parameterizations (covering all intrinsic parameters) as in LocMoFit. The model RPDs (relative position distributions) were derived from the model in the original work (Curd *et al.*, 2021) for describing the Nup107 distribution in the xy plane. Therefore, the PERPL fitting models include three inherited terms for localization precision, unresolvable substructure, and background, respectively.

To ensure a fair comparison with LocMoFit, the settings for boundaries and initial values of the intrinsic parameters (see Table 6.5 and Table 6.12) were the same in both softwares. The maximum pairwise distance for PERPL were set to 450 nm for the 2D arc structures and 250 nm for the 3D NPCs). PERPL assumes a linear RPD for the background, which is only fulfilled for large ROIs. To reduce the edge effect, we exported the single particles for PERPL within a sufficiently large ROI (1,800 nm × 1,800 nm for the arc and 1,000 nm × 1,000 nm × 250 nm for the NPC structures). We performed LocMoFit fitting on the same ROIs. Analysis on smaller ROI sizes lead to qualitatively similar results (data not shown).

6.2.3 Sample preparation

6.2.3.1 Preparation of coverslips

Round glass coverslips (24 mm) were left in the stirring mixture of methanol and hydrochloric (1:1 in volume) acid overnight. Next, they were rinsed with ddH_2O a few times. After a neutral pH of the washing solution can be retained, they were then dried in a laminar flow hood overnight. Then the cleaning was finalized by exposing the coverslips to ultraviolet irradiation for 30 min.

For yeast samples, the following steps were included. First, the coverslips underwent 5–10 min plasma clean. 20 µL ConA solution was dropped onto each coverslip before spreading out by a pipette tip. The coverslips were then incubated in a humidified atmosphere for 30 min. Next, after the residual liquid was removed, the coverslips were dried at 37 °C overnight. The coverslips were rinsed with ddH_2O a few times to remove the remaining salts just before the experiment.

6.2.3.2 Cell culture

The U2OS and SK-MEL-2 cells were cultured in the corresponding medium at 37 °C under adherent conditions and a 100 % humid atmosphere with 5 % CO_2. Cells were passaged using Tryp-LE for dissociation when they reached 70–80 percent confluency.

6.2.3.3 Sample seeding

Two days before fixation, cells were seeded on a clean glass coverslip to reach a confluence of about 50–70 % on the day of fixation. Then, the cells were grown in growth medium at 37 °C and 5 % CO_2 for approximately two days. Prior to the experiment, the growth medium was aspirated and dead cells and debris were removed from the samples by two rinses with PBS.

6.2.3.4 Preparation of NPC samples

Single-color imaging Coverslips with Nup96-SNAP-tag cells seeded on were cleaned by two rinses with warm PBS. The sample was pre-fixed in FA fixation solution for 40 s before a 3 min permeabilization in permeabilization solution. Complete fixation was performed in FA fixation solution for 30 min followed by 3 times of 5 min wash in PBS. Next, the sample was incubated in Image-iT FX Signal Enhancer for 30 min. Staining was carried out in 100 µL SNAP-tag staining solution for 2 h at room temperature. Coverslips were washed three times for 5 min in PBS to remove unbound dye. The sample was ready for imaging at this stage.

Dual-color imaging For imaging with immunostaining, following the previous steps, samples were blocked in blocking buffer for 1 h. The coverslips were then incubated in antibody dilution buffer containing the corresponding primary antibody for 1 h. After 3 times 5 min washes with PBS to remove unbound antibody, the coverslips were incubated for 1 h in antibody dilution buffer containing 1:150 diluted secondary antibody. After three 5 min washes in PBS, the sample was post-fixed for 30 min in FA fixation solution. The sample was then rinsed with PBS before being quenched in quenching solution for 5 min, followed by three 5 min washes in PBS. The sample was ready for imaging at this stage.

For imaging with WGA staining, the above-mentioned fixation, permeabilization, and stating were first applied. Subsequently, the sample was incubated in WGA staining buffer for 10 min. The sample was ready for imaging at this stage.

Before imaging, the samples were mounted on a customized sample holder and kept in the imaging buffer. Parafilm was then used to seal the holder.

6.2.3.5 Preparation of clathrin samples

The SK-MEL-2 cells were fixed in FA fixation solution for 20 min, followed by an incubation with the quenching solution for 7 min. After three times of wash with PBS, the sample was incubated with the digitonin permeabilization solution for 30 min. The sample was washed 3 times for 5 min each with PBS to remove unbound antibody prior to staining with 1:150 diluted secondary antibody in antibody dilution buffer for 1 h. After two times brief washes with PBS, the sample was then incubated in the blocking buffer for 1 h. The sample was briefly washed with PBS before the binding of the primary antibodies was achieved by incubation with the anti-clathrin light chain and anti-clathrin heavy chain rabbit polyclonal antibodies diluted in antibody dilution buffer for 3–12 h. The sample was washed 3 times with PBS for 5 min each to remove unbound antibody prior to staining with a secondary donkey anti-rabbit antibody that was conjugated to Alexa Fluor 647–NHS (average degree of labeling: 1.5) in antibody dilution buffer for 3–4 h. After three 5 min washes in PBS, the sample was mounted in blinking buffer for imaging.

6.2.3.6 Yeast sample preparation

Yeast cells from a single colony on a plate were inoculated into 10 mL YPAD in an Erlenmeyer flask. The flask was then incubated at 30 °C with shaking overnight. The next morning, the overnight culture was diluted in a new glass flask to have an OD_{600} of 0.25 in 10 mL YPAD. The cells were further grown at 30 °C to reach an OD_{600} of 0.6–1.0 , which usually took 3 h. At this stage, 2 mL of the culture were then transferred and centrifuged at 500 rcf. for 3 min to collect cells for sample preparation. During incubation in the following steps, the sample was protected from light. The cell pellet was resuspended in 100–150 mL YPAD, and pipetted onto a ConA-coated coverslip. After incubation for 15 min in a humidified atmosphere to allow a settling of the cells, the residual YPAD was removed from the coverslip. After incubation with gentle orbital shaking for 15 min in the freshly prepared fixation solution, the sample was then incubated in quenching solution twice for 15 min each. The coverslip was incubated for 5 min with gentle orbital shaking in PBS, followed by an incubation in the permeabilization solution for 30 min. After twice incubation with gentle orbital shaking for 5 min each in PBS, the sample was incubated for 90 min in SNAP-tag staining solution (coverslip upside-down on a drop of the solution). After 3 times of incubation for 5 min each with gentle orbital shaking in PBS, the sample was ready for sample mounting.

6.2.4 Microscopy

6.2.4.1 Microscope setup

Microscope 1 (M1) The custom-built microscope M1 has a commercial laser box (iChrome MLE, Toptica, Gräfelfing) containing 405 nm, 561 nm, and 640 nm lasers plus a 640 nm booster laser (Toptica). All lasers were coupled via single-mode fiber, whose output was collimated before its focus on the BFP of the TIRF objective (60×/NA 1.49, Nikon), followed by an adjustment for epi illumination. The fluorescence emission(s) was then filtered by a corresponding bandpass filter(s) before being imaged on the EMCCD camera (iXON Ultra, Andor).

Microscope 2 (M2) This microscope setup was published in Deschamps *et al.*, 2016 and also described in Mund *et al.*, 2018 previously. The custome-built microscope M2 has a commercial laser box (iChrome MLE, Toptica, Gräfelfing) containing Luxx 405 nm, 488 nm, and 638 nm and Cobolt 561 nm lasers plus a 640 nm booster laser (iBeam Smart, Toptica). The free output from the box was collimated and guided through a speckle reducer (LSR-3005-17S-VIS; Optotune, Dietikon, Switzerland) before being coupled into a 2 m long multi-mode fiber (catalog no. M105L02S-A, Thorlabs) that was coiled to additionally mix the laser modes. The fiber output was then magnified by an achromatic lens and filtered by a laser clean-up filter (390/482/563/640 HC Quad; AHF, Tübingen, Germany) to remove fiber generated fluorescence. The cleaned-up beam was reflected into a high NA oil immersion objective (HCX PL APO 160×/1.43 NA, Leica) by a dichroic mirror (TIRF Quad Line Beamsplitter, zt405/488/561/640rpc, Chroma, Bellows Falls, VT, USA) before being focused into the sample. This allows for a homogeneous illumination of an area of about 1,000 μm^2. Emitted fluorescence was collected through the objective, filtered by a corresponding band pass filter before being imaged onto an Evolve512D EMCCD camera (Photometrics). The z-focus was stabilized through closed-loop feedback with the piezo objective positioner (Physik Instrumente) based on the signal of an a quadrant photodiode detecting the infrared laser totally internally reflected off the coverslip. This feedback system ensured z-focus stability over hours, in the range of ±10 nm. A field-programmable gate array (Mojo, Embedded Micro) was used to perform laser control, focus stabilization, and movement of filters. The microscope was controlled by µManager (Edelstein *et al.*, 2014) via the Easier Micro-Manager User interface (EMU; Deschamps and Ries, 2020).

6.2.4.2 Single-color SMLM

In this work, single-color SMLM on M2 (see Paragraph *Microscope 2 (M2)*) were performed on samples with the fluorophore AF647. Either a 676/37 or 700/100 bandpass filter (AHF, Tübingen, Germany) was placed to filter the fluorescence emission before it was imaged onto the EMCCD camera. To maintain a predefined number of localizations per frame, the 405 nm laser (intensity $\approx 28\,\mathrm{W\,cm^{-2}}$) was used with a pulse length controlled by a feedback algorithm throughout the acquisition. Acquisition parameters were set per sample as followed.

NPC samples The text of this paragraph has been adapted from Wu *et al.*, 2021 and was originally written by myself. About 100,000 frames were acquired with a frame rate of 10 Hz and the laser intensity of $\approx 6\,\mathrm{W\,cm^{-2}}$. The choice of the slower frame rate and lower laser intensity was for a balance between localization precision and imaging time (Diekmann *et al.*, 2020).

Clathrin samples The text of this paragraph has been adapted from Wu *et al.*, 2021 and was originally written by myself. 100,000–300,000 frames were acquired with a frame time of 15 ms or 30 ms and the laser intensity of $\approx 15\,\mathrm{W\,cm^{-2}}$.

Samples were mounted and imaged until almost all fluorophores were bleached and no further localizations were detected under continuous UV irradiation.

6.2.4.3 Ratiometric dual-color SMLM

In this work, the pair of AF647 and CF680 was used for ratiometric dual-color imaging. With a 665LP dichroic mirror (catalog no. ET665lp, Chroma), the emitted fluorescence was split into two beams. The transmitted light was filtered by a 685/70 (catalog no. ET685/70m, Chroma) bandpass filter and the reflected light by a 676/37 (catalog no. FF01-676/37-25, Semrock) bandpass filter. The two beams were then imaged on two different regions of the same EMCCD camera. Colors were assigned to individual localizations based on their calculated ratio of intensities in the two channels.

6.2.4.4 Dual-color SMLM in yeast

The dual-color imaging of yeast samples were achieved based on spectrally separated fluorophores AF647 and mMaple. The data were acquired on M1 (see Paragraph *Microscope 1 (M1)*). A dichroic mirror (640LP, ZT640rdc, Chroma) was used to split the emitted fluorescence, after it was constricted laterally by a slit. The transmitted light (AF647) was filtered by a 676/37 (catalog no. FF01-676/37-25, Semrock) bandpass filter and the reflected light (mMaple) by a 600/60 (catalog no. NC458462, Chroma) bandpass filter. The two beams were then imaged on two different regions of the same EMCCD camera (iXON Ultra, Andor). The stabilization of z-focus was achieved as described in Section 6.2.4.1. Each camera frame was acquired with a frame rate of 30 ms. Colors were assigned to individual localizations based on their channels. The localizations acquired in the channel of AF647 were transformed into the region of mMaple according to the calibration determined using beads (TetraSpeck) that have fluorescent signals in the two channels.

6.2.4.5 Automated high-throughput SMLM

This workflow has been developed by Joran Deschamps and Markus Mund in our lab and was described previously in Deschamps, 2017; Mund *et al.*, 2018; Deschamps and Ries, 2020. Briefly, a list of stage positions (see Paragraphs *Positions for mammalian samples* and *Positions for yeast samples*) were supplied, and the positions therein were imaged subsequently. At each position, the imaging was performed automatically according to pre-defined steps. The first step was the positioning of the stage to center the pre-defined position to the illumination area. The next step was the acquisition of the camera frames of the fluorescence emitters according to the acquisition parameters described above in Sections *Single-color SMLM* and *Dual-color SMLM in yeast*. Here, the acquisition ended differently when it reached the maximum number of frames or 5 s after the 405 nm laser reached a pre-defined maximal pulse length. The last step was the acquisition of a BFP (back focal plane) image. A buffering time of 3 s was defined for applying the change of hardware (e.g., moving filters & lenses) in the microscope or for the equilibration of the stage.

Positions for mammalian samples For mammalian samples, individual regions of interest were searched for in live mode and the positions were saved in the *Stage Position List* of µManager.

Positions for yeast samples For yeast samples, an automatically generated grid could be applied because the yeast cells formed a dense layer on the coverslip. The individual grid positions had a 200 µm spacing between each other to avoid pre-activation and pre-bleaching by scattered laser light.

6.2.5 Data processing

6.2.5.1 3D bead calibration

A dilution of Tetra-Speck beads (catalog no. T7279, Thermo Fisher) were prepared by mixing 0.75 µL from stock with 360 µL dH_2O, followed by mixing with 40 µL 1 M $MgCl_2$. The mixture was then placed on a coverslip for 10 min in a custom-made sample holder. After removing the mixture, 400 µL dH_2O was placed on the coverslip. ~20 positions on the coverslip were marked and imaged to acquire z-stacks of beads (−1 to 1 µm, 10 nm step size), controlled by Micro-Manager. Note that the used filters have to be the same as for the specimens to be imaged.

6.2.5.2 Fitting and post-processing

For each localization, the PSF size, position, photon counts, and background were defined as free-fitting parameters of a PSF model and acquired by model fitting using maximum likelihood estimation (Li *et al.*, 2018). The used PSF model was a symmetric Gaussian PSF model for 2D data and an experimentally derived PSF model for 3D data (Li *et al.*, 2019). Multiple yielded localizations were then grouped into one if they were persistent over continuous frames (a gap of one dark frame is allowed) and were no more than 35 nm away from each other. For each grouped localization, its position was defined as the weighted average of x, y and z positions of the composite localizations, and its photon count and the background were calculated by summing that of the composite localizations. Next, a custom drift correction based on redundant cross-correlation was applied to correct the drifts in x, y, and z, with an estimated accuracy better than 1.5 nm in x and y and 2 nm in z, according to the spread of the redundant displacements.

Finally, bad fits and localizations far away from the focal plane were excluded based on the following filtering (the text of the following paragraphs has been adapted from Wu *et al.*, 2021 and was originally written by myself):

3D data of Nup96 lateral localization precision: $[0, 5]$ nm, z position: the range of the nuclear envelope, log-likelihood: exclusion of the left tail of the distribution, and frames: exclusion of the first and last 1,000 frames.

3D data of microtubules lateral localization precision: $[0, 5]$ nm, and frames: $[30,000, 90,000]$ frames for efficiency.

3D dual-color data of NPCs lateral localization precision: $[0, 10]$ nm for Nup96 and $[0, 5]$ nm for target proteins, z position: the range of the nuclear envelope, log-likelihood: exclusion of the left tail of the distribution, and frames: exclusion of the first and last 1,000 frames.

2D dual-color data of endocytic sites in yeast localization precision: $[0, 25]$ nm for the mMaple channel; $[0, 15]$ nm for the AF647 channel, PSF size: $[0, 175]$ nm, and frames: exclusion of the first and last ~20,000 frames.

6.2.5.3 Segmentation of sites

Segmentation of the single NPCs All steps were performed in the ROIManager of SMAP. Rendered images of the cells were convolved with a kernel, a Gaussian convolved ring with a radius approximating that of the NPC. Candidate nuclear pores were then identified by local maxima above a certain threshold. Localizations of each candidate pore were fitted with a circle, with only localizations distributed in the range of $[40, 70]$ nm from the center were included in the fit. The ROI containing the pore was then centered to the origin of a refitted circle with a fixed radius. To remove potentially non-NPC structures or adjacent wrongly segmented NPCs, two zones were defined: 1) within 40 nm from the center and 2) more than 70 nm away from the center. Pores with more than 25 % of localizations in zone 1 or 40 % in zone 2 were rejected. Last, only pores with at least 30 localizations were kept to make sure that the underlying structure is sufficiently sampled.

Segmentation of microtubule segments All steps were performed in the ROIManager of SMAP. In the cells, regions that contain long non-overlapping segments of microtubules were first picked. The segments were then centered within a circular ROI with a radius of 500 nm, which ensured that the segments were at least one micrometer long. When multiple microtubules were present in a ROI, the segment of interest was further retained in a manually drawn polygon mask.

Manual segmentation of endocytic sites All steps were performed in the ROIManager of SMAP. First, in each file, yeast cells with obvious endocytic sites were picked. In the cells, single endocytic sites were then picked manually, followed by a manual rotation to ensure an upward pointing axis of invagination.

Automatic segmentation of endocytic sites This workflow is one of the main results of this work and has been described in Section 3.7.2.3 and Figure 3.21.

6.2.5.4 Correction of depth-dependent distortions

The text of this section has been adapted from Wu *et al.*, 2021 and was originally written by myself.

We observed a depth-dependent distortion of the NPC along the z-axis, as reported previously (Li *et al.*, 2019). The distortion is reflected by the depth-dependent ring separations s of NPCs (Figure 3.8). As we previously measured the precise ring separation for Nup96 (Thevathasan *et al.*, 2019), we used it as the standard to correct the distortion. By definition, the ring separation is the distance between the two rings of one NPC so that $s = |\vec{x}_{r1} - \vec{x}_{r2}|$, where $\vec{x}_{r1}$ and $\vec{x}_{r2}$ are the center positions of the two rings. As the orientation of an NPC is not necessary perpendicular to the xy plane, we measured the tilt angle in radian of an NPC from the z-axis as $\psi = \tan^{-1}\left(\left(1 - \boldsymbol{R}_{3,3}^2\right)^{1/2} / \boldsymbol{R}_{3,3}\right)$ where $\boldsymbol{R}$ is defined by Equation 6.3. We used this angle to derive the vertical component of the separation as $s_z = s\cos\psi = z_{r1} - z_{r2}$. We also calculated the expected s_z as $E(s_z) = E(s)\cos\psi$, with $E(s)$ defined as 49.3 nm, the previously determined average separation of the Nup96 rings (Thevathasan *et al.*, 2019). With these values, we could calculate a scaling factor for each NPC $\mathrm{E}\left(s_z\right) = \mathrm{E}\left(s_z\right)/s_z$. We found that the moving median of s_z along the z-axis appeared as a quadratic-like curve. We then fitted a quadratic function $s_z = c_1 z^2 + c_2 z + c_3$ to the data. Given that the correction factor represents the change of the expected z position over the change of measured z position, $s_f(z) \approx \partial E(z)/\partial z$. We then defined z_0 which makes $s_f(z) = 1$, as the origin of distortion. The expected or undistorted z position can then be acquired as $E(z) = \int S_f(z)$ with $E(z_0) = z_0$. The corrected z position of each localization k was then defined as $z_k' = E\left(z_k\right) - E(0)$ for keeping the focal point zero. This correction was applied to all the NPC data sets before further quantifications.

LaTeX

I composed this thesis with Overleaf, and used a custom document structure based on the 'Masters/Doctoral Thesis' LaTeXtemplate (www.latextemplates.com, authors Steve Gunn, Sunil Patel, vel@latextemplates), modified by Markus Mund, Jervis Vermal Thevathasan & Philipp Hoess, which is available under CC BY-NC-SA 3.0.

Bibliography

Abbe, E. 1873. Beiträge zur Theorie des Mikroskops und der mikroskopischen Wahrnehmung. *Archiv für Mikroskopische Anatomie* **9(1)**: 413–468. DOI: `10.1007/BF02956173`.

Aguet, F., C. N. Antonescu, M. Mettlen, S. L. Schmid, and G. Danuser. 2013. Advances in Analysis of Low Signal-to-Noise Images Link Dynamin and AP2 to the Functions of an Endocytic Checkpoint. *Developmental Cell* **26(3)**: 279–291. DOI: `10.1016/j.devcel.2013.06.019`.

Ando, R., H. Mizuno, and A. Miyawaki. 2004. Regulated Fast Nucleocytoplasmic Shuttling Observed by Reversible Protein Highlighting. *Science* **306(5700)**: 1370–1373. DOI: `10.1126/science.1102506`.

Andronov, L., I. Orlov, Y. Lutz, J.-L. Vonesch, and B. P. Klaholz. 2016. ClusterViSu, a Method for Clustering of Protein Complexes by Voronoi Tessellation in Super-Resolution Microscopy. *Scientific Reports* **6(1)**: 1–9. DOI: `10.1038/srep24084`.

Antonny, B., C. Burd, P. De Camilli, E. Chen, O. Daumke, K. Faelber, M. Ford, V. A. Frolov, A. Frost, J. E. Hinshaw, T. Kirchhausen, M. M. Kozlov, M. Lenz, H. H. Low, H. McMahon, C. Merrifield, T. D. Pollard, P. J. Robinson, A. Roux, and S. Schmid. 2016. Membrane Fission by Dynamin: What We Know and What We Need to Know. *The EMBO Journal* **35(21)**: 2270–2284. DOI: `10.15252/embj.201694613`.

Avinoam, O., M. Schorb, C. J. Beese, J. A. G. Briggs, and M. Kaksonen. 2015. Endocytic Sites Mature by Continuous Bending and Remodeling of the Clathrin Coat. *Science* **348(6241)**: 1369–1372. DOI: `10.1126/science.aaa9555`.

Babcock, H. P. and X. Zhuang. 2017. Analyzing Single Molecule Localization Microscopy Data Using Cubic Splines. *Scientific Reports* **7(1)**: 552. DOI: `10.1038/s41598-017-00622-w`.

Baddeley, D., M. B. Cannell, and C. Soeller. 2010. Visualization of Localization Microscopy Data. *Microscopy and Microanalysis* **16(1)**: 64–72. DOI: `10.1017/S143192760999122X`.

Ball, G., J. Demmerle, R. Kaufmann, I. Davis, I. M. Dobbie, and L. Schermelleh. 2015. SIMcheck: A Toolbox for Successful Super-resolution Structured Illumination Microscopy. *Scientific Reports* **5(1)**: 15915. DOI: `10.1038/srep15915`.

Balzarotti, F., Y. Eilers, K. C. Gwosch, A. H. Gynnå, V. Westphal, F. D. Stefani, J. Elf, and S. W. Hell. 2017. Nanometer Resolution Imaging and Tracking of Fluorescent Molecules with Minimal Photon Fluxes. *Science* **355(6325)**: 606–612. DOI: `10.1126/science.aak9913`.

Barentine, A. E. S., Y. Lin, M. Liu, P. Kidd, L. Balduf, M. R. Grace, S. Wang, J. Bewersdorf, and D. Baddeley. 2019. 3D Multicolor Nanoscopy at 10,000 Cells a Day. DOI: `10.1101/606954`.

Barker, S. L., L. Lee, B. D. Pierce, L. Maldonado-Báez, D. G. Drubin, and B. Wendland. 2007. Interaction of the Endocytic Scaffold Protein Pan1 with the Type I Myosins Contributes to the Late Stages of Endocytosis. *Molecular Biology of the Cell* **18(8)**: 2893–2903. DOI: `10.1091/mbc.e07-05-0436`.

Bates, M., B. Huang, G. T. Dempsey, and X. Zhuang. 2007. Multicolor Super-Resolution Imaging with Photo-Switchable Fluorescent Probes. *Science* **317(5845)**: 1749–1753. DOI: `10.1126/science.1146598`.

Beck, M. and E. Hurt. 2017. The Nuclear Pore Complex: Understanding Its Function through Structural Insight. *Nature Reviews Molecular Cell Biology* **18(2)**: 73–89. DOI: `10.1038/nrm.2016.147`.

Beghin, A., A. Kechkar, C. Butler, F. Levet, M. Cabillic, O. Rossier, G. Giannone, R. Galland, D. Choquet, and J.-B. Sibarita. 2017. Localization-Based Super-Resolution Imaging Meets High-Content Screening. *Nature Methods* **14(12)**: 1184–1190. DOI: `10.1038/nmeth.4486`.

Berning, S., K. I. Willig, H. Steffens, P. Dibaj, and S. W. Hell. 2012. Nanoscopy in a Living Mouse Brain. *Science* **335(6068)**: 551–551. DOI: `10.1126/science.1215369`.

Betzig, E., G. H. Patterson, R. Sougrat, O. W. Lindwasser, S. Olenych, J. S. Bonifacino, M. W. Davidson, J. Lippincott-Schwartz, and H. F. Hess. 2006. Imaging Intracellular Fluorescent Proteins at Nanometer Resolution. *Science* **313(5793)**: 1642–1645. DOI: `10.1126/science.1127344`.

Boczkowska, M., G. Rebowski, and R. Dominguez. 2013. Glia Maturation Factor (GMF) Interacts with Arp2/3 Complex in a Nucleotide State-dependent Manner *. *Journal of Biological Chemistry* **288(36)**: 25683–25688. DOI: `10.1074/jbc.C113.493338`.

Boettner, D. R., J. L. D'Agostino, O. T. Torres, K. Daugherty-Clarke, A. Uygur, A. Reider, B. Wendland, S. K. Lemmon, and B. L. Goode. 2009. The F-BAR Protein Syp1 Negatively Regulates WASp-Arp2/3 Complex Activity during Endocytic Patch Formation. *Current Biology* **19(23)**: 1979–1987. DOI: `10.1016/j.cub.2009.10.062`.

Bourg, N., C. Mayet, G. Dupuis, T. Barroca, P. Bon, S. Lécart, E. Fort, and S. Lévêque-Fort. 2015. Direct Optical Nanoscopy with Axially Localized Detection. *Nature Photonics* **9(9)**: 587–593. DOI: `10.1038/nphoton.2015.132`.

Brach, T., C. Godlee, I. Moeller-Hansen, D. Boeke, and M. Kaksonen. 2014. The Initiation of Clathrin-Mediated Endocytosis Is Mechanistically Highly Flexible. *Current Biology* **24(5)**: 548–554. DOI: `10.1016/j.cub.2014.01.048`.

Breuninger, T., K. Greger, and E. H. K. Stelzer. 2007. Lateral Modulation Boosts Image Quality in Single Plane Illumination Fluorescence Microscopy. *Optics Letters* **32(13)**: 1938. DOI: `10.1364/OL.32.001938`.

Bucher, D., F. Frey, K. A. Sochacki, S. Kummer, J.-P. Bergeest, W. J. Godinez, H.-G. Kräusslich, K. Rohr, J. W. Taraska, U. S. Schwarz, and S. Boulant. 2018. Clathrin-Adaptor Ratio and Membrane Tension Regulate the Flat-to-Curved Transition of the Clathrin Coat during Endocytosis. *Nature Communications* **9(1)**: 1109. DOI: `10.1038/s41467-018-03533-0`.

Bui, K. H., A. von Appen, A. L. DiGuilio, A. Ori, L. Sparks, M.-T. Mackmull, T. Bock, W. Hagen, A. Andrés-Pons, J. S. Glavy, and M. Beck. 2013. Integrated Structural Analysis of the Human Nuclear Pore Complex Scaffold. *Cell* **155(6)**: 1233–1243. DOI: `10.1016/j.cell.2013.10.055`.

Burston, H. E., L. Maldonado-Báez, M. Davey, B. Montpetit, C. Schluter, B. Wendland, and E. Conibear. 2009. Regulators of Yeast Endocytosis Identified by Systematic Quantitative Analysis. *Journal of Cell Biology* **185(6)**: 1097–1110. DOI: `10.1083/jcb.200811116`.

Carrington, G., D. Tomlinson, and M. Peckham. 2019. Exploiting Nanobodies and Affimers for Superresolution Imaging in Light Microscopy. *Molecular Biology of the Cell* **30(22)**: 2737–2740. DOI: `10.1091/mbc.E18-11-0694`.

Cavanaugh, J. E. 1997. Unifying the Derivations for the Akaike and Corrected Akaike Information Criteria. *Statistics & Probability Letters* **33(2)**: 201–208. DOI: `10.1016/S0167-7152(96)00128-9`.

Chalfie, M., Y. Tu, G. Euskirchen, W. W. Ward, and D. C. Prasher. 1994. Green Fluorescent Protein as a Marker for Gene Expression. *Science* **263(5148)**: 802–805. DOI: `10.1126/science.8303295`.

Chen, F., P. W. Tillberg, and E. S. Boyden. 2015. Expansion Microscopy. *Science* **347(6221)**: 543–548. DOI: `10.1126/science.1260088`.

Chen, Z. and S. L. Schmid. 2020. Evolving Models for Assembling and Shaping Clathrin-Coated Pits. *Journal of Cell Biology* **219(9)**: e202005126. DOI: `10.1083/jcb.202005126`.

Chozinski, T. J., L. A. Gagnon, and J. C. Vaughan. 2014. Twinkle, Twinkle Little Star: Photoswitchable Fluorophores for Super-Resolution Imaging. *FEBS Letters* **588(19)**: 3603–3612. DOI: `10.1016/j.febslet.2014.06.043`.

Cocucci, E., F. Aguet, S. Boulant, and T. Kirchhausen. 2012. The First Five Seconds in the Life of a Clathrin-Coated Pit. *Cell* **150(3)**: 495–507. DOI: `10.1016/j.cell.2012.05.047`.

Coons, A. H., H. J. Creech, R. N. Jones, and E. Berliner. 1942. The Demonstration of Pneumococcal Antigen in Tissues by the Use of Fluorescent Antibody. *The Journal of Immunology* **45(3)**: 159–170.

Curd, A. P., J. Leng, R. E. Hughes, A. J. Cleasby, B. Rogers, C. Trinh, M. A. Baird, Y. Takagi, C. Tiede, C. Sieben, S. Manley, T. Schlichthaerle, R. Jungmann, J. Ries, H. Shroff, and M. Peckham. 2020. Nanoscale Pattern Extraction from Relative Positions of Sparse 3D Localisations. *bioRxiv*: 2020.02.13.947135. DOI: `10.1101/2020.02.13.947135`.

Curd, A. P., J. Leng, R. E. Hughes, A. J. Cleasby, B. Rogers, C. H. Trinh, M. A. Baird, Y. Takagi, C. Tiede, C. Sieben, S. Manley, T. Schlichthaerle, R. Jungmann, J. Ries, H. Shroff, and M. Peckham. 2021. Nanoscale Pattern Extraction from Relative Positions of Sparse 3D Localizations. *Nano Letters* **21(3)**: 1213–1220. DOI: `10.1021/acs.nanolett.0c03332`.

Damenti, M., G. Coceano, F. Pennacchietti, A. Bodén, and I. Testa. 2021. STED and Parallelized RESOLFT Optical Nanoscopy of the Tubular Endoplasmic Reticulum and Its Mitochondrial Contacts in Neuronal Cells. *Neurobiology of Disease* **155** 105361. DOI: `10.1016/j.nbd.2021.105361`.

Danial, J. S. H. and A. J. Garcia-Saez. 2019. Quantitative Analysis of Super-Resolved Structures Using ASAP. *Nature Methods* **16(8)**: 711–714. DOI: `10.1038/s41592-019-0472-1`.

Dasgupta, A., J. Deschamps, U. Matti, U. Hübner, J. Becker, S. Strauss, R. Jungmann, R. Heintzmann, and J. Ries. 2021. Direct Supercritical Angle Localization Microscopy for Nanometer 3D Superresolution. *Nature Communications* **12(1)**: 1180. DOI: `10.1038/s41467-021-21333-x`.

Daumke, O., A. Roux, and V. Haucke. 2014. BAR Domain Scaffolds in Dynamin-Mediated Membrane Fission. *Cell* **156(5)**: 882–892. DOI: `10.1016/j.cell.2014.02.017`.

Dempsey, G. T., M. Bates, W. E. Kowtoniuk, D. R. Liu, R. Y. Tsien, and X. Zhuang. 2009. Photoswitching Mechanism of Cyanine Dyes. *Journal of the American Chemical Society* **131(51)**: 18192–18193. DOI: `10.1021/ja904588g`.

Dempsey, G. T., J. C. Vaughan, K. H. Chen, M. Bates, and X. Zhuang. 2011. Evaluation of Fluorophores for Optimal Performance in Localization-Based Super-Resolution Imaging. *Nature Methods* **8(12)**: 1027–1036. DOI: `10.1038/nmeth.1768`.

Deschamps, J. 2017. Towards Quantitative High-Throughput 3D Localization Microscopy. Heidelberg: Dissertation, Ruperto-Carola University of Heidelberg, 2017.

Deschamps, J., M. Mund, and J. Ries. 2014. 3D Superresolution Microscopy by Supercritical Angle Detection. *Optics Express* **22(23)**: 29081. DOI: `10.1364/OE.22.029081`.

Deschamps, J. and J. Ries. 2020. EMU: Reconfigurable Graphical User Interfaces for Micro-Manager. *BMC Bioinformatics* **21(1)**: 456. DOI: `10.1186/s12859-020-03727-8`.

Deschamps, J., A. Rowald, and J. Ries. 2016. Efficient Homogeneous Illumination and Optical Sectioning for Quantitative Single-Molecule Localization Microscopy. *Optics Express* **24(24)**: 28080–28090. DOI: `10.1364/OE.24.028080`.

Deschout, H., A. Shivanandan, P. Annibale, M. Scarselli, and A. Radenovic. 2014. Progress in Quantitative Single-Molecule Localization Microscopy. *Histochemistry and Cell Biology* **142(1)**: 5–17. DOI: `10.1007/s00418-014-1217-y`.

Diekmann, R., M. Kahnwald, A. Schoenit, J. Deschamps, U. Matti, and J. Ries. 2020. Optimizing Imaging Speed and Excitation Intensity for Single-Molecule Localization Microscopy. *Nature Methods* **17** 909–912. DOI: `10.1038/s41592-020-0918-5`.

Djakbarova, U., Y. Madraki, E. T. Chan, and C. Kural. 2021. Dynamic Interplay between Cell Membrane Tension and Clathrin-Mediated Endocytosis. *Biology of the Cell* **113(8)**: 344–373. DOI: `10.1111/boc.202000110`.

Dmitrieff, S. and F. Nédélec. 2015. Membrane Mechanics of Endocytosis in Cells with Turgor. *PLOS Computational Biology* **11(10)**: e1004538. DOI: `10.1371/journal.pcbi.1004538`.

Dominguez, R. and K. C. Holmes. 2011. Actin Structure and Function. *Annual Review of Biophysics* **40(1)**: 169–186. DOI: `10.1146/annurev-biophys-042910-155359`.

Douglass, K. M., C. Sieben, A. Archetti, A. Lambert, and S. Manley. 2016. Super-Resolution Imaging of Multiple Cells by Optimized Flat-Field Epi-Illumination. *Nature Photonics* **10(11)**: 705–708. DOI: `10.1038/nphoton.2016.200`.

Doyon, J. B., B. Zeitler, J. Cheng, A. T. Cheng, J. M. Cherone, Y. Santiago, A. H. Lee, T. D. Vo, Y. Doyon, J. C. Miller, D. E. Paschon, L. Zhang, E. J. Rebar, P. D. Gregory, F. D.

Urnov, and D. G. Drubin. 2011. Rapid and Efficient Clathrin-Mediated Endocytosis Revealed in Genome-Edited Mammalian Cells. *Nature Cell Biology* **13(3)**: 331–337. DOI: `10.1038/ncb2175`.

Duncan, M. C., M. J. T. V. Cope, B. L. Goode, B. Wendland, and D. G. Drubin. 2001. Yeast Eps15-like Endocytic Protein, Pan1p, Activates the Arp2/3 Complex. *Nature Cell Biology* **3(7)**: 687–690. DOI: `10.1038/35083087`.

Durisic, N., A. G. Godin, C. M. Wever, C. D. Heyes, M. Lakadamyali, and J. A. Dent. 2012. Stoichiometry of the Human Glycine Receptor Revealed by Direct Subunit Counting. *Journal of Neuroscience* **32(37)**: 12915–12920. DOI: `10.1523/JNEUROSCI.2050-12.2012`.

Edelstein, A. D., M. A. Tsuchida, N. Amodaj, H. Pinkard, R. D. Vale, and N. Stuurman. 2014. Advanced Methods of Microscope Control Using μManager Software. *Journal of Biological Methods* **1(2)**: e10. DOI: `10.14440/jbm.2014.36`.

Ehrlich, M., W. Boll, A. van Oijen, R. Hariharan, K. Chandran, M. L. Nibert, and T. Kirchhausen. 2004. Endocytosis by Random Initiation and Stabilization of Clathrin-Coated Pits. *Cell* **118(5)**: 591–605. DOI: `10.1016/j.cell.2004.08.017`.

Eilers, Y., H. Ta, K. C. Gwosch, F. Balzarotti, and S. W. Hell. 2018. MINFLUX Monitors Rapid Molecular Jumps with Superior Spatiotemporal Resolution. *Proceedings of the National Academy of Sciences* **115(24)**: 6117–6122. DOI: `10.1073/pnas.1801672115`.

Elia, N. 2021. Using Unnatural Amino Acids to Selectively Label Proteins for Cellular Imaging: A Cell Biologist Viewpoint. *The FEBS Journal* **288(4)**: 1107–1117. DOI: `10.1111/febs.15477`.

Endesfelder, U., K. Finan, S. J. Holden, P. R. Cook, A. N. Kapanidis, and M. Heilemann. 2013. Multiscale Spatial Organization of RNA Polymerase in Escherichia Coli. *Biophysical Journal* **105(1)**: 172–181. DOI: `10.1016/j.bpj.2013.05.048`.

Fazel, M., M. J. Wester, B. Rieger, R. Jungmann, and K. A. Lidke. 2019. Sub-Nanometer Precision Using Bayesian Grouping of Localizations. *bioRxiv*: 752287. DOI: `10.1101/752287`.

Ford, M. G. J., I. G. Mills, B. J. Peter, Y. Vallis, G. J. K. Praefcke, P. R. Evans, and H. T. McMahon. 2002. Curvature of Clathrin-Coated Pits Driven by Epsin. *Nature* **419(6905)**: 361–366. DOI: `10.1038/nature01020`.

Förster, R., K. Wicker, W. Müller, A. Jost, and R. Heintzmann. 2016. Motion Artefact Detection in Structured Illumination Microscopy for Live Cell Imaging. *Optics Express* **24(19)**: 22121. DOI: `10.1364/OE.24.022121`.

Fotin, A., Y. Cheng, P. Sliz, N. Grigorieff, S. C. Harrison, T. Kirchhausen, and T. Walz. 2004. Molecular Model for a Complete Clathrin Lattice from Electron Cryomicroscopy. *Nature* **432(7017)**: 573–579. DOI: `10.1038/nature03079`.

Friesen, H., C. Humphries, Y. Ho, O. Schub, K. Colwill, and B. Andrews. 2006. Characterization of the Yeast Amphiphysins Rvs161p and Rvs167p Reveals Roles for the Rvs Heterodimer In Vivo. *Molecular Biology of the Cell* **17(3)**: 1306–1321. DOI: `10.1091/mbc.e05-06-0476`.

Früh, S. M., U. Matti, P. R. Spycher, M. Rubini, S. Lickert, T. Schlichthaerle, R. Jungmann, V. Vogel, J. Ries, and I. Schoen. 2021. Site-Specifically-Labeled Antibodies for Super-Resolution Microscopy Reveal *In Situ* Linkage Errors. *ACS Nano*: acsnano.1c03677. DOI: `10.1021/acsnano.1c03677`.

Gandhi, M., B. A. Smith, M. Bovellan, V. Paavilainen, K. Daugherty-Clarke, J. Gelles, P. Lappalainen, and B. L. Goode. 2010. GMF Is a Cofilin Homolog That Binds Arp2/3 Complex to Stimulate Filament Debranching and Inhibit Actin Nucleation. *Current Biology* **20(9)**: 861–867. DOI: `10.1016/j.cub.2010.03.026`.

Gautier, A., A. Juillerat, C. Heinis, I. R. Corrêa, M. Kindermann, F. Beaufils, and K. Johnsson. 2008. An Engineered Protein Tag for Multiprotein Labeling in Living Cells. *Chemistry & Biology* **15(2)**: 128–136. DOI: `10.1016/j.chembiol.2008.01.007`.

Geli, M. I. and H. Riezman. 1996. Role of Type I Myosins in Receptor-Mediated Endocytosis in Yeast. *Science* **272(5261)**: 533–535. DOI: `10.1126/science.272.5261.533`.

Gheorghe, D. M., S. Aghamohammadzadeh, I. I. S.-d. Rooij, E. G. Allwood, S. J. Winder, and K. R. Ayscough. 2008. Interactions between the Yeast SM22 Homologue Scp1 and Actin Demonstrate the Importance of Actin Bundling in Endocytosis*. *Journal of Biological Chemistry* **283(22)**: 15037–15046. DOI: `10.1074/jbc.M710332200`.

Goode, B. L., J. A. Eskin, and B. Wendland. 2015. Actin and Endocytosis in Budding Yeast. *Genetics* **199(2)**: 315–358. DOI: `10.1534/genetics.112.145540`.

Görlich, D. and U. Kutay. 1999. Transport Between the Cell Nucleus and the Cytoplasm. *Annual Review of Cell and Developmental Biology* **15(1)**: 607–660. DOI: `10.1146/annurev.cellbio.15.1.607`.

Griffié, J., T. A. Pham, C. Sieben, R. Lang, V. Cevher, S. Holden, M. Unser, S. Manley, and D. Sage. 2020. Virtual-SMLM, a Virtual Environment for Real-Time Interactive SMLM Acquisition. *bioRxiv*: 2020.03.05.967893. DOI: `10.1101/2020.03.05.967893`.

Grimm, J. B., A. K. Muthusamy, Y. Liang, T. A. Brown, W. C. Lemon, R. Patel, R. Lu, J. J. Macklin, P. J. Keller, N. Ji, and L. D. Lavis. 2017. A General Method to Fine-Tune Fluorophores for Live-Cell and in Vivo Imaging. *Nature Methods* **14(10)**: 987–994. DOI: `10.1038/nmeth.4403`.

Grimm, J. B., A. J. Sung, W. R. Legant, P. Hulamm, S. M. Matlosz, E. Betzig, and L. D. Lavis. 2013. Carbofluoresceins and Carborhodamines as Scaffolds for High-Contrast Fluorogenic Probes. *ACS Chemical Biology* **8(6)**: 1303–1310. DOI: `10.1021/cb4000822`.

Guo, S., O. S. Sokolova, J. Chung, S. Padrick, J. Gelles, and B. L. Goode. 2018. Abp1 Promotes Arp2/3 Complex-Dependent Actin Nucleation and Stabilizes Branch Junctions by Antagonizing GMF. *Nature Communications* **9(1)**: 2895. DOI: `10.1038/s41467-018-05260-y`.

Gustafsson, M. G. L. 2000. Surpassing the Lateral Resolution Limit by a Factor of Two Using Structured Illumination Microscopy. SHORT COMMUNICATION. *Journal of Microscopy* **198(2)**: 82–87. DOI: `10.1046/j.1365-2818.2000.00710.x`.

Gustafsson, M. G. L. 2005. Nonlinear Structured-Illumination Microscopy: Wide-field Fluorescence Imaging with Theoretically Unlimited Resolution. *Proceedings of the National Academy of Sciences* **102(37)**: 13081–13086. DOI: `10.1073/pnas.0406877102`.

Gustafsson, M. G., L. Shao, P. M. Carlton, C. J. R. Wang, I. N. Golubovskaya, W. Z. Cande, D. A. Agard, and J. W. Sedat. 2008. Three-Dimensional Resolution Doubling in Wide-Field Fluorescence Microscopy by Structured Illumination. *Biophysical Journal* **94(12)**: 4957–4970. DOI: `10.1529/biophysj.107.120345`.

Gwosch, K. C., J. K. Pape, F. Balzarotti, P. Hoess, J. Ellenberg, J. Ries, and S. W. Hell. 2020. MINFLUX Nanoscopy Delivers 3D Multicolor Nanometer Resolution in Cells. *Nature Methods* **17(2)**: 217–224. DOI: `10.1038/s41592-019-0688-0`.

Hajj, B., J. Wisniewski, M. El Beheiry, J. Chen, A. Revyakin, C. Wu, and M. Dahan. 2014. Whole-Cell, Multicolor Superresolution Imaging Using Volumetric Multifocus Microscopy. *Proceedings of the National Academy of Sciences* **111(49)**: 17480–17485. DOI: `10.1073/pnas.1412396111`.

Heimstädt, O. 1911. Das Fluoreszenzmikroskop. *Zeitschrift für wissenschaftliche Mikroskopie und mikroskopische Technik* **28** 330–337.

Hell, S. and E. H. K. Stelzer. 1992. Properties of a 4Pi Confocal Fluorescence Microscope. *Journal of the Optical Society of America A* **9(12)**: 2159. DOI: `10.1364/JOSAA.9.002159`.

Hell, S. W. and J. Wichmann. 1994. Breaking the Diffraction Resolution Limit by Stimulated Emission: Stimulated-Emission-Depletion Fluorescence Microscopy. *Optics Letters* **19(11)**: 780. DOI: `10.1364/OL.19.000780`.

Hellen, E. H. and D. Axelrod. 1987. Fluorescence Emission at Dielectric and Metal-Film Interfaces. *JOSA B* **4(3)**: 337–350. DOI: `10.1364/JOSAB.4.000337`.

Henderson, R. 2013. Avoiding the Pitfalls of Single Particle Cryo-Electron Microscopy: Einstein from Noise. *Proceedings of the National Academy of Sciences* **110(45)**: 18037–18041. DOI: `10.1073/pnas.1314449110`.

Henne, W. M., E. Boucrot, M. Meinecke, E. Evergren, Y. Vallis, R. Mittal, and H. T. McMahon. 2010. FCHo Proteins Are Nucleators of Clathrin-Mediated Endocytosis. *Science* **328(5983)**: 1281–1284. DOI: `10.1126/science.1188462`.

Hess, S. T., T. P. K. Girirajan, and M. D. Mason. 2006. Ultra-High Resolution Imaging by Fluorescence Photoactivation Localization Microscopy. *Biophysical Journal* **91(11)**: 4258–4272. DOI: `10.1529/biophysj.106.091116`.

Heuser, J. 1980. Three-Dimensional Visualization of Coated Vesicle Formation in Fibroblasts. *Journal of Cell Biology* **84(3)**: 560–583. DOI: `10.1083/jcb.84.3.560`.

Heydarian, H., M. Joosten, A. Przybylski, F. Schueder, R. Jungmann, B. van Werkhoven, J. Keller-Findeisen, J. Ries, S. Stallinga, M. Bates, and B. Rieger. 2021. 3D Particle Averaging and Detection of Macromolecular Symmetry in Localization Microscopy. *Nature Communications* **12(1)**: 2847. DOI: `10.1038/s41467-021-22006-5`.

Heydarian, H., F. Schueder, M. T. Strauss, B. van Werkhoven, M. Fazel, K. A. Lidke, R. Jungmann, S. Stallinga, and B. Rieger. 2018. Template-Free 2D Particle Fusion in Localization Microscopy. *Nature Methods* **15(10)**: 781–784. DOI: `10.1038/s41592-018-0136-6`.

Hofmann, M., C. Eggeling, S. Jakobs, and S. W. Hell. 2005. Breaking the Diffraction Barrier in Fluorescence Microscopy at Low Light Intensities by Using Reversibly Photoswitchable Proteins. *Proceedings of the National Academy of Sciences* **102(49)**: 17565–17569. DOI: `10.1073/pnas.0506010102`.

Holden, S. J., T. Pengo, K. L. Meibom, C. Fernandez Fernandez, J. Collier, and S. Manley. 2014. High Throughput 3D Super-Resolution Microscopy Reveals Caulobacter Crescentus in Vivo Z-ring Organization. *Proceedings of the National Academy of Sciences* **111(12)**: 4566–4571. DOI: `10.1073/pnas.1313368111`.

Holliger, P. and P. J. Hudson. 2005. Engineered Antibody Fragments and the Rise of Single Domains. *Nature Biotechnology* **23(9)**: 1126–1136. DOI: `10.1038/nbt1142`.

Homma, K., S. Terui, M. Minemura, H. Qadota, Y. Anraku, Y. Kanaho, and Y. Ohya. 1998. Phosphatidylinositol-4-Phosphate 5-Kinase Localized on the Plasma Membrane Is Essential for Yeast Cell Morphogenesis *. *Journal of Biological Chemistry* **273(25)**: 15779–15786. DOI: `10.1074/jbc.273.25.15779`.

Hooke, R. 1667. Micrographia: Or, Some Physiological Descriptions of Minute Bodies Made by Magnifying Glasses. With Observations and Inquiries Thereupon. John Martyn.

Horisawa, K. 2014. Specific and Quantitative Labeling of Biomolecules Using Click Chemistry. *Frontiers in Physiology* **5**

Höß, P. 2021. Towards a Dynamic Reconstruction of the Endocytic Machinery by Dual-Color Localization Microscopy. PhD thesis. Heidelberg. DOI: `10.11588/heidok.00029646`.

Huang, F., G. Sirinakis, E. S. Allgeyer, L. K. Schroeder, W. C. Duim, E. B. Kromann, T. Phan, F. E. Rivera-Molina, J. R. Myers, I. Irnov, M. Lessard, Y. Zhang, M. A. Handel, C. Jacobs-Wagner, C. P. Lusk, J. E. Rothman, D. Toomre, M. J. Booth, and J. Bewersdorf. 2016. Ultra-High Resolution 3D Imaging of Whole Cells. *Cell* **166(4)**: 1028–1040. DOI: `10.1016/j.cell.2016.06.016`.

Huijben, T. A., H. Heydarian, A. Auer, F. Schueder, R. Jungmann, S. Stallinga, and B. Rieger. 2021. Detecting Structural Heterogeneity in Single-Molecule Localization Microscopy Data. *Nature Communications* **12(1)**: 3791. DOI: `10.1038/s41467-021-24106-8`.

Idrissi, F.-Z., H. Grötsch, I. M. Fernández-Golbano, C. Presciatto-Baschong, H. Riezman, and M.-I. Geli. 2008. Distinct Acto/Myosin-I Structures Associate with Endocytic Profiles at the Plasma Membrane. *Journal of Cell Biology* **180(6)**: 1219–1232. DOI: `10.1083/jcb.200708060`.

Jia, S., J. C. Vaughan, and X. Zhuang. 2014. Isotropic Three-Dimensional Super-Resolution Imaging with a Self-Bending Point Spread Function. *Nature Photonics* **8(4)**: 302–306. DOI: `10.1038/nphoton.2014.13`.

Juette, M. F., T. J. Gould, M. D. Lessard, M. J. Mlodzianoski, B. S. Nagpure, B. T. Bennett, S. T. Hess, and J. Bewersdorf. 2008. Three-Dimensional Sub–100 Nm Resolution Fluorescence Microscopy of Thick Samples. *Nature Methods* **5(6)**: 527–529. DOI: `10.1038/nmeth.1211`.

Jungmann, R., M. S. Avendaño, J. B. Woehrstein, M. Dai, W. M. Shih, and P. Yin. 2014. Multiplexed 3D Cellular Super-Resolution Imaging with DNA-PAINT and Exchange-PAINT. *Nature Methods* **11(3)**: 313–318. DOI: `10.1038/nmeth.2835`.

Jungmann, R., C. Steinhauer, M. Scheible, A. Kuzyk, P. Tinnefeld, and F. C. Simmel. 2010. Single-Molecule Kinetics and Super-Resolution Microscopy by Fluorescence Imaging of Transient Binding on DNA Origami. *Nano Letters* **10(11)**: 4756–4761. DOI: `10.1021/nl103427w`.

Kadlecova, Z., S. J. Spielman, D. Loerke, A. Mohanakrishnan, D. K. Reed, and S. L. Schmid. 2016. Regulation of Clathrin-Mediated Endocytosis by Hierarchical Allosteric Activation of AP2. *Journal of Cell Biology* **216(1)**: 167–179. DOI: `10.1083/jcb.201608071`.

Kaksonen, M. and A. Roux. 2018. Mechanisms of Clathrin-Mediated Endocytosis. *Nature Reviews Molecular Cell Biology* **19(5)**: 313–326. DOI: `10.1038/nrm.2017.132`.

Kaksonen, M., Y. Sun, and D. G. Drubin. 2003. A Pathway for Association of Receptors, Adaptors, and Actin during Endocytic Internalization. *Cell* **115(4)**: 475–487. DOI: `10.1016/S0092-8674(03)00883-3`.

Kaksonen, M., C. P. Toret, and D. G. Drubin. 2005. A Modular Design for the Clathrin- and Actin-Mediated Endocytosis Machinery. *Cell* **123(2)**: 305–320. DOI: `10.1016/j.cell.2005.09.024`.

Kaksonen, M., C. P. Toret, and D. G. Drubin. 2006. Harnessing Actin Dynamics for Clathrin-Mediated Endocytosis. *Nature Reviews Molecular Cell Biology* **7(6)**: 404–414. DOI: `10.1038/nrm1940`.

Kaplan, C., S. J. Kenny, X. Chen, J. Schöneberg, E. Sitarska, A. Diz-Muñoz, M. Akamatsu, K. Xu, and D. G. Drubin. 2021. Load Adaptation of Endocytic Actin Networks. DOI: `10.1101/2020.04.05.026559`.

Keller, P. J., A. D. Schmidt, A. Santella, K. Khairy, Z. Bao, J. Wittbrodt, and E. H. K. Stelzer. 2010. Fast, High-Contrast Imaging of Animal Development with Scanned Light Sheet–Based Structured-Illumination Microscopy. *Nature Methods* **7(8)**: 637–642. DOI: `10.1038/nmeth.1476`.

Kelly, B. T., S. C. Graham, N. Liska, P. N. Dannhauser, S. Höning, E. J. Ungewickell, and D. J. Owen. 2014. Clathrin Adaptors. AP2 Controls Clathrin Polymerization with a Membrane-Activated Switch. *Science (New York, N.Y.)* **345(6195)**: 459–463. DOI: `10.1126/science.1254836`.

Kennedy, J. and R. Eberhart. 1995. Particle Swarm Optimization. *Proceedings of ICNN'95 - International Conference on Neural Networks*. **4** Perth, WA, Australia: IEEE: 1942–1948. ISBN: 978-0-7803-2768-9. DOI: `10.1109/ICNN.1995.488968`.

Keppler, A., S. Gendreizig, T. Gronemeyer, H. Pick, H. Vogel, and K. Johnsson. 2003. A General Method for the Covalent Labeling of Fusion Proteins with Small Molecules in Vivo. *Nature Biotechnology* **21(1)**: 86–89. DOI: `10.1038/nbt765`.

Kirchhausen, T. and T. Toyoda. 1993. Immunoelectron Microscopic Evidence for the Extended Conformation of Light Chains in Clathrin Trimers. *Journal of Biological Chemistry* **268(14)**: 10268–10273. DOI: `10.1016/S0021-9258(18)82199-8`.

Klein, M. G., W. Shi, U. Ramagopal, Y. Tseng, D. Wirtz, D. R. Kovar, C. J. Staiger, and S. C. Almo. 2004. Structure of the Actin Crosslinking Core of Fimbrin. *Structure* **12(6)**: 999–1013. DOI: `10.1016/j.str.2004.04.010`.

Klevanski, M., F. Herrmannsdoerfer, S. Sass, V. Venkataramani, M. Heilemann, and T. Kuner. 2020. Automated Highly Multiplexed Super-Resolution Imaging of Protein Nano-Architecture in Cells and Tissues. *Nature Communications* **11(1)**: 1552. DOI: `10.1038/s41467-020-15362-1`.

Koide, Y., Y. Urano, K. Hanaoka, T. Terai, and T. Nagano. 2011. Evolution of Group 14 Rhodamines as Platforms for Near-Infrared Fluorescence Probes Utilizing Photoinduced Electron Transfer. *ACS Chemical Biology* **6(6)**: 600–608. DOI: `10.1021/cb1002416`.

Kozak, M. and M. Kaksonen. 2019. Phase Separation of Ede1 Promotes the Initiation of Endocytic Events. DOI: `10.1101/861203`.

Kukulski, W., A. Picco, T. Specht, J. A. Briggs, and M. Kaksonen. 2016. Clathrin Modulates Vesicle Scission, but Not Invagination Shape, in Yeast Endocytosis. *eLife* **5** e16036. DOI: `10.7554/eLife.16036`.

Kukulski, W., M. Schorb, M. Kaksonen, and J. A. G. Briggs. 2012. Plasma Membrane Reshaping during Endocytosis Is Revealed by Time-Resolved Electron Tomography. *Cell* **150(3)**: 508–520.

Lacy, M. M., D. Baddeley, and J. Berro. 2019. Single-Molecule Turnover Dynamics of Actin and Membrane Coat Proteins in Clathrin-Mediated Endocytosis. *eLife* **8** e52355. DOI: `10.7554/eLife.52355`.

Lagarias, J. C., J. A. Reeds, M. H. Wright, and P. E. Wright. 1998. Convergence Properties of the Nelder–Mead Simplex Method in Low Dimensions. *SIAM Journal on Optimization* **9(1)**: 112–147. DOI: `10.1137/S1052623496303470`.

Laine, R. F., A. Albecka, S. van de Linde, E. J. Rees, C. M. Crump, and C. F. Kaminski. 2015. Structural Analysis of Herpes Simplex Virus by Optical Super-Resolution Imaging. *Nature Communications* **6(1)**: 1–10. DOI: `10.1038/ncomms6980`.

Landgraf, D., B. Okumus, P. Chien, T. A. Baker, and J. Paulsson. 2012. Segregation of Molecules at Cell Division Reveals Native Protein Localization. *Nature Methods* **9(5)**: 480–482. DOI: `10.1038/nmeth.1955`.

Legant, W. R., L. Shao, J. B. Grimm, T. A. Brown, D. E. Milkie, B. B. Avants, L. D. Lavis, and E. Betzig. 2016. High-Density Three-Dimensional Localization Microscopy across Large Volumes. *Nature Methods* **13(4)**: 359–365. DOI: `10.1038/nmeth.3797`.

Lewellyn, E. B., R. T. A. Pedersen, J. Hong, R. Lu, H. M. Morrison, and D. G. Drubin. 2015. An Engineered Minimal WASP-Myosin Fusion Protein Reveals Essential Functions for Endocytosis. *Developmental Cell* **35(3)**: 281–294. DOI: `10.1016/j.devcel.2015.10.007`.

Li, C., A. Goryaynov, and W. Yang. 2016. The Selective Permeability Barrier in the Nuclear Pore Complex. *Nucleus* **7(5)**: 430–446. DOI: `10.1080/19491034.2016.1238997`.

Li, D., L. Shao, B.-C. Chen, X. Zhang, M. Zhang, B. Moses, D. E. Milkie, J. R. Beach, J. A. Hammer, M. Pasham, T. Kirchhausen, M. A. Baird, M. W. Davidson, P. Xu, and E. Betzig. 2015. Extended-Resolution Structured Illumination Imaging of Endocytic and Cytoskeletal Dynamics. *Science* **349(6251)**: aab3500. DOI: `10.1126/science.aab3500`.

Li, Y., M. Mund, P. Hoess, J. Deschamps, U. Matti, B. Nijmeijer, V. J. Sabinina, J. Ellenberg, I. Schoen, and J. Ries. 2018. Real-Time 3D Single-Molecule Localization Using Experimental Point Spread Functions. *Nature Methods* **15(5)**: 367–369. DOI: `10.1038/nmeth.4661`.

Li, Y., W. Shi, S. Liu, U. Matti, D. Wu, and J. Ries. 2021. Global Fitting for High-Accuracy Multi-Channel Single-Molecule Localization. DOI: `10.1101/2021.09.22.461230`.

Li, Y., Y.-L. Wu, P. Hoess, M. Mund, and J. Ries. 2019. Depth-Dependent PSF Calibration and Aberration Correction for 3D Single-Molecule Localization. *Biomedical Optics Express* **10(6)**: 2708–2718. DOI: `10.1364/BOE.10.002708`.

Lin, Y., J. J. Long, F. Huang, W. C. Duim, S. Kirschbaum, Y. Zhang, L. K. Schroeder, A. A. Rebane, M. G. M. Velasco, A. Virrueta, D. W. Moonan, J. Jiao, S. Y. Hernandez, Y. Zhang, and J. Bewersdorf. 2015. Quantifying and Optimizing Single-Molecule Switching Nanoscopy at High Speeds. *PLOS ONE* **10(5)**: e0128135. DOI: `10.1371/journal.pone.0128135`.

Liu, S., P. Hoess, and J. Ries. 2022. Super-Resolution Microscopy for Structural Cell Biology. *Annual Review of Biophysics* **51(1)**: null. DOI: `10.1146/annurev-biophys-102521-112912`.

Loerke, D., M. Mettlen, D. Yarar, K. Jaqaman, H. Jaqaman, G. Danuser, and S. L. Schmid. 2009. Cargo and Dynamin Regulate Clathrin-Coated Pit Maturation. *PLOS Biology* **7(3)**: e1000057. DOI: `10.1371/journal.pbio.1000057`.

Los, G. V., L. P. Encell, M. G. McDougall, D. D. Hartzell, N. Karassina, C. Zimprich, M. G. Wood, R. Learish, R. F. Ohana, M. Urh, D. Simpson, J. Mendez, K. Zimmerman, P. Otto, G. Vidugiris, J. Zhu, A. Darzins, D. H. Klaubert, R. F. Bulleit, and K. V. Wood. 2008. HaloTag: A Novel Protein Labeling Technology for Cell Imaging and Protein Analysis. *ACS Chemical Biology* **3(6)**: 373–382. DOI: `10.1021/cb800025k`.

Lukinavičius, G., K. Umezawa, N. Olivier, A. Honigmann, G. Yang, T. Plass, V. Mueller, L. Reymond, I. R. Corrêa Jr, Z.-G. Luo, C. Schultz, E. A. Lemke, P. Heppenstall, C. Eggeling, S. Manley, and K. Johnsson. 2013. A Near-Infrared Fluorophore for Live-Cell Super-Resolution Microscopy of Cellular Proteins. *Nature Chemistry* **5(2)**: 132–139. DOI: `10.1038/nchem.1546`.

Lukyanov, K. A., D. M. Chudakov, S. Lukyanov, and V. V. Verkhusha. 2005. Photoactivatable Fluorescent Proteins. *Nature Reviews Molecular Cell Biology* **6(11)**: 885–890. DOI: `10.1038/nrm1741`.

M'Saad, O. and J. Bewersdorf. 2020. Light Microscopy of Proteins in Their Ultrastructural Context. *Nature Communications* **11(1)**: 3850. DOI: `10.1038/s41467-020-17523-8`.

Ma, L., P. K. Umasankar, A. G. Wrobel, A. Lymar, A. J. McCoy, S. S. Holkar, A. Jha, T. Pradhan-Sundd, S. C. Watkins, D. J. Owen, and L. M. Traub. 2016. Transient Fcho1/2·Eps15/R·AP-2 Nanoclusters Prime the AP-2 Clathrin Adaptor for Cargo Binding. *Developmental Cell* **37(5)**: 428–443. DOI: `10.1016/j.devcel.2016.05.003`.

Ma, R. and J. Berro. 2021. Endocytosis against High Turgor Pressure Is Made Easier by Partial Coating and Freely Rotating Base. *Biophysical Journal* **120(9)**: 1625–1640. DOI: `10.1016/j.bpj.2021.02.033`.

Manenschijn, H. E., A. Picco, M. Mund, A.-S. Rivier-Cordey, J. Ries, and M. Kaksonen. 2019. Type-I Myosins Promote Actin Polymerization to Drive Membrane Bending in Endocytosis. *eLife* **8** e44215. DOI: `10.7554/eLife.44215`.

Massol, R. H., W. Boll, A. M. Griffin, and T. Kirchhausen. 2006. A Burst of Auxilin Recruitment Determines the Onset of Clathrin-Coated Vesicle Uncoating. *Proceedings of the National Academy of Sciences* **103(27)**: 10265–10270. DOI: `10.1073/pnas.0603369103`.

McEvoy, A. L., H. Hoi, M. Bates, E. Platonova, P. J. Cranfill, M. A. Baird, M. W. Davidson, H. Ewers, J. Liphardt, and R. E. Campbell. 2012. mMaple: A Photoconvertible Fluorescent Protein for Use in Multiple Imaging Modalities. *PLoS ONE* **7(12)**: e51314. DOI: `10.1371/journal.pone.0051314`.

McMahon, H. T. and E. Boucrot. 2011. Molecular Mechanism and Physiological Functions of Clathrin-Mediated Endocytosis. *Nature Reviews Molecular Cell Biology* **12(8)**: 517–533. DOI: `10.1038/nrm3151`.

Merrifield, C. J., B. Qualmann, M. M. Kessels, and W. Almers. 2004. Neural Wiskott Aldrich Syndrome Protein (N-WASP) and the Arp2/3 Complex Are Recruited to Sites of Clathrin-Mediated Endocytosis in Cultured Fibroblasts. *European Journal of Cell Biology* **83(1)**: 13–18. DOI: `10.1078/0171-9335-00356`.

Messa, M., R. Fernández-Busnadiego, E. W. Sun, H. Chen, H. Czapla, K. Wrasman, Y. Wu, G. Ko, T. Ross, B. Wendland, and P. De Camilli. 2014. Epsin Deficiency Impairs Endocytosis by Stalling the Actin-Dependent Invagination of Endocytic Clathrin-Coated Pits. *eLife* **3** e03311. DOI: `10.7554/eLife.03311`.

Mikati, M. A., D. Breitsprecher, S. Jansen, E. Reisler, and B. L. Goode. 2015. Coronin Enhances Actin Filament Severing by Recruiting Cofilin to Filament Sides and Altering F-Actin Conformation. *Journal of Molecular Biology* **427(19)**: 3137–3147. DOI: `10.1016/j.jmb.2015.08.011`.

Miller, S. E., S. Mathiasen, N. A. Bright, F. Pierre, B. T. Kelly, N. Kladt, A. Schauss, C. J. Merrifield, D. Stamou, S. Höning, and D. J. Owen. 2015. CALM Regulates Clathrin-Coated Vesicle Size and Maturation by Directly Sensing and Driving Membrane Curvature. *Developmental Cell* **33(2)**: 163–175. DOI: `10.1016/j.devcel.2015.03.002`.

Mooren, O. L., B. J. Galletta, and J. A. Cooper. 2012. Roles for Actin Assembly in Endocytosis. *Annual Review of Biochemistry* **81(1)**: 661–686. DOI: `10.1146/annurev-biochem-060910-094416`.

Mortensen, K. I., L. S. Churchman, J. A. Spudich, and H. Flyvbjerg. 2010. Optimized Localization Analysis for Single-Molecule Tracking and Super-Resolution Microscopy. *Nature Methods* **7(5)**: 377–381. DOI: `10.1038/nmeth.1447`.

Mund, M. 2016. Superresolution Imaging of Clathrin-Mediated Endocytosis in Yeast. PhD thesis.

Mund, M., J. A. van der Beek, J. Deschamps, S. Dmitrieff, P. Hoess, J. L. Monster, A. Picco, F. Nédélec, M. Kaksonen, and J. Ries. 2018. Systematic Nanoscale Analysis of Endocytosis Links Efficient Vesicle Formation to Patterned Actin Nucleation. *Cell* **174(4)**: 884–896.e17. DOI: `10.1016/j.cell.2018.06.032`.

Mund, M., A. Tschanz, Y.-L. Wu, F. Frey, J. L. Mehl, M. Kaksonen, O. Avinoam, U. S. Schwarz, and J. Ries. 2022. Superresolution Microscopy Reveals Partial Preassembly and Subsequent Bending of the Clathrin Coat during Endocytosis. DOI: `10.1101/2021.10.12.463947`.

Nannapaneni, S., D. Wang, S. Jain, B. Schroeder, C. Highfill, L. Reustle, D. Pittsley, A. Maysent, S. Moulder, R. McDowell, and K. Kim. 2010. The Yeast Dynamin-like Protein Vps1:Vps1 Mutations Perturb the Internalization and the Motility of Endocytic Vesicles and Endosomes via Disorganization of the Actin Cytoskeleton. *European Journal of Cell Biology* **89(7)**: 499–508. DOI: `10.1016/j.ejcb.2010.02.002`.

Nehme, E., D. Freedman, R. Gordon, B. Ferdman, L. E. Weiss, O. Alalouf, T. Naor, R. Orange, T. Michaeli, and Y. Shechtman. 2020. DeepSTORM3D: Dense 3D Localization Microscopy and PSF Design by Deep Learning. *Nature Methods* **17(7)**: 734–740. DOI: `10.1038/s41592-020-0853-5`.

Newpher, T. M. and S. K. Lemmon. 2006. Clathrin Is Important for Normal Actin Dynamics and Progression of Sla2p-Containing Patches During Endocytosis in Yeast. *Traffic* **7(5)**: 574–588. DOI: `10.1111/j.1600-0854.2006.00410.x`.

Nicovich, P. R., D. M. Owen, and K. Gaus. 2017. Turning Single-Molecule Localization Microscopy into a Quantitative Bioanalytical Tool. *Nature Protocols* **12(3)**: 453–460. DOI: `10.1038/nprot.2016.166`.

Nienhaus, K., G. U. Nienhaus, J. Wiedenmann, and H. Nar. 2005. Structural Basis for Photo-Induced Protein Cleavage and Green-to-Red Conversion of Fluorescent Protein EosFP. *Proceedings of the National Academy of Sciences* **102(26)**: 9156–9159. DOI: `10.1073/pnas.0501874102`.

Novotny, L. 1997. Allowed and Forbidden Light in Near-Field Optics. I. A Single Dipolar Light Source. *JOSA A* **14(1)**: 91–104. DOI: `10.1364/JOSAA.14.000091`.

Nyquist, H. 1928. Certain Topics in Telegraph Transmission Theory. *Transactions of the American Institute of Electrical Engineers* **47(2)**: 617–644. DOI: `10.1109/T-AIEE.1928.5055024`.

Owen, D. M., C. Rentero, J. Rossy, A. Magenau, D. Williamson, M. Rodriguez, and K. Gaus. 2010. PALM Imaging and Cluster Analysis of Protein Heterogeneity at the Cell Surface. *Journal of Biophotonics* **3(7)**: 446–454. DOI: `10.1002/jbio.200900089`.

Pageon, S. V., T. Tabarin, Y. Yamamoto, Y. Ma, P. R. Nicovich, J. S. Bridgeman, A. Cohnen, C. Benzing, Y. Gao, M. D. Crowther, K. Tungatt, G. Dolton, A. K. Sewell, D. A. Price, O. Acuto, R. G. Parton, J. J. Gooding, J. Rossy, J. Rossjohn, and K. Gaus. 2016. Functional Role of T-cell Receptor Nanoclusters in Signal Initiation and Antigen Discrimination. *Proceedings of the National Academy of Sciences* **113(37)**: E5454–E5463. DOI: `10.1073/pnas.1607436113`.

Patterson, G. H. and J. Lippincott-Schwartz. 2002. A Photoactivatable GFP for Selective Photolabeling of Proteins and Cells. *Science* **297(5588)**: 1873–1877. DOI: `10.1126/science.1074952`.

Pedersen, R. T., J. E. Hassinger, P. Marchando, and D. G. Drubin. 2020. Spatial Regulation of Clathrin-Mediated Endocytosis through Position-Dependent Site Maturation. *Journal of Cell Biology* **219(11)**: e202002160. DOI: `10.1083/jcb.202002160`.

Picco, A., W. Kukulski, H. E. Manenschijn, T. Specht, J. A. G. Briggs, and M. Kaksonen. 2018. The Contributions of the Actin Machinery to Endocytic Membrane Bending and Vesicle Formation. *Molecular Biology of the Cell* **29(11)**: 1346–1358. DOI: `10.1091/mbc.E17-11-0688`.

Picco, A., M. Mund, J. Ries, F. Nédélec, and M. Kaksonen. 2015. Visualizing the Functional Architecture of the Endocytic Machinery. *eLife* **4** e04535. DOI: `10.7554/eLife.04535`.

Pike, J. A., A. O. Khan, C. Pallini, S. G. Thomas, M. Mund, J. Ries, S. Natalie, and I. B. Styles. 2018. Topological Data Analysis Quantifies Biological Nano-Structure from Single Molecule Localization Microscopy: 1–16. DOI: `10.1016/B978-0-12-385469-8.00041-1`. arXiv: `1305.4210`.

Pike, J. A., A. O. Khan, C. Pallini, S. G. Thomas, M. Mund, J. Ries, N. S. Poulter, and I. B. Styles. 2020. Topological Data Analysis Quantifies Biological Nano-Structure from Single Molecule Localization Microscopy. *Bioinformatics* **36(5)**: 1614–1621. DOI: `10.1093/bioinformatics/btz788`.

Planade, J., R. Belbahri, M. B. Sanders, A. Guillotin, O. du Roure, A. Michelot, and J. Heuvingh. 2019. Mechanical Stiffness of Reconstituted Actin Patches Correlates Tightly with Endocytosis Efficiency. *PLOS Biology* **17(10)**: e3000500. DOI: `10.1371/journal.pbio.3000500`.

Pleiner, T., M. Bates, S. Trakhanov, C.-T. Lee, J. E. Schliep, H. Chug, M. Böhning, H. Stark, H. Urlaub, and D. Görlich. 2015. Nanobodies: Site-Specific Labeling for Super-Resolution Imaging, Rapid Epitope-Mapping and Native Protein Complex Isolation. *eLife* **4** e11349. DOI: `10.7554/eLife.11349`.

Pontes, B., P. Monzo, and N. C. Gauthier. 2017. Membrane Tension: A Challenging but Universal Physical Parameter in Cell Biology. *Seminars in Cell & Developmental Biology*. Mechanosensing: From Molecules to Tissues **71** 30–41. DOI: `10.1016/j.semcdb.2017.08.030`.

Prasher, D. C., V. K. Eckenrode, W. W. Ward, F. G. Prendergast, and M. J. Cormier. 1992. Primary Structure of the Aequorea Victoria Green-Fluorescent Protein. *Gene* **111(2)**: 229–233. DOI: `10.1016/0378-1119(92)90691-H`.

Rayleigh, L. 1903. On the Theory of Optical Images, with Special Reference to the Microscope. *Journal of the Royal Microscopical Society* **23(4)**: 474–482. DOI: `10.1111/j.1365-2818.1903.tb04831.x`.

Rego, E. H., L. Shao, J. J. Macklin, L. Winoto, G. A. Johansson, N. Kamps-Hughes, M. W. Davidson, and M. G. L. Gustafsson. 2012. Nonlinear Structured-Illumination Microscopy with a Photoswitchable Protein Reveals Cellular Structures at 50-Nm Resolution. *Proceedings of the National Academy of Sciences* **109(3)**: E135–E143. DOI: `10.1073/pnas.1107547108`.

Reichelt, R., A. Holzenburg, E. L. Buhle, M. Jarnik, A. Engel, and U. Aebi. 1990. Correlation between Structure and Mass Distribution of the Nuclear Pore Complex and of Distinct Pore Complex Components. *Journal of Cell Biology* **110(4)**: 883–894. DOI: `10.1083/jcb.110.4.883`.

Reider, A., S. L. Barker, S. K. Mishra, Y. J. Im, L. Maldonado-Báez, J. H. Hurley, L. M. Traub, and B. Wendland. 2009. Syp1 Is a Conserved Endocytic Adaptor That Contains Domains Involved in Cargo Selection and Membrane Tubulation. *The EMBO Journal* **28(20)**: 3103–3116. DOI: `10.1038/emboj.2009.248`.

Ries, J. 2020. SMAP: A Modular Super-Resolution Microscopy Analysis Platform for SMLM Data. *Nature Methods* **17(9)**: 870–872. DOI: `10.1038/s41592-020-0938-1`.

Rodal, A. A., A. L. Manning, B. L. Goode, and D. G. Drubin. 2003. Negative Regulation of Yeast WASp by Two SH3 Domain-Containing Proteins. *Current Biology* **13(12)**: 1000–1008. DOI: `10.1016/S0960-9822(03)00383-X`.

Rodriguez, E. A., R. E. Campbell, J. Y. Lin, M. Z. Lin, A. Miyawaki, A. E. Palmer, X. Shu, J. Zhang, and R. Y. Tsien. 2017. The Growing and Glowing Toolbox of Fluorescent and Photoactive Proteins. *Trends in Biochemical Sciences* **42(2)**: 111–129. DOI: `10.1016/j.tibs.2016.09.010`.

Rust, M. J., M. Bates, and X. Zhuang. 2006. Sub-Diffraction-Limit Imaging by Stochastic Optical Reconstruction Microscopy (STORM). *Nature Methods* **3(10)**: 793–796. DOI: `10.1038/nmeth929`.

Saelens, W., R. Cannoodt, H. Todorov, and Y. Saeys. 2019. A Comparison of Single-Cell Trajectory Inference Methods. *Nature Biotechnology* **37(5)**: 547–554. DOI: `10.1038/s41587-019-0071-9`.

Sage, D., T.-A. Pham, H. Babcock, T. Lukes, T. Pengo, J. Chao, R. Velmurugan, A. Herbert, A. Agrawal, S. Colabrese, A. Wheeler, A. Archetti, B. Rieger, R. Ober, G. M. Hagen, J.-B. Sibarita, J. Ries, R. Henriques, M. Unser, and S. Holden. 2019. Super-Resolution Fight Club: Assessment of 2D and 3D Single-Molecule Localization Microscopy Software. *Nature Methods* **16(5)**: 387–395. DOI: `10.1038/s41592-019-0364-4`.

Saleem, M., S. Morlot, A. Hohendahl, J. Manzi, M. Lenz, and A. Roux. 2015. A Balance between Membrane Elasticity and Polymerization Energy Sets the Shape of Spherical Clathrin Coats. *Nature Communications* **6(1)**: 6249. DOI: `10.1038/ncomms7249`.

Sample, V., R. H. Newman, and J. Zhang. 2009. The Structure and Function of Fluorescent Proteins. *Chemical Society Reviews* **38(10)**: 2852–2864. DOI: `10.1039/B913033K`.

Schaefer, L. H., D. Schuster, and J. Schaffer. 2004. Structured Illumination Microscopy: Artefact Analysis and Reduction Utilizing a Parameter Optimization Approach. *Journal of Microscopy* **216(2)**: 165–174. DOI: `10.1111/j.0022-2720.2004.01411.x`.

Schermelleh, L., P. M. Carlton, S. Haase, L. Shao, L. Winoto, P. Kner, B. Burke, M. C. Cardoso, D. A. Agard, M. G. L. Gustafsson, H. Leonhardt, and J. W. Sedat. 2008. Subdiffraction Multicolor Imaging of the Nuclear Periphery with 3D Structured Illumination Microscopy. *Science* **320(5881)**: 1332–1336. DOI: `10.1126/science.1156947`.

Schlichthaerle, T., M. T. Strauss, F. Schueder, A. Auer, B. Nijmeijer, M. Kueblbeck, V. Jimenez Sabinina, J. V. Thevathasan, J. Ries, J. Ellenberg, and R. Jungmann. 2019. Direct Visualization of Single Nuclear Pore Complex Proteins Using Genetically-Encoded Probes for DNA-PAINT. *Angewandte Chemie International Edition* **58(37)**: 13004–13008. DOI: `10.1002/anie.201905685`.

Schmidt, R., T. Weihs, C. A. Wurm, I. Jansen, J. Rehman, S. J. Sahl, and S. W. Hell. 2021. MINFLUX Nanometer-Scale 3D Imaging and Microsecond-Range Tracking on a Common Fluorescence Microscope. *Nature Communications* **12(1)**: 1478. DOI: `10.1038/s41467-021-21652-z`.

Schnitzbauer, J., Y. Wang, S. Zhao, M. Bakalar, T. Nuwal, B. Chen, and B. Huang. 2018. Correlation Analysis Framework for Localization-Based Superresolution Microscopy. *Proceedings of the National Academy of Sciences* **115(13)**: 3219–3224. DOI: `10.1073/pnas.1711314115`.

Schönle, A. and S. W. Hell. 2007. Fluorescence Nanoscopy Goes Multicolor. *Nature Biotechnology* **25(11)**: 1234–1235. DOI: `10.1038/nbt1107-1234`.

Schueder, F., M. T. Strauss, D. Hoerl, J. Schnitzbauer, T. Schlichthaerle, S. Strauss, P. Yin, H. Harz, H. Leonhardt, and R. Jungmann. 2017. Universal Super-Resolution Multiplexing by DNA Exchange. *Angewandte Chemie International Edition* **56(14)**: 4052–4055. DOI: `10.1002/anie.201611729`.

Schwartz, T. U. 2016. The Structure Inventory of the Nuclear Pore Complex. *Journal of Molecular Biology* **428(10)**: 1986–2000. DOI: `10.1016/j.jmb.2016.03.015`.

Scott, B. L., K. A. Sochacki, S. T. Low-Nam, E. M. Bailey, Q. Luu, A. Hor, A. M. Dickey, S. Smith, J. G. Kerkvliet, J. W. Taraska, and A. D. Hoppe. 2018. Membrane Bending Occurs at All Stages of Clathrin-Coat Assembly and Defines Endocytic Dynamics. *Nature Communications* **9(1)**: 419. DOI: `10.1038/s41467-018-02818-8`.

Sengupta, P., T. Jovanovic-Talisman, D. Skoko, M. Renz, S. L. Veatch, and J. Lippincott-Schwartz. 2011. Probing Protein Heterogeneity in the Plasma Membrane Using PALM and Pair Correlation Analysis. *Nature Methods* **8(11)**: 969–975. DOI: `10.1038/nmeth.1704`.

Shi, X., G. Garcia, J. C. V. D. Weghe, R. McGorty, G. J. Pazour, D. Doherty, B. Huang, and J. F. Reiter. 2017. Super-Resolution Microscopy Reveals That Disruption of Ciliary Transition-Zone Architecture Causes Joubert Syndrome. *Nature Cell Biology* **19(10)**: 1178–1188. DOI: `10.1038/ncb3599`.

Shivanandan, A., J. Unnikrishnan, and A. Radenovic. 2016. On Characterizing Protein Spatial Clusters with Correlation Approaches. *Scientific Reports* **6(1)**: 1–12. DOI: `10.1038/srep31164`.

Shroff, H., C. G. Galbraith, J. A. Galbraith, and E. Betzig. 2008. Live-Cell Photoactivated Localization Microscopy of Nanoscale Adhesion Dynamics. *Nature Methods* **5(5)**: 417–423. DOI: `10.1038/nmeth.1202`.

Sieben, C., N. Banterle, K. M. Douglass, P. Gönczy, and S. Manley. 2018. Multicolor Single-Particle Reconstruction of Protein Complexes. *Nature Methods* **15(10)**: 777. DOI: `10.1038/s41592-018-0140-x`.

Smith, C. S., N. Joseph, B. Rieger, and K. A. Lidke. 2010. Fast, Single-Molecule Localization That Achieves Theoretically Minimum Uncertainty. *Nature Methods* **7(5)**: 373–375. DOI: `10.1038/nmeth.1449`.

Sochacki, K. A., B. L. Heine, G. J. Haber, J. R. Jimah, B. Prasai, M. A. Alfonzo-Méndez, A. D. Roberts, A. Somasundaram, J. E. Hinshaw, and J. W. Taraska. 2021. The Structure and Spontaneous Curvature of Clathrin Lattices at the Plasma Membrane. *Developmental Cell* **56(8)**: 1131–1146.e3. DOI: `10.1016/j.devcel.2021.03.017`.

Sochacki, K. A. and J. W. Taraska. 2019. From Flat to Curved Clathrin: Controlling a Plastic Ratchet. *Trends in Cell Biology* **29(3)**: 241–256. DOI: `10.1016/j.tcb.2018.12.002`.

Soulard, A., S. Friant, C. Fitterer, C. Orange, G. Kaneva, G. Mirey, and B. Winsor. 2005. The WASP/Las17p-interacting Protein Bzz1p Functions with Myo5p in an Early Stage of Endocytosis. *Protoplasma* **226(1-2)**: 89–101. DOI: `10.1007/s00709-005-0108-4`.

Speiser, A., L.-R. Müller, P. Hoess, U. Matti, C. J. Obara, W. R. Legant, A. Kreshuk, J. H. Macke, J. Ries, and S. C. Turaga. 2021. Deep Learning Enables Fast and Dense Single-Molecule Localization with High Accuracy. *Nature Methods* **18(9)**: 1082–1090. DOI: `10.1038/s41592-021-01236-x`.

Steffens, H., A. C. Mott, S. Li, W. Wegner, P. Švehla, V. W. Y. Kan, F. Wolf, S. Liebscher, and K. I. Willig. 2021. Stable but Not Rigid: Chronic in Vivo STED Nanoscopy Reveals Extensive Remodeling of Spines, Indicating Multiple Drivers of Plasticity. *Science Advances* **7(24)**: eabf2806. DOI: `10.1126/sciadv.abf2806`.

Stehr, F., J. Stein, F. Schueder, P. Schwille, and R. Jungmann. 2019. Flat-Top TIRF Illumination Boosts DNA-PAINT Imaging and Quantification. *Nature Communications* **10(1)**: 1268. DOI: `10.1038/s41467-019-09064-6`.

Stephan, T., A. Roesch, D. Riedel, and S. Jakobs. 2019. Live-Cell STED Nanoscopy of Mitochondrial Cristae. *Scientific Reports* **9(1)**: 12419. DOI: `10.1038/s41598-019-48838-2`.

Stimpson, H. E. M., C. P. Toret, A. T. Cheng, B. S. Pauly, and D. G. Drubin. 2009. Early-Arriving Syp1p and Ede1p Function in Endocytic Site Placement and Formation in Budding Yeast. *Molecular Biology of the Cell* **20(22)**: 4640–4651. DOI: `10.1091/mbc.e09-05-0429`.

Strauss, S., P. C. Nickels, M. T. Strauss, V. Jimenez Sabinina, J. Ellenberg, J. D. Carter, S. Gupta, N. Janjic, and R. Jungmann. 2018. Modified Aptamers Enable Quantitative Sub-10-Nm Cellular DNA-PAINT Imaging. *Nature Methods* **15(9)**: 685–688. DOI: `10.1038/s41592-018-0105-0`.

Sun, Y., A. C. Martin, and D. G. Drubin. 2006. Endocytic Internalization in Budding Yeast Requires Coordinated Actin Nucleation and Myosin Motor Activity. *Developmental Cell* **11(1)**: 33–46. DOI: `10.1016/j.devcel.2006.05.008`.

Sydor, A. M., K. J. Czymmek, E. M. Puchner, and V. Mennella. 2015. Super-Resolution Microscopy: From Single Molecules to Supramolecular Assemblies. *Trends in Cell Biology* **25(12)**: 730–748. DOI: `10.1016/j.tcb.2015.10.004`.

Szymborska, A., A. de Marco, N. Daigle, V. C. Cordes, J. A. G. Briggs, and J. Ellenberg. 2013. Nuclear Pore Scaffold Structure Analyzed by Super-Resolution Microscopy and Particle Averaging. *Science* **341(6146)**: 655–658. DOI: `10.1126/science.1240672`.

Tagiltsev, G., C. A. Haselwandter, and S. Scheuring. 2021. Nanodissected Elastically Loaded Clathrin Lattices Relax to Increased Curvature. *Science Advances* **7(33)**: eabg9934. DOI: `10.1126/sciadv.abg9934`.

Tang, H.-Y., J. Xu, and M. Cai. 2000. Pan1p, End3p, and Sla1p, Three Yeast Proteins Required for Normal Cortical Actin Cytoskeleton Organization, Associate with Each Other and Play Essential Roles in Cell Wall Morphogenesis. *Molecular and Cellular Biology* **20(1)**: 12–25. DOI: `10.1128/MCB.20.1.12-25.2000`.

Taylor, M. J., D. Perrais, and C. J. Merrifield. 2011. A High Precision Survey of the Molecular Dynamics of Mammalian Clathrin-Mediated Endocytosis. *PLOS Biology* **9(3)**: e1000604. DOI: `10.1371/journal.pbio.1000604`.

Thevathasan, J. V., M. Kahnwald, K. Cieśliński, P. Hoess, S. K. Peneti, M. Reitberger, D. Heid, K. C. Kasuba, S. J. Hoerner, Y. Li, Y.-L. Wu, M. Mund, U. Matti, P. M. Pereira, R. Henriques, B. Nijmeijer, M. Kueblbeck, V. J. Sabinina, J. Ellenberg, and J. Ries. 2019. Nuclear Pores as Versatile Reference Standards for Quantitative Superresolution Microscopy. *Nature Methods* **16(10)**: 1045–1053. DOI: `10.1038/s41592-019-0574-9`.

Thompson, R. E., D. R. Larson, and W. W. Webb. 2002. Precise Nanometer Localization Analysis for Individual Fluorescent Probes. *Biophysical Journal* **82(5)**: 2775–2783. DOI: `10.1016/S0006-3495(02)75618-X`.

Thorn, K. 2016. A Quick Guide to Light Microscopy in Cell Biology. *Molecular Biology of the Cell* **27(2)**: 219–222. DOI: `10.1091/mbc.e15-02-0088`.

Tolsma, T. O., H. P. Febvre, D. M. Olson, and S. M. Di Pietro. 2020. Cargo-Mediated Recruitment of the Endocytic Adaptor Protein Sla1. *Journal of Cell Science*: jcs.247684. DOI: `10.1242/jcs.247684`.

Toret, C. P., L. Lee, M. Sekiya-Kawasaki, and D. G. Drubin. 2008. Multiple Pathways Regulate Endocytic Coat Disassembly in Saccharomyces Cerevisiae for Optimal Downstream Trafficking. *Traffic* **9(5)**: 848–859. DOI: `10.1111/j.1600-0854.2008.00726.x`.

Toshima, J. Y., J. Toshima, M. Kaksonen, A. C. Martin, D. S. King, and D. G. Drubin. 2006. Spatial Dynamics of Receptor-Mediated Endocytic Trafficking in Budding Yeast Revealed by Using Fluorescent α-Factor Derivatives. *Proceedings of the National Academy of Sciences* **103(15)**: 5793–5798. DOI: `10.1073/pnas.0601042103`.

Umasankar, P. K., S. Sanker, J. R. Thieman, S. Chakraborty, B. Wendland, M. Tsang, and L. M. Traub. 2012. Distinct and Separable Activities of the Endocytic Clathrin-Coat Components Fcho1/2 and AP-2 in Developmental Patterning. *Nature Cell Biology* **14(5)**: 488–501. DOI: `10.1038/ncb2473`.

van Leewenhoeck, A. 1677. Observations, Communicated to the Publisher by Mr. Antony van Leewenhoeck, in a Dutch Letter of the 9th of Octob. 1676. Here English'd: Concerning Little Animals by Him Observed in Rain-Well-Sea. and Snow Water; as Also in Water Wherein Pepper Had Lain Infused. *Philosophical Transactions (1665-1678)* **12** 821–831.

Venkataramani, V., F. Herrmannsdörfer, M. Heilemann, and T. Kuner. 2016. SuReSim: Simulating Localization Microscopy Experiments from Ground Truth Models. *Nature Methods* **13(4)**: 319–321. DOI: `10.1038/nmeth.3775`.

Verdier, T., J. Gunzenhauser, S. Manley, and M. Castelnovo. 2017. Single Particle Maximum Likelihood Reconstruction from Superresolution Microscopy Images. *PLOS ONE* **12(3)**: e0172943. DOI: `10.1371/journal.pone.0172943`.

von Appen, A., J. Kosinski, L. Sparks, A. Ori, A. L. DiGuilio, B. Vollmer, M.-T. Mackmull, N. Banterle, L. Parca, P. Kastritis, K. Buczak, S. Mosalaganti, W. Hagen, A. Andres-Pons, E. A. Lemke, P. Bork, W. Antonin, J. S. Glavy, K. H. Bui, and M. Beck. 2015. *In Situ* Structural Analysis of the Human Nuclear Pore Complex. *Nature* **526(7571)**: 140–143. DOI: `10.1038/nature15381`.

Waltz, R., J. Morales, J. Nocedal, and D. Orban. 2006. An Interior Algorithm for Nonlinear Optimization That Combines Line Search and Trust Region Steps. *Mathematical Programming* **107(3)**: 391–408. DOI: `10.1007/s10107-004-0560-5`.

Wang, L., A. Brock, B. Herberich, and P. G. Schultz. 2001. Expanding the Genetic Code of Escherichia Coli. *Science* **292(5516)**: 498–500. DOI: `10.1126/science.1060077`.

Wang, S., J. R. Moffitt, G. T. Dempsey, X. S. Xie, and X. Zhuang. 2014. Characterization and Development of Photoactivatable Fluorescent Proteins for Single-Molecule–Based Superresolution Imaging. *Proceedings of the National Academy of Sciences* **111(23)**: 8452–8457. DOI: `10.1073/pnas.1406593111`.

Warren, D. T., P. D. Andrews, C. W. Gourlay, and K. R. Ayscough. 2002. Sla1p Couples the Yeast Endocytic Machinery to Proteins Regulating Actin Dynamics. *Journal of Cell Science* **115(8)**: 1703–1715. DOI: `10.1242/jcs.115.8.1703`.

Wassie, A. T., Y. Zhao, and E. S. Boyden. 2019. Expansion Microscopy: Principles and Uses in Biological Research. *Nature Methods* **16(1)**: 33–41. DOI: `10.1038/s41592-018-0219-4`.

Willy, N. M., J. P. Ferguson, A. Akatay, S. Huber, U. Djakbarova, S. Silahli, C. Cakez, F. Hasan, H. C. Chang, A. Travesset, S. Li, R. Zandi, D. Li, E. Betzig, E. Cocucci, and C. Kural. 2021. De Novo Endocytic Clathrin Coats Develop Curvature at Early Stages of Their Formation. *Developmental Cell* **56(22)**: 3146–3159.e5. DOI: `10.1016/j.devcel.2021.10.019`.

Winter, D., T. Lechler, and R. Li. 1999. Activation of the Yeast Arp2/3 Complex by Bee1p, a WASP-family Protein. *Current Biology* **9(9)**: 501–505. DOI: `10.1016/S0960-9822(99)80218-8`.

Wu, Y.-L., P. Hoess, A. Tschanz, U. Matti, M. Mund, and J. Ries. 2021. Maximum-Likelihood Model Fitting for Quantitative Analysis of SMLM Data.

Wu, Y.-L., A. Tschanz, L. Krupnik, and J. Ries. 2020. Quantitative Data Analysis in Single-Molecule Localization Microscopy. *Trends in Cell Biology* **0(0)**. DOI: `10.1016/j.tcb.2020.07.005`.

Xu, K., H. P. Babcock, and X. Zhuang. 2012. Dual-Objective STORM Reveals Three-Dimensional Filament Organization in the Actin Cytoskeleton. *Nature Methods* **9(2)**: 185–188. DOI: `10.1038/nmeth.1841`.

Xu, K., G. Zhong, and X. Zhuang. 2013. Actin, Spectrin, and Associated Proteins Form a Periodic Cytoskeletal Structure in Axons. *Science* **339(6118)**: 452–456. DOI: `10.1126/science.1232251`.

Yeung, B. G., H. L. Phan, and G. S. Payne. 1999. Adaptor Complex-independent Clathrin Function in Yeast. *Molecular Biology of the Cell* **10(11)**: 3643–3659. DOI: `10.1091/mbc.10.11.3643`.

Yoshida, A., N. Sakai, Y. Uekusa, Y. Imaoka, Y. Itagaki, Y. Suzuki, and S. H. Yoshimura. 2018. Morphological Changes of Plasma Membrane and Protein Assembly during Clathrin-Mediated Endocytosis. *PLOS Biology* **16(5)**: e2004786. DOI: `10.1371/journal.pbio.2004786`.

Zeno, W. F., J. B. Hochfelder, A. S. Thatte, L. Wang, A. K. Gadok, C. C. Hayden, E. M. Lafer, and J. C. Stachowiak. 2021. Clathrin Senses Membrane Curvature. *Biophysical Journal* **120(5)**: 818–828. DOI: `10.1016/j.bpj.2020.12.035`.

Zhang, Y., L. K. Schroeder, M. D. Lessard, P. Kidd, J. Chung, Y. Song, L. Benedetti, Y. Li, J. Ries, J. B. Grimm, L. D. Lavis, P. De Camilli, J. E. Rothman, D. Baddeley, and J. Bewersdorf. 2020. Nanoscale Subcellular Architecture Revealed by Multicolor Three-Dimensional Salvaged Fluorescence Imaging. *Nature Methods* **17(2)**: 225–231. DOI: `10.1038/s41592-019-0676-4`.

Zhao, H., A. Michelot, E. V. Koskela, V. Tkach, D. Stamou, D. G. Drubin, and P. Lappalainen. 2013. Membrane-Sculpting BAR Domains Generate Stable Lipid Microdomains. *Cell Reports* **4(6)**: 1213–1223. DOI: `10.1016/j.celrep.2013.08.024`.

Zhu, L., W. Zhang, D. Elnatan, and B. Huang. 2012. Faster STORM Using Compressed Sensing. *Nature Methods* **9(7)**: 721–723. DOI: `10.1038/nmeth.1978`.

Zwettler, F. U., S. Reinhard, D. Gambarotto, T. D. M. Bell, V. Hamel, P. Guichard, and M. Sauer. 2020. Molecular Resolution Imaging by Post-Labeling Expansion Single-Molecule Localization Microscopy (Ex-SMLM). *Nature Communications* **11(1)**: 3388. DOI: `10.1038/s41467-020-17086-8`.